SAPIENZA
UNIVERSITÀ DI ROMA

Dottorato di Ricerca in Fisica, XXVI Ciclo

Ph.D. Thesis

Soft electronic matter in underdoped cuprates

Supervisors:
Dott. José Lorenzana
Prof. Marco Grilli

Candidate:
Matteo Capati

A.A. 2013-2014

Contents

Introduction

Since the discovery in 1986 of superconductivity in cuprates, this class of materials has represented a paradigmatic example of strongly correlated systems. The intense research activity has led to the understanding of many interesting properties. In particular the complex magnetic phases in the underdoped region of the phase diagram, in addition to their possible relevance for superconducting mechanisms, seem to have remarkable analogies with soft matter physics.

Typically the key structural elements are represented by CuO_2 layers. They are separated by other elements (La, Ce, O, Y, Ba) which play the role of charge reservoirs. The parent compound is a Mott insulator with long-range antiferromagnetic order, that can be modelled by a two-dimensional Heisenberg model describing Cu spins. The partial substitution of the interlayer elements with atoms of different valence, brings extra electrons or holes in the CuO_2 layers. Increasing chemical doping can destroy the antiferromagnetic ordered phase of the stoichiometric compound.

Higher doping (overdoping) eventually leads to a conventional Fermi liquid. But the subject of this work will be the complex electronic phases which appear reducing the doping with respect to the optimal one (underdoping). Although the low temperature long-range order is destroyed above a concentration of added holes per planar copper $x \approx 0.02$, signatures of the magnetic order persist in the dynamical spin and charge correlations up to the overdoped regime.

In unconventional superconductors, like for example heavy-fermion systems or pnictides, superconductivity arises in a region of the phase diagram close to an ordered phase [L. Taillefer, Ann. Rev. Cond. Matt. Phys. **1**, 51 (2010)]. Does this scenario hold for cuprates? If so, an important question is what is the ordered phase in the underdoped regime.

A peculiar characteristic of the normal phase of the underdoped cuprates is the presence of a region characterized by a pseudogap that is a suppression of the electronic density of states at the Fermi level observed only in certain directions of the Brillouin zone. This pseudogap can suggest the pre-formation of the Cooper pairs that lead to superconductivity only when a phase coherence is established. Although we will not deal with the electronic spectra, we will explore the idea according to which there is some form of real-space electronic order between the antiferromagnetic state and the superconducting state. In this case the pseudogap can represent a signature of this ordered state. Indeed the region of the doping-temperature phase diagram in which the pseudogap appears, is represented by a line which decreases for increasing doping and extrapolates to zero

inside the superconducting region. This behavior is very similar to that of the ordered phases of a wide class of unconventional superconductors. Does the pseudogap represent a real thermodynamic transition? In this case cuprates would belong to the same phenomenology of the other unconventional superconducting materials. Our purpose will be to investigate the possibility of a broken symmetry which characterizes an ordered state in the region of the phase diagram characterized by the pseudogap, and also the possible existence of a real thermodynamic transition. We find indeed broken symmetries that have interesting analogies with the liquid crystal phases and that can explain neutron scattering experiments.

In this thesis we will focus our attention mainly on the hole-doped lanthanum cuprates like $La_{2-x}Sr_xCuO_4$. In particular we want to clarify the way in which the system destroys the long-range magnetic order to reorganize itself with another type of order still not well defined. We will use a variety of approaches starting from a microscopic model. While in chapter 1 we briefly describe structure and properties of cuprates, their typical phase diagram and the experiments performed to investigate the underdoped compounds, in chapter 2 we introduce the microscopic physics of these materials by means of the Hubbard model, which allows to deal with strongly correlated electron systems like cuprates. We also discuss the variational methods we will use to treat this model when applied to hole-doped CuO_2 planes. In chapter 3 we define a classical spin model arising from the quantum model treated in the mean field approximation. We will see that topological defects, like vortices, interact with each other in the same way as two-dimensional Coulomb charges. In chapter 4 we describe the Monte Carlo techniques which we will use to simulate a two-dimensional lattice Coulomb gas, reproducing the physics of the vortices within the spin model.

As a starting point of our work, in chapter 5, we look at the results of the variational computations, which suggest that at very small concentration holes tend to localize in the core of a vortex of the antiferromagnetic spin order. Such vortices have an energy which diverges logarithmically with the system size. The system avoids this large energy cost by forming tightly bound vortex-antivortex (VA) pairs. The residual attraction between pairs competes with the Coulomb repulsion due to the charged doping holes in the core of the spin vortices. The idea which we will explore in this work is that the neutron scattering experiments on underdoped region of lanthanum cuprates can be explained in terms of a phase which breaks rotational and inversion symmetry. Such phase is formed by oriented stripe segments which do not need to have positional order, thus we call it *ferronematic*. The building blocks of this phase are represented by the VA pairs, which tend to aggregate each other in a 'head-to-tail' way to form chains, being their reciprocal interaction dominated by an anisotropic short-range core-core contribution.

In chapter 6 we describe how the resulting spin textures can be well described by an XY-model with an appropriate value of the spin stiffness. It reproduces the long-range physics of the Hubbard model without the complications of the fermionic degrees of freedom, and allows us to use a large cluster. We analyse the connection between the spin current due to these oriented segments, the polarization of such segments and the incommensurability of the peaks in the resulting spin structure factor.

Using the correspondence between the XY-model and the two-dimensional Coulomb gas, we can construct an effective lattice model, described in chapter 7, according to which each vortex is mapped in a positive 2D topological charge and each antivortex in a negative 2D topological charge.

The object of the chapter 8 is the discussion of the results of the Monte Carlo simulations performed to study the temperature and doping evolution of the complex phases of cuprates described in the previous sections. In this way we can leave the interacting topological charges free to evolve in the thermal bath, without taking into account the spin configuration. Only at the end of the simulations we can reconstruct the total spin distribution. With these simulations we want to characterize possible thermodynamic transitions and reconstruct the phase diagram of the underdoped cuprates.

Chapter 1

Basic properties of cuprates

In this chapter we briefly overview of properties of cuprates referring to [2, 3, 4]. After a short discussion about the crystal structure and the electronic properties, we report the phase diagram of $La_{2-x}Sr_xCuO_4$, chosen as the prototype of cuprates, highlighting the experimental evidences of the underdoped region. We focus mainly on the neutron scattering experiments which suggest magnetic and charge correlations even after the disruption of the long-range antiferromagnetic order due to an increasing concentration of dopant holes. In particular magnetic neutron scattering peaks have been detected at a wave-vector different from that characterizing the antiferromagnetic state. In a family of lanthanum cuprate both spin and charge Bragg peaks have been detected. They have been interpreted with the presence of static unidirectional long-range structures of charge, called "stripes". Although evidences of long-range order have been found only in a particular compound, the broadened magnetic peaks detected in many cuprate materials, suggest the presence of complex phases which can exhibit particular types of spin and charge order. Our purpose is to explain these complex phases in terms of the broken symmetry phases of soft matter physics.

1.1 General properties

More than twenty-five years ago, Bednorz and Müller [1] announced the discovery of superconductivity in a ceramic copper oxide material at a temperature of about 30 K. It generated a frenetic race for the preparation of materials with even higher critical temperatures, that reached in a brief time surprising values ($\sim 170K$). The common feature of these compounds, commonly called "cuprates", is the presence of one or more CuO_2 planes, in which the most relevant physical mechanisms take place.

1.1.1 Crystal structure

A striking feature of all the cuprate superconductors is their nearly two-dimensional nature. These materials have a layered structure with a stacking sequence of planes with a CuO_2 unit cell and charge-reservoir blocks (see Fig.1.1). The left panel shows the structure of La_2CuO_4 (LCO), one of the first discovered high T_c superconductors (HTSC). In this

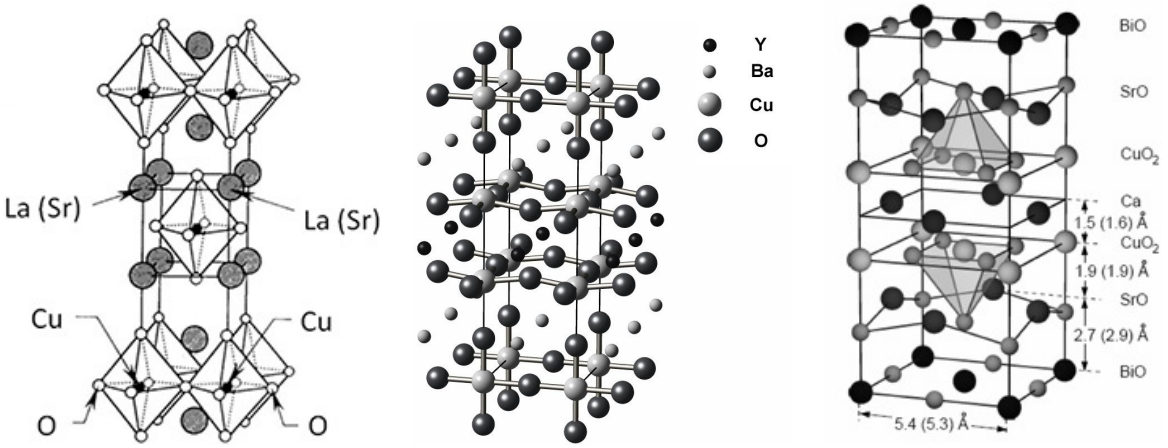

Figure 1.1: LSCO, YBCO and BSCCO crystal structures.

compound, the CuO_2 planes are alternated with LaO planes, in such a way that each Cu atom is at the center of an octahedron made by four planar and two apical oxygen atoms. The former are distant ~ 1.9 Å from the copper ion, while the latter ~ 2.4 Å. In order to be in a stable closed-shell configuration Lanthanum (La:[Xe](5d)(6s)^2) loses three electrons and becomes La^{3+}, while each oxygen (O:[He](2s)^2(2p)^4) completes the p shell gaining two electrons, and passing to a valence state O^{2-}. To conserve charge neutrality, the copper atoms (Cu:[Ar](3d)^{10}(4s)) must be in a Cu^{2+} state, which is obtained by losing the 4s (weakly bounded to the atom) and one d electron. The remaining panels of Fig.1.1 show the crystalline structure of other cuprates, i.e. $YBa_2Cu_3O_{6+x}$ (YBCO) and $Bi_2Sr_2CaCu_2O_8$ (BSCCO). They have both two CuO_2 planes per cell. A peculiar characteristic of YBCO is the presence of Cu-O chains between the planes.

Although each cuprate material has its peculiar characteristics, the valence states of Cu and O in the planes are the same in all these compounds. Now we focus on the electronic configuration of the CuO_2 planes.

1.1.2 Electronic structure

As already mentioned, Cu^{2+} has one unpaired d electron. In a isolated Cu atom, the five d orbitals are degenerate. This degeneracy produced by the rotational invariance of isolated ions is removed by the tetragonal lattice structure. The perfect oxygens octahedron surrounding the Cu atom would split the Cu d orbitals in the doublet given by $d_{x^2-y^2}$ and $d_{3z^2-r^2}$ and the triplet constituted by d_{xy}, d_{yz} and d_{zx}. Actually the octahedron results elongated because of the Jahn-Teller distortion which further removes the electronic degeneration as schematically shown in Fig. 1.2. So the highest partially occupied orbital has $d_{x^2-y^2}$ character. The lobes of this orbital point directly to the p orbitals of the neighboring oxygen, forming a strong covalent bond with a large hopping integral t_{pd}, which represents the energy gained by an electron by hopping from one Cu d orbital to the O p orbitals. The other Cu orbitals at lower energies are filled, and in first approximation

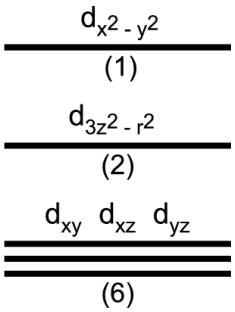

Figure 1.2: Splitting of the Cu d orbitals due to the crystal field and the Jahn-Teller distortion in cuprates. The numbers in parentheses indicate the occupations of the different levels in the stoichiometric compound.

they will be neglected. So, since in each unit cell we have the Cu $3d_{x^2-y^2}$ orbital and two oxygen p orbitals (p_x and p_y), a starting point to describe the electronic structure of the cuprates is given by the so-called 3-band model [5, 6], in which the $d_{x^2-y^2}$ Cu orbital and the p_x, p_y O orbitals are admixed by t_{pd}. Also the admixtures between the oxygen orbitals must be taken into account. To describe the correlation energy for doubly occupying the copper orbitals, it is more convenient to go to the "hole" picture. As already mentioned, the Cu d^9 configuration is represented by the highest electron energy level E_d^e occupied by a single electron, while the oxygen p orbitals at energy E_p^e lower than E_d^e, are both doubly occupied. In "hole" picture E_d^e corresponds to the lower hole energy level E_d^h, which is occupied by a single hole with spin 1/2, while the oxygen p orbitals are empty of holes and lies at energy E_p^h higher than E_d^h (see Fig. 1.3). The energy to doubly occupy E_d^h

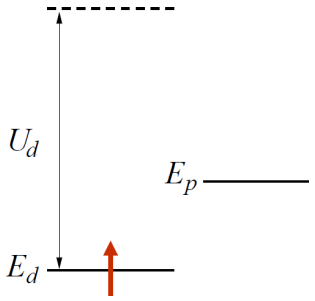

Figure 1.3: From Ref. [3]. Copper d and oxygen p orbitals in the hole picture. A single hole with spin 1/2 occupies the copper d orbital in the insulator.

(leading to a d^8 configuration) is U_d, which is very large and it can be considered infinite in a first approximation. The lowest energy excitation is the charge transfer excitation where the hole hops from d to p with amplitude $-t_{pd}$. If $E_p^h - E_d^h$ is sufficiently large compared with t_{pd}, the hole will form a local moment on Cu. This is referred to as a charge transfer insulator in the scheme of Ref. [7]. What occurs upon doping? As an example, let us consider $La_{2-x}Sr_xCuO_4$ (LSCO), where an additional electron is removed from the CuO_2 plane by the substitution of a La atom by a Sr atom. So, in the hole

picture, x holes per Cu are added to the layer. Due to the large U_d, the hole will reside on the oxygen p orbital. A hole at the oxygen can be in a symmetric or antisymmetric state with respect to the central hole at the copper ion. These states can be combined with the Cu hole to form a spin singlet or triplet state. To second order in perturbation theory around the atomic limit, Zhang and Rice [8] showed that the spin singlet state has the lowest energy, and assumed that it is possible to work in this singlet subspace without changing the physics of the problem.

Notice that there are hole-doped and electron-doped cuprates. Together with LSCO, also BSCCO and YBCO, with two planes CuO_2 per unit cell, are doped by adding holes. An example of electron doped cuprates is represented by $Nd_{2-x}Ce_xCuO_4$, in which electrons in the CuO_2 plane can be added by substitution of Ce^{4+} with Nd^{3+}.

1.1.3 Phase diagram

The generic phase diagram of the cuprates is reported in Fig. 1.4. The balance between the different phases is controlled by the temperature T and the doping concentration x. The results for different cuprate families tend to be similar, so we will focus on

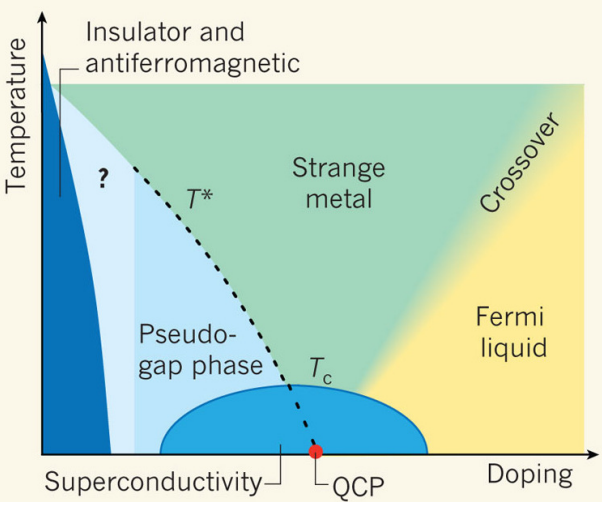

Figure 1.4: Phase diagram of the cuprates, from Ref. [9].

$La_{2-x}Sr_xCuO_4$, which is the compound we will mainly refer to in the following of this thesis. The other compounds have the same peculiar characteristics[1]. For $x = 0$ there are no free carriers and as long as T is lower than the Néel temperature $T_N \sim 300$K, the system has long-range antiferromagnetic (AF) order. Although band calculations predict a metal character for this phase, the strong electron-electron repulsion makes the material

[1]The doping concentration x in $La_{2-x}Sr_xCuO_4$ corresponds to the hole concentration n_h within the CuO_2 planes. The case of $YBa_2Cu_3O_{6+x}$ is slightly different, since the dopant holes are not distributed uniquely within the CuO_2 planes, due to the presence of Cu-O chains between the planes. Typically in YBCO, n_h represents the 20% of the doping concentration x [10].

a Mott insulator. When the doping concentration increases the long-range AF order is destroyed, but short-range magnetic correlations survive up to the high doping regime. In the low doping region, a low-temperature spin-glass phase appears just before the occurrence of the superconductivity which takes place at relatively low doping ($x \sim 0.05$) and low temperatures. The critical temperature T_c of the transition between the low temperature superconducting phase and the normal state, is an increasing function of the doping until the optimal doping $\bar{x} \sim 0.15$, which is the doping concentration maximizing T_c. For $x > \bar{x}$, i.e. in the overdoped regime, T_c decreases with x. Superconductivity definitively disappears at $x \sim 0.3$. At higher doping concentrations the material is a normal metal, namely a Fermi liquid. A structural phase transition was also found in this compound. At high temperature the structure is tetragonal, but at lower temperatures the CuO_6 octahedra are deformed giving rise to an orthorhombic structure. Close to optimal doping, this rich phase diagram exhibits a region characterized by 'strange metal' behavior suggestive of strong fluctuations associated with a quantum critical point. Such a critical point requires a line of classical phase transitions terminating at zero temperature near optimal doping inside the superconducting 'dome'. The underdoped region of the temperature-doping phase diagram from which superconductivity emerges is referred to as the "pseudogap" because evidence exists for partial suppression of the electronic states at the Fermi level in certain directions of the Brillouin zone, but so far it is not clear whether the pseudogap is a distinct phase or a continuous evolution of physical properties on cooling.

The purpose of this work is to shed light on this open issue, assuming that some form of real-space electronic order occurs in the pseudogap region. Thus we look for a broken symmetry phase as soon as the long-range AF phase is destroyed by the increasing concentration of doping (we will focus on the region identified by the question mark '?' in Fig. 1.4). This ordered state would imply the occurrence of a real thermodynamic transition. Such a fact would make the phenomenology of cuprates similar to that of many other unconventional superconductors, like for example organic superconductors, pnictides or heavy-fermion systems, in which superconductivity emerges close to a broken symmetry phase [11] (see the phase diagram of these materials reported in Fig. 1.5). Since this aspect is central in this thesis, we report a brief summary of the experimental evidences of the pseudogap and mainly of the spin and charge correlations occurring in this region of the phase diagram of the cuprates.

1.2 Experimental evidences of the pseudogap

Angle-resolved photoemission experiments

Important elucidations about electronic states come from angle-resolved photoemission (ARPES). In particular this technique measures the dispersion of electronic states near the Fermi level: one shines ultraviolet photons on a flat crystal surface and detects emitted electrons as a function of angle $\Omega(\theta, \varphi)$, analysing the electron current as a function of kinetic energy. The quasi-two-dimensional structure of cuprates allows to

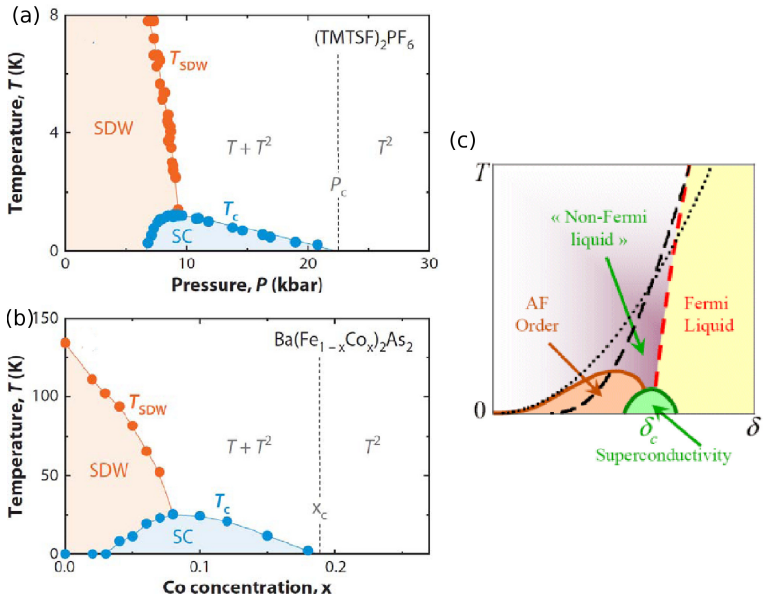

Figure 1.5: Phase diagram of other unconventional superconductors: (a) organic superconductor $(TMTSF)_2PF_6$, (b) iron-pnictide superconductor $Ba(Fe_{1-x}Co_x)_2As_2$ and (c) generic heavy-fermion system. In all these materials the superconducting dome appears associated to a broken symmetry phase.

univocally establish the initial momentum $\hbar k$ and energy $\hbar\omega$ of the photoemitted electron, by using the conservation laws for momentum and energy. The intensity $I(k,\omega)$ of the photoemission spectrum is directly linked the spectral density $A(k,\omega)$ according to $I(k,\omega) \sim f(\omega)A(k,\omega)$, being $f(\omega)$ the Fermi function. ARPES results for the underdoped BSCCO [12] show that the opening of the pseudogap at $T = T^*$ implies the destruction of the Fermi surface at the points $(0,\pi)$ and $(\pi,0)$ (they are called "antinodal point" since they represent the maximum of the gap). When T decreases the Fermi surface progressively shrinks first to the so-called "Fermi arcs" and then to the unique point (called "nodal point" since the gap goes to zero) in the (π,π) direction for $T = T_c$ (see Fig. 1.6). This

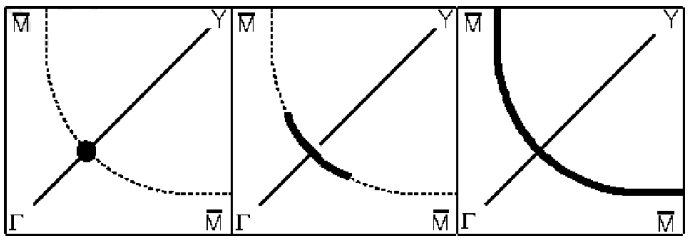

Figure 1.6: From Ref. [12]. Scheme of the Fermi surface evolution in underdoped BSCCO for varying temperature. For $T = T_c$ (left panel) the Fermi surface is shrunk to the d-wave node; (central panel) for increasing T the gap extension shrinks until (right panel) the Fermi surface is totally reconstructed for $T > T^*$.

implies that the pseudogap has the same symmetry $d_{x^2-y^2}$ of the superconducting gap.

These results are confirmed by more recent ARPES measurements on LSCO [13], which suggest the presence of the nodal point in the (π, π) direction even for $x = 0.03$, while in the antinodal directions the gap remains until one approaches optimal doping ($x = 0.15$). Fig. 1.7 shows ARPES measurements of spectral weight along a quadrant of the Fermi surface for a range of dopings in LSCO [14] At low doping, the nodal arc expands, sug-

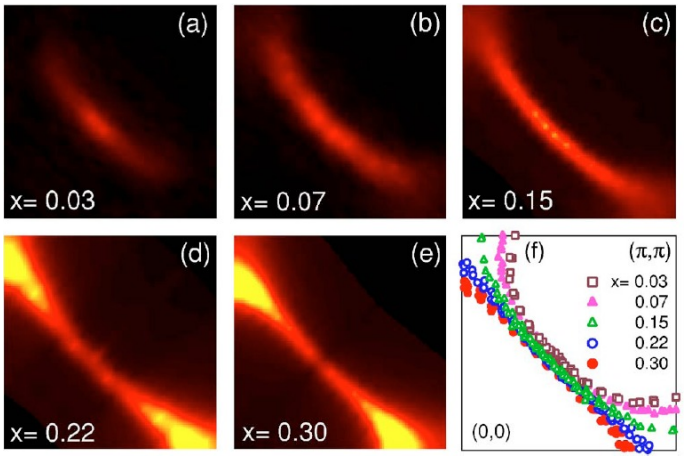

Figure 1.7: From Ref. [14]. (a)-(e) Spectral weight along the Fermi surface (in the first quadrant) measured by ARPES on LSCO crystals for various dopings. (f) Location of the Fermi surface for various dopings determined from the measurements.

gesting the presence of electronic states at the Fermi energy, until it covers most of the nominal Fermi surface near optimal doping. At higher doping the Fermi surface changes from a hole-like shape centered around (π, π) to an electron-like shape, closed around $(0, 0)$. So the pseudogap has a continuous evolution from the superconducting gap and maybe a common origin, i.e. the electron pairing.

Tunnelling spectroscopy experiments

A powerful tool used to investigate the electronic density of states near the Fermi level of a superconductor is the tunnelling spectroscopy. An oxide layer is grown on a superconductor which is then covered with a normal metal layer. In thermodynamic equilibrium at zero degrees, the Fermi levels of the two systems are equal and no current flows through an external circuit connected between the metal and the superconductor. If an external positive voltage exceeding Δ/e (being 2Δ the superconducting gap) is applied to the metal, electrons tunnel from the metal through the insulator to the unoccupied states of the superconductor. Therefore there will be a large peak in the tunnelling conductance as the bias voltage approaches the gap value, $eV = \Delta$. Conversely with negative bias, when $eV = -\Delta$, electrons will tunnel from the occupied states of the superconductor to the normal metal. Thus there will be a gap in the conductance of width 2Δ centred at the Fermi level at zero bias. One of the earliest reports of a pseudogap in

tunnelling spectroscopy is that of Tao *et al.* [15], who found a gap-like depression in the tunnelling conductance of BSCCO junctions in the normal state. An analogous result was found later by Renner *et al.* [16]. Using a scanning tunnelling microscope (STM), they find, below the superconducting transition temperature, a depression in the conductivity at zero bias and two symmetrically placed conductance peaks previously observed by several investigators in this material. While the peaks disappear at T_c, a conductance depression remains in the normal state up to room temperature, which is identified with the pseudogap (see Fig.1.8).

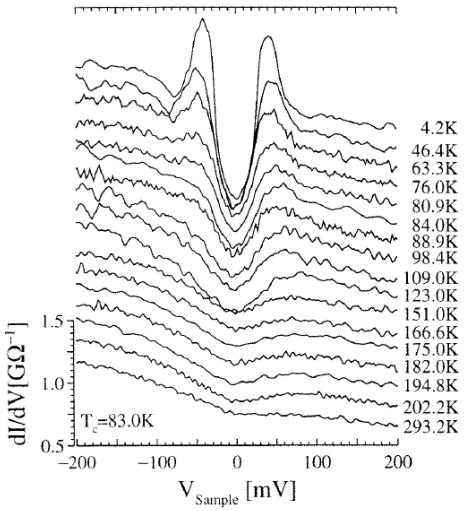

Figure 1.8: Tunnelling conductance for underdoped BSCCO. A gap-like feature at zero bias is seen to persist in the normal state which is direct evidence of a pseudogap in the tunnelling conductance. In the superconducting state a peak develops at ±45 meV followed by a dip and a broad maximum.

Other experimental evidences of pseudogap

Experimental evidences of pseudogap have been found also in underdoped YBCO, using nuclear magnetic resonance (NMR) [17, 18], These experiments detected a suppression in the spin-lattice relaxation rate well above T_c, which was attributed to the pseudogap.

Measurements of in-plane resistivity [19], of bulk susceptibility [20], of Hall coefficient [21] on LSCO, and of magnetic susceptibility [22] on barium doped LCO, confirm the results about the gap in the electronic spectrum and establish that at high temperature, the underdoped cuprates have an are incoherent metal phase in which there is an enhanced effective carrier density but no quasiparticles.

From this experimental picture we can argue that the transport is due to the dopant induced holes, which have a strong oxygen $2p$ character. They develop coherence on cooling and they are reasonably associated with the Fermi arcs detected by ARPES. The 'strange metal' behavior at high temperature breaks down in the region characterized by

the pseudogap. The latter can suggest the pre-formation of the Cooper pairs that lead to superconductivity only when a phase coherence is established. However we wonder if the pseudogap can somehow suggest the presence of a broken symmetry phase competing with superconductivity.

Recent resonant ultrasound spectroscopy measurements conducted on YBCO [23], support the idea that the pseudogap enhancement corresponds to a real phase transition. Ultrasound spectroscopy provides informations about the frequencies and widths of the vibrational normal modes of a crystal acting as a free mechanical resonator. Analysing the temperature evolution of the elastic component of these frequencies, which depends on a linear combination of all elastic moduli, they found anomalies at the pseudogap boundary T^* for different doping concentrations. They explain these anomalies with the occurrence of a phase transition. The doping dependence of the line of phase transitions is such that it terminates at zero temperature inside the superconducting dome.

As already said, the main goal of this work will be the characterization of a low temperature ordered phase in underdoped cuprates, starting from the experimental evidences of the antiferromagnetic spin correlations developing among local Cu moments, even at doping concentrations for which the antiferromagnetic long-range order is not established. To understand the nature of these magnetic correlations, we will consider in the next section, the neutron scattering studies.

1.3 Experimental evidences of magnetic correlations

1.3.1 Neutron scattering experiments

Neutron scattering technique

Neutron scattering is a powerful technique for investigating atomic and magnetic structures. Thermal neutrons, with a typical energy of 30 meV, have a wave-length of order 1.65 Å, which is well matched to common interatomic spacings; it follows that thermal neutrons are quite useful for Bragg diffraction studies of crystal structure. Unlike x-rays or electrons, which are scattered by the electronic charge density of atoms, neutrons scatter from atomic nuclei via the strong force. The nuclear scattering cross section is sensitive to isotope as well as element, and there is no simple formula to characterize it; however, the typical magnitude of the cross section is roughly independent of atomic number. This is beneficial when measuring the structure of a compound such as LCO, where there is a large spread in the atomic number of the constituent elements, from $Z = 16$ for O to $Z = 57$ for La. For x-ray scattering, the weight per atom in the diffraction pattern is proportional to Z^2, providing 13 times less sensitivity to O compared to La, whereas neutrons have roughly uniform sensitivity to all of these elements.

The neutron also has a spin of 1/2, which means that it can scatter from atomic magnetic moments via the dipole-dipole interaction. When large ordered magnetic moments are present in a sample, magnetic diffraction can be of the same strength as nuclear diffraction. The energy of thermal neutrons is comparable to typical phonon and

spin-wave energies in solids, so that only modest energy resolution is needed in order to characterize phonon and spin-wave dispersions. On the other hand, the overall scale of the scattering cross section is quite weak, so that one generally needs rather large samples in order to efficiently measure excitation spectra. To create neutron beams, one has to extract neutrons from atomic nuclei. This can be done either through the fission process in a nuclear reactor, where each uranium fission produces a couple of neutrons, or by knocking neutrons out of heavy-metal nuclei (typically tungsten or mercury) with a high energy proton beam, producing 10 or 20 neutrons per proton collision.

Now we report some elements of the theory of neutron scattering. More details are available in Refs. [24, 25, 26]. In a neutron scattering experiment the neutrons incident on the sample are characterized by an average momentum $\hbar\mathbf{k}_i$, where the magnitude of the wave-vector is inversely proportional to the neutron wave-length, $k = 2\pi/\lambda$; the neutron energy is given by

$$E = \frac{\hbar^2 k^2}{2m_n}, \tag{1.1}$$

where m_n is the mass of the neutron. One detects scattered neutrons with wave-vector $\mathbf{k}_f$. The probability of scattering into a differential solid angle $d\Omega_f$ and energy dE_f corresponds to the double-differential cross section $d^2\sigma/d\Omega_f dE_f$. To describe this function, it is helpful to introduce the neutron momentum transfer

$$\hbar\mathbf{q} = \hbar\mathbf{k}_f - \hbar\mathbf{k}_i. \tag{1.2}$$

In terms of the scattering angle θ_s, we have

$$|\mathbf{q}|^2 = k_i^2 + k_f^2 - 2k_i k_f \cos(\theta_s). \tag{1.3}$$

The energy transfer to the sample is

$$\hbar\omega = E_i - E_f = \frac{\hbar^2}{2m_n}(k_i^2 - k_f^2). \tag{1.4}$$

It turns out that the differential cross section can be written in the relatively simple form

$$\frac{d^2\sigma}{d\Omega_f dE_f} = N\frac{k_f}{k_i}\left(\frac{\sigma}{4\pi}\right)^2 \mathcal{S}(\mathbf{q},\omega), \tag{1.5}$$

where N is the number of atoms in the sample, σ is the cross section for a particular scattering process, and $\mathcal{S}(\mathbf{q},\omega)$ is the dynamical structure factor. One can use this formula both for nuclear and magnetic scattering, but with different definition of σ and $\mathcal{S}(\mathbf{q},\omega)$. In the case of magnetic scattering, eq. (1.5) still applies, but now

$$\frac{\sigma}{4\pi} = \left(\frac{\gamma r_0}{2}\right) g f(\mathbf{Q}), \tag{1.6}$$

where $\gamma r_0/2 = 0.2695 \times 10^{-12}$ cm, with $r_0 = e^2/m_e c^2$ being the classical electron radius and $\gamma = 1.913$ the neutron's gyromagnetic ratio; g is the Landé factor (with a typical

value $g \sim 2$), and the magnetic form factor $f(\mathbf{q})$ is the Fourier transform of the normalized unpaired spin density $\rho_s(\mathbf{r})$ on an atom,

$$f(\mathbf{q}) = \int d\mathbf{r} \rho_s(\mathbf{r}) e^{i\mathbf{q}\cdot\mathbf{r}}, \tag{1.7}$$

with $f(0) = 1$. The magnetic spins in a sample have a vector character. For the dipole-dipole interaction, it turns out that only the components of atomic spins that are perpendicular to $\mathbf{q}$ contribute to the cross section. To take this into account, we must generalize the dynamic structure factor as follows:

$$S(\mathbf{q},\omega) \to \sum_{\alpha,\beta} \left(\delta_{\alpha,\beta} - \frac{q_\alpha q_\beta}{q^2} \right) \mathcal{S}^{\alpha,\beta}(\mathbf{q},\omega), \tag{1.8}$$

with

$$\mathcal{S}^{\alpha,\beta}(\mathbf{q},\omega) = \frac{1}{2\pi\hbar} \int_{-\infty}^{\infty} dt\, e^{-i\omega t} \sum_{\mathbf{r}_i} e^{i\mathbf{q}\cdot\mathbf{r}_i} \langle S^\alpha(0,0) S^\beta(\mathbf{r}_i,t) \rangle, \tag{1.9}$$

where $\alpha, \beta = x, y, z$ represent the components of the spins. The dynamical structure factor $\mathcal{S}^{\alpha\beta}(\mathbf{q},\omega) = e^{\beta\hbar\omega} \mathcal{S}^{\alpha\beta}(-\mathbf{q},-\omega)$. Integrating $\mathcal{S}^{\alpha,\beta}(\mathbf{q},\omega)$ over all frequencies, one obtains an instantaneous correlation function

$$\mathcal{S}^{\alpha\beta}(\mathbf{Q}, t=0) = \int_{-\infty}^{\infty} d\omega \mathcal{S}^{\alpha\beta}(\mathbf{q},\omega). \tag{1.10}$$

If one assumes that the system is described by localized spins and sums over all the $\mathbf{q}$-points of the Brillouin zone (BZ), a simple sum rule is obtained

$$\frac{1}{N} \sum_{\mathbf{q}\in BZ} \sum_{\alpha} \int_{-\infty}^{\infty} d\omega\, \mathcal{S}^{\alpha\alpha}(\mathbf{q},\omega) = \frac{S(S+1)}{\hbar}. \tag{1.11}$$

Incommensurate neutron scattering response in underdoped cuprates

Inelastic scattering ($\omega \neq 0$) provides informations on the spin dynamics, like spin waves. They consist in magnetic collective excitations, known as "magnons". Elastic scattering is used to study static correlations ($\omega = 0$). In a magnetically ordered material, $\mathcal{S}^{\alpha\beta}(\mathbf{q},0)$ exhibits peaks in correspondence of the wave-vectors of the magnetic Bragg reflections. Let us consider the case of antiferromagnetic (AF) ordering in the CuO_2 planes of LCO for $T < T_N$. As illustrated in Fig. 1.9, the AF ordering doubles the unit cell, resulting in new magnetic superlattice peaks at $\mathbf{q}_{AF} = (1/2, 1/2)$ in reciprocal space. Notice that reciprocal lattice units (rlu) have been used. This means that the length of the Brillouin zone, i.e. $2\pi/a$, becomes unitary. Antiferromagnetism is not the only possible cause of superlattice peaks: structural distortions can change the size of the unit cell, as well. In the case of La_2CuO_4, the CuO_6 octahedra can rotate slightly about a (110) axis of the tetragonal structure. The octahedral tilts cause an in-plane doubling of the unit cell, together with an orthorhombic distortion with lattice vectors along the diagonals of

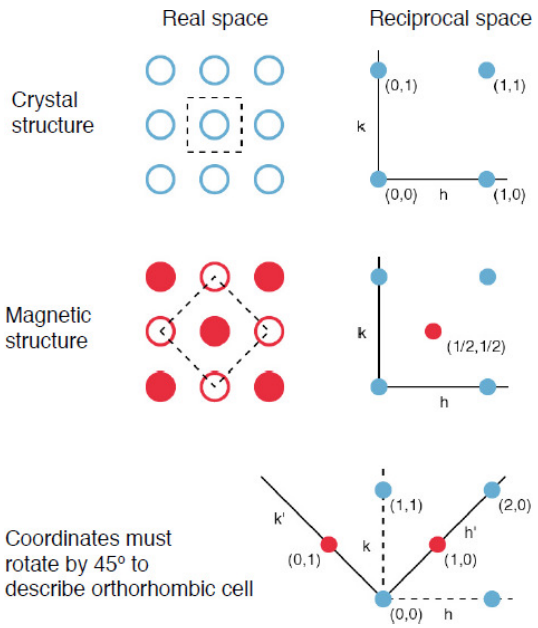

Figure 1.9: From Ref. [4]. Illustration of the relationship between real-space structure and reciprocal lattice vectors for the copper atoms in a CuO_2 plane of La_2CuO_4. In the panels indicating real space structure, the dotted lines denote the unit cell. For the magnetic structure, filled and open circles denote up and down spins. Reciprocal lattice units have been used for the reciprocal space.

the Cu plaquettes. In the orthorhombic structure, the in-plane magnetic wave-vectors are indexed as (1,0) and (0,1), as indicated in the lower panel of Fig. 1.9, and these are no longer equivalent.

As already mentioned, doping concentrations above $x \sim 0.02$ destroy the AF long-range order, and the 'commensurate' Bragg peak at $\mathbf{q}_{AF}$ disappears. However it is replaced by 'incommensurate' peaks which appear at a wave-vector $\mathbf{q}$ shifted with respect to $\mathbf{q}_{AF}$. The first experimental evidences of these incommensurate neutron scattering peaks at low energy on LSCO close to the optimal doping were found by Thurston [27, 28] and Cheong [29]. At the beginning these peaks due to spin fluctuations at low frequency, have not been interpreted unanimously as due to a charge and spin ordering process. Matsuda *et al.* [30] showed more recently that the incommensurate magnetic scattering is the responsible of the reduction of the Néel temperature at small but finite doping ($x \lesssim 0.02$) which is accompanied by a strong depression of the antiferromagnetic Bragg intensities (together with an anomalous loss of intensity at $T < 30$ K probably due to the spin glass phase). In tetragonal coordinates, this scattering is peaked at $\left(\frac{1}{2}, \frac{1}{2}, 0\right) \pm \frac{1}{\sqrt{2}}(\epsilon, \epsilon, 0)$, where ϵ is the "incommensurability". It is necessary to note that the crystal structure is actually orthorhombic, with the unit-cell axes rotated by 45^0 (see Fig. 1.10).

Fig. 1.11 shows incommensurate neutron scattering peaks found in LSCO for different concentrations of doping. Experiments by Wakimoto *et al.* [31, 32, 33, 34, 35] suggest that, coming from the optimal doping, and decreasing the concentration of dopant holes,

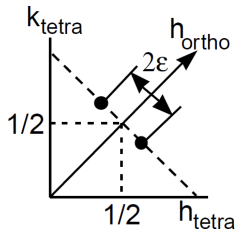

Figure 1.10: Peak positions of the incommensurate magnetic peaks.

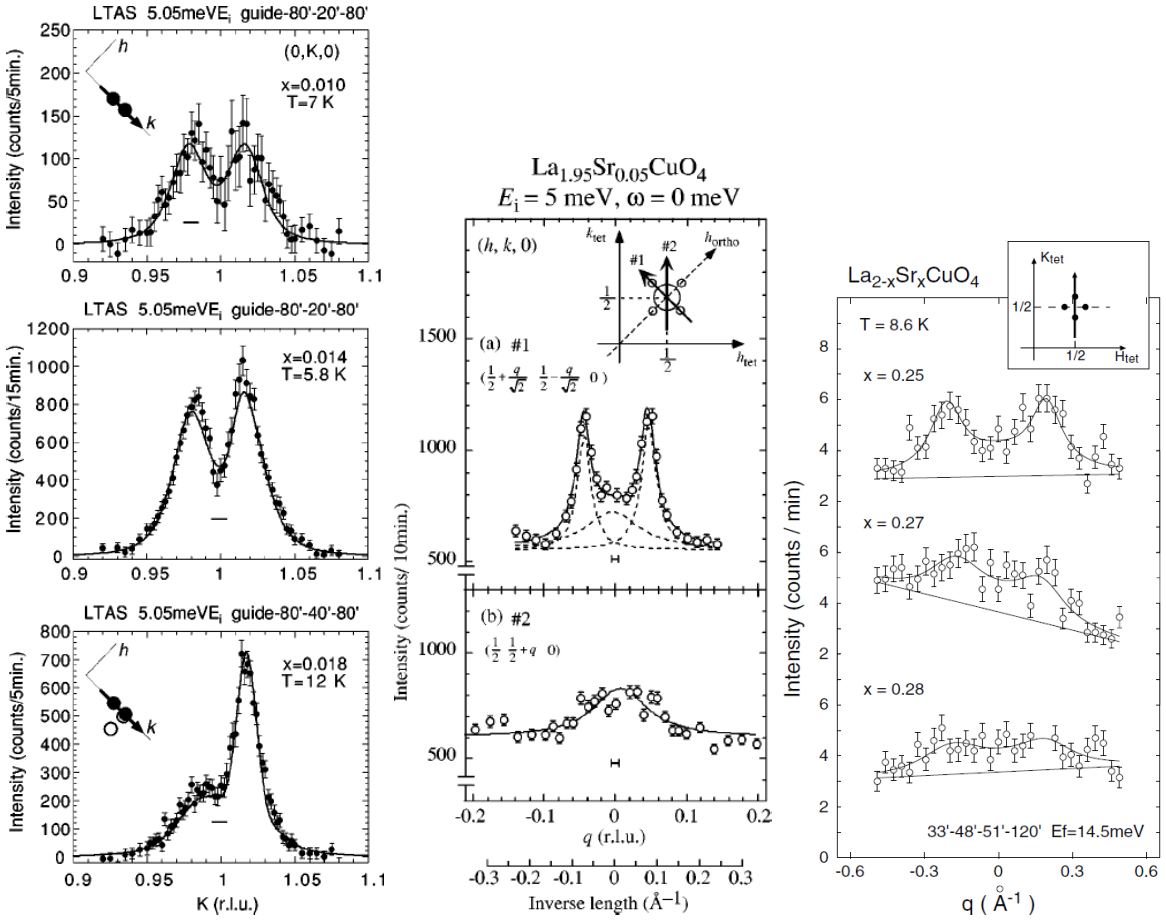

Figure 1.11: Elastic neutron scattering scans along the orthorhombic K axis on $La_{2-x}Sr_xCuO_4$ for doping concentrations still in the AF state [30] (left panel) and just above the disruption of the AF long-range order [31] (central panel). The right panel shows inelastic peaks at higher concentrations of doping along tetragonal K axes [35].

these incommensurate peaks shift from the tetragonal axis (horizontal direction) towards the orthorhombic axis (diagonal direction) in correspondence of $x = 0.05$ close to the lower boundary of the superconducting dome. At this value of doping concentration a twin structure due to orthorhombic distortion, has been detected. It is important to notice that, in this strongly underdoped regime all the incommensurate peaks detected are broad with a well resolved width of the order of the incommensurability indicating a correlation length of the order of the spin periodicity [36, 37]. Only close to $x \sim 0.12$ magnetic Bragg peaks appear quite sharp and often resolution limited [38, 36, 39] indicating long-range order.

An interesting feature emerging from these experiments is the linear dependence of the incommensurability on the doping concentration x, which is called "Yamada plot", from the experimental observations of Yamada *et al.* [40], who performed a systematic experimental study of low energy spin fluctuations in LSCO for increasing values of doping. Their results are reported in the left panel of Fig. 1.12. We can see that the incommensurability saturates around the 'magic fraction' $\epsilon \sim 1/8$, for $x \sim 0.12$. The right panel of Fig. 1.12 shows again the incommensurability as a function of the doping, i.e. hole concentration, as resulting from other neutron scattering experiments and from our Monte Carlo simulations (red squares).

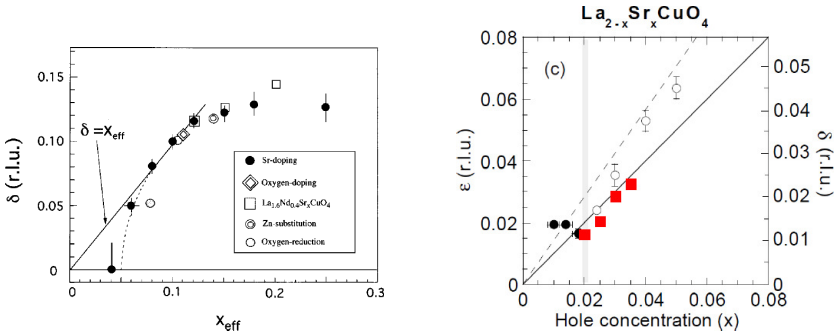

Figure 1.12: Linear trend of the incommensurability as a function of the hole concentration: (left panel) Yamada results [40]; (right panel) results from Refs. [30, 32, 37, 34, 41, 42]. The red squares represent the result of our Monte Carlo simulations. The right scale represents the incommensurability δ measured along the tetragonal axes.

Since we want to study the underdoped cuprates phase diagram, we are interested in the temperature dependence of the physical quantities which characterize these undefined phases. In particular the left panel of Fig. 1.14 reports the height of the elastic incommensurate peaks as a function of the temperature, measured by Wakimoto *et al.* [31]. It has an order-parameter like behavior and defines a transition temperature (called T_{el}).

The temperature dependence of neutron scattering peaks in LSCO is also reported in Ref. [43] (see Fig. 1.13). Although the peaks are not elastic peaks, we can observe the transition from incommensurate behavior to commensurate behavior.

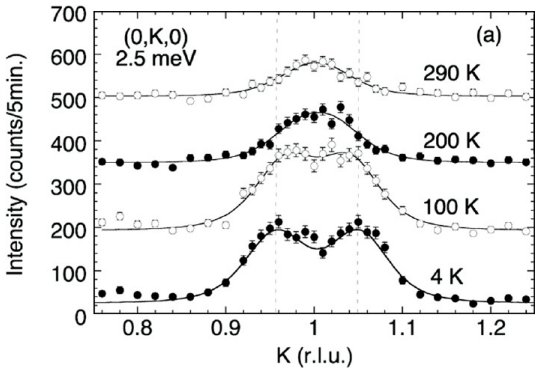

Figure 1.13: From Ref. [43]. Temperature dependence of the low-energy inelastic neutron scattering peaks in $La_{1.96}Sr_{0.04}CuO_4$. Successive scans have been displaced vertically by 150 counts for clarify. The broken lines represent the peak positions at 4 K.

1.3.2 Magnetic susceptibility measurements and muon spin rotation spectroscopy

Magnetic susceptibility χ_m is defined as the ratio between magnetization **M** of the material in the magnetic field and the field intensity **H**. In a ferromagnetic material $\chi_m \gg 1$. Many susceptibility measurements on LSCO were performed using a standard superconducting quantum interference device (SQUID) magnetometer, by Wakimoto *et al.* [33], and by Chou *et al.* [42]. These measurements, made on each crystal under various applied fields in the range $0.02 < H < 5$ T either parallel or perpendicular to the CuO_2 planes, highlight the presence of a low temperature spin glass phase whose transition temperature T_g is lower than T_{el}.

Another effective probe of magnetic order is muon spin rotation (μSR) spectroscopy. Muons have a lifetime of just 2.2 μs, but they can be prepared readily at a proton accelerator. A muon injected into a sample rapidly diffuses to the most electronegative interstitial site in the lattice. If there is a local magnetic field due to ordered moments, the spin of the muon will precess about the field. When the muon decays, the resulting positron is emitted preferentially along the direction of the muon's spin. By putting a pair of detectors on opposite sides of the sample, one can detect when the muon spin is pointing along a particular axis. Binning the detected positrons as a function of time from the initial implantation, one can directly measure the muon precession frequency which is proportional to the local magnetic field at the muon site. The fact that there is a well defined local field indicates that there must be magnetic order, though the measurement, by itself, does not distinguish the type of order, i.e. antiferromagnetic, ferromagnetic or glassy.

μSR experiments [44] confirm a spin-glass transition in underdoped LSCO at low temperature. A 'magnetic' phase diagram is reported in Fig. 1.14. Also more recent μSR measurements by Sanna *et al.* on $YBa_2Cu_3O_{6+x}$ [45] identified local magnetic order at

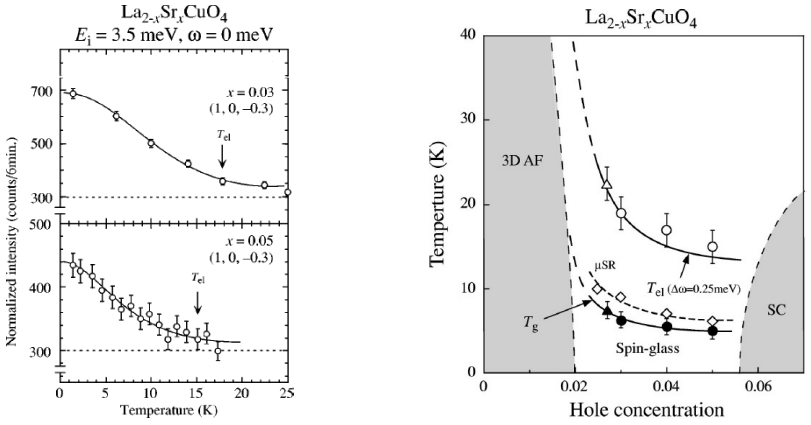

Figure 1.14: (Left panel) From Ref. [31]. Temperature dependence of the elastic peak intensity for $x = 0.03$ and $x = 0.05$. The estimated onset temperatures of the elastic peak are indicated by arrows. (Right panel) From Ref. [33]. Magnetic phase diagram for the lightly doped region resulting from magnetic susceptibility measurements. The circles are the data from Ref. [33] and the triangles are those reported by Chou *et al.* [42]. Open diamonds indicate the temperatures where magnetic signals are observed in the μSR measurements [44].

low temperatures for $x \leq 0.39$, and coexistence with superconductivity for $x \geq 0.39$ [2]. They also detected the presence of a low temperature spin-glass phase coexistent with superconductivity [46].

1.4 Stripes in cuprates

1.4.1 Stripe concept

With the term "stripe" we mean states of unidirectional density waves. We distinguish

- Charge Density Wave (CDW), if only spatial charge modulation occurs;
- Spin Density Wave (SDW), if the charge modulation is accompanied by spin modulation.

The stripe phase represents an example of mesoscopic phase separation in the real space. The dopant holes are arranged in metallic unidimensional structures. If the stripes are centered on the lattice sites, they act as a domain wall between two different spin domains since the AF alignment has to be satisfied. Fig. 1.15 shows how the phase of the AF background shifts by π on crossing the charge stripe. If we take a phase with stripe-order in y direction (like that represented schematically in the left panel of Fig. 1.15), it implies new Bragg peaks resulting from the scattering from electronic charge at the wave-vector of the CDW, $\mathbf{q}_c = \frac{2\pi}{a}(\pm\delta, 0)$, and in correspondence of higher harmonics. $\delta = 1/\lambda_c$ is

[2] As already mentioned, the hole concentration n_h within the CuO_2 planes in YBCO, represents approximately the 20% of the doping concentration x. Thus the doping $x = 0.39$ corresponds to $n_h \sim 0.08$.

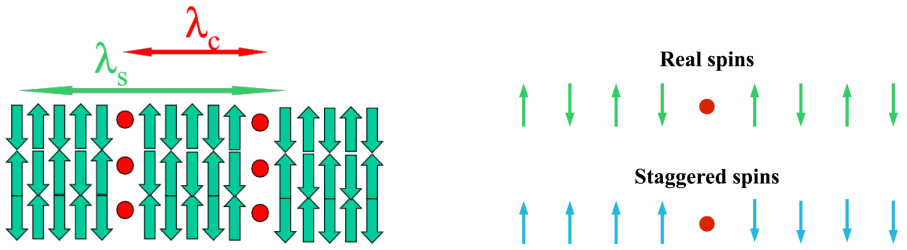

Figure 1.15: Example of site-centered stripes. The left panel is a representaion of a stripe of charges in a two-dimensional antiferromagnetic background. λ_s and λ_c represent respectively spin and charge modulation lengths. The right panels show a cut along a row orthogonal to the stripe. To better highlight the antiphase boundary also staggered spins (blue arrows) are reported.

the charge incommensurability being $\lambda_c a$ the spatial modulation length of the charge distribution. When charge order coexists with spin order, new Bragg magnetic peaks appear at $\mathbf{q}_{AF} \pm \mathbf{q}_s$, where $\mathbf{q}_s = \frac{2\pi}{a}(\pm\epsilon, 0)$ is the wave-vector of the SDW, being $\epsilon = 1/\lambda_s$ the spin incommensurability. It can be easily shown that $\epsilon = \delta/2$. Indeed $\epsilon = \frac{1}{\lambda_s a}$ and $\lambda_s = 2\lambda_c$ as it can be seen in the left panel of Fig. 1.15.

The first suggestion that a hole-doped cuprate layer might develop an inhomogeneous state was provided by Zaanen and Gunnarsson [47], who performed mean field calculation on a 3-band Hubbard model. A key feature of their stripe solution is the π shifting of the phase of the AF background, crossing the charge stripe. This leads to an incommensurate spin order. A problem with this particular solution is that the charge stripe has an effective hole density of one per Cu site along the stripe. This corresponds to an insulating state, and it also gives a spin incommensurability that is a factor of two smaller than the incommensurability observed in early inelastic neutron scattering [29].

Later studies have found stripe states that have a hole density of one-half per Cu site along the charge stripe, consistent with neutron and transport experiments (see for example Refs. [49, 50]). There have also been extensive calculations of stripes using the Gutzwiller approximation by Seibold *et al.* [51]. Charge inhomogeneity have also been proposed from another direction. Indeed a theoretical study, conducted by Castellani *et al.* [48], predicted a charge phase separation instability. Based on early calculations for a t-J model indicating that doped holes would tend to phase separate [52], Emery and Kivelson [53] argued that inclusion of extended Coulomb interactions should frustrate the phase separation, resulting in spatially modulated structures such as striped and checkerboard states [54]. The density of the holes in the stripes would not be fixed, but should correspond to whatever value minimizes the free energy associated with the competing short- and long-range interactions.

1.4.2 Experimental evidences of charge stripe order

First experimental evidences of charge stripe order are found in nickelates, which are neither superconducting nor metallic up to high doping. Pure La_2NiO_4 is an antiferro-

magnetic insulator that is easily doped with oxygen, as well as by Sr substitution for La. Doping the NiO_2 planes with holes reduces T_N more gradually than in cuprates. It is necessary to dope a hole concentration of ~ 0.2 before the commensurate antiferromagnetic order is replaced by stripe order [55, 56]. The charge stripes, with a filling of one hole per Ni site, act as antiphase domain walls for the magnetic order. The characteristic SDW wave-vector is half the characteristic CDW wave-vector.

A peculiar characteristic of lanthanum cuprates, like LSCO, Nd-LSCO and especially LBCO at low temperature, is the so-called "$\frac{1}{8}$-anomaly". It indicates the depression of T_c occurring at the doping concentration $x = 1/8$. The stripe picture provides a natural explanation of this anomaly, which can interpreted as due to a commensuration effect of the stripe structure. Indeed for increasing value of doping, the system prefers to add charge stripes, reducing their average spacing. Keeping constant the concentration of holes within the stripe ("half-filled", i.e. one hole every two lattice sites) the system minimizes its energy. This trend holds until $x = 1/8$, which corresponds to a spatial periodicity of the stripes of $4a$. This tendency suggests, for this particular concentration of doping, the presence of a commensuration energy stabilizing the stripe order which competes with the bulk superconductivity. This is why static charge/spin stripes have only been observed for this specific 1/8 filling. Indeed soon after the discovery of stripe order in nickelates, Bragg peaks associated to charge stripe order have been detected in $La_{1.6-x}Nd_{0.4}Sr_xCuO_4$ (Nd-LSCO) with $x = 0.12$, for $T < 50$ K, by Tranquada *et al.* [57]. A cartoon of stripe order consistent with this spatial periodicity is shown in Fig. 1.16; the

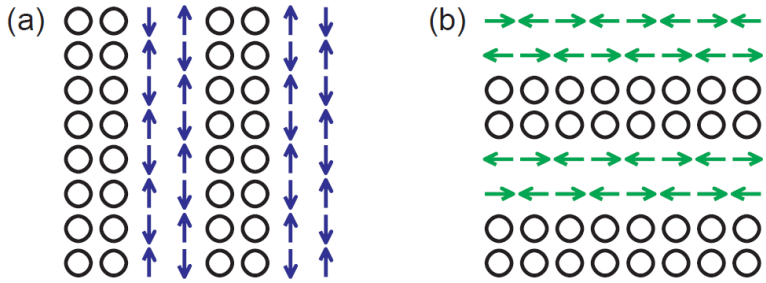

Figure 1.16: Cartoons of equivalent domains of (a) vertical and (b) horizontal bond-centered stripe order within a CuO_2 plane (only Cu sites shown). Note that the magnetic period is twice that of the charge period. The charge density along a stripe is one hole for every two sites in length.

inferred charge density within the charge stripes is approximately one hole every two sites along the length of a stripe. The magnetic unit cell is twice as long as that for charge order. More precisely, SDW and CDW have a modulation length of respectively $8a$ and $4a$, which implies a spin incommensurability of $\epsilon = 0.125$ and a charge incommensurability of 2ϵ. It should be noted that the phase of the stripe order with respect to the lattice has not been determined experimentally, so that it could be either bond-centered, as shown in Fig. 1.16, or site-centered, as shown in Fig. 1.17(b). Notice that the magnetic and charge periodicity does not depend on the bond-centered or site-centered character of the stripes. It is also important to notice that the stripe order imply domain walls for the

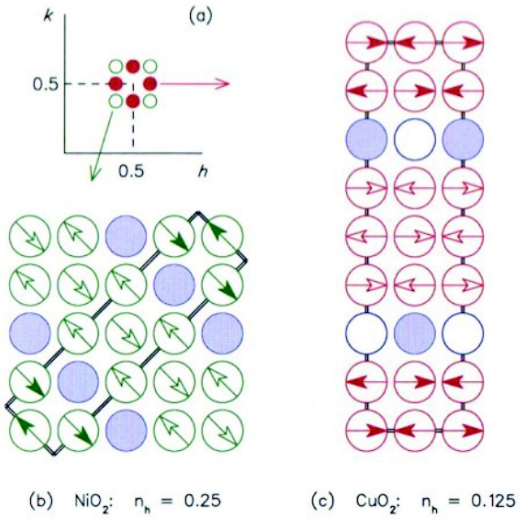

Figure 1.17: From Ref. [57]. (a) Orientation of magnetic superlattice peaks for diagonal (open circles) and horizontal (filled circles) site-centered stripes. (b) Cartoon of stripe found in nickelates; hole density is one per Ni along a diagonal charge stripe. (c) Cartoon of stripe order detected in Nd-LSCO for $x = 0.12$; hole density is approximately one for every two Cu sites along a charge stripe. The double lines in (b) and (c) indicate the magnetic unit cell, which is twice the size of the cell describing charge order.

spin texture but not spin canting. As we will see in the following chapters, this means that there is no spin current on the plane.

Let us analyse more in detail the characteristics of Nd-LSCO. The substitution of La for Nd implies a slight distortion of CuO_6 octahedra, which for $T < 70$ K leads at a transition from a low temperature orthorhombic phase to a low temperature tetragonal phase, where orthogonal Cu-O bonds are inequivalent within each plane, but the special direction rotates by 90^0 from one layer to the next (see left panel of Fig. 1.18). Because planes of each orientation are equally represented in the low temperature tetragonal phase, both stripe domains are equally represented. The resulting reciprocal space is illustrated in the right panel of Fig. 1.18.

The left panels of Fig. 1.19 report the experimental charge peaks detected on Nd-LSCO for $x = 0.12$ [58], whereas the right panels show the elastic magnetic peaks resulting from other neutron scattering experiments conducted on $La_{1.6-x}Nd_{0.4}Sr_xCuO_4$ with $x = 0.12$, $x = 0.15$ and $x = 0.20$ [38]. The sharp peaks detected for $x = 0.12$ suggest the occurrence of a long-range magnetic structure. These experiments have also shown the coexistence and competition of magnetic correlations and superconductivity. In particular magnetic peaks have been detected for T=50K, 46K, 15K, in crystals which a T_c respectively of 4K, 11K, 15K. Furthermore it has been argued that the maximum (minimum) value of the magnetic order parameter occurs for the minimum (maximum) value of T_c.

Static charge and spin stripe orders have been observed also in $La_{1.875}Ba_{0.125}CuO_4$ (LBCO) [59, 60, 61, 36] together with a strongly suppressed T_c. There has also been a

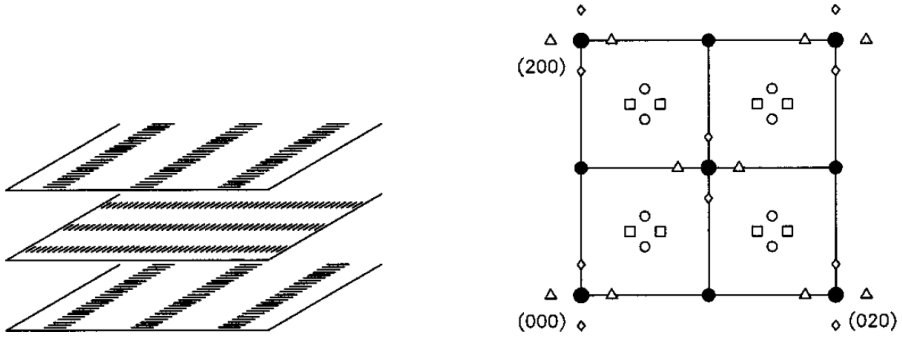

Figure 1.18: From Ref. [58]. (a) Sketch showing relative orientation of stripe patterns in neighboring planes of the low temperature tetragonal phase. (b) Diagram of the reciprocal space. Large filled circles indicate fundamental Bragg peaks; small filled circles indicate superlattice peaks of the low temperature tetragonal phase. Open circles and squares indicate magnetic superlattice peaks from two different domains of the stripe structure; diamonds and triangles indicate charge order superlattice peaks from the two stripe domains. Open circles and diamonds, squares and triangles correspond to the same domain.

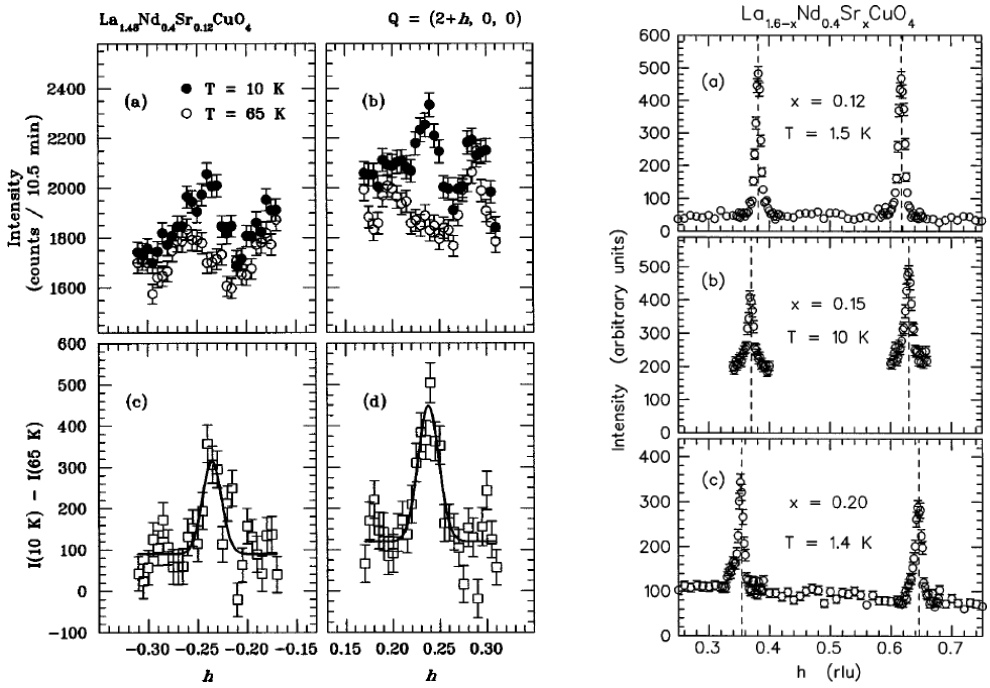

Figure 1.19: The four left panels show the charge order peaks detected on $La_{1.48}Nd_{0.4}Sr_{0.12}CuO_4$ [58], whereas the three right panels show the magnetic peaks measured on crystals of $La_{1.6-x}Nd_{0.4}Sr_xCuO_4$ with $x = 0.12$, $x = 0.15$, and $x = 0.20$ [38].

report of stripe-like charge order and incommensurate spin fluctuations in YBCO sample with a nominal $x = 0.35$ [62]. Weak superlattice peaks, attributed to charge order corresponding to vertical stripes with $2\epsilon = 0.127$, retain finite intensity at room temperature.

1.5 Broken symmetries in underdoped cuprates

We know that an ordered phase implies a broken symmetry. This ordering process is called symmetry "breaking", because it is a spontaneous process by which a system in a symmetrical state ends up in an asymmetrical state. It thus describes systems where the equations of motion or the Lagrangian obey certain symmetries, but the lowest energy solutions do not exhibit that symmetry.

As already mentioned, the main aim of this thesis is to identify a broken symmetry in the underdoped region of the cuprate phase diagram, suggesting the presence of an ordered phase close to the superconducting dome and making the phenomenology of cuprates similar to that of many other unconventional superconductors.

To find a broken symmetry in underdoped cuprates we look at the charge and spin degrees of freedom and we try to explain the experimental evidences of magnetic and charge correlations, in terms of phases typical of soft matter physics, like the "nematic phase" and "smectic phase", which occur in liquid crystals.

1.5.1 Soft-matter phases

The liquid state has short-range order but no long-range order: it has the highest possible symmetry. The crystalline solid state has long-range positional and rotational order; it has a much lower symmetry than the liquid state and can have the lowest possible symmetry consistent with a regular filling of space. Between these extremes, there are systems that exhibit short-range correlations in some directions and long-range order in others and that have symmetries intermediate between those of liquids and the crystals. Among the materials that show intermediate order, the most widely studied are liquid crystals[3]. They are constituted by highly anisotropic molecules, which can be modelled as rigid rods or ellipsoids with lengths greater than their widths. One form of intermediate order is orientational order, that in the case of liquid crystals is caused mostly by the repulsive interactions.

At high temperatures the axes of the anisotropic molecules are randomly oriented and their centers of mass are randomly distributed as depicted in Fig. 1.20(a). Globally the system is an isotropic liquid. When the isotropic liquid is cooled, the first phase that condenses is the nematic phase in which long molecules align so that they are on average parallel to a particular direction specified by a unit vector $\hat{\mathbf{n}}$ called the "director". The positions of the molecular centers of mass remain randomly distributed as they are in an isotropic fluid (see Fig. 1.20(b)). The nematic phase breaks rotational isotropy but not translational invariance. Rotations about an axis parallel to $\hat{\mathbf{n}}$ leave the nematic phase

[3]For an overview on the liquid crystal physics see for example Ref. [63].

unchanged, whereas rotations about axes perpendicular to $\hat{\mathbf{n}}$ do not. So the nematic phase still has an axial rotational symmetry. As temperature is further reduced, molecules begin to segregate into planes giving rise to a smectic liquid crystal. The usual picture of this smectic phase is one with molecules situated in well-defined layers with a spacing that is essentially the rod length as shown in Fig. 1.20(c). There is liquid-like motion of the rods in each layer and no correlation of the positions of the molecules from one layer to the next. In smectic-A liquid crystals, molecules are aligned perpendicular to the layers. In some systems, molecules align along an axis tilted relative to the smectic planes as shown in Fig. 1.20(d). This is the smectic-C phase. It has a lower symmetry than the smectic-A phase because the tilted molecules pick out a special direction in the smectic plane, i.e., their projections in the xy-plane align, like the molecules in a nematic, along a common direction denoted by a unit vector $\hat{\mathbf{c}}$, called $\mathbf{c}$-director.

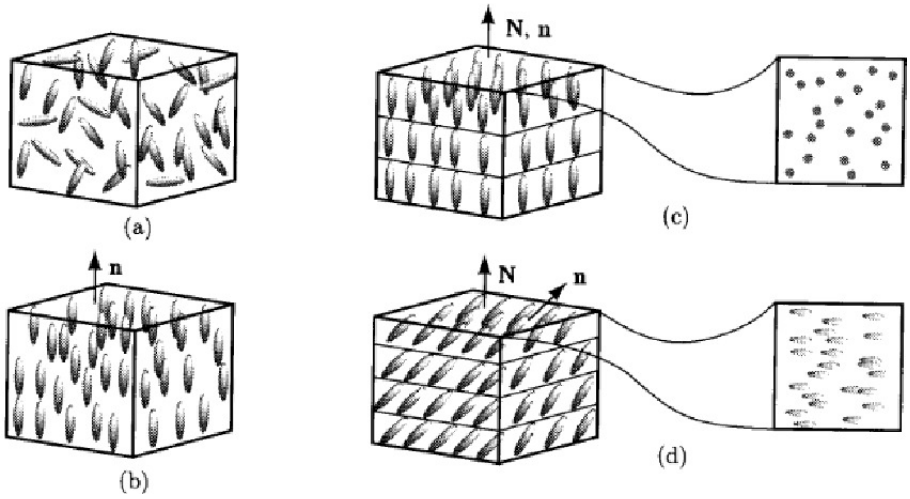

Figure 1.20: From Ref. [63]. Schematic representation of the position and orientation of anisotropic molecules in (a) the isotropic, (b) the nematic, (c) the smectic-A, and (d) the smectic-C phases. The direction of average molecular alignment in all but the isotropic phase is specified by a vector $\mathbf{n}$. The layer normal in the smectic phases is indicated by the vector $\mathbf{N}$, whereas in the smectic-C phase, it is not. (c) and (d) also show the arrangement of molecules in the smectic planes in the smectic-A and smectic-C phases.

In the last years, studies on strongly correlated electron systems, have been performed with the purpose of highlighting the existence of phases with physical properties analogous to those of liquid crystals [64, 65]. The generalization of liquid crystal phases to a two-dimensional square lattice is straightforward: the nematic phase breaks the C_4 rotation symmetry of the lattice, but leaves both translation and reflection symmetries unbroken; it can be thought as an anisotropic liquid with an axis of orientation. The smectic phase breaks translational symmetry in only one direction. Along the other direction, it has the character of an electron liquid; the crystalline phase breaks translation symmetry and has the character of an electronic 'solid', i.e. a Wigner crystal. The authors of Ref. [64] take into account fluctuations of electronic liquid-like stripes to explain these broken symmetry

phases, as shown in Fig. 1.21.

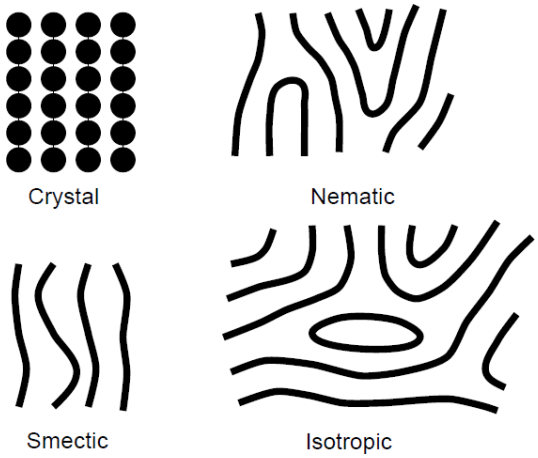

Figure 1.21: From Ref. [64]. Schematic view of the local stripe order in the various phases. Heavy lines represent liquid-like stripes, along which the electrons can flow, whereas the filled circles represent pinned, density-wave order along the stripes.

Experimental evidences of electronic liquid crystal states are found in YBCO [66], where the macroscopic orthorhombic crystal structure, stabilized by the CuO chains between the planes, can enhance anisotropy, found by the authors in the magnetic neutron scattering spectrum (see Fig. 1.22). Two incommensurate low energy peaks appear sym-

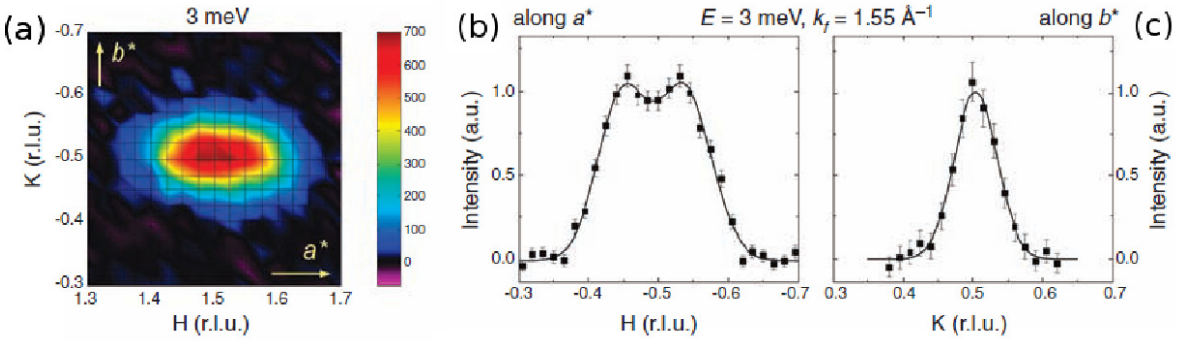

Figure 1.22: Anisotropic magnetic neutron scattering peak detected on $YBa_2Cu_3O_{6.45}$ at a temperature of 5 K [66]: (a) Intensity map of the low-energy peak. a* and b* represent the two perpendicular in-plane axes. (b) Scans along a* and b* through $\mathbf{q}_{AF}$.

metrically displaced from $\mathbf{q}_{AF}$ along only one principal direction of the CuO_2 plane, whereas along the other direction the scattering is commensurate. This anisotropy is strongly reduced when the temperature increases, leading to an order parameter-like behavior of the incommensurability. An in-plane anisotropy of the resistivity has already been found on LSCO and YBCO [67]. It gives evidence for conducting charge stripes in these systems. The temperature dependence and the rather small magnitude of the

anisotropy bear strong similarities to the nematic charge stripes (see Fig. 1.21), suggesting that the electronic liquid crystals are likely to be realized in the cuprates. Moreover, the signature of an electronic liquid crystal is observed in YBCO with T_c up to 50 K, which demonstrates that the electron self-organization is not a minor phenomenon in some extreme of the phase diagram but is rather a relevant part of the physics in the cuprates. Recently Daou *et al.* [68] observed a large in-plane anisotropy of the Nernst effect in YBCO, that sets in precisely at T^* throughout the doping phase diagram. They showed that the CuO chains of the orthorhombic lattice are not responsible for this anisotropy, which is therefore an intrinsic property of the CuO_2 planes.

Lawler *et al.* [69] have analysed spectroscopic-imaging scanning tunnelling microscope images of the intra-unit-cell states in underdoped BSCCO and have found evidence for electronic nematicity of the states close to the pseudogap energy. They have determined a quantitative nematic order parameter describing the breaking of rotational symmetry by the electronic structure within each CuO_2 unit cell. The interplay between this intra-unit-cell nematicity and the smectic phase (stripes) in cuprates, has been studied by Mesaros *et al.* [70], suggesting that the two can coexist.

These experimental results suggest that the pseudogap region of cuprates can exhibit some type of real-space electronic order. Important evidences of this order indicate a broken four-fold rotational symmetry, suggesting the presence of smectic and nematic states in this region of the phase diagram.

Bibliography

[1] J. G. Bednorz and K. A. Müller, Z. Phys B **64**, 189 (1986).

[2] E. Dagotto, Rev. Mod. Phys. **66**, 763 (1994).

[3] P. A. Lee and X. G. Wen, Rev. Mod. Phys. **78**, 17 (2006).

[4] J. M. Tranquada, AIP Conference Proceedings **1550**, 114 (2013).

[5] V. Emery, Phys. Rev. Lett. **58**, 2794 (1987).

[6] C. M. Varma, S. Schmitt-Rink, E. Abrahams, Solid State Commun. **62**, 681 (1987).

[7] J. Zaanen, G. Sawatzky, J. Allen, Phys. Rev. Lett. **55**, 418 (1985).

[8] F. Zhang and T. Rice. Phys. Rev. B **37**, 3759 (1988).

[9] Chandra Varma, Nature **468**, 184 (2010).

[10] Ruixing Liang, D. A. Bonn, W. N. Hardy, Phys. Rev. B **73**, 180505 (2006).

[11] L. Taillefer, Ann. Rev. Cond. Matt. Phys. **1**, 51 (2010).

[12] M. R. Norman, H. Ding, M. Randeria, J. C. Campuzano, T. Yokoya, T. Takeuchi, T. Takahashi, T. Mochiku, K. Kadowaki, P. Guptasarma, D. G. Hinks, Nature **392**, 157 (1998).

[13] T. Yoshida, X. Zhou, T. Sasagawa, W. Yang, P. Bogdanov, A. Lanzara, Z. Hussain, T. Mizokawa, A. Fujimori, H. Eisaki, Z. X. Shen, T. Kakeshita, S. Uchida, Phys. Rev. Lett. **91**, 027001 (2003).

[14] T. Yoshida, X. J. Zhou, K. Tanaka, W. L. Yang, Z. Hussain, Z. X. Shen, A. Fujimori, S. Sahrakorpi, M. Lindroos, R. S. Markiewicz, A. Bansil, Seiki Komiya, Yoichi Ando, H. Eisaki, T. Kakeshita, S. Uchida, Phys. Rev. B **74**, 224510 (2006).

[15] H. J. Tao, F. Lu, E.J. Wolf, Physica C **282-287**, 1507 (1997)

[16] Ch. Renner, B. Revaz, J. Y. Genoud, K. Kadowaki, O. Fischer, Phys. Rev. Lett. **80**, 149 (1998).

[17] W. W. Warren, R. E. Walstedt, J. F. Brennert, J. R.Cava, R. Tycko, R. F. Bell, G. Dabbagh, Phys. Rev. Lett. **62**, 1193 (1989).

[18] R. E. Walstedt, W. W. Warren, R. F. Bell, R. J. Cava, G. P. Espinosa, L. F. Schneemeyer, J. V. Waszczak, Phys. Rev. B **41** 9574 (1990).

[19] K. Takenaka, J. Nohara, R. Shiozaki, S. Sugai, Phys. Rev. B **68**, 134501 (2003).

[20] T. Nakano, M. Oda, C. Manabe, N. Momono, Y. Miura, M. Ido, Phys. Rev. B **49**, 16000 (1994).

[21] Y. Ando, Y. Kurita, S. Komiya, S. Ono, and K. Segawa, Phys. Rev. Lett. **92**, 197001 (2004).

[22] M. Hücker, G. Gu, J. Tranquada, Phys. Rev. B **78**, 214507 (2008).

[23] A. Shekhter, B. J. Ramshaw, R. Liang, W. N. Hardy, D. A. Bonn, F. F. Balakirev, R. D. McDonald, J. B. Betts, S. C. Riggs, A. Migliori, Nature **498**, 75 (2013).

[24] I. A. Zaliznyak and J. M. Tranquada, cond-mat/1304.4214 (2013).

[25] G. L. Squires, *Introduction to the Theory of Thermal Neutron Scattering, Third edition* (Cambridge University Press, 2012).

[26] J. Lorenzana, G. Seibold, R. Coldea, Phys. Rev. B **72**, 224511 (2005).

[27] T. Thurston, R. Birgeneau, M. Kastner, N. Preyer, G. Shirane, Y. Fujii, K. Yamada, Y. Endoh, K. Kakurai, M. Matsuda, Y. Hidaka, T. Murakami, Phys. Rev. B **40**, 4585 (1989).

[28] T. Thurston, P. Gehring, G. Shirane, R. Birgeneau, M. Kastner, Y. Endoh, M. Matsuda, K. Yamada, H. Kojima, I. Tanaka, Phys. Rev. B **46**, 9128 (1992).

[29] S. W. Cheong, G. Aeppli, T. Mason, H. Mook, S. Hayden, P. Canfield, Z. Fisk, K. Clausen, J. Martinez, Phys. Rev. Lett. **67**, 1791 (1991).

[30] M. Matsuda, M. Fujita, K. Yamada, R. Birgeneau, Y. Endoh, G. Shirane, Phys. Rev. B **65**, 134515 (2002).

[31] S. Wakimoto, G. Shirane, Y. Endoh, K. Hirota, S. Ueki, K. Yamada, R. J. Birgeneau, M. A. Kastner, Y. S. Lee, P. M. Gehring, S. H. Lee, Phys. Rev. B **60**, R769 (1999).

[32] S. Wakimoto, R. J. Birgeneau, M. A. Kastner, Y. S. Lee, R. Erwin, P. M. Gehring, S. H. Lee, M. Fujita, K. Yamada, Y. Endoh, K. Hirota, G. Shirane, Phys. Rev. B **61**, 3699 (2000).

[33] S. Wakimoto, S. Ueki, Y. Endoh, K. Yamada, Phys. Rev. B **62**, 3547 (2000).

[34] S. Wakimoto, R. Birgeneau, Y. Lee, G. Shirane, Phys. Rev. B **63**, 172501 (2001).

[35] S. Wakimoto, H. Zhang, K. Yamada, I. Swainson, Hyunkyung Kim, R. Birgeneau, Phys. Rev. Lett. **92**, 217004 (2004).

[36] M. Hücker, M. v. Zimmermann, G. D. Gu, Z. J. Xu, J. S. Wen, Guangyong Xu, H. J. Kang, A. Zheludev, J. M. Tranquada, Phys. Rev. B **83**, 104506 (2011).

[37] M. Matsuda, M. Fujita, K. Yamada, R. Birgeneau, M. Kastner, H. Hiraka, Y. Endoh, S. Wakimoto, G. Shirane, Phys. Rev. B **62**, 9148 (2000).

[38] J. M. Tranquada, J. Axe, N. Ichikawa, A. Moodenbaugh, Y. Nakamura, S. Uchida, Phys. Rev. Lett. **78**, 338 (1997).

[39] H. Kimura *et al.*, Phys. Rev. B **59**, 6517 (1999).

[40] K. Yamada, C. H. Lee, K. Kurahashi, J. Wada, S. Wakimoto, S. Ueki, H. Kimura, Y. Endoh, G. Shirane, R. J. Birgeneau, M. Greven, M. A. Kastner, and Y. J. Kim, Phys. Rev. B **57**, 6165 (1998).

[41] M. Fujita, K. Yamada, H. Hiraka, P. Gehring, S. Lee, S. Wakimoto, G. Shirane, Phys. Rev. B **65**, 064505 (2002).

[42] F. Chou, N. Belk, M. Kastner, R. Birgeneau, Amnon Aharony, Phys. Rev. Lett. **75**, 2204 (1995).

[43] M. Matsuda, M. Fujita, S. Wakimoto, J. A. Fernandez-Baca, J. M. Tranquada, K. Yamada, Phys. Rev. Lett. **101**, 197001 (2008).

[44] Ch. Niedermayer, C. Bernhard, T. Blasius, A. Golnik, A. Moodenbaugh, J. Budnick, Phys. Rev. Lett. **80**, 3843 (1998).

[45] S. Sanna, G. Allodi, G. Concas, A. Hillier, R. De Renzi, Phys. Rev. Lett. **93**, 207001 (2004).

[46] S. Sanna, G. Allodi, G. Concas, R. De Renzi, Journal of Superconductivity **18**, 769 (2005).

[47] J. Zaanen and O. Gunnarsson, Phys. Rev. B **40**, 7391 (1989).

[48] C. Castellani, C. Di Castro, M. Grilli, Phys. Rev. Lett. **75**, 4650 (1995).

[49] S. White and D. Scalapino, Phys. Rev. Lett. **80**, 1272 (1998).

[50] J. Lorenzana and G. Seibold, Phys. Rev. Lett. **89**, 136401 (2002).

[51] G. Seibold, M. Grilli, J. Lorenzana, Physica C **481**, 132 (2012).

[52] V. Emery, S. Kivelson, H. Lin, Phys. Rev. Lett., **64**, 475 (1990).

[53] V. J. Emery and S. A. Kivelson, Physica C **209**, 597 (1993).

[54] U. Löw, V. Emery, K. Fabricius, S. Kivelson, Phys. Rev. Lett. **72**, 1918 (1994).

[55] J. Tranquada, D. Buttrey, V. Sachan, J. Lorenzo, Phys. Rev. Lett. **73**, 1003 (1994).

[56] V. Sachan, D. Buttrey, J. M. Tranquada, J. Lorenzo, G. Shirane, Phys. Rev. B **51**, 12742 (1995).

[57] J. M. Tranquada, B. J. Sternlieb, J. D. Axe, Y. Nakamura, S. Uchida, Nature **375**, 561 (1995).

[58] J. M. Tranquada, J. Axe, N. Ichikawa, Y. Nakamura, S. Uchida, B. Nachumi, Phys. Rev. B **54**, 7489 (1996).

[59] M. Fujita, H. Goka, K. Yamada, J. M. Tranquada, L. Regnault. Phys. Rev. B **70**, 104517 (2004).

[60] J. M. Tranquada, H. Woo, T. G. Perring, H. Goka, G. D. Gu, G. Xu, M. Fujita, K. Yamada, Nature **429**, 534 (2004).

[61] P. Abbamonte, A. Rusydi, S. Smadici, G. D. Gu, G. A. Sawatzky, D. L. Feng, Nature Physics **1**, 155 (2005)

[62] H. Mook, Pengcheng Dai, F. Doğan, Phys. Rev. Lett. **88**, 097004 (2002).

[63] P. M. Chaikin and T. C. Lubensky, *Principles of Condensed Matter Physics* (Cambridge University Press, 1995).

[64] S. A. Kivelson, E. Fradkin, V. J. Emery, Nature **393**, 550 (1998).

[65] E. Fradkin, S. A. Kivelson, E. Manousakis, K. Nho, Phys. Rev. Lett. **84**, 1982 (2000).

[66] V. Hinkov, D. Haug, B. Fauqué, P. Bourges, Y. Sidis, A. Ivanov, C. Bernhard, C. T. Lin, B. Keimer, Science **319**, 597 (2008).

[67] Yoichi Ando, Kouji Segawa, Seiki Komiya, A. N. Lavrov, Phys. Rev. Lett. 88, 137005 (2002).

[68] R. Daou, J. Chang, David LeBoeuf, Olivier Cyr-Choiniere, Francis Laliberte, Nicolas Doiron-Leyraud, B. J. Ramshaw, Ruixing Liang, D. A. Bonn, W. N. Hardy, Louis Taillefer, Nature **463**, 519 (2010).

[69] M. J. Lawler, K. Fujita, Jhinhwan Lee, A. R. Schmidt, Y. Kohsaka, Chung Koo Ki, H. Eisaki, S. Uchida, J. C. Davis, J. P. Sethna, Eun-Ah Kim, Nature **466**, 347 (2010).

[70] A. Mesaros, K. Fujita, H. Eisaki, S. Uchida, J. C. Davis, S. Sachdev, J. Zaanen, M. J. Lawler, Eun-Ah Kim, Science **33**, 426 (2011).

Chapter 2

The Hubbard model in the regime of strong correlations

In this chapter we introduce the one-band Hubbard model, which we will use to describe the microscopic physics of the CuO_2 planes of cuprates. After a brief discussion of the general properties of the model, we analyse the mean-field techniques which allow to solve the model on a lattice. In particular we discuss the unrestricted Hartree-Fock approximation and then the Gutzwiller approximation which accounts for reduced double occupancy of a site. Also the slave-boson method is treated. It leads to the same results as for Gutzwiller approximation, and we will use it for our microscopic calculations.

2.1 Microscopic model for cuprates

As explained in sec. 1.1.2, the ground state of the CuO_2 planes of the undoped cuprates, is represented by an antiferromagnetic state due to the spins localized at the copper site. One additional hole due to chemical doping, is originally located at the oxygen, but combined with the central hole at the copper site, it forms a spin singlet. Thus we can work in this singlet subspace without changing the physics of the problem. In this way one additional hole is equivalent to remove one of the Cu spins. So we obtain an effective model constituted by spins and empty sites (absence of spin), in a two-dimensional square lattice. Notice that the oxygen ions are no longer explicitly present. The latter configuration corresponds to a Zhang-Rice singlet. In this way the original three-band model has been simplified since only an effective copper orbital is taken into account in each unit cell, with a virtual hopping t between two orbitals of different unit cells, and an effective repulsion U between two electrons (holes) on the same orbital. The latter consists essentially on the energy difference between the Cu and O orbitals, i.e. $U \sim E_p^h - E_d^h$, since it represents the difference between the energy the system must pay to add one hole (in the oxygen level being too expensive putting two holes on the Cu level) and that gained to extract one hole (from the Cu level). Experimentally an energy gap of 2.0 eV is observed and interpreted as the charge transfer excitation [1]. This is so-called "one-band Hubbard model", which actually accounts for two energy bands separated by an energy gap proportional to U.

Since the microscopic calculations of this thesis will be based on this model, in the next sections we will analyse it in detail, and we will describe the methods used to obtain approximate solutions.

It is important to notice that, although the high repulsion $U \gg t$ tends to localize the holes, a hole can still lower its kinetic energy by making a virtual hop to a nearest-neighbor site and back again, but it can only hop if its spin is antiparallel to that of an hole already on the neighboring site, due to the Pauli exclusion principle (see Fig. 2.1). This leads to

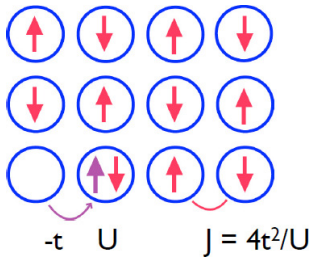

Figure 2.1: Representation of the one-band Hubbard model and the superexchange mechanism.

an effective antiferromagnetic exchange interaction $J(\mathbf{S}_1 \cdot \mathbf{S}_2)$ between two neighboring electron (hole) spins, being $J = 4t^2/U$. The experimental value of J is one possible way to estimate the effective hopping parameter t. Thus the CuO_2 planes can be described by a model of localized spins which gain energy by ordering antiferromagnetically. For this reason La_2CuO_4 can be considered a Mott insulator. In the limit of large U, the microscopic physics is well described by the so called t-J model. This effective model, previously introduced by Anderson [2], considers a hopping term which allows the movement of electrons without causing a change in their spin and explicitly excludes double occupancy, together with an antiferromagnetic interaction J coupling nearest neighbor sites.

2.2 Hubbard model

The Hubbard model is the simplest model of interacting particles in a lattice, with only two terms in the Hamiltonian: a kinetic term allowing for tunneling ("hopping") of particles between two sites of the lattice and a potential term consisting of the one-site interaction. Due to Pauli principle, the two electrons on the same site. must be in different atomic states. In the simplest model, which is a one-band model since a single orbital state is considered for each site, the two electrons must have opposite spins. So to identify the states we must specify both the site and spin index (i, σ). The Hubbard hamiltonian reads:

$$\mathcal{H} = \sum_{i,j,\sigma} t_{ij} \left(c^{\dagger}_{i,\sigma} c_{j,\sigma} + c^{\dagger}_{j,\sigma} c_{i,\sigma} \right) + U \sum_{i} n_{i,\uparrow} n_{i,\downarrow} \tag{2.1}$$

where $c_{i,\sigma}$ ($c^\dagger_{i,\sigma}$) destroys (creates) an electron with spin σ at site i, and $n_{i,\sigma} = c^\dagger_{i,\sigma} c_{i,\sigma}$ is the occupation number of the state (i, σ). The first term of eq. (2.1) represents the kinetic part $\mathcal{H}_t$ of the hamiltonian in the "tight-binding" form. Indeed the hopping parameter t_{ij} between sites i and j, represents the energy gained by an electron by jumping from the site i to the site j. The second term of eq. (2.1) represents the interacting part $\mathcal{H}_U$. As already mentioned, the parameter U constitutes the on-site repulsion, which is the Coulomb interaction between two electrons on the same atom.

The Hubbard model is a very simplified model describing interacting electrons on a lattice, but, although the two terms $\mathcal{H}_t$ and $\mathcal{H}_U$ can be exactly solved separately, this is not true for the sum of the two. Being the tight-binding term translational invariant, since $t_{ij} \equiv t(|\mathbf{r}_i - \mathbf{r}_j|)$, it is diagonal in the basis formed by the eigenvectors of the translation operator, which are given by the Fourier transformations

$$c_{\mathbf{k},\sigma} = \frac{1}{\sqrt{N}} \sum_i c_{i,\sigma} \exp(-i\mathbf{k} \cdot \mathbf{r}_i); \tag{2.2a}$$

$$c^\dagger_{\mathbf{k}.\sigma} = \frac{1}{\sqrt{N}} \sum_i c^\dagger_{i,\sigma} \exp(i\mathbf{k} \cdot \mathbf{r}_i), \tag{2.2b}$$

with the inverse transformations

$$c_{i,\sigma} = \frac{1}{\sqrt{N}} \sum_{\mathbf{k}} c_{\mathbf{k},\sigma} \exp(i\mathbf{k} \cdot \mathbf{r}_i); \tag{2.3a}$$

$$c^\dagger_{i,\sigma} = \frac{1}{\sqrt{N}} \sum_{\mathbf{k}} c^\dagger_{\mathbf{k},\sigma} \exp(-i\mathbf{k} \cdot \mathbf{r}_i). \tag{2.3b}$$

Using these transformations, the kinetic part of the hamiltonian can be rewritten as

$$\mathcal{H}_t = \sum_{\mathbf{k},\sigma} \varepsilon(\mathbf{k}) c^\dagger_{\mathbf{k},\sigma} c_{\mathbf{k},\sigma}, \tag{2.4}$$

where

$$\varepsilon(\mathbf{k}) = \sum_i t_{ij} \exp[-i\mathbf{k} \cdot (\mathbf{r}_i - \mathbf{r}_j)]. \tag{2.5}$$

If we consider only the largest hopping terms, we assume $t_{ij} = -t$ for nearest-neighbor sites, $t_{ij} = -t'$ for next-nearest-neighbors sites (so that we can take both the parameters t and t', positive), and $t_{ij} = 0$ elsewhere. Thus for a two-dimensional square lattice, we have

$$\varepsilon(\mathbf{k}) = -2t[\cos(k_x a) + \cos(k_x a)] - 4t' \cos(k_x a) \cos(k_x a); \tag{2.6}$$

where a is the lattice constant.

The term $\mathcal{H}_U$ is even more trivial to solve exactly. At half-filling, the ground state charge distribution adjusts itself to avoid doubly occupied sites; i.e. each site is occupied by a single electron and the total energy is zero. Therefore charge fluctuations are frozen and one has an insulator.

When $\mathcal{H}_t$ and $\mathcal{H}_U$ are both different from zero, they compete with each other. The kinetic term tends to delocalize electrons by putting individual electrons in Bloch states. The interaction term on the other hand increases the cost of charge fluctuation, leading to an insulator, known as "Mott insulator". Therefore there must be a critical value U_c of the order of the band width, beyond which one has an insulator. This phase transition is known as "Mott metal-insulator transition".

2.3 Mean field approximation

According to what said so far, to study a many electrons problem by means of the Hubbard model in more than one-dimension, some approximations are necessary. One of the most popular and effective is the mean field approximation (MF), which consists in approximating the effect of all the other electrons on any given electron in a single averaged effect, thus reducing a many body problem to an effective self-consistent one body problem.

MF consists in the following operation for an expectation value:

$$\langle AB\rangle \simeq \langle A\rangle\langle B\rangle. \tag{2.7}$$

If we rewrite a generic operator as the sum of the average value plus the fluctuation $O = \langle O\rangle + (O - \langle O\rangle)$, we have

$$\begin{aligned}\langle AB\rangle &= \langle\langle A\rangle\langle B\rangle + \langle A\rangle B - \langle A\rangle\langle B\rangle + A\langle B\rangle - \langle A\rangle\langle B\rangle + (A - \langle A\rangle)(B - \langle B\rangle)\rangle \\ &= \langle A\rangle\langle B\rangle + \langle (A - \langle A\rangle)(B - \langle B\rangle)\rangle. \end{aligned}\tag{2.8}$$

So, the physical meaning of MF is to neglect the term $\langle (A - \langle A\rangle)(B - \langle B\rangle)\rangle$, which represents the correlation between the fluctuation of A and the fluctuation of B.

The two-particle interaction term in second quantization is a product of four fermionic operators. At the operator level, MF consists in the following substitution

$$c_1^\dagger c_2 c_3^\dagger c_4 \to \langle c_1^\dagger c_2\rangle c_3^\dagger c_4 + \langle c_3^\dagger c_4\rangle c_1^\dagger c_2 - \langle c_1^\dagger c_4\rangle c_3^\dagger c_2 - \langle c_3^\dagger c_2\rangle c_1^\dagger c_4 - \langle c_1^\dagger c_2\rangle\langle c_3^\dagger c_4\rangle + \langle c_1^\dagger c_4\rangle\langle c_3^\dagger c_2\rangle, \tag{2.9}$$

which implies

$$\langle c_1^\dagger c_2 c_3^\dagger c_4\rangle \simeq \langle c_1^\dagger c_2\rangle\langle c_3^\dagger c_4\rangle - \langle c_1^\dagger c_4\rangle\langle c_3^\dagger c_2\rangle, \tag{2.10}$$

The minus signs comes from the anticommutation rules for fermions. We don't take the averages of the type $\langle c^\dagger c^\dagger\rangle$ or $\langle cc\rangle$, since they are zero in a system which is not a superconductor. Note that the role of the last two terms of (2.9) is to avoid double counting when we take the average. From (2.9) it is clear the reason why it is a mean field calculation: Each one-particle operator $a^\dagger a$ interacts with a scalar field which is given by the average of the other one-particle operators.

2.3.1 Hartree-Fock methods

According to what said above, to apply MF to hamiltonian (2.1) we must transform the product of four operators in the interaction term $\mathcal{H}_U$, in a product of only two operators,

taking the average, if allowed, of the remaining two. In this way we obtain the so-called "Hartree-Fock" approximation:

$$
\begin{aligned}
&U\sum_i n_{i,\uparrow}n_{i,\downarrow} = U\sum_i c^\dagger_{i,\uparrow}c_{i,\uparrow}c^\dagger_{i,\downarrow}c_{i,\downarrow} \simeq \\
&U\sum_i \langle c^\dagger_{i,\uparrow}c_{i,\uparrow}\rangle c^\dagger_{i,\downarrow}c_{i,\downarrow} + \langle c^\dagger_{i,\downarrow}c_{i,\downarrow}\rangle c^\dagger_{i,\uparrow}c_{i,\uparrow} - \langle c^\dagger_{i,\downarrow}c_{i,\uparrow}\rangle c^\dagger_{i,\uparrow}c_{i,\downarrow} - \langle c^\dagger_{i,\uparrow}c_{i,\downarrow}\rangle c^\dagger_{i,\downarrow}c_{i,\uparrow} \\
&-\langle c^\dagger_{i,\uparrow}c_{i,\uparrow}\rangle\langle c^\dagger_{i,\downarrow}c_{i,\downarrow}\rangle + \langle c^\dagger_{i,\downarrow}c_{i,\uparrow}\rangle\langle c^\dagger_{i,\uparrow}c_{i,\downarrow}\rangle = \\
&U\sum_i \langle n_{i,\uparrow}\rangle c^\dagger_{i,\downarrow}c_{i,\downarrow} + \langle n_{i,\downarrow}\rangle c^\dagger_{i,\uparrow}c_{i,\uparrow} - \langle S^-_i\rangle c^\dagger_{i,\uparrow}c_{i,\downarrow} - \langle S^+_i\rangle c^\dagger_{i,\downarrow}c_{i,\uparrow} \\
&-\langle n_{i,\uparrow}\rangle\langle n_{i,\downarrow}\rangle + \langle S^-_i\rangle\langle S^+_i\rangle,
\end{aligned}
\tag{2.11}
$$

where $S^+_i = c^\dagger_{i,\uparrow}c_{i,\downarrow}$ and $S^-_i = c^\dagger_{i,\downarrow}c_{i,\uparrow}$ are respectively the spin rising and lowering operators.

In a system with axial spins both $\langle S^+_i\rangle$ and $\langle S^-_i\rangle$ are equal to zero. Example of such type of system is represented by the antiferromagnet (AF). It constitutes the low temperature state of the undoped cuprates. We want to start from the AF state and analyse how the spin background changes when holes are introduced.

The AF state is characterized by spins aligned in a regular pattern with neighboring spins (on different sublattices) pointing in opposite directions. This configuration is characterized by a new reciprocal lattice vector $\mathbf{Q} = \left(\frac{\pi}{a}, \frac{\pi}{a}\right)$ which defines a new Brillouin zone reduced by one half with respect to the old one. In this way Bloch states, whose wavevector differs by a vector $\mathbf{Q}$, are coupled. Expanding the c_i and $c^\dagger_i$ operators in the plane wave basis, according to eqs. (2.3), the Hubbard hamiltonian for the antiferromagnetic state, can be rewritten in a matrix form given by $\mathcal{H} = \mathbf{c}^\dagger\hat{\mathbf{H}}\mathbf{c}$, being $\mathbf{c} = (c_{\mathbf{k},\sigma}, c_{\mathbf{k}+\mathbf{Q},\sigma})$ a two-component vector. Thus the entire problem is reduced to the diagonalization of a 2×2 matrix, which provides the dispersion relation for the energy of the two bands

$$
\lambda_{\mathbf{k}} = \pm E_{\mathbf{k}} + \frac{Un}{2}, \tag{2.12}
$$

where we have defined

$$
E^2_{\mathbf{k}} = \varepsilon^2(\mathbf{k}) + \left(\frac{Um}{2}\right)^2, \tag{2.13}
$$

being $\varepsilon(\mathbf{k})$ the dispersion relation deriving from the diagonalization of the kinetic part, while m and n are respectively the staggered magnetization and the average occupation number. From this expression we can see that a gap $\Delta = Um/2$ appears at the edges of the reduced Brillouin zone, making the system a Mott insulator. It can be shown that the staggered magnetization m satisfies the relation

$$
m = \frac{U}{N_s}\sum_{\mathbf{k}\in\mathrm{RBZ}}\frac{m}{E_{\mathbf{k}}}\left[f(-E_{\mathbf{k}} - \mu + \frac{Un}{2}) - f(E_{\mathbf{k}} - \mu + \frac{Un}{2})\right], \tag{2.14}
$$

where N_s is the number of sites, f is the Fermi function and μ is the chemical potential which is equal to $Un/2$ at half-filling (one electron per site). Notice that the sum has to

be performed over all $\mathbf{k}$ vectors of the reduced Brillouin zone. Eq. (2.14) must be solved in a self-consistent way, giving rise to an increasing trend of the staggered magnetization as a function of the on-site repulsion U. Indeed for $U \to \infty$, m becomes closer to 1, since each site never contains more than one spin.

If we allow spin canting, we deal with isotropic spins which make the average values $\langle S_i^+ \rangle$ and $\langle S_i^- \rangle$ different from zero. If we consider nearest-neighbor and next-nearest-neighbor hopping, t and t', the kinetic term $\mathcal{H}_t$ reads

$$\begin{aligned}
&-t \sum_{\langle i,j \rangle,\sigma} \left(c_{i,\sigma}^\dagger c_{j,\sigma} + c_{j,\sigma}^\dagger c_{i,\sigma} \right) - t' \sum_{[i,j],\sigma} \left(c_{i,\sigma}^\dagger c_{j,\sigma} + c_{j,\sigma}^\dagger c_{i,\sigma} \right) = \\
&-t \sum_{i,\sigma} \sum_{\delta=x,y} \left(c_{i,\sigma}^\dagger c_{i+\delta,\sigma} + c_{i+\delta,\sigma}^\dagger c_{i,\sigma} \right) - t' \sum_{i,\sigma} \sum_{\eta=x+y,-x+y} \left(c_{i,\sigma}^\dagger c_{i+\eta,\sigma} + c_{i+\eta,\sigma}^\dagger c_{i,\sigma} \right) = \\
&-t \sum_{i,\sigma} \sum_{\delta'} c_{i,\sigma}^\dagger c_{i+\delta',\sigma} - t' \sum_{i,\sigma} \sum_{\eta'} c_{i,\sigma}^\dagger c_{i+\eta',\sigma},
\end{aligned} \tag{2.15}$$

where δ' and η' run all over the four directions, i.e. $\delta' = x, -x, y, -y$ and $\eta' = x+y, -x+y, -x-y, x-y$.

Using the matrix formalism, we can write the entire approximated hamiltonian $\mathcal{H}_{HF}$ in an unrestricted form

$$\mathcal{H}_{HF} = \mathbf{c}^\dagger \hat{\mathbf{H}} \mathbf{c}, \tag{2.16}$$

where $\mathbf{c}$ is the column vector

$$c_{11,\uparrow}, c_{12,\uparrow}, \ldots, c_{1L,\uparrow}, c_{21,\uparrow}, \ldots, c_{2L,\uparrow}, \ldots, c_{LL,\uparrow}, c_{11,\downarrow}, \ldots, c_{LL,\downarrow}$$

with the subscripts indicating the x and y position of the considered site on the square lattice. $\mathbf{c}^\dagger$ is its adjoint row vector, while $\hat{\mathbf{H}}$ is an hermitian matrix, which we divide in four blocks, each of size $L^2 \times L^2$. The first block, whose indices run in the range $[11, 12, \ldots, 1L, \ldots, L1, \ldots, LL]$, couples the operators $c_\uparrow^\dagger$ with $c_\uparrow$. It is made by L^2 rows like this

$$\begin{pmatrix} U\langle n_{11,\downarrow} \rangle & -t_{12} & \cdots & -t_{1L} & -t_{21} & -t'_{22} & \cdots & -t'_{2L} & \cdots & -t_{L1} & -t'_{L2} & \cdots & -t'_{LL} \end{pmatrix}, \tag{2.17}$$

where we assume periodic boundary conditions. The third block, with indices from L^2+1 to $2L^2$, couples the operators $c_\downarrow^\dagger$ with $c_\downarrow$. It is the exact copy of the previous, but with $U\langle n_{i,\uparrow} \rangle$, i.e. average density of electrons with opposite spin, along the diagonal.
The two off-diagonal blocks are made by diagonal matrices: The one, with row index i running from 1 to L^2, and column index j running from L^2+1 to $2L^2$, couples the operators $c_\uparrow^\dagger$ with $c_\downarrow$ and it has the terms $U\langle S_i^- \rangle$ along the diagonal. The other, with i from L^2+1 to $2L^2$ and j from 1 to L^2, couples the operators $c_\downarrow^\dagger$ with $c_\uparrow$ and it has the terms $U\langle S_i^+ \rangle$ along the diagonal.
Now we can find the base in which the matrix $\hat{\mathbf{H}}$ is diagonal. Being this matrix an hermitian matrix, it can be decomposed in this way:

$$\hat{\mathbf{H}} = \hat{\mathbf{\Phi}} \hat{\mathbf{\Lambda}} \hat{\mathbf{\Phi}}^\dagger, \tag{2.18}$$

where $\hat{\mathbf{\Lambda}}$ is the diagonal matrix made by eigenvalues of $\hat{\mathbf{H}}$, while $\hat{\mathbf{\Phi}}$ is the unitary matrix (i.e. $\hat{\mathbf{\Phi}}\hat{\mathbf{\Phi}}^\dagger = 1 = \hat{\mathbf{\Phi}}^\dagger\hat{\mathbf{\Phi}}$), with the columns made by the orthonormal eigenvectors of $\hat{\mathbf{H}}$. So

$$\mathcal{H}_{HF} = \mathbf{c}^\dagger\hat{\mathbf{H}}\mathbf{c} = \mathbf{c}^\dagger\hat{\mathbf{\Phi}}\hat{\mathbf{\Lambda}}\hat{\mathbf{\Phi}}^\dagger\mathbf{c} = \gamma^\dagger\hat{\mathbf{\Lambda}}\gamma, \tag{2.19}$$

with new creation and annihilation operators

$$\gamma = \hat{\mathbf{\Phi}}^\dagger\mathbf{c} \Rightarrow \gamma_\nu = \sum_{i\sigma} \Phi^*_{(i\sigma),\nu} c_{i\sigma}; \tag{2.20}$$

$$\gamma^\dagger = \mathbf{c}^\dagger\hat{\mathbf{\Phi}} \Rightarrow \gamma^\dagger_\mu = \sum_{j\sigma} c^\dagger_{j\sigma}\Phi_{(j\sigma),\mu}, \tag{2.21}$$

and the inverse relations

$$\mathbf{c} = \hat{\mathbf{\Phi}}\gamma \Rightarrow c_{i\sigma} = \sum_{\nu} \Phi_{(i\sigma),\nu}\gamma_\nu; \tag{2.22}$$

$$\mathbf{c}^\dagger = \gamma^\dagger\hat{\mathbf{\Phi}}^\dagger \Rightarrow c^\dagger_{j\sigma} = \sum_{\mu} \gamma^\dagger_\mu\Phi^*_{(j\sigma),\mu}. \tag{2.23}$$

Now we can construct the Slater determinant with the new operator $\gamma^\dagger_\mu$ where the index $\mu \in [1 : 2L^2]$ assumes the meaning of a quantum number that labels the energy states. So the Hartree-Fock (HF) ground state can be written as

$$|HF\rangle = \prod_{\mu<\mu_F} \gamma^\dagger_\mu|0\rangle, \tag{2.24}$$

where μ_F is the Fermi level equal to the number of electrons in the lattice. If there is an electron for each site i, $\mu_F = L^2$. If there are N_h holes, $\mu_F = L^2 - N_h$. Note that the HF state is normalized:

$$\langle HF|HF\rangle = \langle 0|\gamma_1\gamma_2\cdots\gamma_{\mu_F}\gamma^\dagger_{\mu_F}\cdots\gamma^\dagger_2\gamma^\dagger_1|0\rangle = \langle 0|0\rangle = 1. \tag{2.25}$$

$\hat{\mathbf{H}}$ (and therefore also $\hat{\mathbf{\Phi}}$) depends on the averages $\langle n_{i,\downarrow}\rangle, \langle n_{i,\uparrow}\rangle, \langle S^-_i\rangle, \langle S^+_i\rangle$. This requires an iterative self-consistent procedure. We must guess a starting charge and spin configuration, from which we extract the local occupation number n_i and spin $\mathbf{S}_i$, which we consider as quantum averages. So we have $\langle n_i\rangle$, $\langle S^x_i\rangle$, $\langle S^y_i\rangle$, $\langle S^z_i\rangle$, from which we can obtain

$$\begin{cases} \langle S^+_i\rangle = \langle S^x_i\rangle + i\langle S^y_i\rangle; \\ \langle S^-_i\rangle = \langle S^x_i\rangle - i\langle S^y_i\rangle; \end{cases} \tag{2.26a}$$

$$\begin{cases} \langle n_{i,\downarrow}\rangle = \frac{\langle n_i\rangle}{2} - \langle S^z_i\rangle; \\ \langle n_{i,\uparrow}\rangle = \frac{\langle n_i\rangle}{2} + \langle S^z_i\rangle, \end{cases} \tag{2.26b}$$

that we need to set the starting matrix. Then at the end of each diagonalization we have to reset the matrix $\hat{\mathbf{H}}$ for the following step. Thus we need, for each lattice site, the

new values of $\langle n_{i,\downarrow}\rangle, \langle n_{i,\uparrow}\rangle, \langle S_i^-\rangle, \langle S_i^+\rangle$ resulting from the diagonalization. They must be calculated by averaging the corresponding operators over the state $|HF\rangle$:

$$\begin{aligned}
\langle n_{i,\downarrow}\rangle &= \langle HF|c_{i,\downarrow}^\dagger c_{i,\downarrow}|HF\rangle = \sum_{\mu,\nu}\langle HF|\gamma_\mu^\dagger \Phi_{(i,\downarrow),\mu}^* \Phi_{(i,\downarrow),\nu}\gamma_\nu|HF\rangle \\
&= \sum_{\mu,\nu}\Phi_{(i,\downarrow),\mu}^*\Phi_{(i,\downarrow),\nu}\langle HF|\gamma_\mu^\dagger\gamma_\nu|HF\rangle \\
&= \sum_{\mu,\nu}\Phi_{(i,\downarrow),\mu}^*\Phi_{(i,\downarrow),\nu}\delta_{\mu\nu}\Theta(\mu_F-\mu)\langle HF|HF\rangle \\
&= \sum_{\mu<\mu_F}|\Phi_{(i,\downarrow),\mu}|^2; \qquad (2.27)\\
\langle n_{i,\uparrow}\rangle &= \langle HF|c_{i,\uparrow}^\dagger c_{i,\uparrow}|HF\rangle = \sum_{\mu<\mu_F}|\Phi_{(i,\uparrow),\mu}|^2; \qquad (2.28)\\
\langle S_i^-\rangle &= \langle HF|c_{i,\downarrow}^\dagger c_{i,\uparrow}|HF\rangle = \sum_{\mu<\mu_F}\Phi_{(i,\downarrow),\mu}^*\Phi_{(i,\uparrow),\mu}; \qquad (2.29)\\
\langle S_i^+\rangle &= \langle HF|c_{i,\uparrow}^\dagger c_{i,\uparrow}|HF\rangle = \sum_{\mu<\mu_F}\Phi_{(i,\uparrow),\mu}^*\Phi_{(i,\downarrow),\mu}. \qquad (2.30)
\end{aligned}$$

The procedure ends only when the energy of the system at the step $n+1$ is equal to the one at the step n within a certain threshold. It can be calculated by averaging the hamiltonian over the HF state:

$$\langle HF|\mathcal{H}_{HF}|HF\rangle = \langle HF|\mathcal{H}_t|HF\rangle + \langle HF|\mathcal{H}_{t'}|HF\rangle + \langle HF|\mathcal{H}_U|HF\rangle. \qquad (2.31)$$

We start with the first term

$$\begin{aligned}
&\langle HF|\mathcal{H}_t|HF\rangle = -t\sum_{i,\delta',\sigma}\langle HF|c_{i,\sigma}^\dagger c_{i+\delta',\sigma}|HF\rangle = \\
&-t\sum_{i,\delta',\sigma}\sum_{\mu,\nu}\langle HF|\gamma_\mu^\dagger\Phi_{(i,\sigma),\mu}^*\Phi_{(i+\delta',\sigma),\nu}\gamma_\nu|HF\rangle = \\
&-t\sum_{i,\delta',\sigma}\sum_{\mu,\nu}\Phi_{(i,\sigma),\mu}^*\Phi_{(i+\delta',\sigma),\nu}\langle HF|\gamma_\mu^\dagger\gamma_\nu|HF\rangle = \\
&-t\sum_{i,\delta',\sigma}\sum_{\mu,\nu}\Phi_{(i,\sigma),\mu}^*\Phi_{(i+\delta',\sigma),\nu}\delta_{\mu\nu}\Theta(\mu_F-\mu)\langle HF|HF\rangle = \\
&-t\sum_{i,\delta',\sigma}\sum_{\mu<\mu_F}\Phi_{(i,\sigma),\mu}^*\Phi_{(i+\delta',\sigma),\mu}. \qquad (2.32)
\end{aligned}$$

The second term has the same form:

$$\langle HF|\mathcal{H}_{t'}|HF\rangle = -t'\sum_{i,\eta',\sigma}\sum_{\mu<\mu_F}\Phi_{(i,\sigma),\mu}^*\Phi_{(i+\eta',\sigma),\mu}. \qquad (2.33)$$

Finally the average of the repulsion term:

$$\begin{aligned}
&\langle HF|\mathcal{H}_U|HF\rangle = U\sum_i \Big(\langle HF|c^\dagger_{i,\uparrow}c_{i,\uparrow}|HF\rangle\langle HF|c^\dagger_{i,\downarrow}c_{i,\downarrow}|HF\rangle \\
&-\langle HF|c^\dagger_{i,\uparrow}c_{i,\downarrow}|HF\rangle\langle HF|c^\dagger_{i,\downarrow}c_{i,\uparrow}|HF\rangle\Big) = \\
&U\sum_i \Bigg[\sum_{\mu<\mu_F}\left(\Phi^*_{(i,\uparrow),\mu}\Phi_{(i,\uparrow),\mu}\right)\times\sum_{\nu<\mu_F}\left(\Phi^*_{(i,\downarrow),\nu}\Phi_{(i,\downarrow),\nu}\right) \\
&-\sum_{\mu<\mu_F}\left(\Phi^*_{(i,\uparrow),\mu}\Phi_{(i,\downarrow),\mu}\right)\times\sum_{\nu<\mu_F}\left(\Phi^*_{(i,\downarrow),\nu}\Phi_{(i,\uparrow),\nu}\right)\Bigg] = \\
&U\sum_i\sum_{\substack{\mu<\mu_F\\ \nu<\mu_F}}\left[|\Phi_{(i,\uparrow),\mu}|^2|\Phi_{(i,\downarrow),\nu}|^2 - \Phi^*_{(i,\uparrow),\mu}\Phi_{(i,\downarrow),\mu}\Phi^*_{(i,\downarrow),\nu}\Phi_{(i,\uparrow),\nu}\right]. \qquad (2.34)
\end{aligned}$$

Putting all terms together we have

$$\begin{aligned}
&E_{HF} = \langle HF|\mathcal{H}_{HF}|HF\rangle = \\
&\sum_i\Bigg\{\sum_{\mu<\mu_F}\Bigg[-t\sum_{\delta',\sigma}\left(\Phi^*_{(i,\sigma),\mu}\Phi_{(i+\delta',\sigma),\mu}\right) - t'\sum_{\eta',\sigma}\left(\Phi^*_{(i,\sigma),\mu}\Phi_{(i+\eta',\sigma),\mu}\right) \\
&+U\sum_{\nu<\mu_F}\left(|\Phi_{(i,\uparrow),\mu}|^2|\Phi_{(i,\downarrow),\nu}|^2 - \Phi^*_{(i,\uparrow),\mu}\Phi_{(i,\downarrow),\mu}\Phi^*_{(i,\downarrow),\nu}\Phi_{(i,\uparrow),\nu}\right)\Bigg]\Bigg\}. \qquad (2.35)
\end{aligned}$$

A the end of the iterations, when the energy E_{HF} has converged to a constant quantity, we have the 'right' values of $\langle n_{i,\downarrow}\rangle, \langle n_{i,\uparrow}\rangle, \langle S_i^-\rangle, \langle S_i^+\rangle$. So the resulting charge and spin configuration can be obtained inverting eqs. (2.26):

$$\begin{cases} \langle S_i^x\rangle = \frac{\langle S_i^+\rangle + \langle S_i^-\rangle}{2}; \\ \langle S_i^y\rangle = i\frac{\langle S_i^-\rangle - \langle S_i^+\rangle}{2}. \end{cases} \qquad (2.36a)$$

$$\begin{cases} \langle n_i\rangle = \langle n_{i,\uparrow}\rangle + \langle n_{i,\downarrow}\rangle; \\ \langle S_i^z\rangle = \frac{\langle n_{i,\uparrow}\rangle - \langle n_{i,\downarrow}\rangle}{2}, \end{cases} \qquad (2.36b)$$

To test the algorithm we can perform the numerical Hartree-Fock calculation of an antiferromagnet. As a starting configuration we assume half-filling with an homogeneous distribution of charge ($n_i = 1$ for each site) and we consider spins along z direction, i.e. $\mathbf{S}_i = [0, 0, 1/2(-1)^{x_i+y_i}]$. In particular we study the staggered magnetization m for increasing values of the ratio U/t (only nearest-neighbor hopping is considered). The result is reported in Fig. 2.2. As expected $m \to 1$ for $U/t \to \infty$.

2.3.2 Gutzwiller approximation

To perform a more accurate MF calculation we refer to Ref. [3], which describes the Gutzwiller approximation. It represents a variational method which accounts for reduced

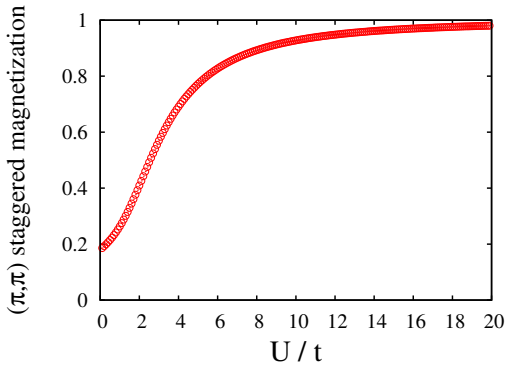

Figure 2.2: Results of the Hartree-Fock calculation for an axial antiferromagnet: staggered (π, π) magnetization as a function of the ratio U/t. The finite value of m for $U/t \to \infty$ is a finite size effect.

double occupancy. We define the double occupancy operator

$$\hat{D} = \sum_i n_{i,\uparrow} n_{i,\downarrow}, \tag{2.37}$$

where the sum runs all over the sites of the lattice. The expectation value $D = \langle \hat{D} \rangle$ represents the number of doubly occupied sites. If we start from the uncorrelated state $|\psi_0\rangle$, for $U = 0$, when the interaction is turned on, the energy minimization makes D lower than in the case of non interacting system. Now, the problem is the research of the ground state ψ of the correlated system. We introduce the trial wave-function

$$|\psi\rangle = \prod_i \left[1 - (1-g) n_{i,\uparrow} n_{i,\downarrow}\right] |\psi_0\rangle = g^{\left(\sum_i n_{i,\uparrow} n_{i,\downarrow}\right)} |\psi_0\rangle = g^{\hat{D}} |\psi_0\rangle, \tag{2.38}$$

where g is a variational parameter that has to be determined so as to minimize the ground state energy functional

$$E[\psi] = \frac{\langle \psi | \mathcal{H} | \psi \rangle}{\langle \psi | \psi \rangle}, \tag{2.39}$$

being $\mathcal{H}$ the Hubbard hamiltonian of eq. (2.1). The boundary values of g are

- $g = 1$: uncorrelated state (exact solution for $U = 0$);
- $g = 0$: all the configurations with non zero double occupancy are projected out.

More generally, the operator $\hat{P}_i(g) = 1 - (1-g) n_{i,\uparrow} n_{i,\downarrow}$, with g in the range $(0, 1)$, reduces the weight of the configurations with doubly occupied sites. While the interaction term is treated exactly in this approach, the evaluation of the norm $\langle \psi | \psi \rangle$ and the average value of the kinetic term $\langle \psi | \mathcal{H}_t | \psi \rangle$, can not be done analytically, except for 0 or ∞ dimensions. Therefore one must use to the so-called "Gutzwiller approximation" (GA). We rewrite the non-interacting state in the following way

$$|\psi_0\rangle = \sum_D \sum_{\{i_D\}} A_{i_D} |\psi_{i_D}\rangle. \tag{2.40}$$

What we have done is, for each value of D (the number of double occupancies), to decompose the non-interacting state in all the possible states $|\psi_{i_D}\rangle$ with D double occupancies. In this way all the interest is focused on the double occupancies. Now we have

$$\begin{aligned}\langle\psi|\psi\rangle &= \langle\psi_0|g^{\hat{D}}g^{\hat{D}}|\psi_0\rangle = \sum_{DD'}\sum_{\{i_D\}\{i_{D'}\}} A^*_{i_D}A_{i_{D'}}\langle\psi_{i_D}|g^{\hat{D}}g^{\hat{D}}|\psi_{i_{D'}}\rangle \\ &= \sum_{DD'}\sum_{\{i_D\}\{i_{D'}\}} A^*_{i_D}A_{i_{D'}}g^{2D}\delta_{i_D,i_{D'}} = \sum_D\sum_{\{i_D\}}|A_{i_D}|^2g^{2D}, \end{aligned} \tag{2.41}$$

where $|A_{i_D}|^2$ is the probability amplitude of a double occupancy in the site i. An approximation of this quantity can be achieved by means of a statistical approach, according to which each process takes place in a mean field. More specifically, the spatial distribution of the doubly occupied sites is completely neglected: different electronic configurations but with the same density of single occupied and double occupied sites, are energetically equivalent. Physically one neglects the specific environment in which the hopping takes place, not distinguishing between more or less favorable configurations, if they have the same value of D. If L is the number of lattice sites, we define

$$d = \frac{D}{L}; \tag{2.42a}$$

$$n_\uparrow = \frac{N_\uparrow}{L}; \tag{2.42b}$$

$$n_\downarrow = \frac{N_\downarrow}{L}. \tag{2.42c}$$

They represent respectively the density of double occupied sites, the density of sites occupied by a single electron $\uparrow$, and the density of sites occupied by a single electron $\downarrow$. Then we transform the quantum probability amplitude in a purely statistical probability in the following way:

$$\sum_{\{i_D\}}|A_{i_D}|^2 = P(N_\uparrow,L)P(N_\downarrow,L)N_D(N_\uparrow,N_\downarrow,L), \tag{2.43}$$

where

$$P(N_\sigma,L) = n_\sigma^{N_\sigma}(1-n_\sigma)^{L-N_\sigma} \tag{2.44}$$

is the probability for a configuration of N_σ spins on L sites to occur (which are all equals and independent because spatial correlations are neglected), while

$$N_D(N_\uparrow,N_\downarrow,L) = \frac{L!}{(N_\uparrow-D)!\,(N_\uparrow-D)!\,D!\,[L-(N_\uparrow-D)-(N_\downarrow-D)-D]!} \tag{2.45}$$

represents the number of different configurations involving D double occupancies, once given $N_\uparrow$ and $N_\downarrow$. Indeed $(N_\uparrow-D)$, $(N_\downarrow-D)$, D and $[L-(N_\uparrow-D)-(N_\downarrow-D)-D]$ represent respectively the number of sites occupied by a single spin up, the number of

sites occupied by a single spin down, the number of doubly occupied sites and the number of empty sites. In this way we obtain the norm

$$\langle\psi|\psi\rangle = \sum_D g^{2D} P(N_\uparrow, L) P(N_\downarrow, L) N_D(N_\uparrow, N_\downarrow, L), \tag{2.46}$$

and the interacting term

$$\langle\psi|U \sum_i n_{i,\uparrow} n_{i,\downarrow}|\psi\rangle = \langle\psi|U\hat{D}|\psi\rangle = U \sum_D D g^{2D} P(N_\uparrow, L) P(N_\downarrow, L) N_D(N_\uparrow, N_\downarrow, L). \tag{2.47}$$

Now we analyse the hopping term. There are four possible processes involving an electron $\uparrow$ which jumps from the site i to the site j. They are shown in Fig. 2.3. So, if we take

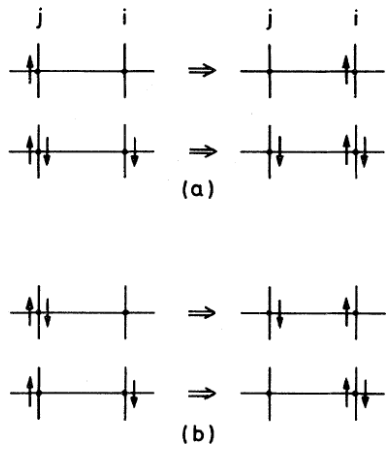

Figure 2.3: The four possible hopping processes for an up-spin particle in the Hubbard mode; (a) leaving the number of doubly occupied sites unchanged, (b) changing the number by one [3].

a lattice with L sites isolating the two sites involved in the hopping process, the number N_D of spin configurations in the remaining part of the lattice depends on the number of spins in the two sites:

1. the first process involves a single electron $\uparrow$ and the number of double occupancies is D in both the initial state and the final state, giving the term $\sum_D g^{2D} N_D(L - 2, N_\uparrow - 1, N_\downarrow)$;

2. the second process involves a single electron $\uparrow$ and two electrons $\downarrow$ and the number of double occupancies is $D + 1$ in both the initial state and the final state, giving the term $\sum_D g^{2D+2} N_D(L - 2, N_\uparrow - 1, N_\downarrow - 2)$;

3. the third process involves one electron $\uparrow$ and one electron $\downarrow$ and the number of double occupancies is $D+1$ in the initial state and D in the final state. The resulting term is $\sum_D g^{2D+1} N_D(L - 2, N_\uparrow - 1, N_\downarrow - 1)$;

4. the fourth process involves again one electron ↑ and one electron ↓ and the number of double occupancies is D in the initial state and $D+1$ in the final state. The resulting term is $\sum_D g^{2D+1} N_D(L-2, N_\uparrow - 1, N_\downarrow - 1)$.

All these terms must be multiplied by the probabilities $P(N_\uparrow - 1, L-2)P(N_\downarrow, L)$ and by the value of the average kinetic energy of the non-interacting case

$$\bar{\varepsilon}_\uparrow = \frac{1}{L}\langle\psi_0| \sum_{ij} t_{ij} c^\dagger_{i\uparrow} c_{j\uparrow} |\psi_0\rangle = \sum_{k<k_F} \varepsilon(\mathbf{k}) < 0$$

. An analogous expression must be considered also for a ↓ electron.

Summarizing, all the terms we have obtained (kinetic term, repulsive term and norm) are of the type

$$\sum_D g^{2D+a} N_D(L-b, N_\uparrow - c, N_\downarrow - d)$$

which in the thermodynamic limit ($L, N_\uparrow, N_\downarrow \to \infty$) becomes

$$\sum_D g^{2D} N_D(L, N_\uparrow, N_\downarrow) = \sum_D \exp[D \ln g^2 + \ln N_D], \tag{2.48}$$

since a, b, c, d can be neglected. Using the Stirling formula $\ln(N!) \simeq N \ln N - N$, we have

$$\begin{aligned} \ln N_D \simeq\ & L \ln L - D \ln D - (N_\uparrow - D)\ln(N_\uparrow - D) - (N_\downarrow - D)\ln(N_\downarrow - D) \\ & -[L - (N_\uparrow - D) - (N_\uparrow - D) - D]\ln[L - (N_\uparrow - D) - (N_\uparrow - D) - D] \end{aligned} \tag{2.49}$$

Now, in the thermodynamic limit, the summation (2.48) can be approximated by the largest term corresponding to the value $\bar{D}$ which maximizes the exponential:

$$\frac{\partial}{\partial D}[D \ln g^2 + \ln N_D] = 0,$$

which implies

$$g^2 = \frac{d(1 - n_\uparrow - n_\downarrow + d)}{(n_\uparrow - d)(n_\downarrow - d)}, \tag{2.50}$$

which is symmetric with respect to σ. Now d is the statistically most probable value of the double occupancy density. Substituting the expression (2.50) in (2.48) we can calculate the statistical form of each energy term. The resulting Gutzwiller energy is given by

$$\frac{E_g}{L} = q_\uparrow(d, n_\uparrow, n_\downarrow)\bar{\varepsilon}_\uparrow + q_\downarrow(d, n_\uparrow, n_\downarrow)\bar{\varepsilon}_\downarrow + Ud, \tag{2.51}$$

with

$$\begin{aligned} q_\sigma \ &= \ \frac{\{(1 - n_\sigma - n_{\bar{\sigma}} + d)(n_\sigma - d)|_0 + d(n_{\bar{\sigma}} - d)|_{\uparrow\downarrow}\}_{\text{prop}}}{n_\sigma(1 - n_\sigma)} \\ &+ \ \frac{\{2[d(1 - n_\sigma - n_{\bar{\sigma}} + d)(n_\sigma - d)(n_{\bar{\sigma}} - d)]^{1/2}\}_{\text{pol}}}{n_\sigma(1 - n_\sigma)}, \end{aligned} \tag{2.52}$$

where the brackets with subscripts *prop* and *pol* refer to the contributions to q_σ from the processes shown in Fig. 2.3(a) (propagation of an empty site (subscript 0) and a doubly occupied site (subscript $\uparrow\downarrow$), respectively) and Fig. 2.3(b) (polarization process). The Gutzwiller variational method consists in the minimization of the expression (2.51) with respect to the parameter d.

For example this method can be applied to the description of the metal-insulator transition: for half-filled band (one electron per site) and $n_\uparrow = n_\downarrow$, which implies $q_\uparrow = q_\downarrow \equiv q$, $\bar{\varepsilon}_\uparrow = \bar{\varepsilon}_\downarrow \equiv \bar{\varepsilon}_0/2$), one has

$$d = \frac{1}{4}\left[1 - \frac{U}{U_c}\right]; \tag{2.53}$$

$$q = 1 - \left[\frac{U}{U_c}\right]^2, \tag{2.54}$$

where $U_c = 8|\bar{\varepsilon}_0|$. This implies that at a finite, critical interaction U_c the number of doubly occupied sites vanishes, such that every lattice point is singly occupied, i.e., that the particles are localized, leading to a Mott insulator. However this value of U is never obtained if we consider an antiferromagnet.

2.3.3 Slave boson method

The "slave boson" method has been proposed by Kotliar and Ruckenstein [4]. Although it approaches the problem of strongly correlated electrons from a completely different point of view, it leads to the results derived from Gutzwiller variational wave-function. The Fock space is enlarged in each site, in order to contain, apart from the original fermions, a set of bosonic operators. The new Hilbert space is defined as follows

$$|0\rangle \longrightarrow e_i^\dagger|\tilde{0}\rangle; \tag{2.55a}$$

$$|\uparrow\rangle = c_{i,\uparrow}^\dagger|0\rangle \longrightarrow f_{i\uparrow}^\dagger p_{i\uparrow}^\dagger|\tilde{0}\rangle; \tag{2.55b}$$

$$|\downarrow\rangle = c_{i,\downarrow}^\dagger|0\rangle \longrightarrow f_{i\downarrow}^\dagger p_{i\downarrow}^\dagger|\tilde{0}\rangle; \tag{2.55c}$$

$$|\uparrow\downarrow\rangle = c_{i,\uparrow}^\dagger c_{i,\downarrow}^\dagger|0\rangle \longrightarrow f_{i\uparrow}^\dagger f_{i\downarrow}^\dagger d_i^\dagger|\tilde{0}\rangle, \tag{2.55d}$$

where $e_i^\dagger$, $p_{i\sigma}^\dagger$ and $d_i^\dagger$ are four bosonic operators which label the empty sites, the singly occupied sites and the doubly occupied sites respectively, while $f_{i\sigma}^\dagger$ are the new fermionic creation operators. However one must put some constraints in order to cancel non-physical states[1]. These constraints are expressed as

$$e_i^\dagger e_i + \sum_\sigma p_{i\sigma}^\dagger p_{i\sigma} + d_i^\dagger d_i = 1; \tag{2.56a}$$

$$f_{i\sigma}^\dagger f_{i\sigma} = p_{i\sigma}^\dagger p_{i\sigma} + d_i^\dagger d_i. \tag{2.56b}$$

[1]For example $e^\dagger f_\downarrow^\dagger d^\dagger|\tilde{0}\rangle$ is not allowed since the state cannot be empty, singly occupied and doubly occupied simultaneously.

Since each site can be exclusively (i) empty, (ii) occupied by an electron ↑, (iii) occupied by an electron ↓, (iv) doubly occupied, the condition (2.56a) tells us that, for a real space configuration, only one of the occupation numbers relative to the four "label" operators, must be one. The others must be zero. The condition (2.56b) equals the two ways to count the fermionic occupation in each site, since the fermions count must be the same whether or not it is done by using fermions or bosons. To better understand the mechanism of the new Hilbert space we report an example relative to the creation of an electron ↑ in an empty site and in a site occupied by an electron ↓

$$c^\dagger_{i,\uparrow} \begin{cases} |0\rangle \to |\uparrow\rangle & \implies \; e^\dagger_i|\tilde{0}\rangle \to f^\dagger_{i,\uparrow} p^\dagger_{i,\uparrow}|\tilde{0}\rangle \\ |\downarrow\rangle \to |\uparrow\downarrow\rangle & \implies \; f^\dagger_{i,\downarrow} p^\dagger_{i,\downarrow}|\tilde{0}\rangle \to f^\dagger_{i,\uparrow} f^\dagger_{i,\downarrow} d^\dagger_i|\tilde{0}\rangle \end{cases}$$

So the creation of a spin σ can takes place in the two ways:

1. one empty site is destroyed and a site occupied by a spin σ is created: $f^\dagger_{i,\sigma} p^\dagger_{i,\sigma} e_i$;
2. a singly occupied site (by a spin $\bar{\sigma}$) is destroyed, and a doubly occupied site is created: $f^\dagger_{i,\sigma} d^\dagger_i p_{i,\bar{\sigma}}$.

So the correspondence of the operators of the conventional Hilbert space and the new space is given by

$$c^\dagger_{i,\sigma} \longrightarrow f^\dagger_{i,\sigma}(p^\dagger_{i,\sigma} e_i + d^\dagger_i p_{i,\bar{\sigma}}) = f^\dagger_{i,\sigma} z^\dagger_{i,\sigma}, \tag{2.57}$$

where $z^\dagger_{i,\sigma} = p^\dagger_{i,\sigma} e_i + d^\dagger_i p_{i,\bar{\sigma}}$ is associated to the creation of a spin σ on the site i. If we apply the operator $f^\dagger_{i,\sigma} z^\dagger_{i,\sigma}$ to a site already occupied by a spin σ, it returns the vacuum. In the same way we have

$$c_{i,\sigma} \longrightarrow f_{i,\sigma}(e^\dagger_i p_{i,\sigma} + p^\dagger_{i,\bar{\sigma}} d_i) = f_{i,\sigma} z_{i,\sigma}, \tag{2.58}$$

where $z_{i,\sigma} = e^\dagger_i p_{i,\sigma} + p^\dagger_{i,\bar{\sigma}} d_i$ is associated to the annihilation of a spin σ on the site i.

The Hubbard hamiltonian (2.1) rewritten in terms of these new bosonic operators, reads

$$\tilde{\mathcal{H}} = \sum_{\langle i,j\rangle,\sigma} t_{ij} f^\dagger_{i,\sigma} f_{j,\sigma} z^\dagger_{i,\sigma} z_{j,\sigma} + U \sum_i d^\dagger_i d_i, \tag{2.59}$$

where the correlation term is entirely constituted by the bosons. Eq. (2.59), together with the constraints (2.56a), (2.56b) forms a system that requires approximations in order to be solved.

The first approximation one can do is the "saddle-point" approximation, i.e. a mean field calculation. Unfortunately, it can be shown that this approximation leads to incorrect result in the non-interacting limit. In order to resolve this problem we make use of the fact that there are many different hamiltonians $\tilde{\mathcal{H}}$ in the enlarged Hilbert space which lead to the same spectrum as (2.1) when restricted to the physical subspace defined by conditions (2.56). Clearly this arbitrariness presents no difficulty as long as the constraints are handled exactly. However, any application which relaxes the constraints is sensitive

to the precise choice of $\tilde{\mathcal{H}}$. In a practical calculation the form of $\tilde{\mathcal{H}}$ can be determined by requiring that the approximation scheme leads to physically sensible results in known limiting cases. In particular we can rewrite $z_{i,\sigma}$ as

$$z_{i,\sigma} = \frac{1}{\sqrt{e_i^\dagger e_i + p_{i,\bar{\sigma}}^\dagger p_{i,\bar{\sigma}}}} (e_i^\dagger p_{i,\sigma} + p_{i,\bar{\sigma}}^\dagger d_i) \frac{1}{\sqrt{d_i^\dagger d_i + p_{i,\sigma}^\dagger p_{i,\sigma}}}. \tag{2.60}$$

This choice allows us to overcome the difficulties encountered for $U = 0$ in the saddle-point approximation. In Ref. [4], this approximation has been applied to the paramagnetic phase of the half-filled Hubbard model. This leads to the same results (2.53) and (2.54) as in the Gutzwiller approximation.

In our case the saddle-point approximation can be achieved simply by treating all bosonic operators as numbers. It consists in a sort of Hartree-Fock approximation applied to the bosonic part of hamiltonian (2.59), which reads

$$\tilde{\mathcal{H}} \simeq \sum_{\langle i,j\rangle,\sigma} t_{ij} \langle z_{i,\sigma}^\dagger z_{j,\sigma}\rangle f_{i,\sigma}^\dagger f_{j,\sigma} + U \sum_i \langle d_i^\dagger d_i\rangle \simeq \sum_{\langle i,j\rangle,\sigma} t_{ij} z_{i,\sigma}^* z_{j,\sigma} f_{i,\sigma}^\dagger f_{j,\sigma} + U \sum_i d_i^2, \tag{2.61}$$

and to the constraints. This single-particle hamiltonian (2.61) describes the dynamics of particles with modulated hopping amplitude and can be diagonalized by the transformation

$$f_{i,\sigma} = \sum_k \Phi_{(i,\sigma),k}\, a_k, \tag{2.62}$$

where the orthogonality of the transformation requires

$$\sum_{i,\sigma} \Phi^*_{(i,\sigma),k} \Phi_{(i,\sigma),k'} = \delta_{kk'}. \tag{2.63}$$

Given a system with N_e particles we finally obtain for the total energy

$$E_{tot} = \sum_{ij,\sigma} t_{ij} z^*_{i,\sigma} z_{j,\sigma} \sum_{k=1}^{N_e} \Phi^*_{(i,\sigma),k} \Phi_{(i,\sigma),k} + U \sum_i d_i^2, \tag{2.64}$$

This expression has to be evaluated within the constraints (2.56) and (2.63). Within the same level of approximation, this can be achieved by adding these constraints quadratically by means of Lagrange multipliers:

$$E_{C1} = \lambda_1 \sum_i \left(e_i^2 + \sum_\sigma p_{i,\sigma}^2 + d_i^2 - 1 \right)^2, \tag{2.65a}$$

$$E_{C2} = \lambda_2 \sum_{i,\sigma} \left(\sum_{k=1} \Phi^*_{(i,\sigma),k} \Phi_{(i,\sigma),k} - p_{i,\sigma}^2 - d_i^2 \right)^2 \tag{2.65b}$$

$$E_{C3} = \lambda_3 \sum_{k,k'} \left(\sum_{i,\sigma} \Phi^*_{(i,\sigma),k} \Phi_{(i,\sigma),k'} - \delta_{kk'} \right)^2. \tag{2.65c}$$

Now the energy functional

$$E\left\{\Phi_{(i,\sigma),k}, e_i, p_{i,\sigma}, d_i\right\} = E_{tot} + E_{C1} + E_{C2} + E_{C3}$$

has to be minimized with respect to the fermionic and bosonic fields.

Eq. (2.61) is the appropriate Gutzwiller energy functional[2] when one restricts on the longitudinal spin degrees of freedom (i.e. S_i^z). However, transverse components can be straightforwardly incorporated within the spin rotationally invariant slave boson formulation [5, 6]. It is convenient to introduce the spinor operators

$$\mathbf{\Psi}_i^\dagger = (c_{i,\uparrow}^\dagger, c_{i,\downarrow}^\dagger); \qquad \mathbf{\Psi}_i = \begin{pmatrix} c_{i,\uparrow} \\ c_{i,\downarrow} \end{pmatrix}, \tag{2.66}$$

and define the spin vector components as

$$S_i^x = \frac{1}{2}\mathbf{\Psi}_i^\dagger \tau_x \mathbf{\Psi}_i = \frac{1}{2}(c_{i,\uparrow}^\dagger c_{i,\downarrow} + c_{i,\downarrow}^\dagger c_{i,\uparrow}); \tag{2.67a}$$

$$S_i^y = \frac{1}{2}\mathbf{\Psi}_i^\dagger \tau_y \mathbf{\Psi}_i = \frac{1}{2}(c_{i,\uparrow}^\dagger c_{i,\downarrow} - c_{i,\downarrow}^\dagger c_{i,\uparrow}); \tag{2.67b}$$

$$S_i^z = \frac{1}{2}\mathbf{\Psi}_i^\dagger \tau_z \mathbf{\Psi}_i = \frac{1}{2}(c_{i,\uparrow}^\dagger c_{i,\uparrow} - c_{i,\downarrow}^\dagger c_{i,\downarrow}), \tag{2.67c}$$

where we are considering the 1/2-spins. τ_i denote the Pauli matrices and one can furtheron define the usual raising and lowering operators as $S_i^+ = S_i^x + iS_i^y$ and $S_i^- = S_i^x - iS_i^y$. The procedure consists essentially of three steps. Assume that in our spin initial reference frame we have non-vanishing spin order pointing locally in some given direction, i.e. $\langle \mathbf{S}_i \rangle \neq 0$. At first we then rotate locally to a new frame where spins point along the z-axis, i.e. $\langle \tilde{\mathbf{S}}_i \rangle = \langle (0, 0, \tilde{S}_i^z) \rangle$. This allows, as a second step, the introduction of slave-bosons and associated fermions $f_{i,\sigma}$. For the bosons we apply the saddle-point approximation. Finally in a third step we rotate the fermions back to the original reference frame. For the details of the calculation see appendix A. The resulting Gutzwiller energy functional for the Hubbard model, reads

$$E^{GA} = \sum_{i,j} t_{ij} \langle \mathbf{\Psi}_i^\dagger \mathbf{z}_i \mathbf{z}_j \mathbf{\Psi}_j \rangle + U \sum_i d_i^2, \tag{2.68}$$

where

$$\mathbf{z}_i = \begin{pmatrix} z_{i,\uparrow} \cos^2 \frac{\varphi_i}{2} + z_{i,\downarrow} \sin^2 \frac{\varphi_i}{2} & \frac{S_i^-}{2S_i^z}[z_{i,\uparrow} - z_{i,\downarrow}] \cos \varphi_i \\ \frac{S_i^+}{2S_i^z}[z_{i,\uparrow} - z_{i,\downarrow}] \cos \varphi_i & z_{i,\uparrow} \sin^2 \frac{\varphi_i}{2} + z_{i,\downarrow} \cos^2 \frac{\varphi_i}{2} \end{pmatrix}, \tag{2.69}$$

[2] Although it is obtained using the slave-bosons formalism, we call "Gutzwiller energy functional", eq. (2.61), since the form (2.60) for the expression of the bosons z_i, guarantees the same results as in the Gutzwiller approximation treated in the previous section. So, hereafter we call "Gutzwiller approximation" (GA) the saddle-point approximation applied to the hamiltonian rewritten in terms of the auxiliary bosons.

with

$$\tan^2 \varphi_i = \frac{S_i^+ S_i^-}{(S_i^z)^2}. \tag{2.70}$$

For clarity the terms S_i^+, S_i^-, S_i^z denote the spin expectation values in the Slater determinant, in spite of the omission of the brackets $\langle \dots \rangle$. Similarly n_i will denote the expectation value of the local occupation number, $\langle c_{i,\uparrow}^\dagger c_{i,\uparrow} + c_{i,\downarrow}^\dagger c_{i,\downarrow} \rangle$.

In the limit of a vanishing rotation angle φ the $\mathbf{z}$ matrix (2.69) becomes diagonal and the renormalization factors

$$z_{i,\sigma} = \frac{\sqrt{(1 - n_i + d_i^2)\left(\frac{1}{2}n_i + \frac{S_i^z}{\cos\varphi_i} - d_i^2\right)} + \sqrt{d_i^2\left(\frac{1}{2}n_i - \frac{S_i^z}{\cos\varphi_i} - d_i^2\right)}}{\sqrt{\left(\frac{1}{2}n_i + \frac{S_i^z}{\cos\varphi_i}\right)\left(1 - \frac{1}{2}n_i - \frac{S_i^z}{\cos\varphi_i}\right)}} \tag{2.71}$$

reduce to those of the standard Gutzwiller approximation. Variational solutions are computed by minimizing E^{GA} with respect to the Slater determinant and to the local double occupancy d_i.

Bibliography

[1] M. Kastner, R. Birgeneau, G. Shirane, Y. Endoh, Rev. Mod. Phys. **70**, 897 (1998).

[2] P. W. Anderson, Science **235** 1196 (1987).

[3] D. Vollhardt, Rev. Mod. Phys. **56**, 99 (1984).

[4] G. Kotliar and A. E. Ruckenstein, Phys. Rev. Lett. **57**, 1362 (1986).

[5] T. Li, P. Wölfle, P. Hirschfeld, Phys. Rev. B **40**, 6817 (1989).

[6] R. Frésard and P. Wölfle, Int. J. Mod. Phys. B **06**, 685 (1992).

Chapter 3

Spin model and topological defects

In this chapter we will describe the mapping of our strongly correlated system into a quantum spin model, namely the Heisenberg model. We will see that the mean field approximation on the Heisenberg model leads to a classical spin model. If we deal with a nearly planar spin configuration the classical XY-model will represent a good approximation of our system. Then we will report a brief overview on the XY-model and its solutions, focusing on the vortex configurations. We will make use of the conformal mapping theory in order to describe a continuous system, exploring the analogy with electrostatics and magnetostatics.

3.1 Quantum spin model

The Hubbard model at half-filling, with the on-site repulsion U much larger than t, can be mapped to an effective Heisenberg model i.e. a purely spin model which accounts for an antiferromagnetic interaction J_{ij} between the spins. Indeed one can show that the low energy states of the Hubbard model are the same as for the Heisenberg model provided one takes the exchange couplings as $J_{ij} = 4t_{ij}^2/U$ [1, 2]. Assuming hopping only between nearest neighbor sites, the effective hamiltonian reads

$$\mathcal{H}_{eff} = J \sum_{\langle i,j \rangle} \mathbf{S}_i \cdot \mathbf{S}_j = \frac{4t^2}{U} \sum_{\langle i,j \rangle} \left[S_i^z S_j^z + \frac{1}{2} \left(S_i^+ S_j^- + S_i^- S_j^+ \right) \right]. \tag{3.1}$$

When this model is treated with mean field approximation, the quantum spin operators $\mathbf{S}_i$ and $\mathbf{S}_j$ are substituted by the expectation values $\langle \mathbf{S}_i \rangle$ and $\langle \mathbf{S}_j \rangle$. In this way the spin fluctuations are neglected and the spins become purely classical isotropic objects, denoted by $\mathbf{s}_i$ and $\mathbf{s}_j$. If we assume a planar spin configuration[1], our effective model becomes an XY-model. Now we briefly analyse the main properties of this model (for a detailed treatment see for example Ref. [3]).

[1] We will see in chapter 5 that this assumption is justified.

3.2 Classical XY-model

The classical XY-model consists of two-dimensional isotropic spins, which interact according to the following hamiltonian:

$$\mathcal{H}_{XY} = \sum_{i,j} J_{ij}[\mathbf{S}_i \cdot \mathbf{S}_j] = \sum_{i,j} J_{ij} S^2 \cos(\theta_i - \theta_j). \tag{3.2}$$

The angle $\theta_i \equiv \theta(\mathbf{r}_i)$ represents the phase of the spin at the site i, whereas S is the absolute value ($S = 1/2$ for definition), so that

$$\mathbf{S}_i = S(\cos\theta_i, \sin\theta_i).$$

For now we restrict the (antiferromagnetic) interactions only to nearest-neighbor spins, so that

$$J_{ij} = \begin{cases} J > 0 & \text{for } i,j \text{ nearest neighbors} \\ 0 & \text{elsewhere} \end{cases} \tag{3.3}$$

So in a two-dimensional $L \times L$ square lattice with N_s sites ($L = \sqrt{N_s}a$), we can rewrite the hamiltonian in this way:

$$\mathcal{H}_{XY} = JS^2 \sum_{i=1}^{N_s} \sum_{\delta=x,y} \cos(\theta_i - \theta_{i+\delta}), \tag{3.4}$$

where x, y indicate the nearest neighbor site in the two directions. For simplicity we can map the antiferromagnetic interaction into a ferromagnetic one by means of a canonical transformation. So we define the staggered spins $\tilde{\mathbf{S}}_i = \mathbf{S}_i \exp(-i\mathbf{Q} \cdot \mathbf{r}_i)$, with $\mathbf{Q} = (\pi/a, \pi/a)$. This implies that $J \to -J$. Hereafter we make use of this transformation skipping the tilde in denoting the spins.

In order to find the stable configurations, we start from eq.(3.4) and minimize it with respect to each spin phase:

$$\begin{aligned} \frac{\partial \mathcal{H}_{XY}}{\partial \theta_i} &= JS^2 \sum_{i=1}^{N_s} \sum_{\delta=x,y} [\sin(\theta_i - \theta_{i+\delta}) - \sin(\theta_{i-\delta} - \theta_i)] = \\ &= JS^2 \sum_{i=1}^{N_s} \sum_{\delta=x,y} [\sin(\theta_i - \theta_{i+\delta}) + \sin(\theta_i - \theta_{i-\delta})] = 0. \end{aligned}$$

If we define

$$I_{i,i+\delta} = -J(\mathbf{S}_i \times \mathbf{S}_{i+\delta}) \cdot \hat{\mathbf{z}} = -JS^2 \sin(\theta_i - \theta_{i+\delta}) \tag{3.5}$$

we obtain

$$\sum_{i=1}^{N_s} \sum_{\delta=x,y} (I_{i,i+\delta} + I_{i,i-\delta}) = \sum_{i=1}^{N_s} (I_{i,i+x} + I_{i,i-x} + I_{i,i+y} + I_{i,i-y}) = 0. \tag{3.6}$$

We see that the quantity I is the analogous of the electric current in a network. Indeed Eq. (3.6) represents the Kirchhoff's first law stating that at any node (junction) in an electrical circuit, the sum of currents flowing into that node is equal to the sum of currents flowing out of that node.

If the spin phase changes slowly passing from a site to its nearest neighbor we can consider $(\theta_i - \theta_{i+\delta})$ a small quantity and we can approximate the hamiltonian using $\cos(x) \approx 1 - \frac{1}{2}x^2 + \mathcal{O}(x^4)$. Thus we obtain

$$\mathcal{H}_{XY} \approx -JS^2 \sum_{i=1}^{N_s} \sum_{\delta=x,y} \left[1 - \frac{(\theta_i - \theta_{i+\delta})^2}{2}\right] = -2JS^2 N_s + \frac{JS^2 a^2}{2} \sum_{i=1}^{N_s} \sum_{\delta=x,y} \left(\frac{\theta_i - \theta_{i+\delta}}{a}\right)^2, \tag{3.7}$$

For a d-dimensional macroscopic system we can take the continuous limit, replacing the sum with an integral all over the d-space. The first term of the hamiltonian is a constant and we focus on the second term, i.e. the elastic term $\mathcal{H}_{el}$:

$$\mathcal{H}_{el} = +\frac{JS^2 a^2}{2} \int \frac{d^d x}{a^d} \sum_{\delta=1,2,\ldots,d} \left(-\frac{\partial\theta(\mathbf{x})}{\partial x_\delta}\right)^2 = \frac{JS^2 a^{2-d}}{2} \int d^d x \left[\nabla\theta(\mathbf{x})\right]^2. \tag{3.8}$$

So we can define the "spin stiffness" $\rho_s = JS^2 a^{2-d}$ in such a way that

$$\mathcal{H}_{el} = \frac{1}{2} \int d^d x \rho_s \left[\nabla\theta(\mathbf{x})\right]^2. \tag{3.9}$$

Passing to continuum limit we can linearly approximate also the spin current (3.5), which can be written as

$$I_{i,i+\delta} \approx -JS^2 a \frac{(\theta_i - \theta_{i+\delta})}{a} \approx JS^2 a \frac{\partial\theta}{\partial x_\delta}, \tag{3.10}$$

then we can define a current density

$$\mathbf{J}(\mathbf{x}) = JS^2 a \left(\frac{\partial\theta}{\partial x}, \frac{\partial\theta}{\partial y}\right) = JS^2 a \nabla\theta = \rho_s \nabla\theta \tag{3.11}$$

Notice that we obtain the same result with the canonical expression of the paramagnetic current in a many body system with the prefactor Ja. Indeed defining the field $\psi(\mathbf{x}) = S\, e^{i\theta(\mathbf{x})}$, we have

$$\mathbf{J}(\mathbf{x}) = \frac{JS^2}{2i} \left[\psi^\dagger(\nabla\psi) - (\nabla\psi^\dagger)\psi\right]. \tag{3.12}$$

The stability condition in the continuum limit can be derived from hamiltonian (3.9):

$$\frac{\delta\mathcal{H}_{el}}{\delta\theta(\mathbf{x})} = -\rho_s \nabla^2\theta(\mathbf{x}) = 0. \tag{3.13}$$

This means that $\theta(\mathbf{x})$ satisfies Laplace equation $\nabla^2\theta(x) = 0$. So the current density (3.11) satisfies

$$\nabla \cdot \mathbf{J} = 0, \tag{3.14}$$

or assuming a constant stiffness,

$$\nabla \cdot \mathbf{v} = 0, \tag{3.15}$$

with $\mathbf{v} = \nabla\theta(\mathbf{x})$. In fluid dynamics a velocity field that can be obtained from a scalar potential is called a "potential flow". Stable solutions obey Laplace equation and thus satisfy eq. (3.13) and eq. (3.14).

Fig. 3.1 shows configurations which are solutions of the XY-model. Spatially uniform

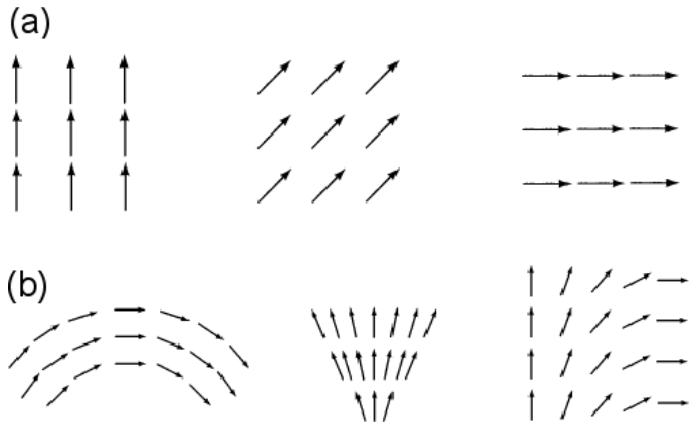

Figure 3.1: (a) Uniform and (b) non uniform spatial variation of the spin phase.

changes in θ ($\Delta\theta$ is the same for each $\mathbf{x}$) do not change the elastic energy contribution, and the system remains in the ground state $\theta(\mathbf{x}) = const$, with all spins aligned (see Fig. 3.1(a)). Spatially non-uniform changes in θ (see Fig. 3.1(b)) however increase the energy. All these solutions therefore represent planar mean field solutions of our effective Heisenberg model, eq. (3.1).

Now we analyse a stable high energy solution of the model, consisting of a topological defects, which will be useful in the following of this thesis, since they will describe the frustration of the magnetic background due to dopant holes in the CuO_2 planes of cuprates.

3.2.1 Vortex and antivortex

Within XY-model, vortices are topologically stable excitations of the ordered phases. A sufficiently large number of vortices can destroy long-range order, and a thermally activated proliferation of vortices can lead to a phase transition to the high-temperature disordered phase. Of course, this physics does not apply directly to Heisenberg spins.

So far we have assumed that the angle variable θ was continuous everywhere and the magnitude S of the order parameter was everywhere nonzero. Since $\mathbf{S}(\mathbf{x}) = S(\cos\theta(\mathbf{x}), \sin\theta(\mathbf{x}))$ is a periodic function of $\theta(\mathbf{x})$, it is possible to have situations in which $\mathbf{S}(\mathbf{x})$ is continuous

everywhere in d-dimensional space except in a subspace of dimensionality d_s less than d. For example in $d = 2$, if we consider

$$\theta(\mathbf{x}) = \theta_0 + \varphi, \tag{3.16}$$

where θ_0 is any constant and φ is the angular coordinate of the position $\mathbf{x}$, such that $\mathbf{x} = (r, \varphi) \Rightarrow \varphi = \arctan(y/x)$, we have

$$\nabla\theta(r, \varphi) = \frac{\partial\theta}{\partial r}\hat{e}_r + \frac{1}{r}\frac{\partial\theta}{\partial\varphi}\hat{e}_\varphi = \frac{1}{r}\hat{e}_\varphi. \tag{3.17}$$

So $\nabla\theta$ is finite everywhere except at the origin. In this region the continuum limit fails and the lattice parameter cuts off the singularity.

The configuration of spins just defined is a vortex. The angle θ, specifying the direction of the order parameter, changes by 2π in one circuit of any closed contour enclosing the core of the vortex. A vortex is characterized only by the winding number k, that specifies the increasing $2k\pi$ of θ in one complete circuit of the core. For example a singularity given by $\theta(\mathbf{x}) = \theta_0 + 2\varphi$, is a vortex with winding number $k = 2$. The constant θ_0 is only an additive angle to each local phase, that keeps the energy unchanged. So the constant θ_0 only changes the shape of a vortex but not its 'strength' (see Fig.3.2). We will fix $\theta_0 = 0$

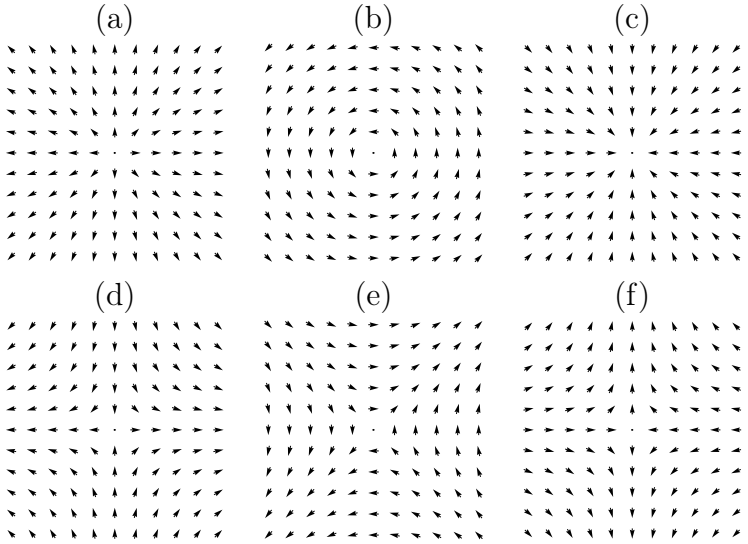

Figure 3.2: Single vortices within XY-model. The upper panels show $k = 1$ vortices with (a) $\theta_0 = 0$, (b) $\theta_0 = \pi/2$, (c) $\theta_0 = \pi$. The lower panels show $k = -1$ antivortices with (d) $\theta_0 = 0$, (e) $\theta_0 = \pi/2$, (f) $\theta_0 = \pi$.

in the following of our discussion.

Now we want to calculate the elastic energy of the vortex. To this purpose we assume the field $\theta = k\varphi$. It satisfies the topological constraint $\oint d\theta = 2k\pi$ for any loop enclosing the vortex. Furthermore it satisfies the equilibrium condition (3.13) everywhere except at

the origin, where there is the singularity. Using Eq.(3.9) we obtain

$$E_{el} = \frac{1}{2}\rho_s \int d^2x [\nabla\theta]^2 = \frac{1}{2}\rho_s 2\pi \int_a^R r dr \left[\frac{k}{r}\hat{e}_\phi\right]^2 = \frac{1}{2}\rho_s 2\pi k^2 \int_a^R \frac{dr}{r} = \pi k^2 \rho_s \ln(R/a), \tag{3.18}$$

where a is the core radius, while R is the linear dimension of the sample. So the energy of a vortex diverges logarithmically with the system size. Notice that the potential generated by a single vortex, eq. (3.18), can be put in analogy with the two-dimensional electrostatic potential of a line of charge perpendicular to the plane that we are considering, or with the magnetic field generated by a line of current perpendicular to the plane. In these two cases the prefactor of the logarithmic interaction is constituted respectively by linear density of charge, and the electric current flowing in the line.

However a field configuration with more vortices can avoid this divergent cost. Indeed if $\mathbf{r}_i$ is the position of each vortex, switching to the complex plane coordinates ($z = x+iy$), we have

$$\theta(x,y) = \sum_{i=1}^{N} k_i \arg(z - z_i), \tag{3.19}$$

and the total elastic energy becomes

$$E_{el} = \frac{1}{2}\rho_s \int d^2r \left[\nabla\left(\sum_{i=1}^{N} k_i \arg(z-z_i)\right) \cdot \nabla\left(\sum_{j=1}^{N} k_j \arg(z-z_j)\right)\right]. \tag{3.20}$$

Now, if the total vorticity is equal to zero, i.e. $\sum_{i=1}^{N} k_i = 0$, it can be shown that

$$E_{el} = -2\pi\rho_s \sum_{1\le i<j\le N} k_i k_j \log\left(\frac{|\mathbf{r}_i - \mathbf{r}_j|}{a}\right). \tag{3.21}$$

So two vortices with opposite vorticity at distance r, tend to attract each other, according to a potential $V_{k_1k_2}(r)$ given by eq. (3.21). They form a vortex-antivortex (VA) pair which removes the energy divergence due to an isolated vortex. Notice that eq. 3.21 represents the interaction between two two-dimensional Coulomb charges k_i and k_j on the lattice. So a VA pair can be viewed as an effective two-dimensional electric dipole .

3.3 Conformal mapping

In two dimensions, solutions of the Laplace equation can be obtained by conformal mapping (see for example Ref. [4]), according to which one defines a complex potential

$$f(z) = \psi(x,y) + i\phi(x,y)$$

with $z = x + iy$. It can be shown that if f is analytic then both $\psi(x,y)$ and $\phi(x,y)$ are solutions of a Laplace problem with different boundary conditions. This follows from the

fact that if $f(z)$ is analytic its derivative, $f'(z)$ should be independent of the direction in which the derivative is made in the complex plane leading to conditions on the $\psi(x, y)$ and $\phi(x, y)$ which imply Laplace equation. The equipotential lines of $\psi(x, y)$ are perpendicular to the lines of constant $\phi(x, y)$. Therefore in the case of potential flow if we interpret $\phi(x, y)$ as a velocity potential the lines of $\psi(x, y) = const$ are the streamlines. In the case of a 2D electrostatic or magnetostatic problem if $\phi(x, y)$ is the scalar potential then $\psi(x, y) = const$ are the fields or flux lines. For the magnetostatic problems it is useful to remember that in regions without free currents $\nabla \times \mathbf{H} = 0$ and therefore $\mathbf{H} = -\nabla\phi$. Furthermore in regions without magnetization $\nabla^2\phi = 0$. We will see below that if we associate $\psi(x, y)$ with an electrostatic potential there is a closely related problem in which charges are replaced by currents and $\phi(x, y)$ plays the role of a magnetostatic potential (and vice versa). The magnetic field also corresponds to minus the velocity of the potential flow problem which is the one that interest us at the end.

Each $f(z)$ represents the solution of two different Laplace problems with different boundary conditions in which the role of the two potentials are interchanged. All this will become clear form the examples below.

The simplest conformal transformation is

$$f(z) = z. \tag{3.22}$$

The resulting fields ϕ and ψ are shown in Fig. 3.3, by means of contour lines. In the

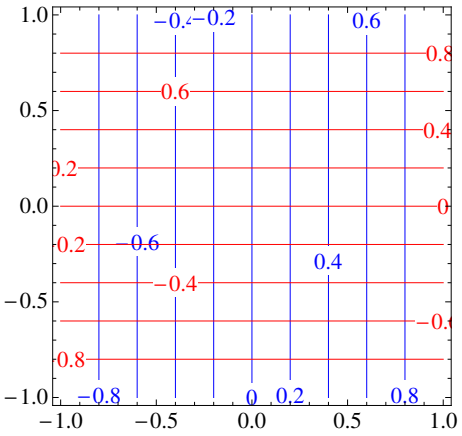

Figure 3.3: Constant potential lines for the map $f(z) = z$. The blue lines represent the contours of $\phi(x, y)$, while the red lines represent the contours of $\psi(x, y)$.

electrostatic analogy the equipotential lines correspond to the problem of a capacitor with one vertical plate at -1 and another at $+1$. The blue lines are equipotential lines and the red lines electric field lines. In the magnetic analogy the plates are replaced by sheets of currents flowing in and out of the paper. The blue lines become the field lines and the red lines the magnetostatic potential lines.

A less trivial mapping (see Fig. 3.4) is

$$f(z) = \log(z). \tag{3.23}$$

Putting $z = re^{i\theta}$ we see that $\psi = \log(r)$ and $\phi = \theta$. In the electrostatic analogy ψ (blue)

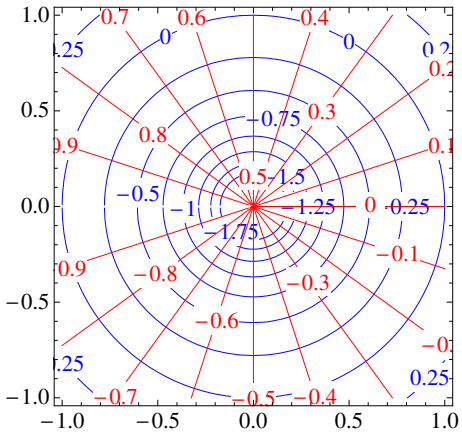

Figure 3.4: Constant potential lines for the map $f(z) = \log(z)$. Red contours are labeled in units of π.

is the 2D potential of a line of charge perpendicular to the paper. More generally in Gaussian units the potential of a charged line is $\psi = -2\gamma \log(r)$ where γ is the charge per unit length so the mapping corresponds to $\gamma = -1/2$. We will call this one negative unit of charge $q = -1$. In the magnetostatic analogy ψ (red) is the magnetostatic potential corresponding to a magnetic field $\mathbf{H} = -\hat{e}_\theta/r$ which corresponds to a line of current perpendicular to the plane with the positive direction defined as the z direction. In the potential flow analogy the red lines are the equipotential lines of a vortex with vorticity $k = +1$, i.e. lines of constant phase in the XY model.

Since any distribution of charges can be decomposed in point charges and the sum of conformal solutions is a conformal solution we see that any arbitrary solution of Laplace equation has a dual solution in which electrostatic charge lines are replaced by currents lines. In the potential flow analogy the charges become vortex cores and the magnetic field is minus the velocity field.

The next example is

$$f(z) = l\frac{d(log(z))}{dz} = l\lim_{h\to 0}\frac{\log(z+h)-\log(z)}{h} = \frac{l}{z}. \tag{3.24}$$

The result is independent of whether h is real or complex as it should be. The above expression shows that $f(z)$ correspond to the potential of a dipole. The strength p is a complex parameter which determines the orientation of the dipoles. A real p indicates that the charges are on the real axis, $p = 1 + i$ represents a dipole at 45^0, etc. Notice that $\log(z + h)$ represents a negative charge at $-h$ therefore p is the dipole moment with the correct sign. In the magnetic analogy we can think the VA pair as generated by a coil perpendicular to the paper. Notice that the current flows upwards which means that the magnetic field points downwards so the complex magnetic dipole is given by $d = -ip$. In Fig. 3.5 we show the complex potential for $p = 1$. The blue lines represent

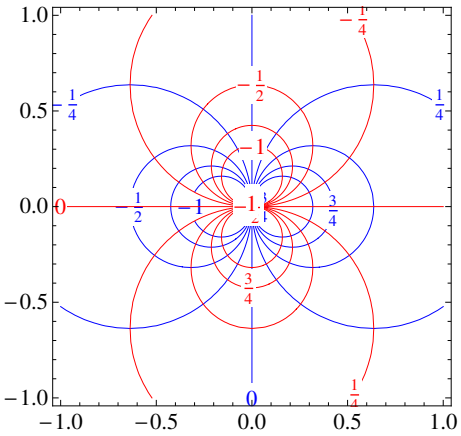

Figure 3.5: Constant potential lines for the map $f(z) = 1/z$. Contour levels are in units of π.

the equipotential lines in the electrostatic analogy, the field lines in the magnetostatic analogy, and the streamlines (velocity field lines) in the potential flow analogy. The red lines represent the electric field lines and the equipotential lines both in the magnetostatic and in the potential flow analogy. So Fig. 3.5 is a representation of the spin deformation (red lines are the lines of constant phase) and the spin current (blue lines) the spin deformation due to a VA pair

Bibliography

[1] E. Manousakis, Rev. Mod. Phys. **63**, 1 (1991).

[2] K. Yosida, *Theory of Magnetism* (Springer-Verlag, 1996).

[3] P. M. Chaikin and T. C. Lubensky, *Principles of Condensed Matter Physics* (Cambridge University Press, 1995).

[4] R. P. Feynman, R. B. Leighton, M.Sands, *The Feynman lectures on physics, Vol.II* (Addison-Wesley Publishing Company, Inc., 1964).

Chapter 4

Numerical methods for statistical systems

In the last section we have derived an effective classical spin model. However we have seen that the vortices interact with each other in the same way as two-dimensional charges. So the spin vortices in a lattice can be treated as a collection of interacting charges, which will be studied in the following by means of a Monte Carlo approach. This chapter consists in a brief introduction to Monte Carlo methods in statistical physics. We also report the description of the parallel tempering method which we will use in our simulation in order to make the thermalization process.

4.1 Statistical mechanics and Monte Carlo methods

To describe a macroscopic system, Gibbs introduced the idea of statistical ensemble. A generic state of a gas can be described by $3N$ canonical coordinates $q_1, \cdots, q_{3N}$ and the respective momenta $p_1, \cdots, p_{3N}$. The $6N$-dimensional space generated p_i, q_i is called Γ space, or phase space, of the system. A point of the Γ space represents a state of the entire N particles system. When we consider a macroscopic configuration, we are referring no to a single state but to a collection of states. According to Gibbs, we call "ensemble" this collection of systems, which is geometrically represented in the Γ space by a distribution of points. The ensemble can be described by a density function $\rho(p, q, t)$ in which (p, q) is an abbreviation of $(p_1, \cdots, p_{3N}; q_1, \cdots, q_{3N})$, defined in such a way that $\rho(p, q, t)\, d^{3N}p\, d^{3N}q$ is the number of points which, at the instant t are contained in the volume element $d^{3N}p\, d^{3N}q$ of the space Γ, centered around the point (p, q). An ensemble is completely determined by $\rho(p, q, t)$. It is worth specifying that the constituents of an ensemble are mental copies of a system and they do not interact with each other.

Since we want to study a system in equilibrium, we focus only on those ensembles whose density function does not depend explicitly on time. In particular, we look for the most suitable ensemble for the description of a non-isolated system, in thermal equilibrium with a larger system, representing a thermal bath. It can be shown (see Ref. [1]) that the

density function of such an ensemble is given by

$$\rho(p,q) = \exp[-\mathcal{H}(p,q)/k_B T], \tag{4.1}$$

$\mathcal{H}(p,q)$ being the hamiltonian of the system. Eq. (4.1) defines the "canonical ensemble". The volume of the Γ space occupied by the canonical ensemble is called "partition function":

$$Z(V,T) = \int \frac{d^{3N}p\, d^{3N}q}{N! h^{3N}} \exp[-\beta \mathcal{H}(p,q)], \tag{4.2}$$

where $\beta = 1/k_B T$ and h is a constant of dimensions *momentum* $\times$ *length*, in order to make Z dimensionless. The thermodynamic of the system, i.e. the link with the macroscopic world, is given by $Z(T,V) = \exp[-\beta F(V,T)]$, where $F(V,T)$ is the Helmholtz free energy. F is related with the internal energy $U = \langle \mathcal{H} \rangle$ and the entropy S according to $F = U - TS$.

In a thermodynamic system a physical quantity is represented by thermal average of the corresponding observable $\mathcal{O}$. Within the canonical ensemble it is defined by

$$\langle \mathcal{O} \rangle = \frac{\int d^{3N}p\, d^{3N}q\, \mathcal{O}(p,q) \exp[-\beta \mathcal{H}(p,q)]}{\int d^{3N}p\, d^{3N}q\, \exp[-\beta \mathcal{H}(p,q)]}. \tag{4.3}$$

Since we are working with a discrete system which does not take into account the kinetic part, the integral in the eq. (4.3), is replaced by a discrete sum over each state μ of the ensemble

$$\langle \mathcal{O} \rangle = \frac{\sum_\mu \mathcal{O}_\mu \exp[-\beta E_\mu]}{\sum_\mu \exp[-\beta E_\mu]} = \frac{1}{Z} \sum_\mu \mathcal{O}_\mu \exp[-\beta E_\mu] = \sum_\mu \mathcal{O}_\mu \mathcal{N}_\mu, \tag{4.4}$$

where $\mathcal{N}_\mu = \exp[-\beta E_\mu]/Z$ represents the probability that the system is in the state μ. As the system size is increased the number of possible states becomes too high to be completely explored. The Monte Carlo (MC) method provides a quite accurate solution to such a problem. The basic idea behind MC simulation is to simulate the random thermal fluctuation of the system from state to state over the course of an experiment. To this purpose it is convenient to regard the calculation of an expectation value as a time average over the states that a system passes through. In some sense this is what happens in a real measurement. Indeed, every experimental measurement of a generic observable $\mathcal{O}$, is not a single instantaneous measurement, but it consists in an integration of the result over some period of time, in which the system explores many microscopic states. The main problem of the MC simulations is that there is no guarantee that the system will pass through a representative selection of the states of the system during the simulation time. To overcame this difficulty we refers to what is called "importance sampling". For a detailed analysis see for example Refs. [2, 3]

4.2 Importance sampling

In larger systems, the best we can do is to average over some subset of the states, although this necessarily introduces some inaccuracy into the calculation. For example,

instead of averaging over the whole set of states μ of the system, weighting each with its own Boltzmann probability, as in eq. (4.4), we can choose a subset of M states at random $i = 1, \ldots, M$, obtaining

$$\langle \mathcal{O} \rangle_M = \frac{\sum_{i=1}^{M} \mathcal{O}_i \exp[-\beta E_i]}{\sum_{j=1}^{M} \exp[-\beta E_j]}. \tag{4.5}$$

Importance sampling consists in generating the random states according to a probability distribution p_i, in such a way that the thermal averages are performed only over the most thermodynamically 'important' states. With these assumptions $\langle \mathcal{O} \rangle_M$ can be rewritten as

$$\langle \mathcal{O} \rangle_M = \frac{\sum_{i=1}^{M} \mathcal{O}_i \, p_i^{-1} \exp[-\beta E_i]}{\sum_{j=1}^{M} p_j^{-1} \exp[-\beta E_j]}. \tag{4.6}$$

In this way the inaccuracy of the calculation is reduced and the closer is p_i to the Boltzmann weight $e^{-\beta E_i}$, the smaller is the error committed. Finally, choosing $p_i = Z^{-1} e^{-\beta E_i}$, we have

$$\langle \mathcal{O} \rangle_M = \frac{1}{M} \sum_{i=1}^{M} \mathcal{O}_i, \tag{4.7}$$

which is a time average provided that the increasing of i corresponds to the progressive passing of the time. So we directly simulate the thermal fluctuations, creating a model system on our computer and making it pass through a variety of states in such a way that the probability of it being in any particular state i is equal to the weight $\mathcal{N}_i$. Now the question is how we can generate a sequence of states so that each one appears with its correct Boltzmann probability. To this purpose it is convenient to generate a "Markov process". It is a mechanism which, given a system in one state o (old), generates a new state n (new) of the system, but it will not generate the same new state every time it is given the initial state o. The probability of generating the state n, given o is called the transition probability $\pi(o \to n)$. For a true Markov process all the transition probabilities should not vary over time and they should depend only on the properties of the current states o and n, and not on any other states the system has passed through. Furthermore the $\pi(o \to n)$ do not destroy such an equilibrium distribution once it is reached. This means that, in equilibrium, the average number of accepted trial moves that result in the system leaving state o must be exactly equal to the number of accepted trial moves from all other states n to state o. It is convenient to impose much stronger condition; namely, that in equilibrium the average number of accepted moves from o to any other state n is exactly canceled by the number of reverse moves. This detailed balance condition implies that

$$\mathcal{N}(o)\pi(o \to n) = \mathcal{N}(n)\pi(n \to o). \tag{4.8}$$

A MC move consists in two stages: first we perform a trial move from state o to state n and we denote the probability of this trial move with $\alpha(o \to n)$; the next stage is the decision to either accept or reject this trial move. Let us denote the probability of accepting a trial move by $acc(o \to n)$. Since the transition probability π is the product

between these two probabilities, eq. (4.8) becomes

$$\mathcal{N}(o) \times \alpha(o \to n) \times acc(o \to n) = \mathcal{N}(n) \times \alpha(n \to o) \times acc(n \to o). \tag{4.9}$$

So we can write

$$\frac{acc(o \to n)}{acc(n \to o)} = \frac{\alpha(n \to o)}{\alpha(o \to n)} \frac{\mathcal{N}(n)}{\mathcal{N}(o)} = \frac{\alpha(n \to o)}{\alpha(o \to n)} \exp[-\beta(E_n - E_o)]. \tag{4.10}$$

Now if each trial move and its reverse move have the same probability to be picked, we have $\alpha(n \to o) = \alpha(o \to n)$. Many choices for $acc(o \to n)$ satify the condition (4.10) (and the obvious condition that a cannot exceed 1). The choice of Metropolis is

$$\begin{array}{rcll} acc(o \to n) & = & \exp[-\beta(E_n - E_o)] & \text{if } E_n > E_o \\ & = & 1 & \text{if } E_n \leq E_o \end{array} \tag{4.11}$$

or in a more compact form

$$acc(o \to n) = \min\left(1, \exp[-\beta(E_n - E_o)]\right). \tag{4.12}$$

To implement this algorithm we generate a random number r from a uniform distribution in the interval $[0, 1]$. If $E_n > E_o$, then $acc(o \to n) < 1$, and this means that the probability that r is less than $acc(o \to n)$ is equal to $acc(o \to n)$. So we accept the trial move only if $r < \exp[-\beta(E_n - E_o)]$. If, instead $E_n \leq E_o$, we always accept the move.

It is worth mentioning that what said so far requires the condition of ergodicity, according to which, every accessible point in configuration space can be reached in a finite number of MC steps from any other point. Indeed, every state ν appears with some non-zero probability p_ν in the Boltzmann distribution, and if that state were inaccessible from another state μ no matter how long we continue our process for, then our goal is thwarted if we start in state μ: the probability of finding ν in our Markov chain of states will be zero, and not p_ν as we require it to be. The condition of ergodicity tells us that we are allowed to make some of the transition probabilities of our Markov process zero, but that there must be at least one path of non-zero transition probabilities between any two states that we pick.

4.3 Parallel tempering method

Summarizing what said in the previous section, the Monte Carlo (MC) method is one of the most powerful techniques for the simulation of statistical systems. Since the Boltzmann-Gibbs distribution is strongly concentrated in configuration space, MC methods implement what is called "importance sampling": points in configuration space are not generated randomly, but according to desired probability distribution. In practice, in a MC simulation one only generates typical configurations, i.e. those that give the most important contribution to thermodynamic averages. From a mathematical point of view,

a MC algorithm is a Markov chain that (i) is stationary with respect to the Boltzmann-Gibbs distribution and (ii) satisfies ergodicity. If these two conditions are satisfied, time averages converge to configuration averages: hence by using the MC results one can compute ensemble averages for the system at hand. But while condition (i) is ensured by the Metropolis algorithm, condition (ii) is more subtle. Indeed, in the presence of phase transitions or quenched disorder, the system can exhibit metastable free energy minima which can act as traps for the MC dynamics at low temperature (LT). To escape from these metastable states one can rise the temperature till that of the critical point, where all minima merge, then move into the HT phase, where a single thermodynamic state exists. If the system spends enough time in the high temperature (HT) phase, it loses memory of the thermodynamic LT phase it was coming from. Hence, when temperature is decreased again, it may fall into a different LT thermodynamic state. So, an algorithm that allows temperature changes may be a powerful tool for the study of the ordered phases in the presence of second-order phase transitions, for which there is no need to go over the energy barriers (they disappear at the transition). An algorithm of such a type is represented by "parallel tempering". The following description refers to [4].

The general idea of parallel tempering (PT) is to simulate R replicas of the original system of interest, each replica typically in the canonical ensemble, and usually each replica at a different temperature. PT allows the systems at different temperatures to exchange complete configurations. Thus, the inclusion of higher temperature systems ensures that the lower temperature systems can access a representative set of low-temperature regions of phase-space. This concept is illustrated in Fig. 4.1. Simulation of R replicas, rather

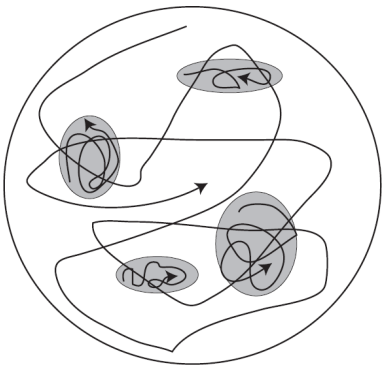

Figure 4.1: 2D representation of phase space. A simulation at lower temperatures can become trapped in a non-representative sample of the low free energy minima (shaded regions). At higher temperatures, a simulation can sample more of phase space (light plus shaded areas). Configuration swaps between the lower and higher temperature systems allow the lower temperature systems to escape from one region of phase space where they were effectively 'stuck' and to sample a representative set of the low free energy minima.

than one, requires on the order of R times more computational effort. This 'extra expense' of parallel tempering is one of the reasons for the initially slow adoption of the method. Eventually, it became clear that a parallel tempering simulation is more than $1/R$ times more efficient than a standard, single-temperature Monte Carlo simulation. This increased

efficiency derives from allowing the lower temperature systems to sample regions of phase space that they would not have been able to access in a single-temperature simulation that was R times as long. While not essential to the method, it is also the case that parallel tempering can make efficient use of large CPU clusters, where different replicas can be run in parallel.

If $\mathcal{N}_i(x_i)$ is the probability that the system at temperature T_i displays the configuration x_i (with $i = 1, \ldots, R$), then the probability distribution of total system constituted by R replicas the is given by

$$\prod_{i=1}^{R} \mathcal{N}_i(x_i) \tag{4.13}$$

The PT algorithm usually works as follows:

1. if $(x_1, \ldots, x_R)$ is the present configuration, one updates in parallel each x_i using an MC algorithm that leaves $\mathcal{N}_i$ invariant. This is ensured by the Metropolis algorithm implemented on each replica: usually PT algorithm implemented for R replicas, i.e. R different temperatures, needs the use of R processors which can work in parallel.

2. one proposes a swapping move[1]:

$$(x_1, \ldots, x_i, x_{i+1}, \ldots, x_R) \to (x_1, \ldots, x_{i+1}, x_i, \ldots, x_R),$$

which is accepted with probability

$$\begin{aligned} acc_{swap} &= \min\left(1, \frac{\mathcal{N}_{i+1}(x_i)\mathcal{N}_i(x_{i+1})}{\mathcal{N}_{i+1}(x_{i+1})\mathcal{N}_i(x_i)}\right) = \min\left(1, \frac{e^{-\beta_{i+1}E_i}e^{-\beta_i E_{i+1}}}{e^{-\beta_{i+1}E_{i+1}}e^{-\beta_i E_i}}\right) \\ &= \min\left(1, \exp\left[(\beta_{i+1} - \beta_i)(E_{i+1} - E_i)\right]\right) \end{aligned} \tag{4.14}$$

It is immediate to verify that the algorithm satisfies the stationarity condition with respect to (4.13).

To numerically implement the swapping move, we generate again a random number r from a uniform distribution in the interval $[0, 1]$ and we accept the trial swap between to temperatures T_i and T_{i+1}, only if $r < \exp[(\beta_{i+1} - \beta_i)(E_{i+1} - E_i)]$. In order to perform a PT simulation, one must decide the number R of temperatures and their values: temperatures should be close enough, so that the typical configuration domains at nearby temperatures overlap. If this does not occur, no swap is accepted. Whenever a PT run is performed, it is important to make checks to verify that the algorithm is working correctly. The simplest quantity to measure is the swapping rate $a_{i,i+1}$ between adjacent temperatures, that is the fraction of accepted swaps. The algorithm works efficiently only if, for all i, $a_{i,i+1}$ is not too small. The optimal value for $a_{i,i+1}$ lies between 0.2 and 0.3, but larger, or slighly smaller values, although not optimal, are still acceptable. A reasonable swapping rate is, however, not enough to guarantee that the algorithm is working correctly. Indeed, there

[1] In principle the swapping can be attempted among any pair of replicas, but only for nearby replicas the swap has a reasonable probability of being accepted.

are situations in which the swapping rates take the desired values, but the PT simulation is inefficient. This typically occurs when there is a "bottleneck" at a certain temperature β_K (usually it is closest to the critical temperature). In this case $a_{K-1,K}$ and $a_{K,K+1}$ are both reasonable, but the algorithm is unable to move a low temperature configuration to the high temperature side. In this case, high temperature replicas mix very slowly with the low temperature replicas, so that the dynamics, which is based on the idea that low temperature replicas rapidly move into the high temperature phase, becomes very slow. To identify bottlenecks, it is not enough to compute the swapping acceptances. One should measure quantities that take into account how temperature changes for each individual replica. Often one considers the average round-trip time,i.e., the time for a replica to start from the lowest temperature, reach the highest one, and finally go back to the lowest one. If the swapping procedure is working efficiently. the round-trip time should be comparable to the return time of a random walker moving among temperatures with the swapping rates actually measured in the simulation. On the contrary, if the swapping procedure has a bottleneck, then the round-trip time becomes large and is essentially controlled by the time it takes for a replica to go through the bottleneck. If the PT method is applied to a system undergoing a first-order transition, the swapping procedure would be highly inefficient, because high temperature replicas would hardly swap with low temperature replicas (they have to overcome an energy barrier). The two sets of replicas would remain practically non-interacting. In our work all the transitions have a first-order character (even though weak), but since the size of the system is not too large, and the temperature difference ΔT between to neighbor replicas is very low, the replicas are able to pass through the critical temperature, albeit not frequently.

Bibliography

[1] K. Huang, *Statistical mechanics* (2Ed, Wiley, 1987).

[2] M. E. J. Newman and G. T. Barkema, *Monte Carlo Methods in Statistical Physics* (Oxford University Press, 1999).

[3] D. Frenkel and B. Smit, *Understanding Molecular Simulation* (Academic Press, 1996).

[4] A. Pelissetto and F. Ricci-Tersenghi, *Large Deviations in Monte Carlo methods*, unpublished notes.

Chapter 5

Holes in the strongly correlated antiferromagnetic state: vortex and antivortex dimers and polimers

This chapter reports the results of the microscopic calculations based on the one-band Hubbard model treated within Gutzwiller approximation. In particular we will show that two holes in the CuO_2 plane, gain energy by occupying the center of a vortex and an antivortex of the spin background, with respect to two isolated spin polarons. We will observe that the vortex-antivortex pair has a dipolar character. The long-range part of the interaction between two vortex-antivortex pairs is well-described by the classical two-dimensional dipole-dipole interaction, whereas the short-range part is dominated by quantum effects which favor an 'head-to-tail' alignment. The main result of this chapter will be the fact that, when further holes are added, these 'topological dipoles' tend to arrange in polarized chains which act as a domain wall of the spin distribution and break inversion symmetry. The length of the chain will be limited by the real Coulomb repulsion between the positive charged holes.

5.1 Microscopic framework for cuprates

We want to describe the CuO_2 planes by means of the Hubbard model, restricted to nearest-neighbor and next-nearest-neighbor hopping. The numerical value of the parameters, suitable for cuprates, are suggested by previous studies [1]: we take the nearest-neighbor hopping $t = 360$ meV, while the ratio between on-site repulsion U and t is set to $U/t = 8$. The ratio between next-nearest-neighbor hopping t' and t is taken as a material parameter. Within this model we consider the presence of positive charged holes due to impurities out of the plane.

Since the model requires approximations, we start from HF. However HF method completely neglects correlations between electrons and it can heavily penalize the configuration with doubly occupied sites. To better understand the inaccuracy of the HF approximation we make a simple example: consider a linear chain of antiferromagneti-

cally ordered spins with periodic boundary conditions. If the number of spins is odd, the system is frustrated and it generates a domain wall, i.e. two consecutive spins which break the antiferromagnetic ordering. We can have two configurations close in energy: one with a bond-centered domain wall (see Fig.5.1(a)), and one with a site-centered domain wall. The first configuration is characterized by two neighboring spins which pay an energy cost

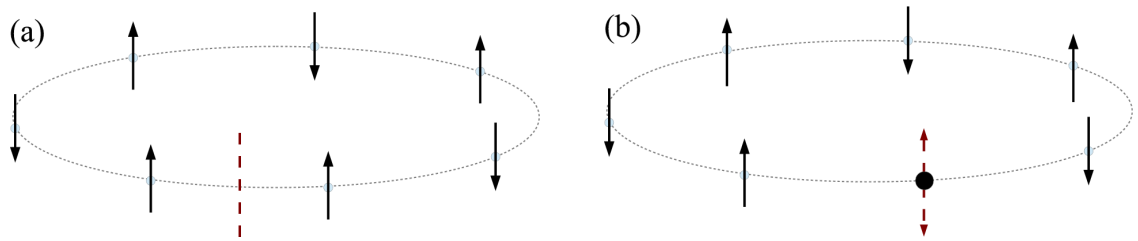

Figure 5.1: (a) Bond-centered domain wall and (b) site-centered domain wall in an antiferromagnetic chain frustrated by periodic boundary conditions.

due to the 'wrong' alignment. The second configuration is characterized by a site k such that $\langle n_k \rangle = \langle n_{k,\uparrow} \rangle + \langle n_{k,\downarrow} \rangle$ with $\langle n_{k,\uparrow} \rangle = \langle n_{k,\downarrow} \rangle = 1/2$. If we consider a strong on-site repulsion, the energy cost of this site, $U\langle n_{k,\uparrow} n_{k,\downarrow} \rangle$, is very high in HF approximation, since, neglecting the correlations, it can be written as $U\langle n_{k,\uparrow} \rangle \langle n_{k,\downarrow} \rangle = U/4$, and there is no way to decrease it. This large energy cost can be avoided by introducing correlations, but since they are neglected in HF scheme, the only way that HF has to avoid this cost is by breaking the symmetry. However this is precluded when the system is forced to stay in the configuration of Fig. 5.1(b).

So, at half-filling (without holes), we have states close in energy (like the two shown in Fig. 5.1), which provide very different HF energies, This problem appears also when we get away from half-filling putting holes in the system. Gutzwiller approach is more efficient in this sense, since the double occupancy is treated as a variational parameter d_k^2 to be minimized by means of a variational calculation, providing values much more suitable than HF. So GA allows to penalize less configurations which are not spin polarized. For this reason all the microscopic calculations in this thesis are performed using GA. However in order not to end up in pathological side minima we generally start the minimization from an Hartree-Fock ansatz for the amplitude $\Phi_{(i,\sigma),k}$.

5.2 Vortex-antivortex pairs

For a single hole relative to half-filling, the most stable GA solution is represented by the conventional Néel ordered spin polaron, which is shown in Fig. 5.2. We see that the spins are collinear and the hole is delocalized is a small ferromagnetic region entrapped in the antiferromagnetic texture. Indeed for a single hole, the ground state of the Hubbard model with infinite U, was proved to be ferromagnetic by Nagaoka [2]. This happens because the hole can move around most efficiently, thus minimizing the kinetic energy, when the spins are fully aligned. Conversely, when the antiparallel alignment of the spins

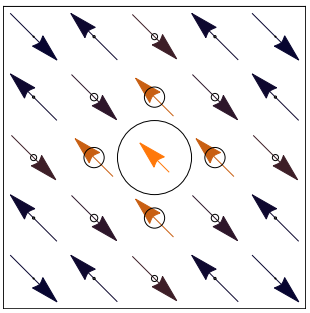

Figure 5.2: Spin polaron solution resulting from the GA calculation performed for a single hole relative to half-filling. The charge distribution is represented by black circles whose radius is proportional to the added hole density. The lighter colors of the arrows denote the spins shortening approaching the polaron.

is favored, a bubble of polarized spins forms around the hole while the spins further away are in the antiferromagnetic configuration. The hole essentially moves around freely only inside this bubble, or polaron.

Vortex states, where the magnetization rotates in a plane by some multiples of 2π around the localized holes, have been obtained as local minima of the energy functional (2.68). However for one hole away from half-filling vortex solutions are always higher in energy than the spin polaron. Moreover, their total energy increases logarithmically with the cluster size as a consequence of the twist between neighboring magnetization [3]. This logarithmic divergency can be compensated when two holes form vortex-antivortex (VA) pair, which turns out to be the energetically most stable solution for two holes, within the variational framework [4]. Indeed, while a single hole deforms the AF background and can be viewed as a self-trapped spin polaron, two holes have lower energy as VA pair rather than two independent spin polarons. The spin configuration due to a diagonal VA pair is shown in Fig. 5.3(a). All the spins are planar (they lie in the xy plane and the z component vanishes) and only in the proximity of the charge accumulation (due to the positive charged holes) the spin texture is sensibly deformed. If we follow the direction orthogonal to the pair we see that passing across its center the spins change their phase by $\sim \pi$.

It is important to specify that the GA solutions are obtained starting from a planar magnetic configuration. Thus the planar spin texture is, in some way, forced. However an analysis of linear excitations around this planar texture has been done in Ref. [5] and it was found that all the excitations are stables since they have real eigenvalues as opposite to unstable excitations which have imaginary eigenvalues. This implies that the planar magnetic configuration due to the VA pairs is a locally stable solution in the sense that it is a local minimum of the energy. One can wonder if other states with a three-dimensional spin texture, can be stabilized within our Gutzwiller approach. Ref. [4] shows that other topological states called "Skyrmions", characterized by a three-dimensional spin configuration, turn out to be stable energy minima within our model. Such a type of state appears only when at least two particles are removed from the half-filled system

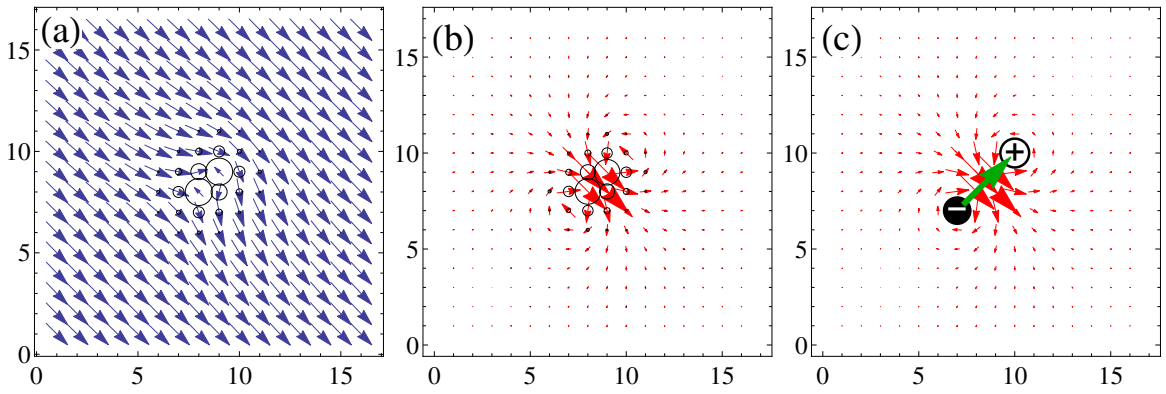

Figure 5.3: (a) Single VA pair obtained by minimizing the GA energy on a 16×16 lattice in the Hubbard model with $t'/t = -0.2$ and $U/t = 8$. The radius of the circles is proportional to the added hole density while the arrows are the staggered magnetization. (b) Representation of the spin current [eq. (5.3)] defined from the conservation law of the z component of the magnetization. Each arrow represents a vector whose components are given by the spin current in the horizontal and vertical bonds connecting a site to the its nearest-neighbor. In the continuum limit the spin current is proportional to the gradient of the phase of the staggered magnetization. (c) Polarized dipole defined by the current vortices at the edge of the charged segment.

and, although its energy is lower than the energy of two isolated spin polarons, the VA solution has significantly lower energy than the Skyrmion state. So we can reasonably assume that at zero temperature, the dopant holes in the AF background induce a planar spin distortion.

The spin textures are conveniently characterized by the associated spin currents (see Fig.5.3(b)) flowing from site $\mathbf{R}_i$ to $\mathbf{R}_j$. These are defined via the continuity equation

$$\partial_t S_i^\alpha + \sum_j J_{i\to j}^\alpha = 0, \tag{5.1}$$

where $\sum_j J_{i\to j}^\alpha$ is the generalized lattice divergence of the α component of the local spin current at site $\mathbf{R}_i$. Together with the Heisenberg equation of motion $\partial_t S_i^\alpha = i[H, S_i^\alpha]$ one thus finds

$$\sum_j J_{i\to j}^\alpha = -i[H, S_i^\alpha]. \tag{5.2}$$

Evaluating the expectation value of Eq. (5.2) within GA yields

$$J_{i\to j}^{GA,\alpha} = t_{ij} \mathrm{Im} \sum_{\sigma_1 \ldots \sigma_4} \sum_{k=1}^{N_e} \Phi^*_{(i,\sigma_1),k} \tau^\alpha_{\sigma_1\sigma_2} z_{i,\sigma_1\sigma_2} z_{j,\sigma_4\sigma_3} \Phi_{(j,\sigma_4),k}, \tag{5.3}$$

where $\Phi_{(i,\sigma_1),k}$ are the amplitudes which diagonalize the Gutzwiller hamiltonian, and $\tau^\alpha_{\sigma_1\sigma_2}$ denote the Pauli matrices. σ_i are the indices of the 2×2 matrices ($\sigma = \uparrow$ corresponds to the first component, while $\sigma = \downarrow$ corresponds to the second component). Since in our case, all the spins lie in the xy plane, only the z component of the spin current has a nonzero

contribution. Although the spin current is defined in the bonds between the neighboring sites, in which it is a conserved quantity, to better visualize it, we can take, for each site, a vector whose $x(y)$-component is given by the spin current in the horizontal (vertical) bond which connects the site with its nearest-neighbor along $\hat{\mathbf{x}}$ ($\hat{\mathbf{y}}$) direction. The resulting spin current vectors for a VA pair, are reported in Fig. 5.3(b). From the figure, we can see a net spin current in the direction orthogonal to the VA pair, which highlights a rotating vortex and an antivortex in the extremes of the short charged segment. So it is clear the reason for which the pair is oriented and the inversion symmetry is broken. Thus, we can associate a "topological dipole" (TD) $\mathbf{p} = k\mathbf{l}$ to the VA pair, k being the vorticity and $\mathbf{l}$ the vector connecting vortex and antivortex. A visualization of this topological dipole can be found in the panel (c) of Fig. 5.3 where a "topological charge" (TC) is associated to each vortex. The values of these charges correspond to the vorticities k.

It is therefore clear from Fig. 5.3, that a TD produces a long-range distortion of the AF background. This kind of long-range dipolar distortion have been proposed many times in studies of a small number of holes in the antiferromagnet.

A first study conducted by Aharony *et al.* [6], suggested that the deformation of the spin texture due to the addition of holes in LSCO, could lead to dipole-dipole attraction between the holes. Soon after Shraiman and Siggia [7] proposed a spin configuration characterized by a dipolar symmetry as a result of a mobile hole. They found a long-range distortion of the direction of the staggered magnetization, which decays as the inverse of the distance. They have also shown [8] that mobile vacancies in a background with at least short-range AF order have dipolar interactions which induce their collective polarization, leading to a spiral AF phase (even if the vacancies are not strongly localized). We propose that the distortion of the AF spin texture is due to an effective TD made by a pair of holes, and we will focus on the long-range part of this dipolar distortion. These TDs will play a fundamental role in the rest of the thesis and we will see that also in our scenario, they induce spin spirals.

5.3 Effective interaction between TDs

We want to study how these VA pairs interact with each other (see Ref. [9]). Analogies with vortex interactions in the XY-model suggest that two topological dipoles will interact with an effective dipole-dipole interaction at long distances which, in two dimensions, takes the form (for the details see appendix B)

$$V_{dip} = \frac{\boldsymbol{p}_1 \cdot \boldsymbol{p}_2}{\mathbf{d}^2} - 2\frac{(\boldsymbol{p}_1 \cdot \mathbf{d})(\boldsymbol{p}_2 \cdot \mathbf{d})}{\mathbf{d}^4} \tag{5.4}$$

where $\mathbf{d}$ connects the center of the two pairs. This long-range interaction will be justified more rigorously in the next chapters. For the moment we limit ourselves to show that the energy of two TDs indeed has a long-range part which is well described by this expression. For this reason we compute the GA energy of various metastable configurations of more than one TD.

For example, we can see in Fig. 5.4, two different configurations (and the relative spin current distribution) consisting in two VA pairs aligned head-to-tail, at different distances: one, which corresponds to the point at $d = 2$ of the red line in Fig. 5.6, is constituted by two consecutive VA pairs, while the other, corresponding to the point at $d = 4$ of the red line in Fig. 5.6, consists of two VA pairs at distance $4\sqrt{2}$. We can see that the

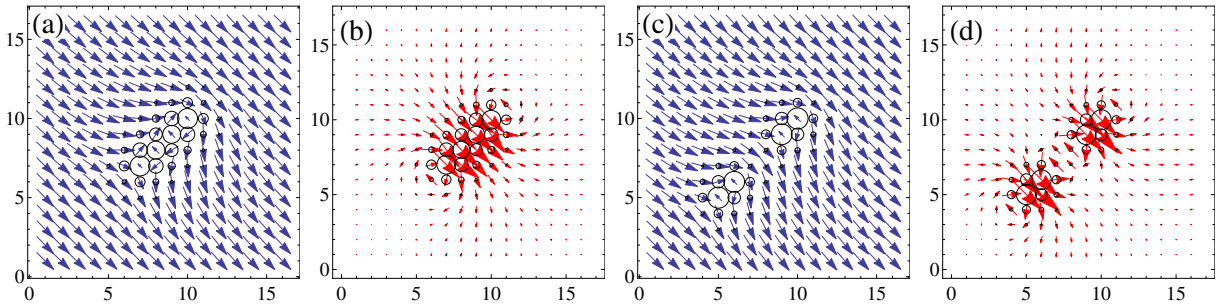

Figure 5.4: Two configurations made by two VA pairs aligned head-to-tail obtained by minimizing the GA energy on a 16×16 lattice in the Hubbard model with $t'/t = -0.2$ and $U/t = 8$: (a) spin configuration and (b) spin current distribution for two VA pairs at distance $2\sqrt{2}$, (c) spin configuration and (d) spin current distribution for two VA pairs at distance $4\sqrt{2}$.

average spin current of the two configurations is equal since it is given by the sum of the contributions of the single VA pairs. Since the two VA pairs point in the same direction in both the configurations the average spin current generated by the segment is equal to that resulting from two separated VA pairs. As explained in the following, the average spin current can be estimated averaging the quantity $\nabla\theta \cdot \hat{\mathbf{u}}$ over a transversal line away from the TDs, which is orthogonal to the unit vector $\hat{\mathbf{u}}$, where $\hat{\mathbf{u}}$ specifies the direction perpendicular to the TDs. For the two cases in Fig. 5.4 we obtain $\langle \nabla\theta \cdot \hat{\mathbf{u}} \rangle \sim 1.6$. This is a further proof that each VA pair represents an effective TD. Indeed the dipolar field at long distance due to a collection of electric dipoles is additive (this means that the total dipole moment of a polarized chain is equal to the sum of the elementary dipole moments which form it).

In Fig. 5.5, we report two different configurations representing two VA pairs pointing in opposite directions. One consists in two VA pairs on the same line, while the other, which corresponds to the point at $d = 4$ of the blue line in Fig. 5.6, consists of two VA pairs arranged side-by-side. These two configurations imply a net average spin current equal to zero, since the effect of a VA pair is balanced by the effect of the other VA pair. This does not depend on the spatial configuration of the VA pairs but only on the orientation.

Contrary to the three-dimensional case, for the 2D dipole-dipole interaction, the head-to-tail alignment and the side-by-side quadrupolar configurations in the insets of Fig. 5.6 are energetically degenerate. However, our GA computations reveal the presence of an anisotropic short-range contribution for the interaction among TDs. Fig. 5.6 shows the comparison between the Gutzwiller energy and the energy eq. (5.4) for two VA pairs aligned side-by-side and head-to-tail. The previous equation gives, for the two alignments,

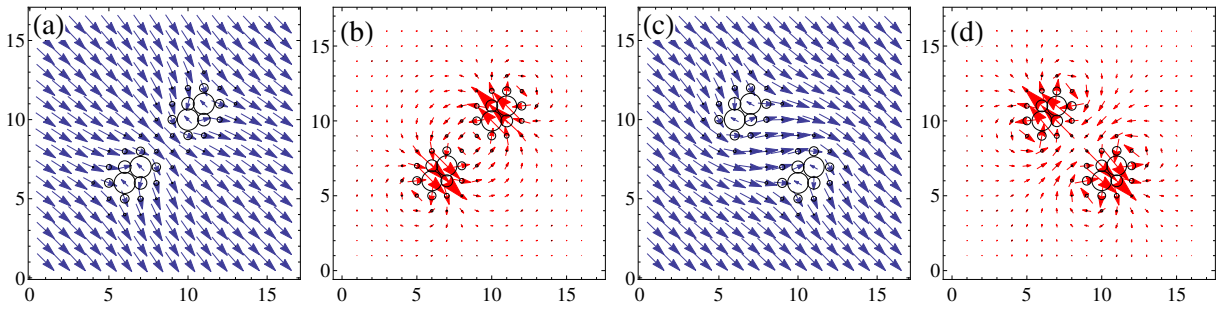

Figure 5.5: Two different arrangements of opposite VA pairs obtained by minimizing the GA energy on a 16×16 lattice in the Hubbard model with $t'/t = -0.2$ and $U/t = 8$: (a) spin configuration and (b) spin current distribution for two VA pairs on the same line, (c) spin configuration and (d) spin current distribution for two VA pairs arranged side-by-side.

nearly degenerate energy values of the form $A - B/d^2$, where A contains the the self-energy of a dipole, while B depends on the dipole strength p. They are both fitting parameters.

We must specify that the Gutzwiller energy of some configurations (those with a net spin current), has a spurious contribution due to the limited size of the cluster. Thus the Gutzwiller energy values of these configurations have to be corrected, using a procedure which will be explained in the chapter 7. For the moment we anticipate that the overall

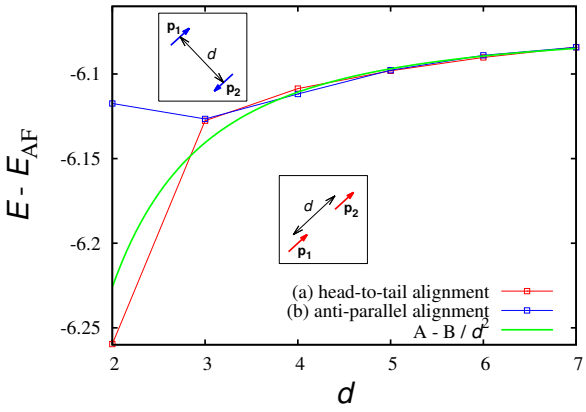

Figure 5.6: Interaction energy of side-by-side (blue squares) and head-to-tail (red squares) alignments as a function of the distance d computed within the GA for $U/t = 8$ and $t'/t = -0.2$. The green line represents the dipole-dipole interaction (5.4) which approaches the GA result at large distances.

effect of the anisotropic short-range contributions is to favor an head-to-tail rather than a quadrupolar side-by-side aggregation of VA pairs, which tend to form chains with a dipolar like distortion of the antiferromagnetic background. An example is reported in Fig. 5.7 which shows the GA result of a diagonal segment made by 8 holes (4 VA pairs), together with the resulting spin current which better highlights the inversion symmetry breaking due to the vortex-antivortex structure at the extremes of the segment, since the

internal vortices annihilate with each other. Actually if we consider a path which goes around only one extreme of the segment, the spins rotate by $\sim \pi$. This means that this configuration can be visualized as a string ending in a VA pair of 1/2 topological charge [10]. Notice that the segments tend to form an antiphase domain wall (jump of π of the

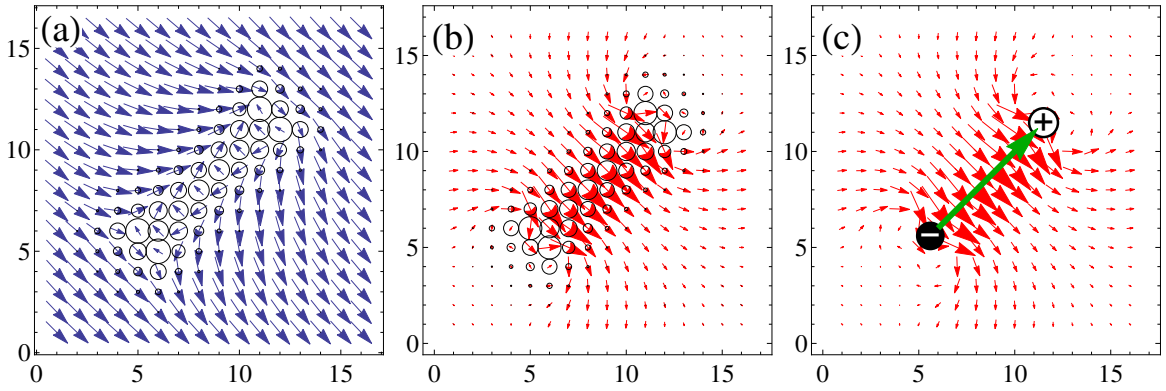

Figure 5.7: (a) Diagonal chain of four VA pairs, obtained by minimizing the GA energy on a 16×16 lattice in the Hubbard model with $t'/t = -0.2$ and $U/t = 8$. (b) Resulting Spin current. (c) Polarized dipole defined by the current vortices at the edges of the segment.

spin phase) of the antiferromagnetic order (see Fig. 5.8). So it is reasonable to think

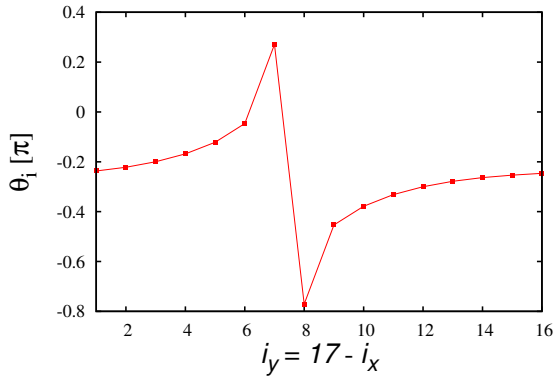

Figure 5.8: Spin phase for a diagonal cut through the chain of VA pair shown in Fig. 5.7(a).

that these objects are the precursor of the stripes introduced in the chapter 1 from the experimental point of view, although the transition between finite segments and infinite stripes is nontrivial and still not well understood.

Suppose we have N_h holes and we want to find the optimum way to accommodate them in N_{seg} segments each one accommodating N_c holes. Obviously $N_h = N_{seg}N_c$ and the question is whether we should choose few long segments or many short segments. To solve this problem we use the energies obtained from solution of the mean field problem for chains with different number of VA pairs (see Fig. 5.9). The energy to add a pair is, $\epsilon_{VA} = E[1VA] - E_{AF}$, being E_{AF} the Gutzwiller energy of the undoped antiferromagnetic state.

If the pairs are far from each other the energy of N_{VA} pairs is $E[N_{VA}] = N_{VA}\,\epsilon_{VA} + E_{AF}$. If the pairs form a chain the energy becomes

$$E[N_{VA}] = N_{VA}\,\epsilon_{VA} + E_{AF} + (N_{VA} - 1)E_{bind} \tag{5.5}$$

We can subtract the energy E_{pol} of $2N_{VA}$ separated polarons (being $\epsilon_p = E[1p] - E_{AF}$, the energy to add a single polaron), obtaining the energy gained by the system by creating N_{VA} VA pairs instead of $2N_{VA}$ polarons

$$\begin{aligned} & E - E_{pol} = N_{VA}(\epsilon_{VA} - 2\epsilon_p) + (N_{VA} - 1)E_{bind} \\ \Rightarrow \quad & \Delta E = (\epsilon_{VA} - 2\epsilon_p + E_{bind})\frac{N_c}{2} - E_{bind} \\ \Rightarrow \quad & \Delta E = \gamma N_c - E_{bind}, \end{aligned} \tag{5.6}$$

where we have put $N_{VA} = N_c/2$ and $\gamma = (\epsilon_{VA} - 2\epsilon_p + E_{bind})/2$. Fig. 5.9 shows that segments formed by N_c holes have systematically lower energy than N_c spin polarons, and reveals that the next-nearest-neighbor hopping t' has a strong influence in determining the preferential orientation of the segments. Diagonal segments are more (less) stable than those oriented along the vertical or horizontal bond direction for small (large) values of $|t'/t|$ (see also inset to panel (b)). Parameters appropriate for lanthanum cuprates ($t'/t \sim -0.15, \ldots, -0.2$) [11] yield a slight preference for diagonally oriented segments (11 direction) with respect to the vertical or horizontal directions. In cuprate superconductors larger values of $|t'/t|$ are usually associated with the YBCO and multilayer materials. Indeed the observation of static incommensurate spin scattering in underdoped YBCO along the copper-oxygen bond direction is consistent with our computed segment orientation for larger $|t'/t|$. The calculations in this thesis have been done using $t'/t = -0.2$.

5.3.1 Effect of the long-range Coulomb interaction and optimal length of segment

The length of the segment is limited by the real coulombic repulsion between the positive charged holes. The previous computations suggest that as holes are added to the system, a long segment is formed which grows until it cuts the whole sample with a domain wall. However it is clear that this configuration is unphysical. Indeed holes are positively charged and the compensating ions are uniformly distributed in the system. Therefore the macroscopic segment would have an enormous Coulomb cost. The question then arises of what is the optimum length of segments if we consider the long-range coulomb interaction. To take into account this effect, we must add some terms to eq. (5.6). For simplicity we assume a uniform compensating background. The effect of a random distribution of ions will be taken into account in chapter 7.

We first consider segments which are far apart and thus include only the intra-segment long-range Coulomb energy for a segment accomodating N_c charges:

$$V_{coul} = \frac{e^2}{2\epsilon_0 a_{ortho}} \sum_{n \neq m} \frac{1}{|n - m|} = \frac{e^2 N_c}{2\epsilon_0 a_{ortho}} \sum_{n=1}^{N_c} \frac{1}{n} \approx \frac{e^2 N_c}{2\epsilon_0 a_{ortho}} ln(N_c), \tag{5.7}$$

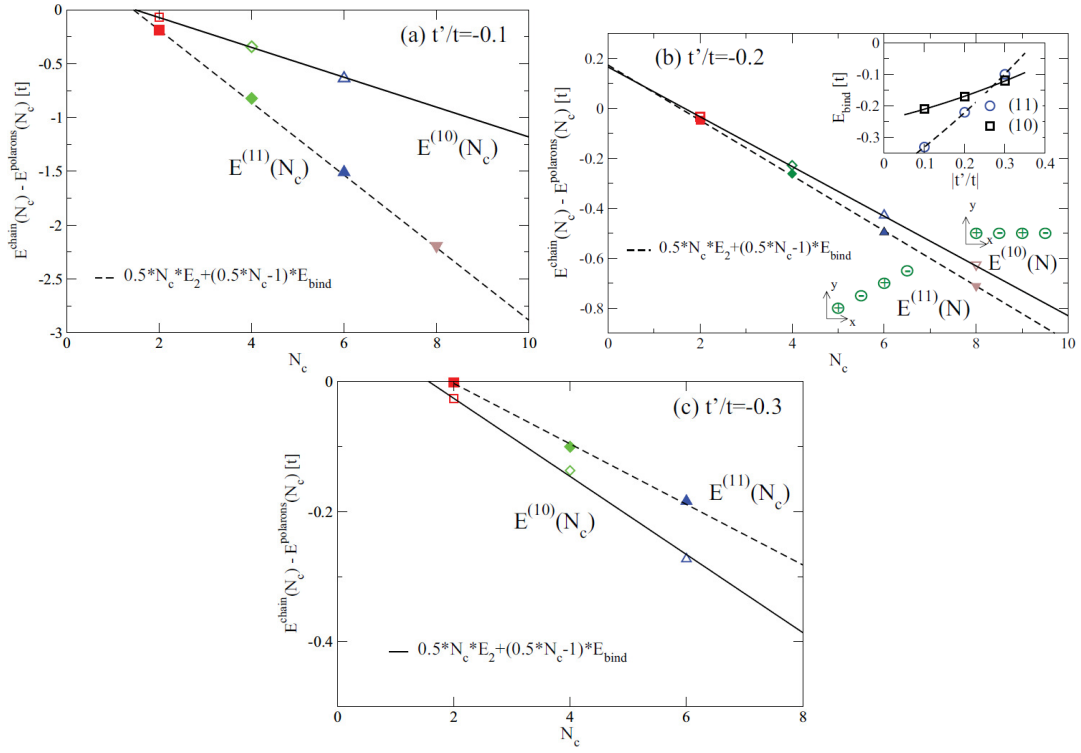

Figure 5.9: Energy of a chain of N_c holes corresponding to $N_c/2$ VA pairs aligned along the vertical (open symbols, solid line) and diagonal direction (full symbols, dashed line) as compared to the energy of N_c polarons. Parameters: $U/t = 8$, (a) $t'/t = -0.1$, (b) $t'/t = -0.2$, and (c) $t'/t = -0.3$. The upper right inset to panel (b) shows the binding energy as a function of t'/t for vertical (squares) and diagonal (circles) directions. Lines are guides to eyes. Computations were done in systems with up to 20×20 sites.

being a_{ortho} the lattice constant of the low-temperature orthorhombic phase. Notice that we made an asymptotic expansion of the harmonic series for large N_c. Thus if we have N_{seg} segments which are far apart the total energy, including the Coulomb self-energy is then,

$$E = N_{seg}[N_c E_c \ln(N_c) + N_c\gamma - E_{bind}]$$

with $E_c = e^2/(\epsilon_0 a_{orhto})$

Using the constraint $N_h = N_{seg}N_c$ and defining $x = N_h/L^2$ one obtains

$$\frac{E[N_c]}{L^2} = x[E_c \ln(N_c) + \gamma + \frac{1}{N_c}|E_{bind}|]. \tag{5.8}$$

The last term is the "surface" energy cost due to the cutting of segments. The minimum of E/L^2 is obtained for

$$N_c = \frac{|E_{bind}|}{E_c}.$$

The result above is valid if the segments are far apart. However, as the segment become closer the interaction energy between them becomes important and it can be estimated in close analogy to the evaluation of the Wigner crystal [12]. In the low-density limit, the energy per segment (charge Q) of a "Wigner crystal" of segments is given by

$$\frac{E_W}{N_{seg}} = \frac{Q^2}{2a_B}\left[-\frac{\alpha}{r_s} + \frac{\beta}{r_s^{3/2}} + \cdots\right], \tag{5.9}$$

where $a_B = \hbar^2/(mQ^2)$ denotes the Bohr radius and $r_s = r_0/a_B$, with r_0 defined from the volume per segment $L^D/N_{seg} = r_0^D$ in D dimensions. The coefficients α, β are of the order unity and have been derived for the two- and three-dimensional Wigner solid in Refs. [13] and [14].

Each of the segments consists of N_c charges (charge e), i.e., $Q = N_c e$, and the total number of charges is given by $N_h = N_{seg}N_c$. The Wigner energy becomes

$$E_W = \frac{E_W}{N_{seg}} = N_s N_c^4 \frac{e^2}{2a_0}\frac{1}{r_s}\left[-\alpha + \frac{\beta}{r_s^{1/2}}\right], \tag{5.10}$$

with $a_0 = \hbar^2/(me^2)$. Furthermore one has

$$r_s^D = \left(\frac{r_0 N_c^2}{a_0}\right)^D = \frac{L^D}{N_{seg}}\left(\frac{N_c^2}{a_0}\right)^D = \frac{N_c}{x}\left(\frac{N_c^2}{a_0}\right)^D. \tag{5.11}$$

Inserting eq. (5.11) into eq. (5.10) yields

$$\frac{E_W}{L^D} = \frac{e^2}{2}x^{1+1/D}N_c^{1-1/D}\left[-\alpha + \beta\frac{\sqrt{a_0}}{N_c}\left(\frac{x}{N_c}\right)^{1/(2D)}\right], \tag{5.12}$$

which, in the two-dimensional case becomes

$$\begin{aligned}\frac{E_W}{L^2} &= \frac{e^2}{2}x^{3/2}N_c^{1/2}\left[-\alpha+\beta\frac{\sqrt{a_0}}{N_c}\left(\frac{x}{N_c}\right)^{1/4}\right] \\ &= -\frac{\alpha e^2}{2}x\sqrt{xN_c}+\frac{\beta e^2\sqrt{a_0}}{2}x\left(\frac{x}{N_c}\right)^{3/4}\end{aligned} \tag{5.13}$$

Adding this energy contribution to eq. (5.8), we finally obtain the energy for the formation of the individual segments

$$\frac{E[N_c]}{L^2} = xE_c\left\{\frac{\gamma}{E_c}+\ln(N_c)+\frac{1}{N_c}\frac{|E_{bind}|}{E_c}-\frac{\alpha}{2}\sqrt{xN_c}+\mathcal{O}\left[\left(\frac{x}{N_c}\right)^{3/4}\right]\right\}, \tag{5.14}$$

which shows that an infinitesimal Wigner contribution completely changes the picture. The energy has two minima, one at finite N_c and the other at infinite N_c as the square root dominates the energy. Essentially, the previous solution becomes metastable with respect to a spurious lower energy solution with negative divergent energy. Notice that, once N_c tends to diverge, it is not any longer correct to compute the energy in the Wigner way (valid as long as the segment length is much smaller that r_0) and one needs to consider the Coulomb interaction between large segments which will cut off the energy.

It is interesting that there is a critical value of the doping at which the metastable short segment solution disappears (see Fig. 5.10). Probably it is a good approximation

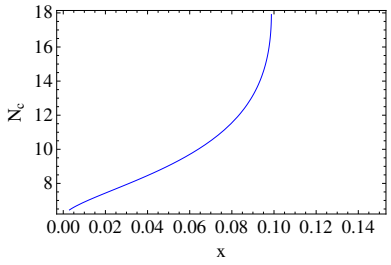

Figure 5.10: Optimum N_c for the metastable solution for $|E_{bind}|/E_c = 6$ and $\alpha = 2$.

to consider that it represents the doping concentration at which the stripes become long.

5.4 Topological charge location

Within this framework, we have studied a lot of configurations in which a given number of holes is self-trapped in VA pairs located at several positions in the lattice. So far we have reported only configurations involving diagonal TDs, made by TCs at distance $\sqrt{2}$. However we can calculate the GA energy of horizontal (or vertical) TDs or chains. Fig. 5.11 shows chains of horizontal VA pairs of different length, constituted respectively by two and three VA pairs. Notice that when the segments are horizontal (or vertical),

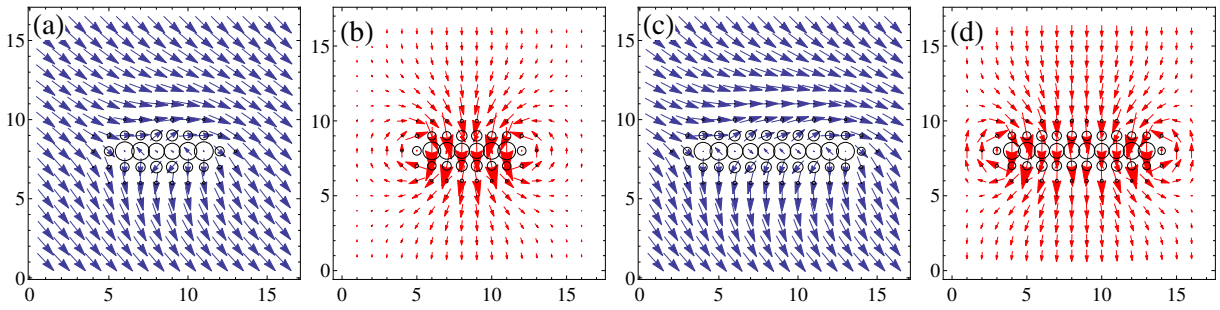

Figure 5.11: Horizontal chains of consecutive VA pairs obtained by minimizing the GA energy on a 16×16 lattice in the Hubbard model with $t'/t = -0.2$ and $U/t = 8$: (a) spin configuration and (b) spin current distribution for two VA pairs aligned head-to-tail, (c) spin configuration and (d) spin current distribution for three VA pairs aligned head-to-tail.

they are elongated: the segment made by 2 VA pairs (Fig. 5.11(a)) has a length of approximately 5 lattice units, while the segment made by 3 VA pairs (Fig. 5.11(c)) has a length of approximately 9 lattice units. So it is not too wrong to assume that the horizontal VA pairs have a length of 2 lattice units. This assumption will hold in the following of this thesis. The larger spacing between two neighboring TCs in the horizontal arrangement makes the configurations of Fig. 5.11 unfavorable with respect to the diagonal counterparts, since the binding energy E_{bind} between to TCs is lowered.

Bibliography

[1] G. Seibold and J. Lorenzana, Phys. Rev. Lett. **94**, 107006 (2005).

[2] Y. Nagaoka, Phys. Rev. **147**, 392 (1966).

[3] J. Vergés, E. Louis, P. Lomdahl, F. Guinea, A. Bishop, Phys. Rev. B **43**, 6099 (1991).

[4] G. Seibold, Phys. Rev. B **58**, 15520 (1998).

[5] G. Seibold, C. Di Castro, M. Grilli, J. Lorenzana, Scientific Reports **4**, 5319 (2014).

[6] A. Aharony, R. J. Birgeneau, A. Coniglio, M. A. Kastner, H. E. Stanley, Phys. Rev. Lett. **60**, 1330 (1988).

[7] B. Shraiman and E. Siggia, Phys. Rev. Lett. **61**, 467 (1988).

[8] B. Shraiman and E. Siggia, Phys. Rev. Lett. **62**, 1564 (1989).

[9] G. Seibold, M. Capati, C. Di Castro, M. Grilli, J. Lorenzana, Phys. Rev. B **87**, 035138 (2013).

[10] J. Villain, J. Phys. **36**, 581 (1975).

[11] E. Pavarini, I. Dasgupta, T. Saha-Dasgupta, O. Jepsen, O. K. Andersen, Phys. Rev. Lett. **87**, 047003 (2001).

[12] E. Wigner, Trans. Faraday Soc. **34**, 678 (1938).

[13] W. J. Carr, Phys. Rev. **122**, 1437 (1961).

[14] Lynn Bonsall and A. Maradudin, Phys. Rev. B **15**, 1959 (1977).

Chapter 6

Holes as topological defects and the classical spin background

In this chapter we will focus on the spin deformation due to both a single and a collection of VA pairs, since the microscopic calculations of the previous section have shown that these objects are stable solutions for the low doped cuprates. Our purpose is to map the microscopic results into a classical lattice model which correctly mimics the long-range behavior of the GA results. Therefore we have to find a relevant physical quantity which, when calculated within the classical model, matches that calculated within the microscopic model. This quantity will be the average spin current. We will analyse its dependence on the number of VA pairs. Finally we study how the periodic boundary conditions of the lattice affect the average spin current.

6.1 Dipolar texture in the XY-model

We have seen that the GA yields diagonal VA pairs as the more stable configurations. Now we analyse similar textures within the XY-model, like that shown in Fig.6.1(a), in which the effects of a vortex and an antivortex at distance $l = \sqrt{2}$ are linearly combined. We see that abrupt changes in the phase occurs only in the direction orthogonal to the VA pair. In Fig.6.1(b) we can see that a VA pair generates a net current in the direction orthogonal to the segment.

Notice that the two fields represented in Fig. 3.5 correspond exactly to the spin phase field resulting from the spin texture of Fig.6.1(a) and to the vector field arising from the spin current of Fig.6.1(b), generalised to the continuous case (apart a rotation of 45 degrees). Since the two fields describe also the dipolar electric and potential field, the analogy between a VA pair and an electric dipole is straightforward.

6.1.1 Macroscopic spin current in the lattice

Working in a linear regime, we imagine a collection of diagonal TDs of length l oriented along $(-1, -1)$ direction and randomly distributed in a continuous system. A computation

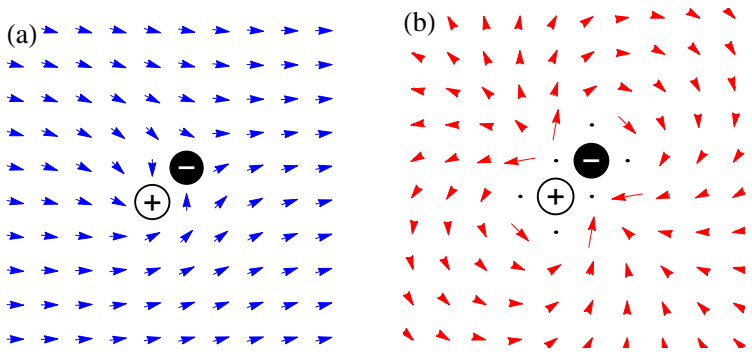

Figure 6.1: (a) Spin phase distribution due to a VA pair within XY-model. The resulting phase in each site has been obtained summing the phase due to a vortex in (x_0, y_0) and an antivortex in (x_0+1, y_0+1), i.e. $\theta(x,y) = \left[\arctan(\frac{y-y_0}{x-x_0}) - \arctan(\frac{y-(y_0+1)}{x-(x_0+1)})\right]$. (b) Spin current generated by a VA pair. Each red arrow represents a vector $\bar{\mathbf{J}}$ located in each lattice site, whose components are given by the average value of the current in the four bonds connecting it to the nearest neighbor sites, i.e. $\bar{J}_x = (I_{i,i+x} - I_{i,i-x})/2$ and $\bar{J}_y = (I_{i,i+y} - I_{i,i-y})/2$.

of the overall trend of the spin-phase distribution, is presented in appendix C and yields

$$\begin{aligned} & \theta(x,y) \sim n\pi k l_x (x-y) \\ \Longrightarrow \quad & \nabla\theta = n\pi k l_x \begin{pmatrix} 1 \\ -1 \end{pmatrix} = n\pi k\sqrt{2} l_x \frac{1}{\sqrt{2}} \begin{pmatrix} 1 \\ -1 \end{pmatrix} \\ & = n\pi k l \, \hat{\mathbf{u}}_{(1,-1)} = n\pi p \, \hat{\mathbf{u}}_{(1,-1)}, \end{aligned} \tag{6.1}$$

where n is the concentration of the TDs (which is equal to one half the concentration x of single TCs), p is the dipole strength and $\hat{\mathbf{u}}_{(1,-1)}$ is the unitary vector specifying the direction of the gradient. Notice that, if the dipoles pointed in the opposite direction, the direction of the gradient would be $\hat{\mathbf{u}}_{(-1,1)}$. We have to specify that eq. (6.1) does not take into account the spin deformation in the regions surrounding each TD, but it represents only the average linear growth of the spin-phase over the whole the lattice.

6.1.2 Periodic boundary conditions

As we said, the lowest energy state of the XY-model without any topological excitation, is that with spatially uniform θ, as suggested by eq. (3.13). This does not create any problem in a lattice with periodic boundary condition. However when we put a collection of N_p TDs in the $L \times L$ lattice, we generate a phase gradient given by eq. (6.1), and the periodic boundary conditions are satisfied only if

$$\theta(x, y = L) - \theta(x, y = 0) = -2m_y\pi \tag{6.2a}$$
$$\theta(x = L, y) - \theta(x = 0, y) = 2m_x\pi \tag{6.2b}$$

with m_x, m_y integers. So our system must obey to the following constraints

$$n\pi pL = \frac{N_p \pi p}{L^2} L = \frac{N_p \pi p}{L} = 2m_x \pi \tag{6.3a}$$

$$n\pi pL = \frac{N_p \pi p}{L^2} L = \frac{N_p \pi p}{L} = -2m_y \pi \tag{6.3b}$$

where the "lattice winding numbers" m_x and m_y count the number of 2π-rotation of the spins, i.e. the number of spirals, running from one edge of the lattice to the other. If the TDs are diagonal, we have $m_x = -m_y = m$.

This implies that, with periodic boundary conditions, only for specific values $\bar{n}_m$ of the TDs concentration, the boundary conditions (6.3) can be satisfied. Clearly for those values of n the macroscopic current created by the TDs is not frustrated. However as soon as $n \neq \bar{n}_m$, the periodic boundary conditions frustrate the current and to overcome the problem we can use the superposition principle, since we are in the linear regime. For example, if we have a single TD, we can add a phase gradient, 'smoothing' the spin-phase distribution generated by the TD. This phase gradient must be opposite to that of eq. (6.1). We obtain in this way

$$\theta_{1\mathrm{TD},PBC}(x,y) = \theta_{1\mathrm{TD}}(x,y) - \pi(x-y)/L^2. \tag{6.4}$$

Now, for a concentration n of TDs (equal to one-half the concentration n_v of single vortices), we can sum all contributions $\theta_{1d,PBC}$ due to each TD:

$$\theta_{tot,PBC}(x,y) = \sum_{i=1}^{N_p} \theta_{1\mathrm{TD},PBC}(x-x_i, y-y_i), \tag{6.5}$$

(x_i, y_i) being the coordinates of the center of the i-th TD. However, when we start to increase the number of TDs in our lattice, when n exceeds half the distance between $\bar{n}_{m=0}$ and $\bar{n}_{m=1}$, we expect that the lowest energy lattice winding number becomes $m = 1$. The same is valid for a generic value of n, to which we can associate a specific value of m. So we must superimpose to the spin phase distribution, a number m of spin twists (along both directions), such that the energy eq. (3.2) is minimized. This can be done adding to $\theta_{tot,PBC}(x,y)$ the liner term $2m\pi(x-y)/L$ (for TDs pointing toward $(-1,-1)$). The two panels of Fig. 6.2 show how the energy (3.2) changes increasing the lattice winding number, both for a $n = 0$ system and for a system with a finite concentration of VA pairs. Notice that the energy per site is quadratic in m, and while for a $n = 0$ system $E/L^2 = -2J + (2\pi^2 J/L^2)m^2$, implying a stable spatially uniform distribution of the spin phase, a system with $n_v = 0.03$ gains energy by making two twists along both the directions. Indeed $n_v = 0.03$ corresponds to $m = 2.1$ according to eqs. (6.3), and we expect that the integer closest to it, namely $m = 2$, is the one with the lowest energy. Now it is clear the reason for which periodic boundary conditions frustrate the system for all values of n but $\bar{n}_m$.

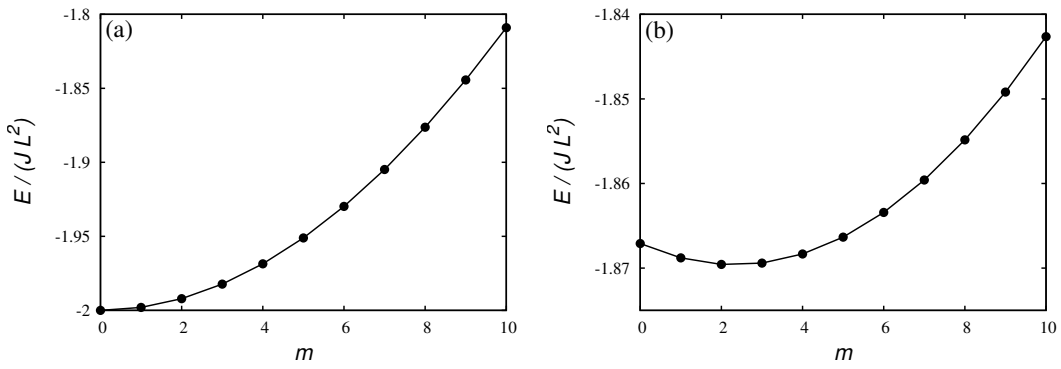

Figure 6.2: XY-model energy as a function of the winding number $m_x = m_y = m$, for (a) $n_v = 0$ and (b) $n_v = 0.03$.

Spin current saw-tooth

In the previous section we have seen that the number of spin spirals along the lattice increases with the number of TDs. Now we want to look at the average spin currents which determines the inversion symmetry breaking. To calculate the average spin current we use the conservation law (3.6). Indeed it implies that if we calculate I_{ij} between two neighbor sites in the direction orthogonal to the TDs and we average it over the entire side of the lattice (parallel to the segments), the value so obtained corresponds to the average spin current all over the lattice. For simplicity we take horizontal TDs of unitary length, and we calculate the average spin current along vertical direction, as a function of the number of TDs, N_p. To recover the phase slope removed by the imposition of periodic boundary conditions we have to superimpose m spin twists by subtracting the term $2m\pi y/L$. For each value of N_p, we take the value of m which minimizes the energy (3.2). Fig. 6.3 shows the average spin current compared to the average phase slope $-\Delta\theta/L$ due to the superimposed spin spirals[1]. The points where horizontal segments cross the blue lines correspond to $\bar{n}_m$, for which the system is not frustrated. The average spin current has a saw-tooth behavior, since it increases linearly until the concentration of TDs exceeds the value $(\bar{n}_{m+1} - \bar{n}_m)/2$, after that it is convenient for the system to increase by one the lattice winding number m, which implies an abrupt decrease of the spin current $(= 2\pi/L)$, which restarts immediately to increase with the same slope. Clearly the step down of the average spin current corresponds to an analogous step up of the $\Delta\theta$ between the borders of the lattice due to a new spin spiral, as indicated by the red line in Fig. 6.3. However we can see that the system fluctuates before changing definitively the lattice winding number.

As confirmed by the slope of the plot in Fig. 6.3, the average spin current in the vertical direction, with periodic boundary conditions, can be written as

$$\langle Js^2 \sin(\theta_i - \theta_{i+y})\rangle = \frac{2\pi p}{L^2} N_p = 2\pi n p, \tag{6.6}$$

[1]Notice that the minus sign arises since the average increment of the spin phase along the lattice due to a collection of TDs, described by eq. (6.1), has an opposite sign with respect to the average spin current.

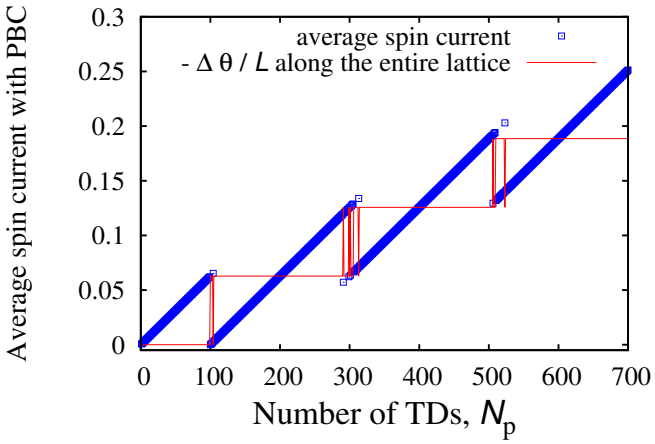

Figure 6.3: Average spin current (blue square) as function of the number of unitary horizontal TDs in a 100×100 lattice. Also the quantity $-\Delta\theta/L$, where $\Delta\theta$ is the phase jump between the borders of the lattice, is plotted (red line).

which is two times larger than the same quantity calculated with open boundary condition. The same results can be found with diagonal TDs, provided that p is taken in the correct way, being along the diagonal. This result is not immediate since, although we sum a negative linear term superimposing the spin spirals, the resulting average spin current is positive and doubled. Notice that the spiral twist which is generated can be thought as due to a macroscopic current which has the opposite sign of the average current.

6.2 Macroscopic spin current in the continuum

The same results found so far can be obtained analytically using the conformal mapping introduced in chapter 3. We consider a dipole lattice in a box

$$f(z) = \sum_{m,n} \frac{1}{z - (m + in)} \tag{6.7}$$

as in Fig. 6.4. From the last panel it is clear that a macroscopic electric field has appeared in the system in the x direction with strength $E_x = -\pi$. Clearly one should be able to compute the field using the theory of macroscopic dielectrics. We can define a dipole density $P = p/a^2$ where $a = 1$ is the lattice constant. Now we can use well known arguments from the theory of dielectrics. For this it is convenient to rederive some equations from Ref. [1] in our 2D geometry. The electric field can be expressed as

$$\mathbf{E} = q\hat{\mathbf{r}}/r, \tag{6.8}$$

and the two-dimensional version of the Gauss law reads

$$\oint \mathbf{E} \cdot \hat{\mathbf{n}}\, dl = 2\pi \int d^2r\, \sigma, \tag{6.9}$$

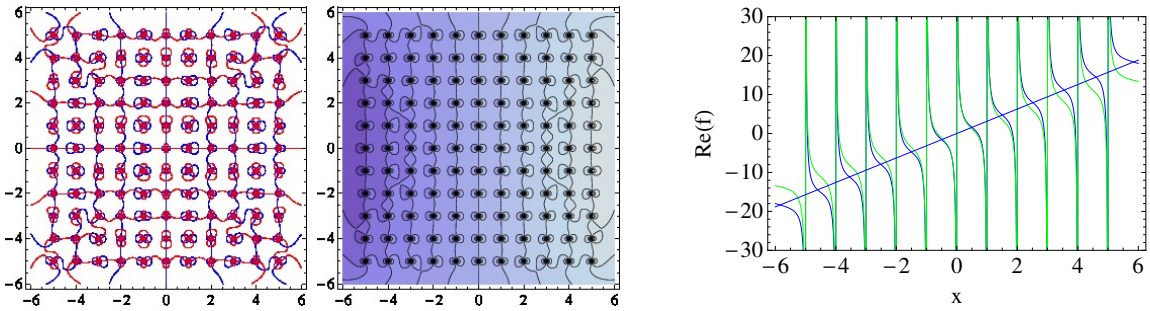

Figure 6.4: Constant potential lines for a 11×11 dipole lattice. Dipoles are at integer positions. The central panel shows only the real part which corresponds to the "electrostatic" potential with color proportional to the intensity. The right panel shows a cut of the real part at $y = 0$ (blue) and at $y = 5$ (green) together with the line πx.

with $\hat{\mathbf{n}}$ the normal oriented outwardly in the enclosing line and σ is the 2D charge density. Using the divergence theorem one obtains

$$\nabla \cdot \mathbf{E} = 2\pi\sigma. \tag{6.10}$$

For a line distribution λ (corresponding to charged plane perpendicular to the paper) one obtains that the change of electric field normal to the line is $(\mathbf{E}_2 - \mathbf{E}_1) \cdot \hat{\mathbf{n}} = 2\pi\lambda$.

Coming back to our dielectric box, if it is very large we can consider the charges of the dipoles to cancel in the interior of the box and a macroscopic field appears due to the uncompensated dipoles on the surface. We have on the right $\lambda = p/a = 1$ which would lead to $E_x = -2\pi$. This result is right in sign but wrong in magnitude because it neglects demagnetization factors. Indeed it is right if we consider a box of size $L_x \times L_y$ with $L_y >> L_x$. Fig. 6.5 shows the result of the same calculation as in the right panel of Fig. 6.4, but for a 10×110 dipole lattice. We can see that the resulting electric field

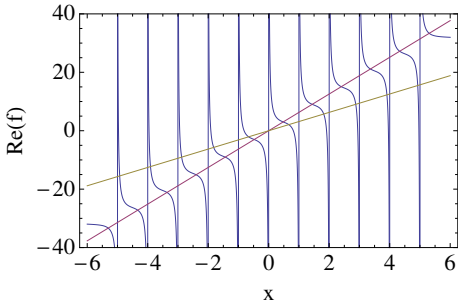

Figure 6.5: Real part of the complex potential for a 11×110 dipole compared with the lines πx and $2\pi x$.

agrees with our analytical calculation.

For our square lattice we have to compute the field in a square capacitor which is not a trivial problem. It is more easy to consider a lattice with a circular boundary (see left panel of Fig. 6.6). In this case the electric field becomes uniform inside the circle and can

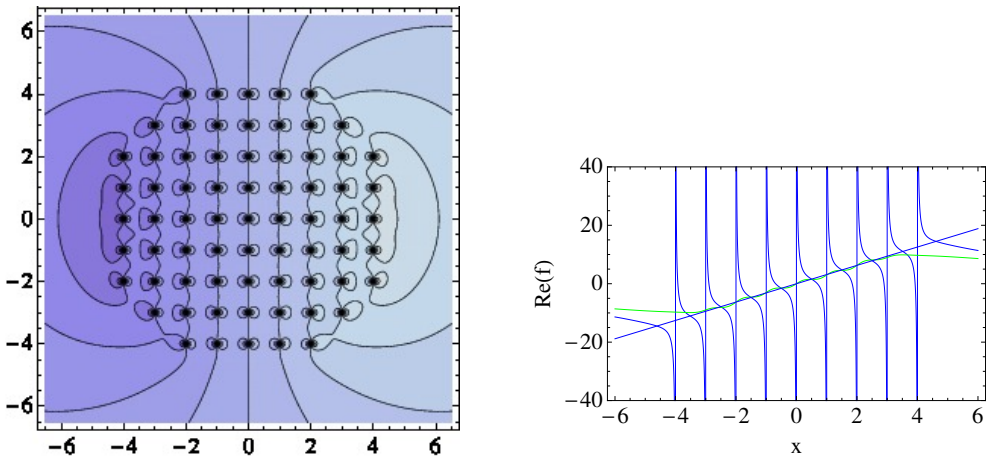

Figure 6.6: Real part of the constant potential lines for a dipole lattice. Dipoles are at integer positions which are at distance less than 5 from the origin. The bottom panel shows a cut of the real part at $y = 0$ (blue) and at $y = 3.5$ (green) together with the line πx.

be computed analytically when the radius become much larger than the lattice spacing. We compute the field at the center of the circle. The infinitesimal charge on the border of the circle at position $r(\cos\vartheta, \sin\vartheta)$ (here ϑ is the angle with the x-axis) is:

$$dq = P\cos\vartheta r d\vartheta \tag{6.11}$$

The electric field on the x direction due to this charge is

$$dE = \frac{dq\cos\vartheta}{r} \tag{6.12}$$

and the total field in x is

$$E = -\int_0^{2\pi} d\vartheta P\cos^2\vartheta = -\pi P \tag{6.13}$$

which now it is right in sign and magnitude.

For the electrostatic problem the complex macroscopic potential is given by the real part of

$$f^{mac}(z) = P\pi z^*, \tag{6.14}$$

which is the same result as in eq. (6.1). In the example of the Fig. 6.6 the electric dipoles are 1 and the magnetic dipoles $d = -i$. If we rotate the system 90^0 anticlockwise we get magnetic dipoles $d = 1$. We can redo the argument, recalling that the magnetic potential is given by the imaginary part of f, we obtain,

$$f^{mac}(z) = M\pi i z^*. \tag{6.15}$$

with $M = d/a^2$ the macroscopic magnetization. Notice that since $d = -ip$ $M = -iP$ the two expression are the same. Obviously the macroscopic magnetic field corresponds to a

macroscopic current. As a further check of the conjugate in the above expressions, notice that the regions of large potential are to the right and to the top in Fig. 3.3 while they are to the right and to the bottom in Fig. 3.5, which leads to a macroscopic field in the y direction which is opposite to the one defined by Eq. (3.22). This justifies the conjugation in Eq. (6.14).

From the theory of dielectrics we know that this result does not depend on the microscopic arrangement of the dipoles. They can be ordered or disordered as far as the average P is constant on large scales. In addition from the figures it is clear that the circle result is a good approximation also for the square lattice which is reasonable since they have similar demagnetization factors. In general it will be correct for domains of random shape if they do not tend to have a nematic shape deformation themselves.

6.2.1 Periodic boundary conditions

Now we consider a lattice. When we implement periodic boundary conditions, there must be no phase difference between the bottom and the top of the lattice. one can wonder, therefore, if there is a current. Naively one would assume that there is no current whereas, as we shall see, there is even more current than in the free case.

Fig. 6.7 shows, for an horizontal VA pair the cuts of the phase variation along y direction, with periodic boundary condition. We see that there is no phase difference

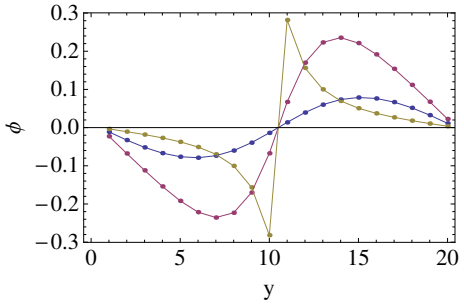

Figure 6.7: Cuts along y of the spatial dependence of the phase field (in unit of π) generated by an horizontal VA pair located at the center of a 20×20 lattice. Three different values of x are chosen : 1 (blue full line), 6 (red line) and 10 (yellow line). The cuts for $x = 1, 6$ have been multiplied by 10.

between the bottom and the top, but that the spin current in y is finite at the boundary since the phase arrives to the boundary with a finite slope. As expected this solutions conserves the current at each bond and there is a net current flowing in the y direction but the phase difference is zero.

To understand the lattice result we compute the phase distribution in the continuum for a VA pair of length 2. In order to obtain a periodic pattern we add images of the VA pair on $N_{cell} - 1$ neighboring cells around the central cell we are studying. Fig. 6.8 shows the complex potential. As can be seen there is a separatrix for the streamlines, all the current entering in the upper bound passes between the VA pair. In addition there

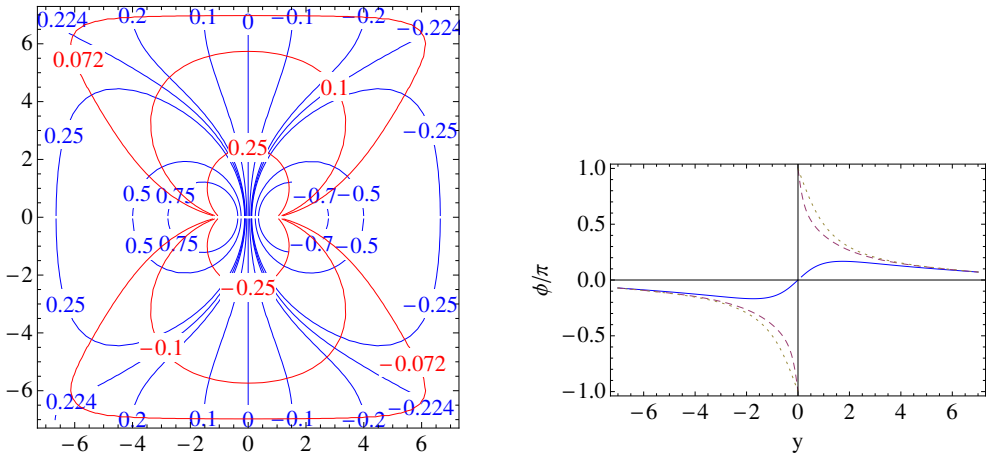

Figure 6.8: Left panel: constant potential lines for a VA pair of length 2 (antivortex in the left, vortex in the right). The imaginary part in red gives the lines of constant phase in units of π. The blue lines are the streamlines of the current. Notice that there is a separatrix for the streamline close to the value $\psi = 0.223$ for the potential. Right panel: Cuts of the phase dependence along y for different values of x:2 (blue full line), 0.8 (dashed line) and 0 (dotted line).

are closed loops so that there is no current crossing the lateral boundaries as would be for the solution without images. The cut of the phase shows that there is a jump of 2π in the phase when the cut passes in between the VA pair. We see that the phase in the boundaries is constant which is consistent with the presence of the separatrix described above since the streamlines are perpendicular to the contour phase levels. However despite the presence of the images the solution is not periodic. There is a net change of phase between the upper and the lower boundary as can be seen from the right panel. The change of phase is exactly

$$\phi(L/2) - \phi(-L/2) = \frac{p\pi}{L}. \tag{6.16}$$

If we compute the average current we get,

$$\overline{v}_y = \langle \frac{\partial \phi}{\partial y} \rangle = -\frac{p\pi}{L^2} \tag{6.17}$$

where with our definitions $p = 2$ so that the average current is negative. This is the same as it would be obtained by a single dipole therefore the images do not contribute to the average inside the box. This can be understand in the following way. If we consider the $L \times L$ system plus its $N_{cell} - 1$ images and extend the integral to all the domain $\Omega = N_{cell} - 1$. We have N_{cell} times the average of a single free dipole in a large box which yields the average current,

$$\langle \frac{\partial \phi}{\partial y} \rangle = -\frac{N_{cell} p\pi}{\Omega} = -\frac{p\pi}{L^2}. \tag{6.18}$$

In order to recover the correct periodic solution we subtract the function $p\pi y/L^2$. Notice that if the cut of the phase goes in between the VA pair then $\partial\phi/\partial y < 0$ however

the current we are subtracting has opposite sign so the result will be a state with even more current in the negative y direction.

Fig. 6.9 shows the same plots as Fig. 6.8 but for the periodic solution which again shows a separatrix. According to the previous discussion the current of the cuts that

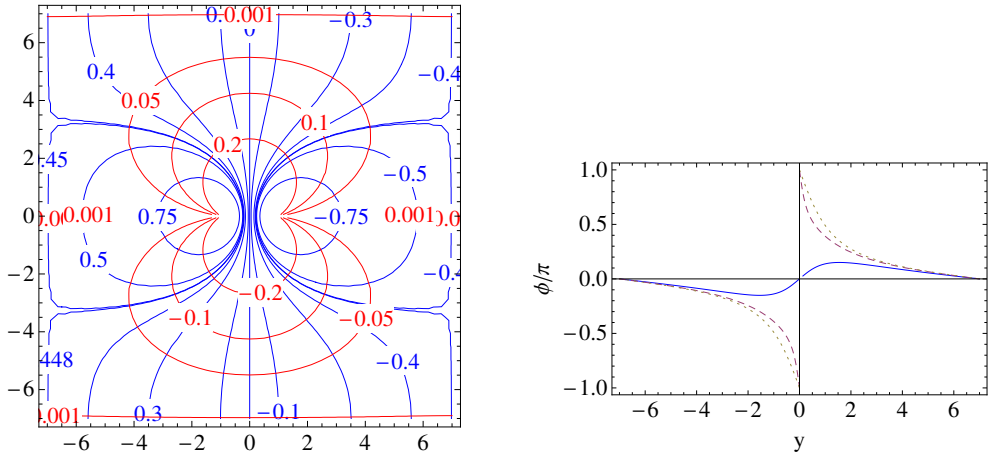

Figure 6.9: Left panel:Constant potential lines for a VA pair of length 2. The imaginary part in red gives the lines of constant phase in units of π. The blue lines are the streamlines of the current. Notice that there is a separatrix for the streamline close to the value $\psi = 0.448$ for the potential. Right panel: Cuts of the phase dependence along y for different values of x: 2 (blue full line), 0.8 (dashed line) and 0 (dotted line).

passes in between the VA pair is more negative. If we compute the average current we get,

$$\langle \frac{\partial \phi}{\partial y} \rangle = -\frac{2p\pi}{L^2}. \tag{6.19}$$

This is a useful result because it shows how to evaluate the strength of the dipole inside a box in a given solution and matches the result (6.6) obtained within the XY-model (the different sign depends on the orientation of the VA pair). Notice that since the current is conserved it is enough to compute the current in a row which can be far from the dipole.

Eq. (6.19) can be easily obtained analytically. The integral

$$\frac{1}{L^2} \int dx dy \frac{\partial \phi}{\partial y}$$

is first performed in y as a function of x. If $p/2 < |x| < L/2$, the integral goes outside the VA pair as in the full blue curve in the lower panel of Fig. 6.9. Since the function is analytic, the result is

$$\int dy \frac{\partial \phi}{\partial y} = \phi(L/2) - \phi(-L/2) = 0 \qquad \text{if} \qquad p/2 < |x| < L/2 \tag{6.20}$$

If x lays between the VA pairs (dashed and dotted curves in Fig. 6.9) we separate the integral in two parts to avoid the discontinuity,

$$\int dy \frac{\partial \phi}{\partial y} = \phi(L/2) - \phi(0^+) + \phi(0^-) - \phi(-L/2) = -2\pi \qquad \text{if} \qquad 0 < |x| < p/2. \tag{6.21}$$

Integrating this result in x along the entire length of the VA pair, we get Eq. (6.19).

So, with simple considerations of electrostatic, we have obtained the same results as for the XY-model in a lattice.

6.3 Polarized segments and spin incommensurability

Now we want to study the effect on the spin incommensurability, of a collection of oriented dipoles which arrange to form polarized segments. Since it depends on the dipole moment of these topological segments, we must ensure it matches the dipole moment resulting from the microscopic calculations of a segment of holes. So we will go back to the microscopic model and we will 'measure' the dipole strength of a segment resulting from the Gutzwiller calculations, for some values of N_c (number of TCs contained in the segment).

Since a collection of equally oriented TDs (pointing towards $(-1,-1)$), each with strength p, gives a phase field given by eq. (6.1) or equivalently by eq. (6.14), we can write the average spin field as follows:

$$\begin{array}{l} S^x(\mathbf{r}) = S\cos(\mathbf{q}\cdot\mathbf{r}); \\ S^y(\mathbf{r}) = S\sin(\mathbf{q}\cdot\mathbf{r}), \end{array} \tag{6.22}$$

where $\mathbf{q} = \pi P \hat{\mathbf{u}}_{(1,-1)} \equiv q\hat{\mathbf{u}}_{(1,-1)}$, with $P = np = N_p p/L^2$. We have seen that periodic boundary conditions take account of this spin periodicity by means of a quantized number of spirals, which give rise to a macroscopic spin current.

We have seen in the previous chapter that when we put together more VA pairs, they tend to aggregate to form a polarized chain, with the internal vortices annihilating with each other. Now, if we consider a number N_{seg} of segments with dipole strength p_{seg}, instead of N_p single TDs of strength p, we have

$$q = \pi P = \pi N_{seg} p_{seg}/L^2, \tag{6.23}$$

where p_{seg} is well defined from the average spin current in the same way as the dipole strength of a single TD, according to what said so far.

If we call p_2 the dipole strength of a segment containing $N_c = 2$ TCs, assuming a linear regime so that the dipole moment is additive, one finds that

$$p_{seg} = p_2 N_c/2, \tag{6.24}$$

as shown in Fig. 6.10. We can now compute the magnetic wave-vector of a collection of

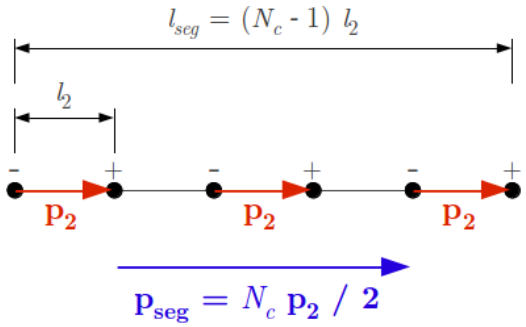

Figure 6.10: Dipole strength p_{seg} of a segment made by N_c holes, compared with the length l_{seg}. The figure shows the case with $N_c = 6$.

segments as

$$q = \pi N_{seg} p_{seg}/L^2 = N_{seg} N_c p_2 \pi/(2L^2) = n_h p_2 \pi/2, \tag{6.25}$$

where $n_h = N_{seg} N_c/L^2$ represents the total concentration of TCs, i.e. holes in the microscopic system (previously we called this quantity n_v since it corresponds to the concentration of the vortices). From Fig. 6.10 we see also that

$$l_{seg} = l_2(N_c - 1) = \frac{p_2}{k}(N_c - 1), \tag{6.26}$$

where we have used the definition of the dipole moment, i.e. $p_2 = k l_2$, being k the absolute value of the TCs. Inverting the previous equation $p_2 = k l_{seg}/(N_c - 1)$ and defining a "filling factor"

$$\nu = \frac{N_c - 1}{l^x_{seg}}, \tag{6.27}$$

where the horizontal length is defined as $l^x_{seg} = l_{seg}/\sqrt{2}$, we obtain

$$p_2 = \sqrt{2} k/\nu, \tag{6.28}$$

and finally

$$q = n_h p_2 \pi/2 = \frac{n_h \pi k}{\sqrt{2}\nu}. \tag{6.29}$$

Notice that the filling factor has been defined in such a way that it quickly converges to the filling factor one would find for a long segment. Indeed for segments like those of Fig. 5.7 this definition gives $\nu = 1$ which is what one expects for a long segment in this class of solutions. There is another class of solution with vortices and antivortices centered in plaquetes which have $\nu \sim 0.7$. As a further check consider a segment like the one shown in Fig.6.11. The expression correctly gives $\nu = 1/2$ which is what one would get for a long segment.

So far we have used $k = \pm 1$. Notice that since we are on the lattice and the vortex and the antivortex are at a microscopic distance there is no reason why k should be quantized.

Figure 6.11: Segment made by 5 holes separated by 2. Since $N_c = 5$ and $l_{seg} = 8$, we have $\nu = 1/2$.

In fact we find numerically that it is not. From eq. (6.24) we find $p_2 = 2p_{seg}/N_c$, and putting it into eq. (6.26), we find

$$l_{seg} = \frac{p_2}{k}(N_c - 1) = \frac{2p_{seg}}{k}\frac{N_c - 1}{N_c}. \tag{6.30}$$

We can now use this equation to find the value of the topological charges. We want that this length matches the "geometric" length of the segment which one measures directly from the solutions of the microscopic calculations. For example the 8-holes segment shown in Fig.5.7, has a length of approximately $7\sqrt{2}$ lattice units. For the present solutions we find that the geometric length l_{seg} is well approximated by $(N_c - 1)\sqrt{2}$ as can be seen by inspection. Fig. 6.12 shows the horizontal length l^x_{seg} of a segment calculated using eq.(6.30) for different values of k, compared with $l^x_{seg} = (N_c - 1)$, at varying N_c. We see that the value the topological charge for which the calculation matches the geometric length is $k = 0.8$. Notice that the agreement is still poor for large N_c. We expect this

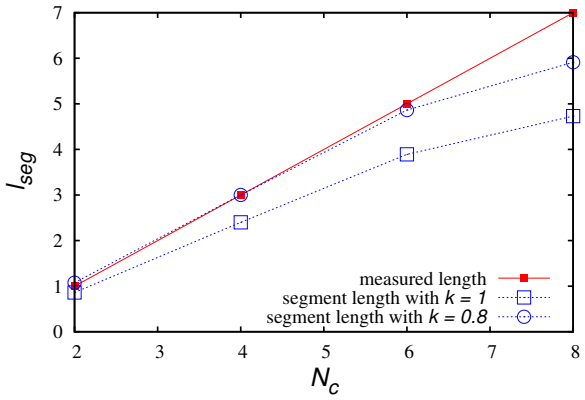

Figure 6.12: Segment length obtained from the Gutzwiller value of p_{seg} by means of eq. (6.26), compared with the 'measured' value $l^x_{seg} = (N_c - 1)$.

simply because the length of the segment is of the order of the system size and the effect of frustration of the system gets weakened. Actually it will disappear when the stripe closes around itself across the system. If we fix N_c and increase the system size we expect to recover the linear relation for sufficiently large sizes.

We work in units in which a_{tetra} is the Cu-Cu distance and $a_{ortho} = \sqrt{2}a_{tetra}$. The incommensurability in orthorombic reciprocal lattice units is defined as

$$\epsilon^{ortho} = \frac{q}{2\pi/\sqrt{2}} = \frac{n_h k}{2\nu} \tag{6.31}$$

6.4 Non-linear corrections and comparison with experiments

The theory developed so far is a linear theory since it is a result of the linear superposition of the phase fields generated by each vortices. However it is possible that when the concentration of TDs is large, non-linear corrections become important. Thus to compare with the experimental magnetic neutron cross section me must minimize the classical energy (3.2), allowing the spin to relax. To do this we go back to the lattice XY-model and we introduce an antiferromagnetic interaction J' across the center of the TCs, besides to the antiferromagnetic[2] nearest-neighbor interactions J (see Fig. 6.13). J'

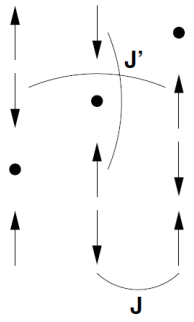

Figure 6.13: Definition of couplings used in XY-model calculations.

stabilizes the antiphase boundary of the segments and avoids the VA annihilation. We fix the value of $|J'/J|$ for the XY-model by comparing for a segment of two VA pairs the resulting charge and spin structure obtained from the GA (Fig. 6.14(a)) and from the minimization of the XY-model energy [Fig. 6.14(b)]. . Indeed it can be shown that the spin phase distribution nearly coincides within the two approaches when $|J'/J| \sim 1$.

The minimization procedure consists in the alignment of a picked spin with the Weiss field generated by the neighboring spins (those connected via a finite exchange coupling). Notice that we consider again periodic boundary conditions. For a given spin $\mathbf{s}_k$, the corresponding field $\mathbf{h}_k$ can be derived from the hamiltonian (3.2), which we rewrite as $\frac{1}{2}\sum_{i\neq j} J_{ij}(S_i^x S_j^x + S_i^y S_j^y)$:

$$h_k^x = -\frac{\partial \mathcal{H}}{\partial S_k^x} = -\frac{1}{2}\sum_{j\neq k} J_{kj} S_j^x - \frac{1}{2}\sum_{i\neq k} J_{ik} S_i^x = -\sum_{i\neq k} J_{ik} S_i^x = -\sum_{i\neq k} J_{ik} S_i \cos\theta_i \quad (6.32a)$$

$$h_k^y = -\frac{\partial \mathcal{H}}{\partial S_k^y}; = -\frac{1}{2}\sum_{j\neq k} J_{kj} S_j^y - \frac{1}{2}\sum_{i\neq k} J_{ik} S_i^y = -\sum_{i\neq k} J_{ik} S_i^y = -\sum_{i\neq k} J_{ik} S_i \sin\theta_i. \quad (6.32b)$$

Since the stable configuration must satisfy $\mathbf{h}_k \cdot \mathbf{S}_k = 0$, with k running all over the spins, we must require that $\varphi_{h_k} - \theta_k = 0$, being φ_{h_k} the angular coordinate of the field $\mathbf{h}$. So

[2]Notice that we can use ferromagnetic nearest neighbor interactions provided we consider staggered spins.

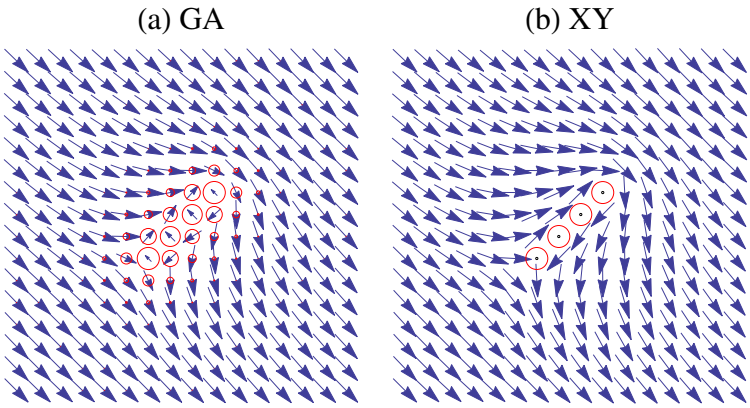

Figure 6.14: Segment of two VA pairs on a 16×16 lattice. (a) Gutzwiller approximation of the Hubbard model with $U/t = 8$,$t'/t = -0.2$. (b) XY-model with $|J'/J| = 1$. In (a) the radius of the circles indicates the (hole) charge density abd in (b) corresponds to an empty site.

the new phase of the spin k must be

$$\theta_k = \arctan\left(\frac{h_k^y}{h_k^x}\right) = \arctan\left(\frac{-\sum_{i\neq k} J_{ik} S_i \sin\theta_i}{-\sum_{i\neq k} J_{ik} S_i \cos\theta_i}\right) = \pi + \arctan\left(\frac{\sum_{i\neq k} J_{ik} S_i \sin\theta_i}{\sum_{i\neq k} J_{ik} S_i \cos\theta_i}\right) \tag{6.33}$$

Once all the spins of the lattice have been picked, we can start another iteration until the arbitrary precision is reached.

Now we take a distribution of segments, with length of 8 sites at $n_h = 0.03$, all polarized along the $(-1, 1)$ direction, on a lattice of 160×160 (see Fig. 6.15(a)). Since there is no reason for which these segments must be spatially ordered, we consider randomly distributed segments. One observes a monotonic increase on the phase of the staggered magnetization

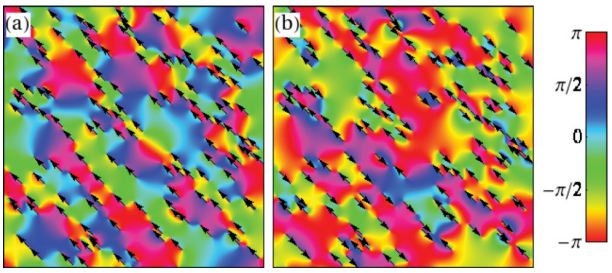

Figure 6.15: Spin phase distribution for (a) macroscopically and (b) randomly polarized distribution of stripe dipoles in a 160×160 site system. Segments have a length of 8 sites on the diagonal (4 VA pairs) and are represented by arrows indicating the length and polarization. With a filling factor $\nu = 0.7$ the total number of segment sites corresponds to a doping of $n_h = 0.03$.

along the $(1, 1)$ direction, which will lead to the incommensurate modulation of the spin response. In Fig. 6.15(b), for the same distribution of segments, the associated dipole orientation is now completely random. Contrary to the case of Fig. 6.15(a), the system

now disaggregates into large areas with similar phase. As already stated, the short-range contribution to the dipole-dipole interaction favors the ferromagnetic alignment (i.e., the configuration Fig. 6.15(a) is energetically more stable than Fig. 6.15(b)). We call "ferronematic" the state shown in Fig. 6.15(a), since the C_4 rotational symmetry breaking (imposed manually) is accompanied by the inversion symmetry breaking testified by the presence of a spin spiral state which sustains a net spin current.

For a set of configurations of macroscopically polarized VA segments on a lattice of 160×160 sites as shown in Fig. 6.15(a) we now evaluate, for different values n_h, the magnetic neutron cross section

$$\frac{d\sigma}{d\Omega dE} \sim \sum_{\alpha\beta} (\delta_{\alpha\beta} - \hat{q}_\alpha \hat{q}_\beta) S_\alpha(\mathbf{q}) S^\beta(\mathbf{q}), \tag{6.34}$$

where $S^\alpha(\mathbf{q})$ is the Fourier transform of the α coordinate of the spin-spin spatial correlation function. Our results are compared in Fig. 6.16 with elastic neutron scattering data from Ref. [2]. The specific scattering geometry (Fig. 2(b) of Ref. [2]) which is composed of two twin domains with population 2 : 1 has been taken into account. This gives rise to the asymmetry of the spectra since Q_{AF} of the B twin does not coincide with Q_{AF} of the A twin. The incommensurate peak position q_c is independent from the segment size as expected from eq. (6.29). On the other hand the size influences the peak width as can be seen in the lowest panel of Fig. 6.16. By decreasing the dipole moment p_{seg} at fixed doping, the increasing number of segments decreases the fluctuations of the dipole polarization. The strength of the incommensurate response is then favored with respect to the commensurate one. As can be seen from Fig. 6.16 one finds excellent agreement with the experimental data for segments with 4 VA pairs (i.e., 8 sites) whereas shorter segments underestimate the intensity at Q_{AF} (see lower panel of Fig. 6.16).

A spin glass phase of cuprates, due to a dipolar frustration of the antiferromagnetic environment by the dopant holes, was already proposed by Hasselmann *et al.* [3, 4] Their theory explained the existence of short-range incommensurate magnetic correlations in LSCO, in terms of a state with an ordered orientation of the effective dipole moments. Non-collinear spin spiral states have also been proposed for small doping, in the context of the Hubbard and the t-J models, by Sushkov and Kotov [5, 6]. They showed that such states, whose stability is due to quantum fluctuations (order from disorder effect), describe correctly [7] the incommensurate neutron scattering peaks detected on LSCO, and [8] the transport anisotropy measured in underdoped LSCO, already mentioned in sec. 1.5.1.

Our theory has some similarity with these proposals. However the state emerging from our analysis is different in many respects. First of all we find that in the absence of pinning potentials the charge organizes forming rather long segments, which might be the seeds for the formation of the stripes observed at higher dopings. Of course when the pinning potential due to the out-of-plane impurities dominates, the segments are disrupted because its constituents are attracted around each Sr impurity. However, the rather large dielectric constant of LSCO, the relatively large impurity density, and their out-of-plane location conspire to produce a rather smooth potential landscape on the planes, which

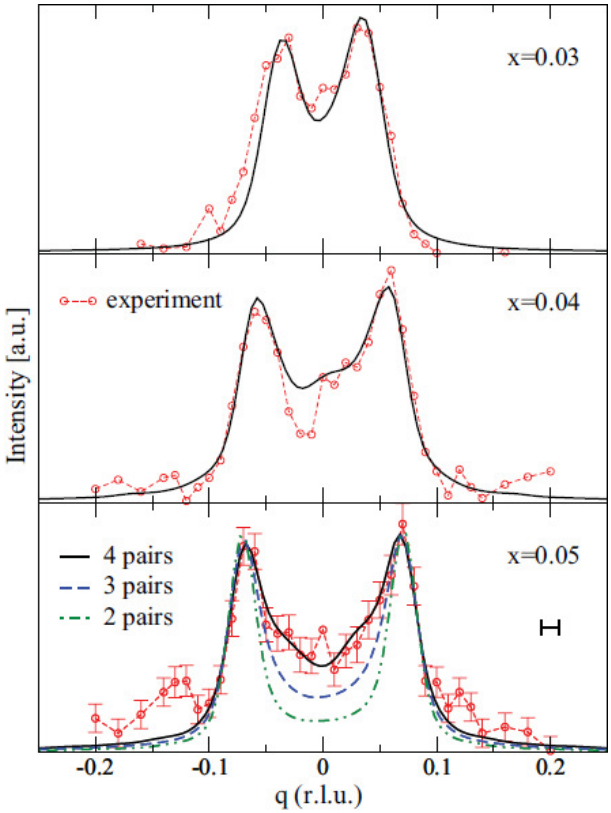

Figure 6.16: Fits of the spin structure factor (LSCO) at different dopings for $N_c = 8$ segments as explained in the text. For $x = 0.05$ we also show spectra for $Nc = 4, 6$ segments for comparison. Computations have been done on lattices with up to 160×160 sites and we average over 20-30 segment configurations where the experimental resolution (horizontal bar in the lower panel) has been taken into account by convoluting with a Gaussian.

suggests that the aggregation tendency might be dominant and longer segments should be considered, as we will show in chapter 8 by means of Monte Carlo simulations. Of course the smooth quenched disorder landscape still provides a pinning source for the charge segments thereby disrupting any segment positional order. Another difference with respect to the works of Hasselmann *et al.*, and of Sushkov and Kotov, is that in our scenario topological spin textures are present at each extreme of the charge segments producing the spin spiral state with the ferronematic order. Therefore in the present case the spiral spin state is a collective effect, which is slaved by the ferronematic order of the stripe segments.

Summarizing, in this chapter we have calculated quantitatively the spin deformation due to a collection of aligned TDs. It consists in a certain number of spin twists, which can be described with the occurrence of a spin current. However we have seen that the finite size of our cluster and the periodic boundary conditions frustrates the spin structure, fixing an integer number of twists. This result has been obtained also by applying general arguments of electrostatics and magnetostatics to a continuous system. Then we have studied what happens when TDs aggregate into segments. In particular we have seen how the characteristics of these segments (total dipole moment, length, filling factor) affect the spin incommensurability of the system. We have stated that, once fixed the value of the TCs and the filling factor, it depends linearly on the hole concentration. Finally we have calculated the spin structure factor due to a collection of equally oriented segments and we have compared it to the experimental neutron scattering peaks, obtaining an optimal agreement.

Bibliography

[1] J. D. Jackson, *Classical Electrodynamics* (3Ed, Wiley, 1998).

[2] S. Wakimoto, R. J. Birgeneau, M. A. Kastner, Y. S. Lee, R. Erwin, P. M. Gehring, S. H. Lee, M. Fujita, K. Yamada, Y. Endoh, K. Hirota, G. Shirane, Phys. Rev. B **61**, 3699 (2000).

[3] N. Hasselmann, A. H. Castro Neto, C Morais Smith, Europhys. Lett. **56**, 870âĂŞ876 (2001).

[4] N. Hasselmann, A. H. Castro Neto, C Morais Smith, Phys. rev. B **69**, 014424 (2004).

[5] O. P. Sushkov and V. N. Kotov, Phys. Rev. B **70**, 024503 (2004).

[6] V. N. Kotov and O. P. Sushkov, Phys. Rev. B **70**, 195105 (2004).

[7] O. P. Sushkov and V. N. Kotov, Phys. Rev. Lett. **94**, 097005 (2005).

[8] V. N. Kotov and O. P. Sushkov, Phys. Rev. B **72**, 184519 (2005).

Chapter 7

Effective Coulomb lattice gas model

We have seen that at long distances the system can be described using generalized elasticity. Exploiting the correspondence between a spin vortex and a two-dimensional (2D) Coulomb charge [1] explored in chapter 3, we construct an effective lattice gas model suitable for Monte Carlo simulations. Treating the vortices as fractional topological charges $\pm k$ (TCs), we will consider temperatures at which they are bound at least in pairs making topological neutral objects, which we have referred to as topological dipoles (TDs), so that there are no restrictions on k. The model will also contain short-range interactions extracted from the microscopic calculations in the Gutzwiller approximation, the real three-dimensional Coulomb repulsion between the positive charged holes, as well as the effect of the negative ions randomly distributed out of the plane. The strength of the latter contribution will be treated as a parameter model which describes the intensity of the quenched disorder.

7.1 Long-range and short-range interactions

In order to investigate the finite temperature behavior of the topological defects described in the previous sections, i.e. the spin vortices, we have to study the statistical mechanics of these objects. One can wonder if these topological defects, which are the building blocks (namely the TCs) of our effective model, are stable at finite temperature. As explained in chapter 5 the VA pairs within a planar spin texture represent local energy minima as proved by the real value of the spin excitation energy [2], and they can persist in a certain range of temperature. As already mentioned (see Ref. [3]) another type of topological excitation, involving a three-dimensional spin texture, can exist. However such a type of state, namely the skyrmion, has an higher energy with respect to the spin vortices and the temperature values which will be considered in our simulations, are low enough to allow us to neglect it in the construction of our effective model, which thus involves only the topological defects of a planar spin model, treated as TCs. Now we study the effective interactions between them.

The finite extension λ of magnetic correlations provides a natural cut-off to the long-range interactions (3.21) between TCs, so that at long distances the interaction energy is

well described by,

$$\tilde{V}_{k_1k_2}(r) = \rho_s k_1 k_2 \int_0^{2\pi} \mathrm{d}\theta \int_0^{\infty} \mathrm{d}q \, \frac{q \, \mathrm{e}^{iqr\cos\theta}}{q^2 + \lambda^{-2}} = 2\pi\rho_s k_1 k_2 K_0 \left(r/\lambda\right), \tag{7.1}$$

where ρ_s is the spin stiffness of the antiferromagnetic background, k_1 and k_2 are the values of the two TCs (vorticities) and K_0 is the zeroth order modified Bessel function, which reproduces the logarithmic interaction of sec. 3.2.1 at short/intermediate distances ($r \lesssim \lambda$) and decays exponentially at long distances ($r \gg \lambda$).

Assuming the interaction (7.1) between the TCs, we report the energy characterization of a dipolar lattice in appendix D, showing that a triangular arrangement of the TDs allows for ferroelectric orientations.

The expression (7.1) reproduces well the interaction energy of topological defects in Gutzwiller calculations for the single-band Hubbard model at long distances but, as expected, it fails at short distances where the short-range physics of the Hubbard model becomes relevant, as it can be seen in Fig. 5.6. Indeed at short distances the interaction between the vortices is modified by quantum effects related to the overlap of the holes wave-functions within the core of the segment. Therefore we also include in our model, short-range terms obtained by studying, by means of GA, metastable configurations in which a fixed number of holes is self-trapped in VA configurations located at several position in the lattice. These configurations of vortices, i.e. TCs (once the mapping to the Coulomb gas is done), are shown in Fig. 7.1.

Since the texture is long-ranged and the cluster has periodic boundary conditions the energy of each configuration is strongly dependent on the system size which is limited to small clusters (16×16) in the Hubbard model. This effect is specially severe when the configuration leads to a macroscopic spin current. One expects, however, that the short-range part of the interaction, due to the overlap of the hole wave-functions, is well converged in our cluster. Fortunately, since all the textures are planar, the long-range part of the interaction can be well reproduced with an effective XY-model which allows to extrapolate the results to very large cluster, as follows. We assume that the energy of each configuration for the cluster of size L can be written as the sum of short-range (sr) terms plus long-range (lr) terms,

$$E_{\mathrm{Hub},L\times L} = E_{\mathrm{Hub,sr},L\times L} + E_{\mathrm{lr},L\times L}. \tag{7.2}$$

We make the assumption that we can reproduce $E_{\mathrm{lr},L\times L}$ with a lattice XY-model which has the same stiffness as the one obtained in the Hubbard model and has topological dipoles with the same dipole strength as in the Hubbard computations. In order to compute the dipole strength we compute the average spin current in the direction $\hat{\mathbf{u}} = \frac{1}{\sqrt{2}}(1,-1)$, as $\langle \nabla\theta \cdot \hat{\mathbf{u}} \rangle = \frac{2\pi p}{L^2}$, by averaging over a line perpendicular to $\hat{\mathbf{u}}$, according to the discussion in sec. 6.1. Then we adjust J' of the XY-model, playing the role of elementary topological dipole, in such a way to match the dipole strength of the Hubbard model computed in the same way. This ensures that the long-range part of the energy of the XY-model coincides with the long-range part of the energy of the Hubbard model for the same

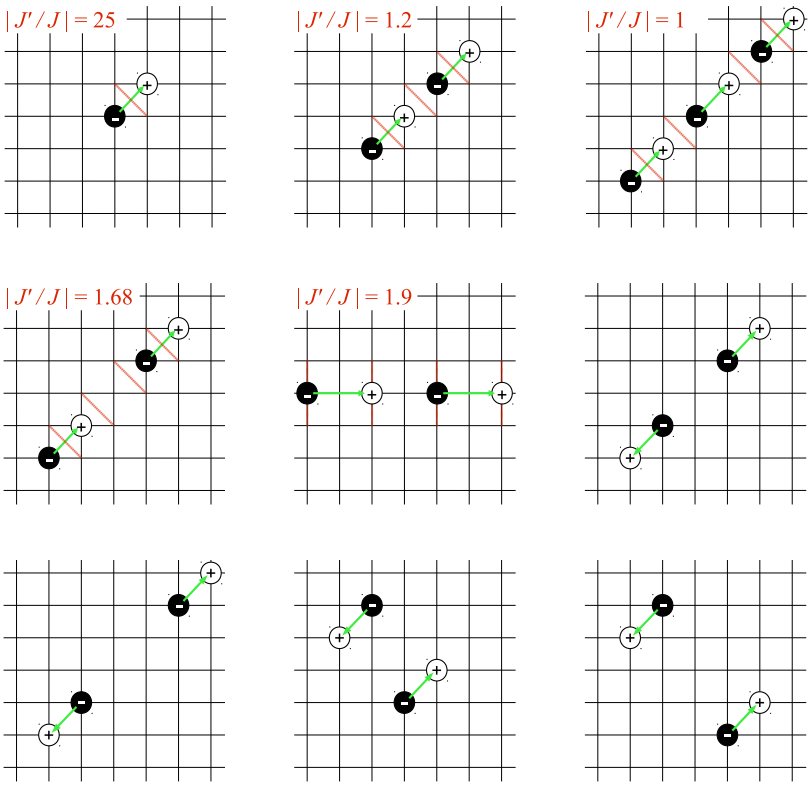

Figure 7.1: Configurations of topological charges used to extrapolate the short-range terms. The black and white circles represent respectively negative ($k = -0.8$) and positive ($k = +0.8$) charges. The green arrows represent the dipole moments generated by the pairs of opposite charges. The red segments represent the antiferromagnetic coupling J' (whose numerical value is reported in each panel), used to stabilize antiphase boundaries and to reproduce, within XY-model, the long-range part of the GA calculations, only for the configurations with aligned TDs.

texture. Notice that the way in which we take the exchange coupling J' (and also its strength) must depend on the specific configuration, if we want to reproduce exactly the average spin current resulting from the Hubbard calculation. According to what said so far, we can write

$$E_{\mathrm{XY},L\times L} = E_{\mathrm{XY,sr},L\times L} + E_{\mathrm{lr},L\times L}. \tag{7.3}$$

The energy of the Hubbard model for a large cluster of size L' is obtained assuming that the short-range terms do not depend on the system size according to

$$E_{\mathrm{Hub},L'\times L'} = E_{\mathrm{Hub},L\times L} - E_{\mathrm{XY},L\times L} + E_{\mathrm{XY},L'\times L'}. \tag{7.4}$$

Notice that the configurations with opposite TDs, such that the total polarization is zero, do not give rise to any macroscopic spin current ($\sim \langle\nabla\theta\rangle$) and the spurious effect due to the finite size on the energy ($\sim (\langle\nabla\theta)^2\rangle$), practically disappears making $E_{\mathrm{Hub},L'\times L'} \simeq E_{\mathrm{Hub},L\times L}$. So, for the configurations shown in the last four panels of Fig. 7.1, we do not need to calculate $E_{XY,L\times L}$.

Next according to the Coulomb gas mapping [1], we assume that the long-range part of the energy can be represented by topological charges centered at the lattice sites with topological charges $\pm k$. Here k was determined in such a way that when a dipole $\mathbf{p}$ is formed with charges on the diagonal of a plaquette of length $l = \sqrt{2}a$, the dipole moment $p = kl$ reproduces that of the Gutzwiller and XY-model computations. We find the same results as in the previous chapter, i.e. $|k| = 0.8$. This result is consistent with diagonal TDs of length $\sqrt{2}$ and with horizontal TDs of length 2.

Next we decompose $E_{\mathrm{Hub},L'\times L'}$ for N_h holes in the different contributions,

$$\begin{aligned} E_{\mathrm{Hub},L'\times L'} &= E_{\mathrm{AF},L'\times L'} + N_h\epsilon_0 + 2\pi\rho_s k^2 \sum_{i<j} \eta_i\eta_j \log(r_{ij}) \\ &\quad + \sum_{i<j} \delta V^{\eta_i,\eta_j}(r_{ij}). \end{aligned} \tag{7.5}$$

Here $E_{AF,L'\times L'}$ is the energy of the antiferromagnetic solution in a cluster of the same size, r_{ij} is the distance between topological charges i and j, $\eta_i = \pm$ is the sign of the TC, ϵ_0 is a short distance self-energy term independent of the distance among the TCs and associated with the energy needed to create the vortex core and to add the real charges to the system. The last two terms represent the long- and short-range parts of the interaction. Our aim is to determine the last term which is different form zero only at short distances. GA computations for the configurations shown in Fig. 7.1 allow to equate the corresponding sums $N_h\epsilon_0 + \sum_{ij} \delta V_r^{\eta_i,\eta_j}$ to known energies. This provides a system of equations which can be inverted to obtain the various $\delta V_r^{\eta_i,\eta_j}$. Notice that ϵ_0 is irrelevant in the Monte Carlo computations since we work at a fixed number of particles.

To obtain the spin stiffness ρ_s, which is equal to the exchange coupling Js^2, we have calculated the Gutzwiller energy of a configuration constituted by a spin spiral in x direction with a fixed value of the the wave vector $\mathbf{Q}$, in such a way that $\nabla\theta = (Q, 0)$. The energy increment with respect to the uniform spin state is given by $\Delta E = \frac{1}{2}L^2\rho_s Q^2$.

Putting this expression equal to the numerical result of ΔE, we obtain $\rho_s = 0.11\,t = 39.6$ meV.

Fig. 7.2 shows the total potential $V(r)$ between two TCs of the same sign (a) and of different sign (b), as a function of their distance r, including short- and long-range parts (green and magenta lines) and compared with the long-range part alone (red and blue).

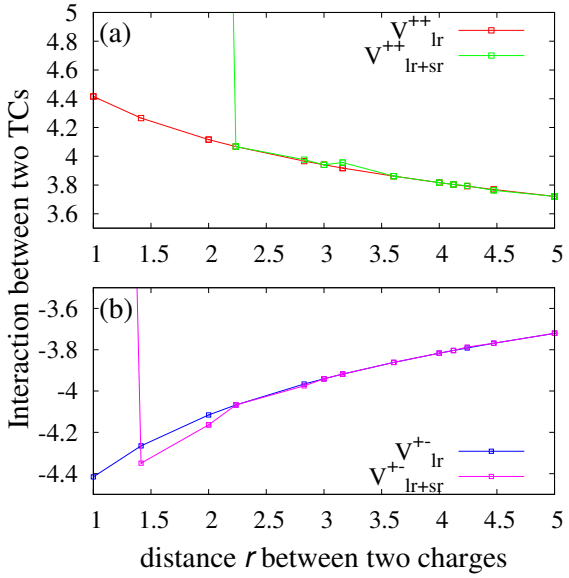

Figure 7.2: (a) Interaction between two TCs of the same sign for some discrete values of the distance: the long-range part of the potential (red line) is compared to the total potential including both the short and the long-range part (green line). (b) Interaction between two opposite TCs: long-range part (blue line) and total potential (magenta line).

We have assigned high energy values to the terms $\delta V^{+-}_{r=1}$ and $\delta V^{++}_{r=2}$, since these configurations cannot be stabilized even as metastable states. This effectively has the effect of eliminating these configurations from the Monte Carlo computations, so that the computations will not depend on the precise value of these constants. We see that the effect of the short-range part is essentially to add an hard-core to $\tilde{V}$.

Notice that the effective interaction between topological charges should not be taken literally. Indeed if two holes are separated at a long distance the Coulomb gas energy is logarithmically large because it assumes a VA pair. Instead the GA solution converges to two collinear spin polarons which have a smaller energy. Thus for those configurations the effective interaction makes sense only if the VA pairs are at short distances and form dipoles. Thus in the Monte Carlo computations we restrict the temperature in such a way that this condition is met.

7.2 Hole-hole and hole-impurity coulombic interactions

Furthermore, each TC arising from the spin texture corresponds to a positive electrically charged hole in the CuO_2 planes of the doped cuprate. Therefore, our model includes also the three-dimensional Coulomb repulsion between the doped holes

$$V_{hh}(r) = \frac{Q_{rep}}{r} \tag{7.6}$$

where Q_{rep}, incorporating, e.g., the static dielectric constant, represents the strength of the repulsion and will set by establishing the average length of the segments (see sec. 7.3).

Finally the positively charged holes doped into the CuO_2 planes leave back negative countercharges. For instance, in LSCO negative Sr ions randomly replace La atoms between two consecutive planes. We therefore introduce quenched disorder, generating a random distribution of point-like negative charges which act as pinning centers for the holes in the plane. These charges are located out of plane, at a distance $\bar{d} \approx 0.58$ (in lattice units), from the center of the in-plane unitary cell. Each Sr impurity interacts with a hole through an attractive three-dimensional Coulomb potential

$$V_{\mathrm{Sr}-h} = -\frac{Q_{\mathrm{Sr}}}{d}, \tag{7.7}$$

where $d \geq \bar{d}$ is the distance between a Sr ion and a hole. The magnitude Q_{Sr} is difficult to estimate because it depends on screening processes not comprised in the model. Therefore, we treat $\eta = Q_{\mathrm{Sr}}/Q_{rep}$ as a phenomenological dimensionless parameter which characterizes the amount of disorder. Henceforth, we shall call 'clean case' the limit $\eta = 0$. An example of random distribution of Sr impurities with the potential field generated on the plane is reported in Fig.7.3.

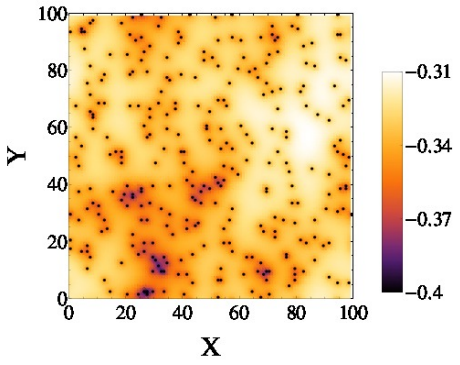

Figure 7.3: Density plot of the attractive potential generated by the negative Strontium ions on the nearest CuO_2 plane. The darker is the color the deeper is the potential well. The projection of the position of the ions on the plane is represented by the black points.

7.3 Numerical values of the model parameters

We consider a $L \times L$ cluster with N positive/negative TCs (spin vortices/antivortices) corresponding to $N_h = 2N$ holes. Although we explored other fillings, we report the results for the typical case $L = 100$ and $N = 150$, corresponding to a hole doping $n_h = 0.03$. For what concerns the other parameters of the model, we have found $\rho_s = 0.11\,t$, $|k| = 0.8$ and $\lambda = 105$. We assume that the magnetic correlation length is much larger than the average distance between the TDs. Thus λ losses its physical meaning and we use it as a convergence parameter. Its magnitude is justified in appendix D. The amplitude Q_{rep} of the coulombic interaction between two holes can be tuned in order to fix the average length of the chains of TDs that form at low temperature. We put $Q_{rep}/t = 0.136$. Although such a choice guarantees segments made by only one TD at low temperature in the low density limit ($n_h \to 0$), at finite density (in our case $n_h = 0.03$) the length of segments increases.

Our model is a dipolar gas of interacting topological dipoles. Thus it is in analogy with dipolar fluids where standard phase separation with isotropic aggregation is replaced by defects induced topological phase separation [4]. However, in 3D, the maximal dipole-dipole attraction is when two dipole spheres touch each other nose-to-tail favoring an endless alignment, as in our case. Only at $T \neq 0$, ends and junctions of chains appear as topological excitations.

Within this model we carried out MC calculations exploiting the parallel tempering technique. Since we are interested also in the spin structure due to the spin vortices and antivortices, we have to specify that the spins should generally obey the MC dynamics, i.e. the Metropolis algorithm, in the same way as the TCs. However, once determined the TCs configuration, also the spin configuration is determined. Indeed, since the spin dynamics is much faster than the TCs dynamics, the spin configuration immediately adjusts to the TCs configuration. Furthermore the high energy of the spin excitations makes them negligible to our purpose and we take into account only the spin ground state, determined by the TCs configuration.

Bibliography

[1] P. Minnhagen, Rev. Mod. Phys. **59**, 1001 (1987).

[2] G. Seibold, C. Di Castro, M. Grilli, J. Lorenzana, Scientific Reports **4**, 5319 (2014).

[3] G. Seibold, Phys. Rev. B **58**, 15520 (1998).

[4] T. Tlusty and S. A. Safran, Science **290**, 1328 (2000).

Chapter 8

Monte Carlo analysis: the phase diagram and the emergence of a ferronematic state

We have seen that holes in an antiferromagnetic (AF) state induce a vortex or antivortex texture in the surrounding spin ordering. While isolated vortices are energetically expensive, a VA pair is stable, because the disturbance of the antiferromagnetic background rapidly dies out at large distances and the strongly correlated character of the doped holes hinders the annihilation of the VA pairs. These pairs contribute to the rapid destruction of long-range AF order [1] and become the fundamental ingredients of a new physical scenario, where these "dimers" interact and give rise to "electronic soft matter" effects. These VA dimers may undergo a "polymerization process", triggering charge segregation into segments, tightly bound to vortex and antivortex spin textures. We have seen also that these segments not only align forming a nematic state, but can also break inversion symmetry due to their intrinsic topological dipolar character (associated with the V and A at the endpoints of the "polymer"). This state, which was named ferronematic, is accompanied by a spin spiral state sustaining a net spin current. We pose here the following two general questions: which other phases can be sustained by the electronic polymers and how are they affected by the quenched disorder in the system and by the temperature. In this chapter we provide a Monte Carlo study which shows a rich phase diagram for the electronic polymers as a function of temperature and disorder and allows to rationalize the charge and the spin response observed experimentally.

8.1 Technical details of our MC simulations

The time unit of our simulation is the 'MC step per particle' (MCs) which corresponds to a number of MC moves equal to the total number of particles in our box. Since we are interested in the range of temperatures for which the opposite charged particles are bound in dipoles, each MC move is represented by an attempt to translate or rotate a randomly chosen dipole. The autocorrelation time τ is of the order of 4000 MCs. To

calculate the time averages, which coincide with the thermal average, we take the values of the physical quantities every $\tau/10$ MCs, and we form blocks containing 100 measures each one. Now each block is characterized by the average over these 100 measures. The values so obtained are certainly uncorrelated. Finally we can take the average of these values and the standard deviation, obtaining the value of the thermal average with the uncertainty. The thermalization time is chosen separately for each simulation looking at the history of the interesting physical quantities.

We perform our MC simulations using the parallel tempering method, described in sec. 4.3. Our simulation is characterized by 32 ranks (from 0 to 31) running in parallel. Each rank from 1 to 31 performs an independent MC simulation of a randomly initialized copy of the system, at a different temperature. Then, in order to make configurations at high temperatures available to the simulations at low temperatures and vice versa, the configurations at different temperatures are exchanged according to the Metropolis criterion. This swapping process is performed by the rank 0, i.e. the 'master rank'. A swapping move is proposed very often, more precisely every 5 MCs, since it is an operation with zero operational cost, being the configurations of two adjacent temperatures very overlapped. The swapping attempts is proposed between each pair of adjacent temperatures: alternatively according to the scheme $(1 \leftrightarrow 2, 3 \leftrightarrow 4, \ldots, 29 \leftrightarrow 30, 31 \leftrightarrow 31)$, and the scheme $(1 \leftrightarrow 1, 2 \leftrightarrow 3, 4 \leftrightarrow 5, \ldots, 30 \leftrightarrow 31)$.

As mentioned above, our transitions have a first-order character, so that the transition temperature constitutes a bottleneck. However the limited system size and the small increment ΔT between the neighbor temperatures make it possible the swapping moves at the critical temperature. Furthermore the increasing disorder lowers the first order character of the transitions and makes easier to cross the transition. Surely the parallel tempering method is not so efficient for our system but it allows us to escape from the local free energy minima that appear at low temperatures anyway. Fig. 8.1 shows how a fixed rank changes its temperature during the MC evolution. Despite a very high

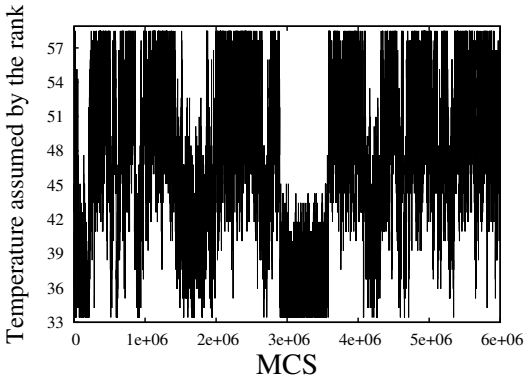

Figure 8.1: Rotation of temperatures in a fixed rank during the MC simulation of a slightly disordered system.

average swapping rate (~ 0.7), it displays a certain difficult to pass through the critical temperature (~ 44 K). However such round-trip time is enough to our purpose.

8.2 Characterizing the stable phases

8.2.1 Order parameters and statistical analysis

To characterize the stable phases of our system we must define a set of order parameters. In order to characterize the rotational C_4 symmetry breaking we define the nematic order parameter

$$\phi = \frac{1}{N_h} \sum_{\mathbf{r}_i} n(\mathbf{r}_i) n(\mathbf{r}_i + \hat{x} + \hat{y}) - n(\mathbf{r}_i + \hat{y}) n(\mathbf{r}_i + \hat{x}), \tag{8.1}$$

where $n(\mathbf{r}_i)$ is the occupation number (0 for an empty site and 1 for a occupied site) of the site $\mathbf{r}_i$. Then we define the polarization $\mathbf{P} = (P_x, P_y)$ as the normalized sum of all the TDs, in order to describe the inversion symmetry breaking. To take into account diagonal polarizations we must introduce the components

$$P_{(1,1)} = (P_x + P_y)/\sqrt{2} \tag{8.2a}$$

$$P_{(1,-1)} = (P_x - P_y)/\sqrt{2} \tag{8.2b}$$

To find the most stable phases at a given temperature we use the method explained in Ref.[2], according to which we construct an histogram over the MC history of the different order parameters. Since the probabilities of an order parameter value X is given by the Boltzmann's factor $\sim \exp(-F(X)/T)$ with F the free-energy, finding the position X of the maximum of the histogram is equivalent to minimize the free-energy and identifies the more stable phase. Now each MC generated configuration can be characterized by the instantaneous value of the three main order parameters $(P_{(1,1)}, P_{(1,-1)}, \phi)$, so that X represents a point in a three-dimensional (3D) space. Other order parameters which will be important to characterize the phases (charge ordering, spin vector chirality) will be introduced below. If we consider the clean system ($\eta = 0$), due to the symmetries in the Hamiltonian for a generic point there are seven other points that correspond to distinct configurations with the same energy. The symmetries are the reflection around the $P_{(1,1)} = 0$ and $P_{(1,-1)} = 0$ planes and the reflection with respect to the $\phi = 0$ plane followed by a 90 degrees rotation respect to the ϕ axis. This last rotation is due to the fact that the sign of ϕ is linked to the direction of the segments. So we can improve the statistics by a factor eight. When we take disorder into account, these symmetries are no longer valid. The only symmetry preserved is the simultaneous reflection around the planes $P_{(1,1)} = 0$ and $P_{(1,-1)} = 0$. Each different phase is characterized by a denser "cloud" of points in different regions of the 3D space. In order to characterize these different phases, we compute the 3D density distribution of points at each temperature of the simulation. This distribution can be visualized by plotting isosurfaces with a given number of points per unit volume. As an example we report in Fig.8.2 this type of analysis for a phase with broken rotational and inversion symmetries and a disordered phase in the clean system. Since at low temperature (Fig.8.2(a)) the highest density of points occurs inside the two regions around $\phi \sim +1$, and $P_{(1,1)} \sim \pm 1$, and the two regions

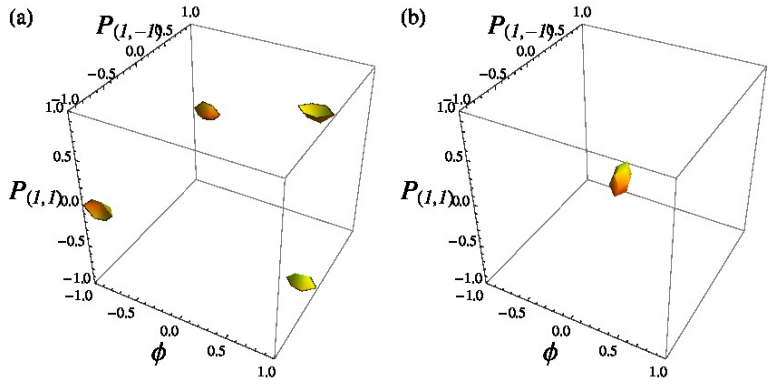

Figure 8.2: Example of an MC simulation of the clean system for (a) $T = 38$ K and (b) $T = 50$ K, respectively. Statistically independent points where binned according to the value of the three order parameters $(P_{(1,1)}, P_{(1,-1)}, \phi)$ in 17 bins per each side (totally 4913 cells). An isosurface with 500 points per bin is plotted.

around $\phi \sim -1$, and $P_{(1,-1)} \sim \pm 1$, this phase is identified as ferrosmectic or ferronematic depending on the presence of charge ordering, which can be checked only from the charge structure factor (see sec.8.2.2). At high temperature (Fig.8.2(b)) the densest cloud of points occurs in correspondence of the zero value of the three order parameters. So this phase is clearly disordered.

If we apply the analysis explained above to the MC results of a simulation with a given value of the disorder ($\eta > 0$), the 3D plots are not so clear as in the clean case. To simplify the analysis we consider only the plane $P_{(1,-1)} = constant$ or $P_{(1,1)} = constant$ (depending on the sign of the nematic parameter) corresponding to the bin which contains the highest number of points. Typically when the nematic parameter has a well defined sign, if we look at corresponding polarization, the other is zero. So if $\phi > 0$, we take the plane $P_{(1,-1)} = 0$ and on this plane we construct a new 2D histogram, whose axes are ϕ and $P_{(1,1)}$, in order to find the order parameters values of the stable phase. This is the procedure which we have used to characterize the phase transition in our system An example can be found in Fig.8.3, where we report such a type of analysis for a MC simulation of a system with $\eta = 0.125$. While for $T = 43$ K the most stable phase is characterized by $\phi \sim 0.4$ and $P_{(1,1)} \sim \pm 0.6$, for $T = 45$ K the values of the order parameters which minimize the free energy are zero. Such an abrupt change of the order parameter in a narrow temperature range clearly indicates a first-order phase transition.

To describe a phase transition we must look at the dependence of the order parameters on the temperature. To do it, we can follow the position of the maximum in the 3D space for each temperature. This method yields sharper transitions than following the thermal average which, in our system sizes, often is not enough to resolve closely separated transitions.

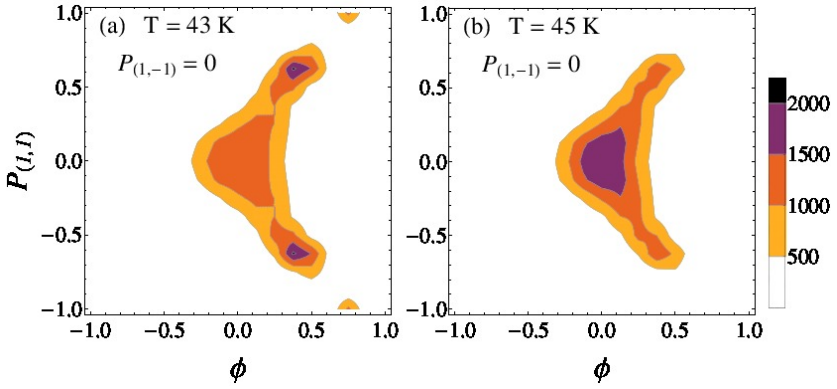

Figure 8.3: Contour plots of the histogram in the two-dimensional space $[\phi, P_{1,1}]$ characterized by the plane $P_{1,-1} = 0$ (data binned in 17 cells per each side). Moderately disordered case, $\eta = 0.125$, is shown. Passing from the panel (a) to panel (b) the temperature increases and the ferronematic order is destroyed like it can be seen from the maximum of the histogram which is shifted towards zero values of the order parameters.

8.2.2 Charge and spin ordering

If we know the charge distribution $n(\mathbf{r}_i)$ for a given configuration arising from MC simulations, we can reconstruct the spin distribution $\mathbf{S}(\mathbf{r}_i) = S(\cos\theta(\mathbf{r}_i), \sin\theta(\mathbf{r}_i))$. Although our effective lattice gas model is based on the validity of the linear superposition principle we can partially take into account non linear effects fixing the topological charges according to a snapshot of a Monte Carlo simulation and then performing an energy minimization of the XY spins. Clearly this procedure is not self-consistent however we expect that the errors introduced are not large. Indeed since the saddle point configurations are stationary first order errors in the spin configurations, they give rise to only second order errors in the energies. So we attach to each TC the spin-phase structure of a spin (anti)vortex and we perform a linear superposition allowing each spin to relax according to the XY-model hamiltonian. We use a unitary antiferromagnetic coupling J between nearest-neighbor spins and a further antiferromagnetic coupling J' across each TC to stabilize the antiphase across a TD, as shown in Fig.6.13. We set $J'/J = 1$.

As explained in chapter 6 each TD implies an offset between the spin-phases at the boundaries of the lattice. With many TDs aligned this offset can become of the order of 2π favoring one or more spin-spirals. If m_x and m_y represent the horizontal and vertical lattice winding numbers respectively, i.e. the number of spirals in the two directions, the spin-phase distribution due to a collection of TDs can be written as

$$\theta_{m_x,m_y}(x,y) = \vartheta(x,y) + \frac{2m_x\pi x}{L} + \frac{2m_y\pi y}{L}, \tag{8.3}$$

where $\vartheta(x,y)$ is the result of the linear superposition of the spin field generated by each (anti)vortex. Now the spin relaxation must be performed for a range of values both for m_x and m_y. The 'ideal' winding numbers are those corresponding to the lowest value of $\theta_{m_x,m_y}(x,y)$.

To identify the spin and charge ordering we take from the MC calculations the thermal averages of the static charge (c) and spin (s) structure factors $\mathcal{S}_c(\mathbf{q}) = (1-\delta_{\mathbf{q},0})|K_c(\mathbf{q})|^2/L^2$ and $\mathcal{S}_s(\mathbf{q}) = |\mathbf{K}_s(\mathbf{q})|^2/L^2$, where

$$K_c(\mathbf{q}) = \frac{1}{\sqrt{N_h}} \sum_{\mathbf{r}_i} \exp(i\mathbf{q}\cdot\mathbf{r}_i)\, n(\mathbf{r}_i) \tag{8.4}$$

$$\mathbf{K}_s(\mathbf{q}) = \frac{1}{\sqrt{L^2}} \sum_{\mathbf{r}_i} \exp(i\mathbf{q}\cdot\mathbf{r}_i)\, \mathbf{S}(\mathbf{r}_i) \tag{8.5}$$

with the sum running over all the lattice sites, N_h denoting the total number of charges. Here, $n(\mathbf{r}_i)$ and $\mathbf{S}(\mathbf{r}_i)$ are the local occupation number and the local spin, respectively. With these definitions (and using unit-length spins), the structure factors have the same normalization and satisfy $\sum_{\mathbf{q}} \mathcal{S}_{s,c}(\mathbf{q}) = 1-n_h$. An analytical derivation of these quantities is reported in Appendix E.

A nematic (smectic) state is characterized by $\phi \neq 0$ and a charge structure factor not peaked (peaked) at non-zero $\mathbf{q}$. Ferronematic or ferrosmectic order are characterized by a finite polarization $\mathbf{P}$. As discussed in the previous chapters the ferronematic state implies a spin ordering characterized by an incommensurate peak of the spin structure factor.

8.3 Monte Carlo Results

In this section a detailed analysis of the MC results first for the clean system ($\eta = 0$) and then for the disordered system ($\eta > 0$) is reported.

8.3.1 Clean system

At high temperatures the MC computations show a classical liquid of dimers which tend to form long polymers as the temperature is lowered and to align along the diagonal direction which is energetically more favorable. Fig. 8.4(a) shows a snapshot of this high-temperature phase taken during the MC evolution, where both the charge and spin phase distribution have been reported. We can see a disordered mixture of segments of various length embedded in a disordered antiferromagnetically correlated spin texture with antiphase ordering across the segments.

When T is low enough the segments orient to form a state with C_4 symmetry breaking. However as it is clearly visible in Fig. 8.4(b), the low-T phase is not the ferronematic state of Fig. 6.15(a). Associating the segments with "polymers", this state corresponds to the so-called smectic order of soft matter [3] in which the system has long-range positional order in one direction, with periodicity $l_c = 2\pi/q_c$, but remains liquid in the transverse direction. This manifests as sharp peaks in the charge structure factor along the diagonal of the Brillouin zone (see central panel of Fig. 8.6 and Fig. 8.7(a)), i.e. perpendicular to the preferred polymer direction. Regarding the charge ordering this state has the same symmetry as a diagonal stripe state, however, the charge is uniform along the stripe direction only after thermal fluctuations have been taken into account. In addition, this

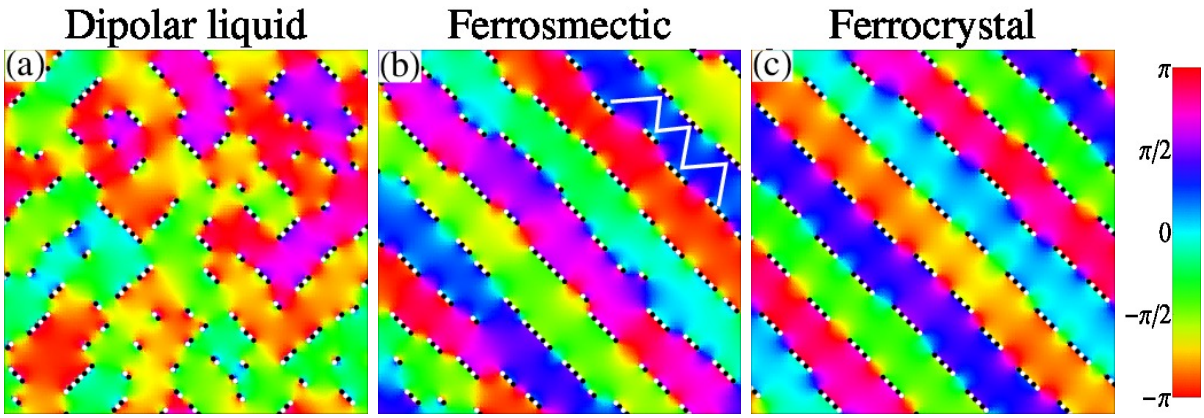

Figure 8.4: Snapshots of the charge and spin configuration in the absence of quenched disorder in the thermally disordered phase ($T = 50K$, panel a), in the ferrosmectic phase ($T = 38K$, panel b) and in the ferrocrystal state ($T = 8K$, panel c). White and black circles represent the positive and negative TCs, respectively. The different colors denote the spin phase angle in the range $[-\pi, \pi]$. The white lines in panel (b) highlight the 'triangular' arrangement of the segments.

state breaks inversion symmetry, i.e. TDs tend to point in the same direction, thus we call it "ferrosmectic".

The ferro ordering associated with this and other phases is not trivial. Indeed, in contrast to a cubic dipole lattice in three dimensions it would not occur if, for example, the dipoles are arranged on fixed positions on a square lattice. This is rooted in the two-dimensional dipole-dipole interaction which is ferroelectric when the TDs are in a nearly head-to-tail configuration, while it becomes antiferroelectric when the TDs are arranged side-by-side as explained in sec. 5.3. In our model the ferro tendency wins because the real Coulomb interaction between electrically charged holes favors short-range triangular arrangements of the segments, i.e., segments in one row tend to face gaps in the neighboring rows (see the white lines in Fig. 8.4(b)) so that the energetic contribution from side-by-side arrangements is reduced.

The colors in Fig. 8.4 show the phase of the local staggered magnetization calculated treating TCs as vortices and antivortices within XY-model. In (b) and (c) the phase increases monotonously along one diagonal indicating that these states have vector chiral order. i.e. $\chi_{1,\pm 1} = \langle [\mathbf{S}_{\mathbf{r}_i} \times \mathbf{S}_{\mathbf{r}_i + \hat{x} \pm \hat{y}}] \cdot \hat{z} \rangle \neq 0$ where the angular brackets include a thermal and spatial average. To better visualize the magnetic structure of the ferrosmectic state we report in Fig. 8.5 the zoom of a limited region of our lattice during the MC evolution of the clean system, for $T = 38$ K. In particular the two panels show (left panel) the charge and spin configuration (we use staggered spins), and (right panel) the spin current, calculated treating the TCs as spin vortices and antivortices within the XY-model. These panels show how the charge and spin channels are strictly connected. The first picture shows a clear inversion symmetry braking due to the polarized segments. Furthermore, looking at the spin texture resulting from the disposition of the TCs, it can be noticed that each

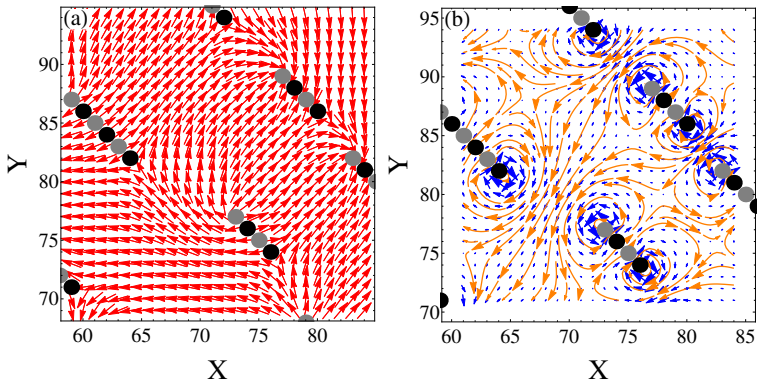

Figure 8.5: (a) Configuration of the selected region for $T = 38$ K: the positive and the negative TCs are represented respectively by gray open circles and black open circles. The red arrows in the left panel, are the staggered spins in each site. (b) Schematic representation of the spin current: the blue arrow in each site is the average value of the currents in the four bonds connecting the site with its nearest neighbors. The orange streamlines show the general trend of the overall current.

segment generates an anti-phase domain, i.e. a jump of π in the phase of the spins. Panel (b) is a representation of the spin current. The latter is a quantity defined in each bond as $I_{ij} = J_{ij}(\mathbf{S}_i \times \mathbf{S}_j) \cdot \hat{\mathbf{z}}$, and its spatial average is a measure of the parameter χ. In the panel it is represented in each site as the average value of the currents in the four bonds connecting the site with its nearest-neighbor sites. Since the spin current is a conserved quantity, we can define a vector field, which can be easily visualized by means of the flux lines. They are represented as orange curved arrows in Fig. 8.5(b), and show manifestly the inversion symmetry breaking in the spin channel.

Upon further lowering the temperature the ferrosmectic phase keeps the ferro ordering (and the vector spin chirality) but forms a Wigner crystal for $T \lesssim 10\,\mathrm{K}$ (see Fig. 8.4(c)). This "ferrocrystal" manifests as additional off-diagonal peaks on the charge structure factor (see right panel of Fig. 8.6).

As shown in Fig. 8.7, which reports a detailed comparison between the diagonal cut of the charge and the spin structure factor for a set of temperatures, the main spin peak (marked by a green point in the panels of Fig.8.6) is twenty times higher than the charge peak, because the spectral weight of the latter is spread over a wider range of wavevectors, due to the very unharmonic charge distribution, which has a step-like form.

We can see that the magnetic peak appears at half the wave-vector of the main charge peaks. At first sight, this relation, which is well known for spin collinear stripes [4, 5, 6], is surprising here since the incommensurability should be linked to the topological polarization, according to what said in the previous chapter. However, close inspection of Fig. 8.4(b) reveals that each chain locally acts as an antiphase domain wall for the AF background which yields jumps of the magnetic order parameter close to π upon crossing the line of polymers. On the other hand the phase is approximately constant in between two polymer rows. Thus effectively the magnetization behaves very similar as in collinear

stripe array and at the same time is proportional to the topological polarization. Spin canting produces small corrections to the 'factor of two' relation, which are below our momentum resolution to be visible in Figs. 8.6 and 8.7.

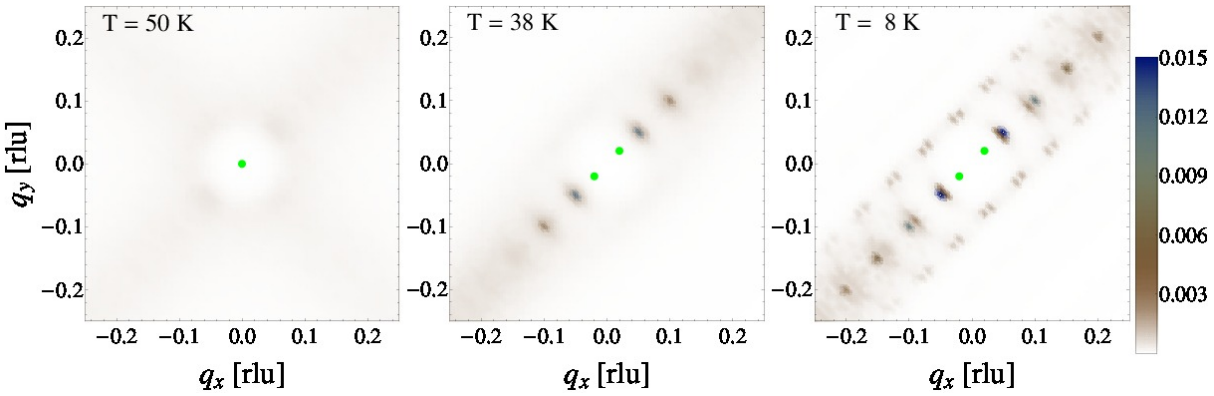

Figure 8.6: Density plot of the charge structure factor in the 2D reciprocal space for (left) $T = 50$ K, (center) $T = 38$ K and (right) $T = 8$ K. The green points represent the position of the peaks of the spin structure factor, shifted by the vector $\mathbf{q}_{AF} = \left(\frac{1}{2}, \frac{1}{2}\right)$.

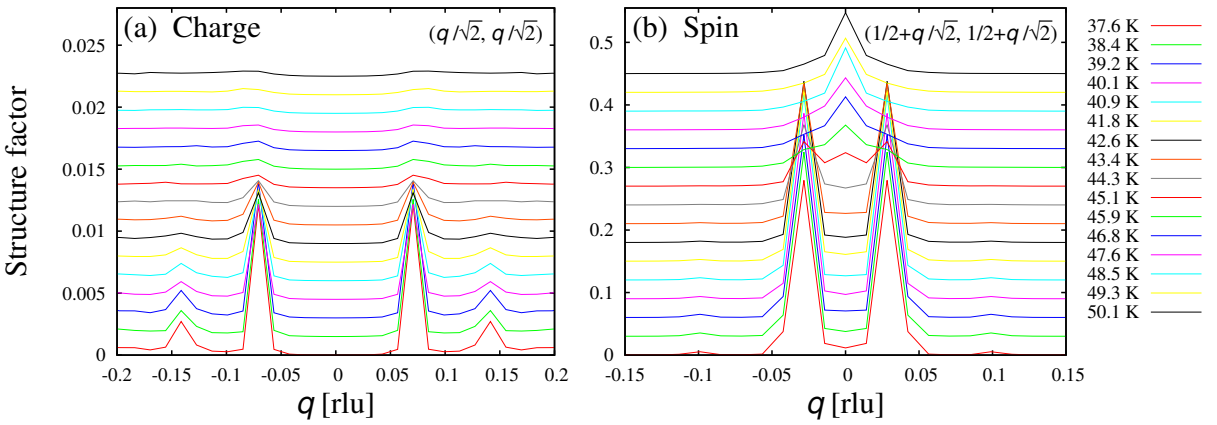

Figure 8.7: Diagonal cut of the (a) charge and (b) spin structure factors for a range of temperatures. Going up within the panels the temperature increases.

To study how the configurations change with the temperature, and the corresponding phase transitions we use the histogram method explained in sec. 8.2.1: for each temperature, the values of $P_{(1,1)}$ (or $P_{(1,-1)}$) and ϕ corresponding to the maximum of the histogram is plotted. They are reported in the left panel of Fig. 8.8, together with the height of the main charge and spin peak as a function of temperature. The height of the peaks is measured with respect to spectral weight of the nearest q-points. In this way an high value of the height of the peak, suggests that it is very narrow and that the correlation length is larger than the system size. The height of the crystal peak at low temperatures

is reported too (by means of an inset). Watching at these plots we can find the critical temperature of the ferrosmectic transition ($\sim$ 45 K) and the critical temperature of the ferrocrystal transition ($\sim$ 10 K). They are marked with a vertical line. The right panel shows the thermal average of the same parameters whose dependence on temperature is rounded because of the size of our lattice. Also the average number of charges per segment is plotted in a wide range of temperature. We can see that at each phase transition, this number increases more rapidly and then it saturates.

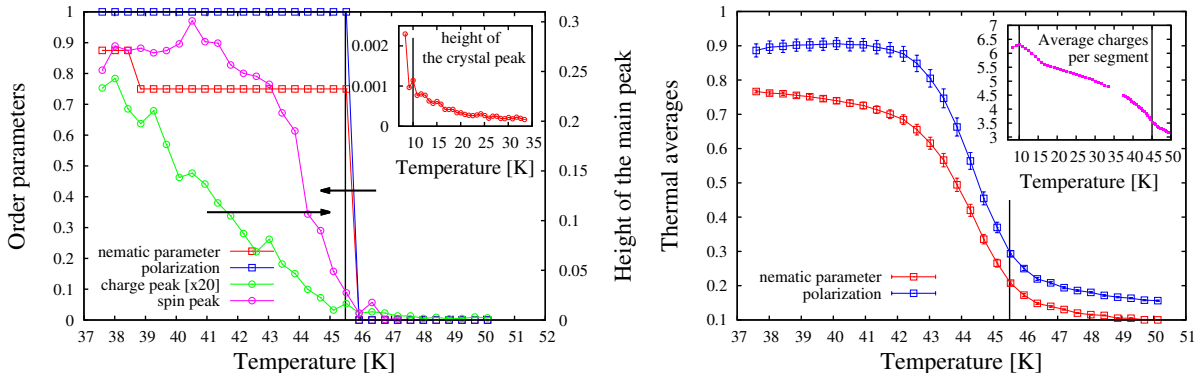

Figure 8.8: Main order parameters as a function of temperature. The left panel reports the value of the (red) nematic parameter and (blue) polarization, corresponding to the maximum of the histogram. Also the height of the main (green) charge and (magenta) spin peak is plotted. The inset shows the height of the crystal peak in a window of very low temperatures. The right panel shows the thermal average of the parameters. Also the average number of charges per segment is reported in a wide range of temperatures.

8.3.2 Effects of the quenched disorder

Since a crucial problem in cuprates is to determine how disorder affects the ordered phases of the ideal clean system [7], we turn on the Sr-disorder potential whose strength is measured by the parameter $\eta = Q_{\rm Sr}/Q_{rep}$. The symmetry of the phases changes dramatically. As disorder increases the ferrosmectic and ferrocrystal peaks broaden and weaken very rapidly (see Fig. 8.10), thus long-range positional order is lost and the ferrosmectic-ferrocrystal transition is smeared. Remarkably long-range nematic and vector chiral order (accompanied by inversion symmetry breaking) remain at finite disorder and the phase become the ferronematic state proposed in Ref. [8] and shown in Fig. 6.15. A snapshot captured during the MC evolution for $\eta = 0.125$ is shown in Fig. 8.9.

The charge structure factor in the 2D reciprocal space for $T = 38$ K, and $T = 8$ K, and disorder $\eta = 0.125$, is reported in Fig. 8.10. The temperature dependence of the cut along diagonal direction of the charge and spin structure factors are reported in Fig. 8.11, for three value of η. Fig. 8.10 and the top panels of Fig. 8.11 show how the charge ordering is almost entirely destroyed by small disorder. Long-range spin order also is destroyed but short-range spin order, signaled by incommensurate peaks with wave-

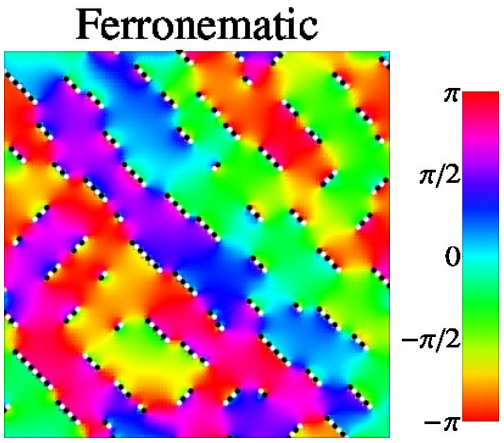

Figure 8.9: Snapshot of the charge and spin configuration for $\eta = 0.125$ and $T = 38$ K. White and black circles represent the positive and negative TCs, respectively. The different colors denote the spin phase angle in the range $[-\pi, \pi]$. It represents a ferronematic configuration.

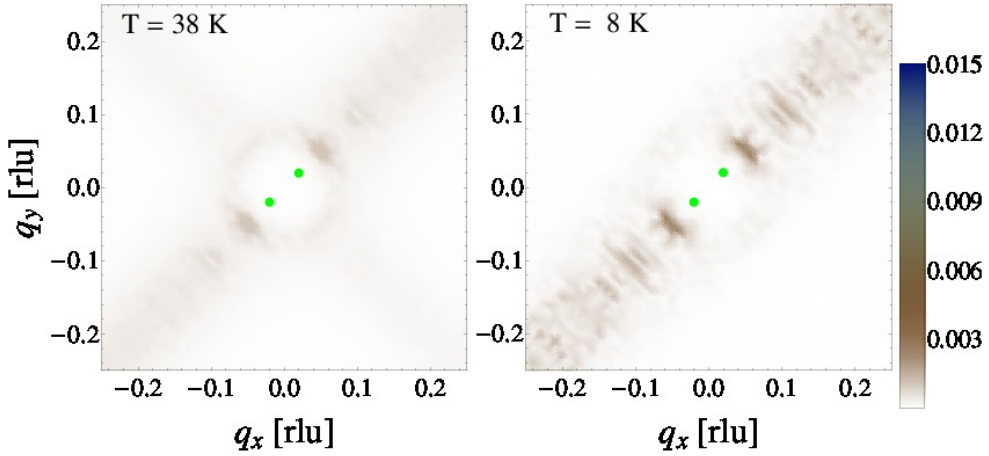

Figure 8.10: Density plot of the charge structure factor in the 2D reciprocal space for (left) $T = 38$ K, and (right) $T = 8$ K, calculated for $\eta = 0.125$. The green points represent the position of the peaks of the spin structure factor, shifted by the vector $\mathbf{q}_{AF} = \left(\frac{1}{2}, \frac{1}{2}\right)$.

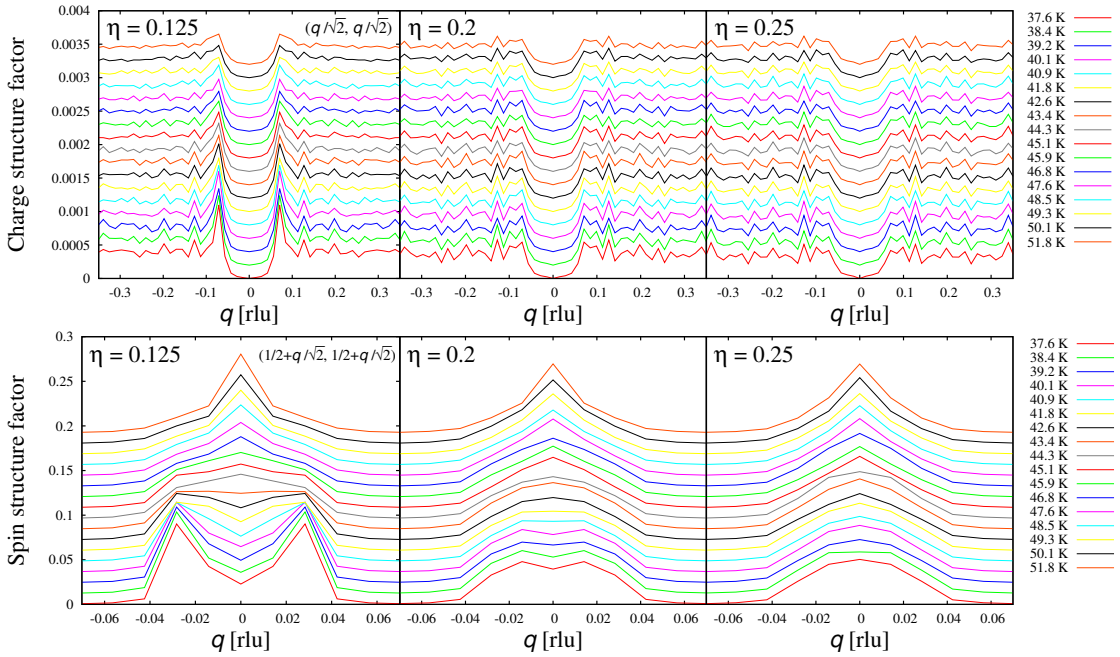

Figure 8.11: Diagonal cut of (first row) the charge structure factor, (second row) the spin structure factor, for a set of temperatures. The three panels in each row represent three different value of the disorder strength, $\eta = 0.125, 0.2, 0.25$. Going up within the panels the temperature increases.

vector $\mathbf{q}_{AF} \pm (\epsilon/\sqrt{2}, \epsilon/\sqrt{2})$ r.l.u., persists (ϵ being the magnetic incommensurability). These peaks are ~ 3 times lower than in the clean case and their width is well resolved in our system size, (see the bottom panels of Fig. 8.11). For $\eta > 0.2$ even the broad incommensurate magnetic peaks disappear. This would contradict experiments, we thus estimate $\eta < 0.2$ in real systems.

For the case $\eta = 0.125$, which is the most studied value of η, exhibiting well resolved spin peaks and very weak charge peaks distinguished from the noise (~ 10 times lower than in the clean case), we show in Fig. 8.12 the main order parameters as a function of temperature, together with the temperature dependence of the spin structure factors convoluted with a Gaussian in order to take into account the finite experimental resolution. Notice that, raising the temperature at small disorder, the broadened spin and charge peaks gradually decrease [see Fig. 8.12(a)] without any sign of a sharp transition in the intensity [Fig. 8.12(b) and Fig. 8.12(c), respectively] as also observed experimentally at similar dopings [see inset of Fig. 8.12(b) and Ref. [10]], and in the average length of the segments [Fig. 8.12(c)]. In contrast studying the polarization and nematic order parameter distribution we find that the transition from the ferronematic to the melted polymers is of first order and remains sharp for our system size. This is shown by the histograms in Fig. 8.3. Notice that in a narrow temperature range (~ 44 K) the maximum of the distribution shifts from a finite value of the polarization and the nematicity to a maximum at zero for the disordered phase. Thus a thermodynamic transition persists

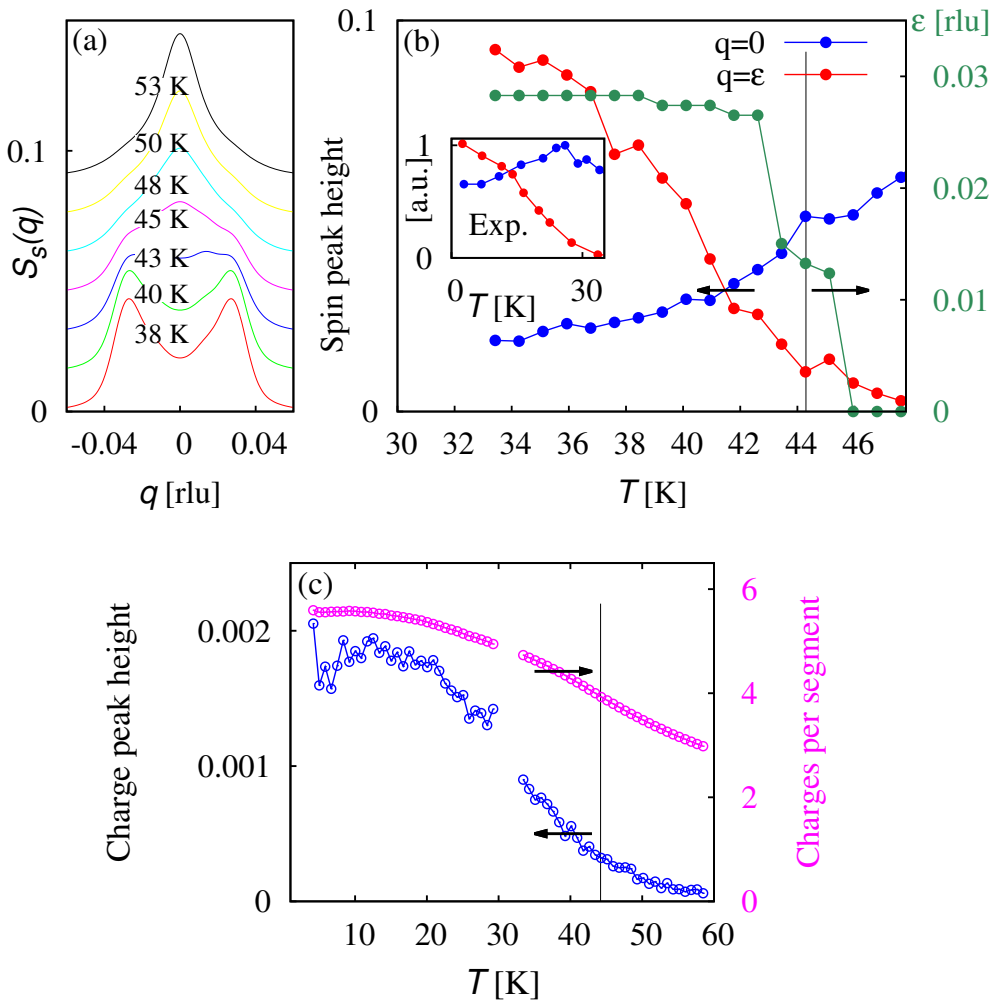

Figure 8.12: Temperature dependence of the main order parameters for disorder $\eta = 0.125$. (a) Diagonal cuts of the spin structure factor for different temperatures as a function of momentum with q defined as in the bottom panels of Fig. 8.11. The peaks have been convoluted with a Gaussian (standard deviation 0.041 [rlu]) to take into account a finite experimental resolution. (b) Height of the spin structure factor at the commensurate antiferromagnetic wave-vector (blue) and at the incommensurate position respect to the background (red) as a function of temperature. The green data (right scale) shows the incommensurability ϵ as a function of temperature. The vertical line marks the ferronematic transition. The inset shows the experimental peaks height from Ref. [9] for doping $n_h = 0.0192$, slightly below the complete disappearance of static antiferromagnetic order as revealed by muons. The evolution of the incommensurate peaks has been shown to be continuous [10] across the critical doping $n_h = 0.02$. (c) Temperature dependence of the main charge peak (blue) and the average charges per segment which coincides with the average length divided by $\sqrt{2}$.

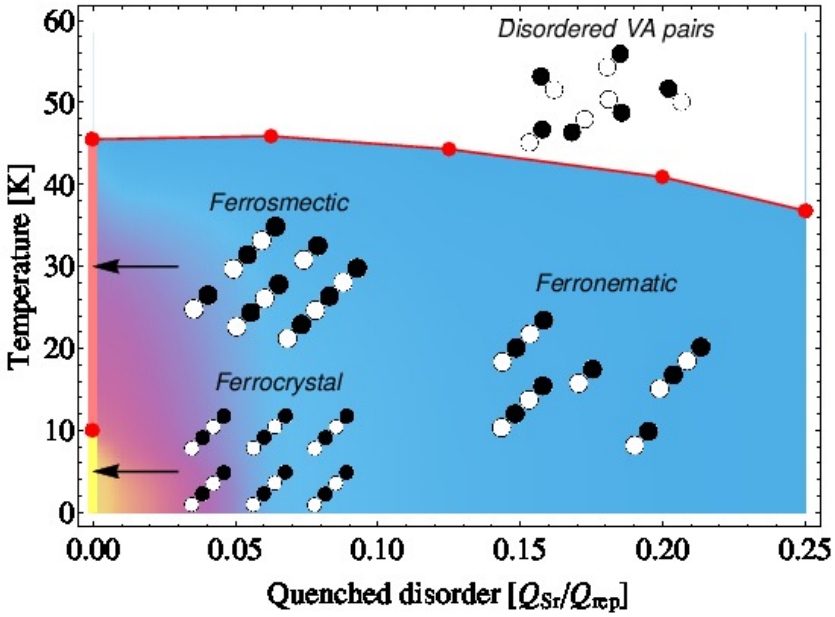

Figure 8.13: Phase diagram as a function of temperature and disorder strength. The yellow (pink) line at zero disorder corresponds to ferrocrystal (ferrosmectic) long-range order. The yellow region is short-range ferrocrystal order while the magenta region corresponds to the short-range ferrosmectic order. At finite disorder below the red line the system has long-range ferronematic order while a polymeric liquid is found above the red line within the temperatures of our study.

even in the presence of disorder. The thermodynamic transition temperature is signaled by a change of behavior in the magnetic structure factor from commensurate to incommensurate [Fig. 8.12(a)], providing a simple experimental tool to detect the transition line. This is because the incommensurability is related to the degree of polarization in the system as described in sec. 6.3, and thus acts as an order parameter.

Fig. 8.13 reports the phase diagram obtained from the above analysis. The ferrocrystal (thick yellow line) and ferrosmectic (thick pink line) phases are well defined only in the absence of disorder. At finite disorder, they survive as short-range order states. This is indicated by the yellow region for the ferrocrystal and by the magenta region for the ferrosmectic. The light blue region is the long-range ordered ferronematic state, while the red line indicates the first-order transition to a liquid of short polymers. We never found a purely nematic phase, characterized by a non-zero nematic order parameter but zero polarization and zero global vector chiral spin order (like the phase shown in Fig. 6.15(b)). This plain nematic phase, which is allowed by our model, can possibly be stabilized in a different parameter regime, as an intermediate phase between the ferronematic and the disordered phase.

Our results are in good qualitative agreement with the phase diagram obtained by completely different methods in Ref. [7]. On the other hand, we find an additional inversion symmetry breaking and we provide realistic estimates of the parameters of the

model, of the experimentally measurable structure factors and of the characteristic temperatures of the transitions. Both ferrosmectic and ferrocrystal charge orderings are not commensurate. Thus, they break a continuous [U(1)] symmetry in two dimensions. Even in the presence of infinitesimal disorder, long-range order is forbidden [11] and only short-range order is possible. In contrast, the nematic order parameter breaks a discrete (Z_2) symmetry and is much more robust against disorder. In our computations we have in addition vector chiral spin order (or equivalently a topological polarization) which also breaks a discrete (Z_2) symmetry, but which does not couple linearly to the local disorder, in contrast to the nematic order parameter [12, 13]. General arguments indicate that the discrete symmetry breaking should be much more robust than the breaking of a continuous symmetry [7, 14], as we indeed find. We expect the nematic order to behave similarly to the random field Ising model: without long-range order in a strictly 2D system, but ordered within a correlation length which can be exponentially large for small disorder [15], favoring a crossover to three-dimensional long-range order in the presence of a small finite inter-layer coupling [12, 16].

Fluctuating nematic domains

During the MC evolution the system explores both the nematic configurations: segments aligned in the $(1,1)$ direction ($\phi > 0$), and segments aligned in the $(1,-1)$ direction ($\phi < 0$). In the clean system we can use symmetry to put together the two cases (increasing the statistics by a factor two): $\phi \to -\phi$ provided the two polarizations are exchanged, $P_{(1,1)} \to P_{(1,-1)}$ and $P_{(1,-1)} \to P_{(1,1)}$. When we put disorder in our system, this symmetry does not hold any more. However we can put together each configuration ϕ with the corresponding $-\phi$ anyway, assuming that they represent two different configurations of disorder (related by a 90^0 rotation). But, while in the clean case the system tends to order according a unique nematic domain, for $\eta \neq 0$ we can find several nematic domains of different orientation, even if the sign of ϕ remains well defined. Indeed the overall nematic parameter is given by the algebraic summation of the nematic parameters of all regions, which have typically different size. For this reason, if we look at the charge structure factor just above the ordering temperature, we can see a marked structure along the diagonal corresponding to the main nematic domain, and a less intense structure along the other diagonal, as shown in the left panel of Fig. 8.14. The right panel shows the height of the main charge peak along the diagonal $(1,-1)$, which displays a weaker structure. It suggests that, above the critical temperature, the segments start to align in both directions until the phase transition forces them to choose a preferred nematic orientation. So the maximum of the curve in Fig. 8.14 can be a measure of the fluctuations of the system.

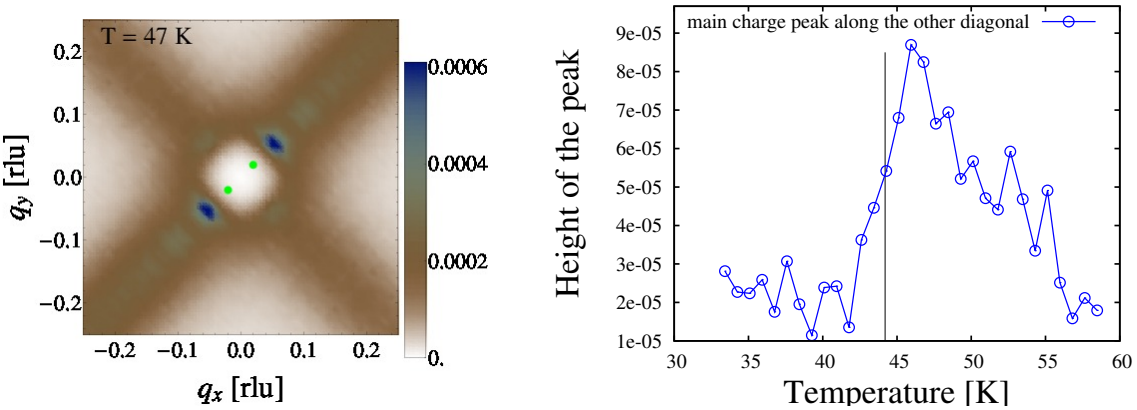

Figure 8.14: Left panel: Density plot of the charge structure factor in the 2D reciprocal space for $\eta = 0.0625$ and $T = 47$ K. Right panel: Height of the main charge peak of the diagonal $(1, -1)$ as a function of temperature.

Bibliography

[1] C. Timm and K. Bennemann, Phys. Rev. Lett. **84**, 4994 (2000).

[2] M. Capati, M. Grilli, J. Lorenzana, Phys. Rev. B **84**, 214520 (2011).

[3] P. M. Chaikin and T. C. Lubensky, *Principles of condensed matter physics*. (Cambridge University Press, 1995).

[4] J. Lorenzana and G. Seibold, Phys. Rev. Lett. **89**, 136401 (2002).

[5] J. Lorenzana and G. Seibold, Phys. Rev. Lett. **90**, 066404 (2003).

[6] G. Seibold and J. Lorenzana, Phys. Rev. Lett. **94**, 107006 (2005).

[7] L. Nie, G. Tarjus, S. A. Kivelson, Proc. Nat. Ac. Sci. **111**, 7980 (2014).

[8] G. Seibold, M. Capati, C. Di Castro, M. Grilli, J. Lorenzana, Phys. Rev. B **87**, 035138 (2013).

[9] G. Drachuck, E. Razzoli, G. Bazalitski, A. Kanigel, C. Niedermayer, M. Shi, Amit Karen, Nature Comm. **5**, 3390 (2013).

[10] M. Matsuda, *et al.*, Phys. Rev. B **65**, 134515 (2002).

[11] Y. Imry and S. K. Ma, Phys. Rev. Lett. **35**, 1399 (1975).

[12] B. Phillabaum, *et al.*, Nature Commun. **3**, 915 (2012).

[13] E. W. Carlson, *et al.*, Phys. Rev. Lett. **96**, 097003 (2006).

[14] P. Chandra, P. Coleman, A. I. Larkin, Phys. Rev. Lett. **64**, 88 (1990).

[15] K. Binder, Z. Phys. B **50**, 343 (1983).

[16] O. Zachar and I. Zaliznyak, Phys. Rev. Lett. **91**, 036401 (2003).

Conclusions

Our results allow to rationalize several experimental findings, and imply some predictions which have not yet been tested.

Experiments show that hole doping destroys commensurate antiferromagnetic order much more rapidly than what would be expected by dilution [1, 2]. Fig. 8.11, shows that this is explained by a small density of TDs and quenched disorder. The ability of VA pairs to rapidly depress commensurate ordering was noticed before [3, 4], although these authors did not considered the collective ordering of the dipoles.

Incommensurate spin scattering has been detected in the early days of high-T_c [5] and interpreted in terms of stripes [6, 7]. However, stripes are associated with charge modulations which are extremely hard to measure, in contrast to spin modulations. Charge ordering generally emerges associated with a structural distortion close to $n_h = 1/8$ which can be controlled by codoping with Nd [6, 7] or doping/codoping with Ba [8, 9, 10]. As mentioned in chapter 1, all these observation of charge ordering are at doping close to $n_h = 1/8$. The intensity of charge ordering decreases strongly with underdoping and extrapolates to zero around $n_h \approx 0.09$ [10]. To the best of our knowledge, incommensurate static charge order has never been reported in the present heavily underdoped region, in contrast to incommensurate spin order [11], which persists. This dichotomy is explained by our simulations which, while reproducing the incommensurate spin ordering, show very weak charge-ordering peaks, barely emerging from the background noise, even for weak disorder (see Fig. 8.11).

Close to $n_h = 1/8$ magnetic Bragg peaks appear quite sharp and often resolution limited [7, 12, 10] indicating long-range order. As doping is reduced static peaks are still observed but become broad with a well resolved width of the order of the incommensurability indicating a correlation length of the order of the spin periodicity [11, 10]. This is in excellent agreement with our magnetic structure factor in Fig. 8.11. We interpret this feature as an indirect signature of long-range vector chiral spin order without long-range magnetic order i.e. the ferronematic state we propose. For $n_h = 0.03$, experimental magnetic peaks have been detected with incommensurability $\epsilon \approx 0.032$ [13] in good agreement with our computations yielding $\epsilon \approx 0.028$ at low temperature.

Neutron scattering experiments in Y-based materials have shown [14] that the magnetic incommensurability as a function of temperature behaves as an order parameter. Such a behavior is naturally explained by our model, where the incommensurability, in the presence of weak or no CO, is closely linked to the topological polarization [15], which is an order parameter (see Fig. 8.12). Furthermore we propose that the temperature where

the static magnetic structure factor changes from a double peak structure to a single peak structure corresponds a thermodynamic phase transition. Below this temperature long-range chiral spin order is established.

The transition from incommensurate behavior to commensurate Neél behavior upon increasing temperature, has been observed also in the specific La-family we focus on in the present computations. Indeed experimental low-energy inelastic neutron scattering peaks as a function of temperature reported in Ref. [16] and in Fig. 1.13 (see also Ref. [11]) show the same behavior as we find for the static structure factor. However the transition from two incommensurate peaks to an antiferromagnetic commensurate peak takes place around $55 - 100$ K. On the other hand quasistatic scattering shows a transition at around 20K $\sim$30K [17, 13]. Our computations provide an energy integrated structure factor which is expected to show the transition between the inelastic and quasistatic cases. Indeed we find the commensurate-incommensurate transition at around 45 K fully consistent with the neutron scattering measurements.

Such an agreement on the temperature scales and qualitative behavior further supports our identification of the low temperature state observed in cuprates as a long-range-ordered ferronematic.

Notice that in contrast with the small ordering scales we find, the starting point electronic Hamiltonian has bare electronic scales of the order of 3000 K or more. This strong reduction of energy scales indicates that our multiscale modeling has identified the correct dynamical variables of the problem.

A question to which we want to provide an answer in this work, is whether the pseudogap is a signature of an ordered state with the pseudogap temperature representing the characteristic temperature of a real thermodynamic transition. Notice that the thermodynamic transition which we have found by means of our MC analysis, occurs at a temperature much lower than the pseudogap temperature (≈ 300 K) which instead nearly extrapolates to the Néel temperature of the undoped sample [18]. We can speculate that the pseudogap temperature represents the temperature at which the dopant holes, which form isolated spin polarons at high temperature, aggregate into bound VA pairs. However our effective model does not consider unpaired holes. Thus we have studied only temperatures much lower than the characteristic temperature of the unbinding process of the VA pairs (corresponding to the binding energy of a vortex and an antivortex).

At even lower temperatures of the proposed ferronematic transition a so called cluster spin glass state is observed consisting of strongly coupled clusters of spins with weaker coupling among clusters [1, 2, 17]. The ferronematic state of Fig. 8.9 corresponds precisely to this physical picture.

In the presence of spin-orbit coupling, long-range vector chiral spin order gives rise to a real electric polarization, i.e., the system becomes an improper ferroelectric [19]. Unfortunately, this effect is hard to observe because, as soon as the system becomes metallic, it cannot support a finite electric polarization. Notwithstanding, a finite ferroelectric polarization has been reported at low temperatures in oxygen [20] and Li [21] doped La_2CuO_4, the samples having a strongly insulating character. The fact that the effect appears independently of the dopant, and that the remnant polarization can be oriented along

different axes with external fields, clearly points to a magnetic origin of the ferroelectric polarization. Furthermore, more recent experiments show a clear correlation between magnetoelectric effects and stripe orientation in Sr doped La_2NiO_4, suggesting that stripe effects are involved [22]. Experiments at finite frequencies suggest that inversion symmetry breaking sets in at temperatures higher than the temperatures at which the sample is insulating enough to support a static polarization. All these experiments support our conclusion that underdoped cuprates show long-range vector chiral spin order.

A possible test to our model would require second harmonic generation to detect inversion symmetry breaking in non-insulating samples. We predict that in the ferronematic phase the inversion symmetry breaking should track the behavior of the incommensurability as a function of T. This relation, however, will break down in the collinear stripe phase found around $n_h = 1/8$.

With the present method we cannot access quantitatively the crossover to collinear stripes. In this regime, the mapping to the Coulomb gas breaks down due to nonlinear effects. One should also consider that our purely classical picture becomes questionable by increasing doping because of an increasing relevance of the fermionic degrees of freedom in the increasingly metallic state. However, one can anticipate that the average length of the segments will keep growing with doping, leading to a concomitant increase of the ferrosmectic correlation length. According to our findings, the disorder induced by the dopants will partially counteract this increase, but the associated impurity potential will also be progressively screened, opening the possibility that segments coalesce into stripes with long-range order and narrow magnetic peaks.

Although the classical picture breaks down by increasing doping and we cannot consider high concentrations of dopant holes, we have performed simulations for other values of doping, still in the strongly underdoped regime. The red squares in the right panel of Fig. 1.12 denote our results. We find that the incommensurability has a nearly linear dependence on the doping in good agreement with the Yamada plot.

We thus propose that underdoped cuprates have a long-range broken symmetry state at low doping. This puts the cuprate phase diagram into the same class of phase diagrams of a wide class of materials [23] in which unconventional superconductivity emerges from a phase characterized by real-space electronic long-range order.

Final considerations

Summarizing, in this thesis we have studied the complex phases of the underdoped cuprates trying to provide an explanation of the experimental evidences, in particular of the neutron scattering experiments. Starting from a microscopic quantum model, we have mapped it into a classical model, which allows us to investigate larger systems and we have used classical Monte Carlo techniques in order to characterize the broken symmetry phases and to study their temperature evolution. The central result of our work is the proposal and the characterization of a new ordered state, namely the ferronematic phase. This state breaks the discrete rotational symmetry and the inversion symmetry of the CuO_2

planes of the underdoped cuprates, and provides a spin response in good agreement with the neutron scattering experiments. We find that the occurrence of this phase is strictly connected to the presence of the quenched disorder which destroys almost entirely the long-range charge order of the 'clean' system, leaving only short-range charge correlations which disappear completely at higher disorder intensities. The good agreement with experiments both for what concerns the overall behavior of the main physical quantities and for what concerns the temperature scales of our phase diagram ($\sim 40\,\mathrm{K}$), suggests that our model can describe some of main physical aspects of the complex phases which occur in underdoped cuprates.

Our next goal is to understand how the polarized segments, which sustain a net spin current, become at higher doping infinite charged stripes which do not imply spin canting.

Bibliography

[1] J. H. Cho, F. Borsa, D. C. Johnston, and D. R. Torgeson, Phys. Rev. B **46**, 3179 (1992); F. C. Chou, F. Borsa, J. H. Cho, D. C. Johnston, A. Lascialfari, D. R. Torgeson, and J. Ziolo, Phys. Rev. Lett. 71, 2323 (1993);

[2] F. Coneri, S. Sanna, K. Zheng, J. Lord, and R. De Renzi, Phys. Rev. B **81**, 104507 (2010).

[3] A. Aharony, R. J. Birgeneau, A. Coniglio, M. A. Kastner, and H. E. Stanley, Phys. Rev. Lett. **60**, 1330 (1988).

[4] C. Timm and K. H. Bennemann, Phys. Rev. Lett. **84**, 4994 (2000).

[5] S-W. Cheong, *et al.*, Phys. Rev. Lett. **67**, 1791 (1991).

[6] J. M. Tranquada, B. J. Sternlieb, J. D. Axe, Y. Nakamura, and S. Uchida, Nature **375**, 561 (1995); J. M. Tranquada, J. D. Axe, N. Ichikawa, Y. Nakamura, S. Uchida, and B. Nachumi, Phys. Rev. B **54**, 7489 (1996).

[7] J. M. Tranquada, J. D. Axe, N. Ichikawa, A. R. Moodenbaugh, Y. Nakamura, and S. Uchida, Phys. Rev. Lett. **78**, 338 (1997).

[8] M. Fujita, *et al.*, Phys. Rev. Lett. **88**, 167008 (2002).

[9] P. Abbamonte, *et al.*, Nature Physics **1**, 155 (2005).

[10] M. Hücker, *et al.*, Phys. Rev. B **83**, 104506 (2011).

[11] M. Matsuda, *et al.*, Phys. Rev. B **62**, 9148 (2000).

[12] Kimura *et al.*, Phys. Rev. B **59**, 6517 (1999)

[13] M. Matsuda, *et al.*, Phys. Rev. B **65**, 134515 (2002).

[14] V. Hinkov, D. Haug, B. Fauqué, P. Bourges, Y. Sidis, A. Ivanov, C. Bernhard, C. T. Lin, and B. Keimer, Science **319**, 597 (2008); D. Haug, V. Hinkov, Y. Sidis, P. Bourges, N. B. Christensen, A. Ivanov, T. Keller, C. T. Lin, B. Keimer, New J. of Phys., **12**, 105006 (2010).

[15] G. Seibold, M. Capati, C. Di Castro, M. Grilli, and J. Lorenzana, Phys. Rev. B **87**, 035138 (2013); G. Seibold, C. Di Castro, M. Grilli and J. Lorenzana, Scientific Reports **4**, 5319 (2014).

[16] M. Matsuda, M. Fujita, S. Wakimoto, J. A. Fernandez-Baca, J. M. Tranquada, and K. Yamada, Phys. Rev. Lett. **101**, 197001 (2008).

[17] S. Wakimoto, S. Ueki, Y. Endoh, and K. Yamada, Phys. Rev. B **62**, 3547 (2000).

[18] Y. Ando, *et al.*, Phys. Rev. Lett. **93**, 267001 (2004).

[19] S.-W. Cheong and M. Mostovoy, Nature Materials **6**, 13 (2007).

[20] Z. Viskadourakis, I. Radulov, A. P. Petrović, S. Mukherjee, B. M. Andersen, G. Jelbert, N. S. Headings, S. M. Hayden, K. Kiefer, S. Landsgesell, D. N. Argyriou, and C. Panagopoulos, Phys. Rev. B **85**, 214502 (2012).

[21] Z. Viskadourakis, S. S. Sunku, S. Mukherjee, B. M. Andersen, T. Ito, T. Sasagawa and C. Panagopoulos, "Generic ferroelectric ground state and magnetoelectric coupling in underdoped La-214 cuprates", unpublished. Available from https://qcn.physics.uoc.gr/sites/files/qcn/Preprints/CCQCN-2014-14.pdf.

[22] C. Panagopoulos, private communication.

[23] L. Taillefer, Ann. Rev. Cond. Matt. Phys. **1**, 51 (2010);

Appendix A

Spin-rotational invariant form of the Gutzwiller approximation.

A detailed derivation of an approximate single-particle hamiltonian which obeys spin rotational invariance, is reported in Ref. [1]. In this section we list the main steps which lead to hamiltonian (2.68). As a first step, we define the local rotations in spin space by the following transformations

$$\boldsymbol{\chi}_i = \mathbf{U}_i^\dagger \boldsymbol{\Psi}_i \tag{A.1a}$$
$$\boldsymbol{\chi}_i^\dagger = \boldsymbol{\Psi}_i^\dagger \mathbf{U}_i, \tag{A.1b}$$

where the unitary transformation matrix is given by

$$\begin{aligned} \mathbf{U}_i &= \cos(\varphi_i/2)\mathbf{1} + i\sin(\varphi_i/2)\boldsymbol{\tau}\cdot\hat{\boldsymbol{\eta}} \\ &= \begin{pmatrix} \cos(\varphi_i/2) & \sin(\varphi_i/2)(\eta_y + i\eta_x) \\ -\sin(\varphi_i/2)(\eta_y - i\eta_x) & \cos(\varphi_i/2) \end{pmatrix} \end{aligned} \tag{A.2}$$

being $\hat{\boldsymbol{\eta}} = (\eta_x, \eta_y, 0)$ is the unitary rotation axis. The inverse transformation reads as

$$\boldsymbol{\Psi}_i = \mathbf{U}_i \boldsymbol{\chi}_i \tag{A.3a}$$
$$\boldsymbol{\Psi}_i^\dagger = \boldsymbol{\chi}_i^\dagger \mathbf{U}_i^\dagger. \tag{A.3b}$$

Now we require that the transformed spinor is given by $\tilde{\mathbf{S}}_i = (0, 0, \tilde{S}_i^z)$. So we have

$$S_i^x = \frac{1}{2}\boldsymbol{\Psi}_i^\dagger \tau_x \boldsymbol{\Psi}_i = \frac{1}{2}\boldsymbol{\chi}_i^\dagger \mathbf{U}_i^\dagger \tau_x \mathbf{U}_i \boldsymbol{\chi}_i = \frac{1}{2}\boldsymbol{\chi}_i^\dagger(-\eta_y \sin\varphi_i)\tau_z \boldsymbol{\chi}_i = -\eta_y \sin\varphi_i \, \tilde{S}_i^z; \tag{A.4a}$$
$$S_i^y = \frac{1}{2}\boldsymbol{\Psi}_i^\dagger \tau_y \boldsymbol{\Psi}_i = \frac{1}{2}\boldsymbol{\chi}_i^\dagger \mathbf{U}_i^\dagger \tau_y \mathbf{U}_i \boldsymbol{\chi}_i = \frac{1}{2}\boldsymbol{\chi}_i^\dagger(\eta_x \sin\varphi_i)\tau_z \boldsymbol{\chi}_i = \eta_x \sin\varphi_i \, \tilde{S}_i^z; \tag{A.4b}$$
$$S_i^z = \frac{1}{2}\boldsymbol{\Psi}_i^\dagger \tau_z \boldsymbol{\Psi}_i = \frac{1}{2}\boldsymbol{\chi}_i^\dagger \mathbf{U}_i^\dagger \tau_z \mathbf{U}_i \boldsymbol{\chi}_i = \frac{1}{2}\boldsymbol{\chi}_i^\dagger(\cos\varphi_i)\tau_z \boldsymbol{\chi}_i = \cos\varphi_i \, \tilde{S}_i^z. \tag{A.4c}$$

Since $\mathbf{U}_i^\dagger \mathbf{U}_i = \mathbf{1}$, the local charge

$$n_i = \boldsymbol{\Psi}_i^\dagger \boldsymbol{\Psi}_i = \boldsymbol{\chi}_i^\dagger \mathbf{U}_i^\dagger \mathbf{U}_i \boldsymbol{\chi}_i = \boldsymbol{\chi}_i^\dagger \mathbf{1} \boldsymbol{\chi}_i = \tilde{n}_i, \tag{A.5}$$

and thus also the interaction term $n_{i,\uparrow}n_{i,\downarrow} = \frac{1}{2}(n_i^2 - n_i)$ are not affected by the transformation. Since by definition transverse spin order vanishes in the rotated frame we can now, as a second step, apply the Kotliar-Ruckenstein slave-boson scheme:

$$\tilde{c}_{i\sigma} = z_{i\sigma}\tilde{f}_{i\sigma} \quad \tilde{c}^\dagger_{i\sigma} = z^\dagger_{i\sigma}\tilde{f}^\dagger_{i\sigma} \tag{A.6}$$

with

$$z_{i\sigma} = \frac{1}{\sqrt{e_i^\dagger e_i + p^\dagger_{i,-\sigma}p_{i,-\sigma}}}\left[e_i^\dagger p_{i\sigma} + p^\dagger_{i,-\sigma}d_i\right]\frac{1}{\sqrt{d_i^\dagger d_i + p^\dagger_{i,\sigma}p_{i,\sigma}}}. \tag{A.7}$$

The double (d), singly (p_σ), and empty (e_i) occupancy bosons are constrained by the following relations:

$$\sum_\sigma p^\dagger_{i,\sigma}p_{i,\sigma} + 2d_i^\dagger d_i = \sum_\sigma \tilde{f}^\dagger_{i,\sigma}\tilde{f}_{i,\sigma} = \tilde{n}_i = n_i \tag{A.8}$$

$$p^\dagger_{i,\uparrow}p_{i,\uparrow} - p^\dagger_{i,\downarrow}p_{i,\downarrow} = \tilde{n}_{i,\uparrow} - \tilde{n}_{i,\downarrow} = 2\tilde{S}_i^z = 2S_i^z/\cos(\varphi_i) \tag{A.9}$$

$$d_i^\dagger d_i + \sum_\sigma p^\dagger_{i,\sigma}p_{i,\sigma} + e_i^\dagger e_i = 1. \tag{A.10}$$

Since we follow essentially a Gutzwiller-type approach we now apply the mean-field approximation for the bosons. With help of Eqs. (A.8), (A.9) and (A.10) we can eliminate all bosons but d_i and express them via expectation values in the original reference frame. One finds

$$e_i^2 = 1 - n_i + d_i^2 \tag{A.11}$$

$$p^2_{i,\uparrow} = \frac{1}{2}n_i + \frac{\langle S_i^z\rangle}{\cos(\varphi_i)} - d_i^2 \tag{A.12}$$

$$p^2_{i,\downarrow} = \frac{1}{2}n_i - \frac{\langle S_i^z\rangle}{\cos(\varphi_i)} - d_i^2. \tag{A.13}$$

The original fermions operators in the rotate frame $\tilde{c}_{i,\sigma}$ are related to the Kotliar-Ruckenstein transformed ones $\tilde{f}_{i,\sigma}$ in the rotated frame, via the transformations (A.6), i.e.

$$\begin{pmatrix} \tilde{c}_{i,\uparrow} \\ \tilde{c}_{i,\downarrow} \end{pmatrix} = \begin{pmatrix} z_{i,\uparrow} & 0 \\ 0 & z_{i,\downarrow} \end{pmatrix}\begin{pmatrix} \tilde{f}_{i,\uparrow} \\ \tilde{f}_{i,\downarrow} \end{pmatrix} \Longrightarrow \boldsymbol{\chi}_i = \mathbf{Z}_i\tilde{\mathbf{f}}_i, \tag{A.14}$$

where

$$z_{i,\sigma} = \frac{\sqrt{(1-n_i+d_i^2)\left(\frac{1}{2}n_i + \frac{S_i^z}{\cos\varphi_i} - d_i^2\right)} + \sqrt{d_i^2\left(\frac{1}{2}n_i - \frac{S_i^z}{\cos\varphi_i} - d_i^2\right)}}{\sqrt{\left(\frac{1}{2}n_i + \frac{S_i^z}{\cos\varphi_i}\right)\left(1 - \frac{1}{2}n_i - \frac{S_i^z}{\cos\varphi_i}\right)}}. \tag{A.15}$$

Then, using (A.3), we obtain

$$\begin{aligned}\boldsymbol{\Psi}_i &= \mathbf{U}_i\boldsymbol{\chi}_i = \mathbf{U}_i\mathbf{Z}_i\tilde{\mathbf{f}}_i \\ &= \begin{pmatrix} \cos(\varphi_i/2) & \sin(\varphi_i/2)(\eta_y+i\eta_x) \\ -\sin(\varphi_i/2)(\eta_y-i\eta_x) & \cos(\varphi_i/2) \end{pmatrix} \begin{pmatrix} z_{i,\uparrow} & 0 \\ 0 & z_{i,\downarrow} \end{pmatrix} \begin{pmatrix} \tilde{f}_{i,\uparrow} \\ \tilde{f}_{i,\downarrow} \end{pmatrix} \\ &= \begin{pmatrix} z_{i,\uparrow}\cos\frac{\varphi_i}{2} & (\eta_y+i\eta_x)\sin\frac{\varphi_i}{2}z_{i,\downarrow} \\ -(\eta_y-i\eta_x)\sin\frac{\varphi_i}{2}z_{i,\uparrow} & z_{i,\downarrow}\cos\frac{\varphi_i}{2} \end{pmatrix} \begin{pmatrix} \tilde{f}_{i,\uparrow} \\ \tilde{f}_{i,\downarrow} \end{pmatrix} = \mathbf{W}_i\tilde{\mathbf{f}}_i \end{aligned} \tag{A.16}$$

Finally we transform the fermion operators $\tilde{f}_{i\sigma}$ back to the original frame, in the same way as in eqs. (A.1):

$$\tilde{\mathbf{f}}_i = \begin{pmatrix} \tilde{f}_{i\uparrow} \\ \tilde{f}_{i\downarrow} \end{pmatrix} = \begin{pmatrix} \cos\frac{\varphi_i}{2} & -\sin\frac{\varphi_i}{2}(\eta_y+i\eta_x) \\ \sin\frac{\varphi_i}{2}(\eta_y-i\eta_x) & \cos\frac{\varphi_i}{2} \end{pmatrix} \begin{pmatrix} f_{i\uparrow} \\ f_{i\downarrow} \end{pmatrix} = \mathbf{U}^\dagger\mathbf{f}_i \tag{A.17}$$

so that the spin-rotational invariant Gutzwiller representation of the fermions is given by

$$\boldsymbol{\Psi}_i = \mathbf{W}_i\tilde{\mathbf{f}}_i = \mathbf{W}_i\mathbf{U}^\dagger\mathbf{f}_i = \mathbf{z}_i\mathbf{f}_i. \tag{A.18}$$

So the complete transformation matrix $\mathbf{z} = \mathbf{W}\mathbf{U}^\dagger = \mathbf{U}_i\mathbf{Z}_i\mathbf{U}^\dagger\mathbf{f}_i$ reads as:

$$\begin{aligned}\mathbf{z}_i &= \begin{pmatrix} z_{i\uparrow}\cos^2\frac{\varphi_i}{2} + z_{i\downarrow}(\eta_x^2+\eta_y^2)\sin^2\frac{\varphi_i}{2} & (\eta_y+i\eta_x)[z_{i\downarrow}-z_{i\uparrow}]\frac{1}{2}\sin\varphi_i \\ (\eta_y-i\eta_x)[z_{i\downarrow}-z_{i\uparrow}]\frac{1}{2}\sin\varphi_i & z_{i\uparrow}(\eta_x^2+\eta_y^2)\sin^2\frac{\varphi_i}{2} + z_{i\downarrow}\cos^2\frac{\varphi_i}{2} \end{pmatrix} \\ &= \begin{pmatrix} z_{i\uparrow}\cos^2\frac{\varphi_i}{2} + z_{i\downarrow}\sin^2\frac{\varphi_i}{2} & \frac{S_i^-}{2S_i^z}[z_{i\uparrow}-z_{i\downarrow}]\cos\varphi_i \\ \frac{S_i^+}{2S_i^z}[z_{i\uparrow}-z_{i\downarrow}]\cos\varphi_i & z_{i\uparrow}\sin^2\frac{\varphi_i}{2} + z_{i\downarrow}\cos^2\frac{\varphi_i}{2} \end{pmatrix}, \end{aligned} \tag{A.19}$$

with

$$\tan^2\varphi_i = \frac{S_i^+S_i^-}{(S_i^z)^2}, \tag{A.20}$$

where we made use of the unitary length of the vector $\boldsymbol{\eta}$, i.e. $\eta_x^2+\eta_y^2 = 1$, and of the relations

$$\eta_y + i\eta_x = -\frac{S_i^x - iS_i^y}{S_i^z}\cot\varphi_i = -\frac{S_i^-}{S_i^z}\cot\varphi_i \tag{A.21}$$

$$\eta_y - i\eta_x = -\frac{S_i^x + iS_i^y}{S_i^z}\cot\varphi_i = -\frac{S_i^+}{S_i^z}\cot\varphi_i \tag{A.22}$$

derived from eqs. (A.4), and for simplicity we have skipped the $\langle\dots\rangle$ symbols in denoting the expectation values of the $\mathbf{S}$ components.

We finally obtain the spin-rotational invariant Gutzwiller energy functional Eq. (2.68) for the Hubbard model

$$E^{GA} = \sum_{i,j} t_{ij}\langle\boldsymbol{\Psi_i}^\dagger\mathbf{z_i}\mathbf{z_j}\boldsymbol{\Psi_j}\rangle + U\sum_i D_i. \tag{A.23}$$

Bibliography

[1] J. Lorenzana and G. Seibold, Low Temp. Phys. **32**, 533 (2006).

Appendix B

Dipolar approximation

We consider a two-dimensional system of electric charges. In particular we take two electric dipoles $\mathbf{a}$ and $\mathbf{b}$. If we assume $f(|\mathbf{r}_1 - \mathbf{r}_2|)$ as the pair interaction between two charges, the total interaction between the four charges (see Fig.(B.1)) is given by

$$V_{dip} = f\left(\left|\mathbf{r} + \frac{\mathbf{a}+\mathbf{b}}{2}\right|\right) + f\left(\left|\mathbf{r} - \frac{\mathbf{a}+\mathbf{b}}{2}\right|\right) - f\left(\left|\mathbf{r} + \frac{\mathbf{a}-\mathbf{b}}{2}\right|\right) - f\left(\left|\mathbf{r} - \frac{\mathbf{a}-\mathbf{b}}{2}\right|\right), \quad \text{(B.1)}$$

where the minus sign holds for repulsive interaction between charges of the same sign. Since we consider the dipole vectors much smaller than $|\mathbf{r}|$, which is the distance between

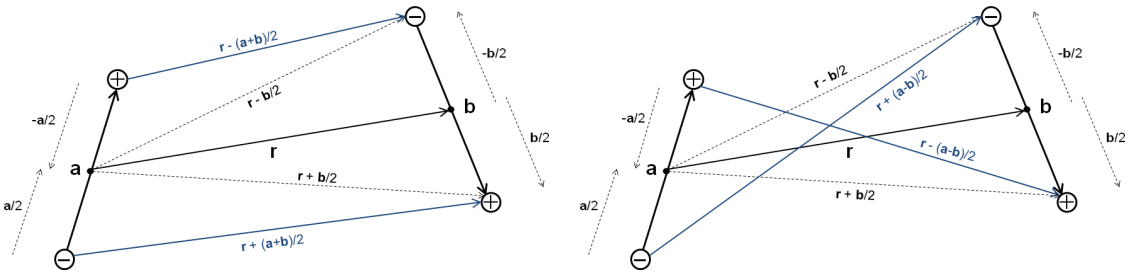

Figure B.1: Distances between each pair of charges.

the center of the two dipoles, we can perform a Taylor expansion of each pair interaction f around $|\mathbf{r}|$. Using

$$\begin{aligned} f(x+\delta x, y+\delta y) &\simeq f(x,y) + (\partial_x f)\,\delta x + (\partial_y f)\,\delta y \\ &\quad + \frac{1}{2}(\partial_{xx} f)\,\delta x^2 + \frac{1}{2}(\partial_{yy} f)\,\delta y^2 + (\partial_{xy} f)\delta x \delta y = \\ &= f(\mathbf{r}) + \nabla f \cdot \delta\mathbf{r} + \frac{1}{2}(\delta\mathbf{r}\cdot\nabla)^2 f, \end{aligned} \quad \text{(B.2)}$$

we obtain

$$
\begin{aligned}
V_{dip} &\simeq 2f(|\mathbf{r}|) - 2f(|\mathbf{r}|) + \nabla f \cdot \left[\frac{\mathbf{a}+\mathbf{b}}{2} - \frac{\mathbf{a}+\mathbf{b}}{2} + \frac{\mathbf{a}-\mathbf{b}}{2} - \frac{\mathbf{a}-\mathbf{b}}{2}\right] + \\
&\quad + \frac{1}{2}\left[\left(\frac{\mathbf{a}+\mathbf{b}}{2}\cdot\nabla\right)^2 + \left(-\frac{\mathbf{a}+\mathbf{b}}{2}\cdot\nabla\right)^2 - \left(\frac{\mathbf{a}-\mathbf{b}}{2}\cdot\nabla\right)^2 - \left(-\frac{\mathbf{a}-\mathbf{b}}{2}\cdot\nabla\right)^2\right] f = \\
&= \frac{1}{8}\left\{[(\mathbf{a}+\mathbf{b})\cdot\nabla]^2 + [(\mathbf{a}+\mathbf{b})\cdot\nabla]^2 - [(\mathbf{a}-\mathbf{b})\cdot\nabla]^2 - [(\mathbf{a}-\mathbf{b})\cdot\nabla]^2\right\} f = \\
&= \frac{1}{4}\left\{[(\mathbf{a}+\mathbf{b})\cdot\nabla]^2 - [(\mathbf{a}-\mathbf{b})\cdot\nabla]^2\right\} f = \\
&= \frac{1}{4}\left\{[(a_x+b_x)\partial_x + (a_y+b_y)\partial_y]^2 - [(a_x-b_x)\partial_x + (a_y-b_y)\partial_y]^2\right\} = \\
&= \frac{1}{4}\left\{(a_x+b_x)^2\partial_x\partial_x + (a_y+b_y)^2\partial_y\partial_y + 2(a_x+b_x)(a_y+b_y)\partial_x\partial_y + \right. \\
&\quad \left. -(a_x-b_x)^2\partial_x\partial_x - (a_y-b_y)^2\partial_y\partial_y - 2(a_x-b_x)(a_y-b_y)\partial_x\partial_y\right\} f = \\
&= \frac{1}{4}\left\{(a_x^2+b_x^2+2a_xb_x - a_x^2 - b_x^2 + 2a_xb_x)\partial_x\partial_x + (a_y^2+b_y^2+2a_yb_y - a_y^2 - b_y^2 + 2a_yb_y)\partial_y\partial_y + \right. \\
&\quad \left. +(2a_xa_y + 2b_xa_y + 2a_xb_y + 2b_xb_y - 2a_xa_y + 2b_xa_y + 2a_xb_y - 2b_xb_y)\partial_x\partial_y\right\} f = \\
&= [(a_xb_x)\partial_{xx} + (a_yb_y)\partial_{yy} + (a_xb_y + a_yb_x)\partial_{xy}]\, f. \qquad \text{(B.3)}
\end{aligned}
$$

Since f depends only on the radial coordinate $r = |\mathbf{r}| = \sqrt{x^2+y^2}$ we have

$$
\partial_x f = \frac{\partial f}{\partial r}\frac{\partial r}{\partial x} = \frac{\partial f}{\partial r}\frac{x}{r}, \qquad \partial_y f = \frac{\partial f}{\partial r}\frac{y}{r} \qquad \text{(B.4)}
$$

$$
\begin{aligned}
\partial_{xy} f &= \partial_y(\partial_x f) = \frac{\partial}{\partial y}\left(\frac{\partial f}{\partial r}\frac{x}{r}\right) = \left(\frac{\partial}{\partial y}\frac{\partial f}{\partial r}\right)\frac{x}{r} + \frac{\partial f}{\partial r}\left(\frac{\partial}{\partial y}\frac{x}{r}\right) = \\
&= \left(\frac{\partial^2 f}{\partial r^2}\frac{y}{r}\right)\frac{x}{r} + \frac{\partial f}{\partial r}\left(-\frac{x}{r^2}\frac{y}{r}\right) = \frac{\partial^2 f}{\partial r^2}\frac{xy}{r^2} - \frac{\partial f}{\partial r}\frac{xy}{r^3} \qquad \text{(B.5)}
\end{aligned}
$$

$$
\begin{aligned}
\partial_{xx} f &= \partial_x(\partial_x f) = \frac{\partial}{\partial x}\left(\frac{\partial f}{\partial r}\frac{x}{r}\right) = \left(\frac{\partial}{\partial x}\frac{\partial f}{\partial r}\right)\frac{x}{r} + \frac{\partial f}{\partial r}\left(\frac{\partial}{\partial x}\frac{x}{r}\right) = \\
&= \left(\frac{\partial^2 f}{\partial r^2}\frac{x}{r}\right)\frac{x}{r} + \frac{\partial f}{\partial r}\left(\frac{1}{r} - \frac{x}{r^2}\frac{x}{r}\right) = \frac{\partial^2 f}{\partial r^2}\frac{x^2}{r^2} + \frac{\partial f}{\partial r}\frac{1}{r} - \frac{\partial f}{\partial r}\frac{x^2}{r^3} \qquad \text{(B.6)}
\end{aligned}
$$

$$
\partial_{yy} f = \partial_y(\partial_y f) = \frac{\partial^2 f}{\partial r^2}\frac{y^2}{r^2} + \frac{\partial f}{\partial r}\frac{1}{r} - \frac{\partial f}{\partial r}\frac{y^2}{r^3}. \qquad \text{(B.7)}
$$

So the interactions energy becomes

$$\begin{aligned}
V_{dip} &= (a_x b_x)\left(\frac{\partial^2 f}{\partial r^2}\frac{x^2}{r^2}+\frac{\partial f}{\partial r}\frac{1}{r}-\frac{\partial f}{\partial r}\frac{x^2}{r^3}\right)+(a_y b_y)\left(\frac{\partial^2 f}{\partial r^2}\frac{y^2}{r^2}+\frac{\partial f}{\partial r}\frac{1}{r}-\frac{\partial f}{\partial r}\frac{y^2}{r^3}\right)+ \\
&\quad (a_x b_y + a_y b_x)\left(\frac{\partial^2 f}{\partial r^2}\frac{xy}{r^2}-\frac{\partial f}{\partial r}\frac{xy}{r^3}\right)= \\
&= \frac{\partial f}{\partial r}\frac{1}{r}(a_x b_x + a_y b_y)+\frac{\partial^2 f}{\partial r^2}\frac{1}{r^2}\left[a_x b_x x^2 + a_y b_y y^2 + (a_x b_y + a_y b_x)xy\right]+ \\
&\quad +\frac{\partial f}{\partial r}\frac{1}{r^3}\left[-a_x b_x x^2 - a_y b_y y^2 - (a_x b_y + a_y b_x)xy\right]= \\
&= \frac{\partial f}{\partial r}\frac{1}{r}(\mathbf{a}\cdot\mathbf{b})+\left[a_x b_x x^2 + a_y b_y y^2 + a_x b_y xy + a_y b_x xy\right]\left(\frac{\partial^2 f}{\partial r^2}\frac{1}{r^2}-\frac{\partial f}{\partial r}\frac{1}{r^3}\right)= \\
&= \frac{\partial f}{\partial r}\frac{\mathbf{a}\cdot\mathbf{b}}{r}+\frac{a_x x(b_x x + b_y y)+a_y y(b_x x + b_y y)}{r^2}\left(\frac{\partial^2 f}{\partial r^2}-\frac{\partial f}{\partial r}\frac{1}{r}\right)= \\
&= \frac{\partial f}{\partial r}\frac{\mathbf{a}\cdot\mathbf{b}}{r}+\frac{(a_x x + b_y y)(b_x x + b_y y)}{r^2}r\frac{\partial}{\partial r}\left(\frac{1}{r}\frac{\partial f}{\partial r}\right)= \\
&= \frac{\partial f}{\partial r}\frac{\mathbf{a}\cdot\mathbf{b}}{r}+\frac{(\mathbf{a}\cdot\mathbf{r})(\mathbf{b}\cdot\mathbf{r})}{r}\frac{\partial}{\partial r}\left(\frac{1}{r}\frac{\partial f}{\partial r}\right) \qquad \text{(B.8)}
\end{aligned}$$

If we consider a two-dimensional coulombic interaction between each couple of charges, such that $f(r) \sim \log r$, we obtain

$$V_{dip} = \frac{\mathbf{a}\cdot\mathbf{b}}{r^2} - 2\frac{(\mathbf{a}\cdot\mathbf{r})(\mathbf{b}\cdot\mathbf{r})}{r^4} \qquad \text{(B.9)}$$

Appendix C

Calculation of the spin field generated from a randomly distributed VA pairs collection

We want to calculate the continuous phase field generated by a collection of randomly distributed VA pairs, like that shown in Fig. C.1. The angular spin distortion due to a

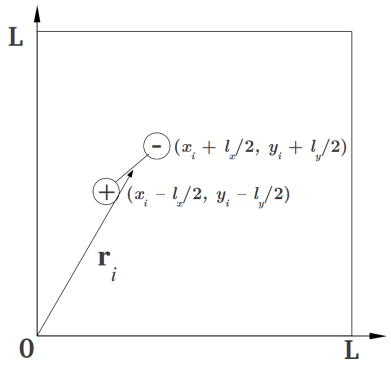

Figure C.1: Diagonal dipole of length $l = \sqrt{l_x^2 + l_y^2}$ in a lattice $L \times L$. The circle with "+" is a vortex k, while the circle with "−" is an antivortex $-k$. The vector $\mathbf{r}_i$ points the center of the dipole.

TD centered at $\mathbf{r}_i$, is given by

$$\theta_i = k \arctan\left[\frac{y - (y_i - l_y/2)}{x - (x_i - l_x/2)}\right] - k \arctan\left[\frac{y - (y_i + l_y/2)}{x - (x_i + l_x/2)}\right]. \tag{C.1}$$

Using the property $\arctan(x_1) \pm \arctan(x_2) = \arctan(\frac{x_1 \pm x_2}{1 \mp x_1 x_2})$ for $\pm x_1 x_2 < 1$, and assuming $l_x = l_y$ (with $l = \sqrt{2} l_x$), one can obtain

$$\theta_i = k \arctan\left[\frac{l_x(x - x_i) - l_x(y - y_i)}{(x - x_i)^2 + (y - y_i)^2 - l_x^2/2}\right], \tag{C.2}$$

which to a very good approximation can be linearized so that, if we consider a collection of TDs, we have to evaluate

$$\theta_{tot}(\mathbf{r}) \approx \sum_{i}^{N_p} \frac{kl_x(x-x_i) - kl_x(y-y_i)}{(x-x_i)^2 + (y-y_i)^2 - l_x^2/2}, \tag{C.3}$$

where N_p is the number of pairs. Replacing the sum by an integral (n: concentration of VA pairs) yields

$$\begin{aligned}
\theta_{tot}(\mathbf{r}) &= nkl_x \int_0^L ds \int_0^L dt \frac{(x-t)-(y-s)}{(x-t)^2 + (y-s)^2 - l_x^2/2}. \\
&= nkl_x \int_0^L ds \int_0^L dt \frac{(x-t)}{(x-t)^2 + (y-s)^2 - l_x^2/2} \\
&\quad -nkl_x \int_0^L ds \int_0^L dt \frac{(y-s)}{(x-t)^2 + (y-s)^2 - l_x^2/2}.
\end{aligned} \tag{C.4}$$

Notice that for arbitrary (x, y) one should in principle also include to ϕ_{tot} the influence of segments from adjacent cells (mirror images). However, we will expand the result for small x and y where this effect (for large cell dimensions) should be negligible. Performing the integral over s in the first integral and over t in the second integral yields

$$\begin{aligned}
\theta_{tot}(\mathbf{r}) &= nkl_x \int_0^L dt \frac{x-t}{\sqrt{(x-t)^2 - l_x^2/2}} \\
&\quad \left[\arctan\left(\frac{L-y}{\sqrt{(x-t)^2 - l_x^2/2}} \right) + \arctan\left(\frac{y}{\sqrt{(x-t)^2 - l_x^2/2}} \right) \right] \\
&\quad -nkl_x \int_0^L ds \frac{y-s}{\sqrt{(y-s)^2 - l_x^2/2}} \\
&\quad \left[\arctan\left(\frac{L-x}{\sqrt{(y-s)^2 - l_x^2/2}} \right) + \arctan\left(\frac{x}{\sqrt{(y-s)^2 - l_x^2/2}} \right) \right].
\end{aligned}$$

Neglecting $l_x^2/4$ with respect to $(x-t)^2$ or $(y-s)^2$ we obtain

$$\begin{aligned}
\theta_{tot}(\mathbf{r}) &\approx nkl_x \int_0^L dt \left[\arctan\left(\frac{L-y}{x-t} \right) + \arctan\left(\frac{y}{x-t} \right) \right] \\
&\quad -nkl_x \int_0^L ds \left[\arctan\left(\frac{L-x}{y-s} \right) + \arctan\left(\frac{x}{y-s} \right) \right].
\end{aligned}$$

Knowing that $\int_M^L \arctan(1/x)dx = -M\arctan(1/M) + L\arctan(1/L) + \frac{1}{2}\ln\left(\frac{1+L^2}{1+M^2}\right)$, we have

$$\begin{aligned}
\theta_{tot}(\mathbf{r}) &= nkl_x\left[x\arctan\left(\frac{L-y}{x}\right) - (L-x)\arctan\left(\frac{L-y}{L-x}\right)\right. \\
&\quad -\frac{L-y}{2}\ln\left(\frac{(L-y)^2+(L-x)^2}{(L-y)^2+x^2}\right) + x\arctan\left(\frac{y}{x}\right) - (L-x)\arctan\left(\frac{y}{L-x}\right) \\
&\quad -\frac{y}{2}\ln\left(\frac{y^2+(L-x)^2}{x^2+y^2}\right) - y\arctan\left(\frac{L-x}{y}\right) + (L-y)\arctan\left(\frac{L-x}{L-y}\right) \\
&\quad +\frac{L-x}{2}\ln\left(\frac{(L-x)^2+(L-y)^2}{(L-x)^2+y^2}\right) - y\arctan\left(\frac{x}{y}\right) + (L-y)\arctan\left(\frac{x}{L-y}\right) \\
&\quad \left.+\frac{x}{2}\ln\left(\frac{x^2+(L-y)^2}{x^2+y^2}\right)\right] \\
&= nkl_x\left[x\left\{\arctan\left(\frac{L-y}{x}\right) + \arctan\left(\frac{y}{x}\right)\right\}\right. \\
&\quad -(L-x)\left\{\arctan\left(\frac{L-y}{L-x}\right) + \arctan\left(\frac{y}{L-x}\right)\right\} \\
&\quad -y\left\{\arctan\left(\frac{L-x}{y}\right) + \arctan\left(\frac{x}{y}\right)\right\} \\
&\quad +(L-y)\left\{\arctan\left(\frac{L-x}{L-y}\right) + \arctan\left(\frac{x}{L-y}\right)\right\} \\
&\quad -\frac{L-y}{2}\ln\left(\frac{(L-y)^2+(L-x)^2}{(L-y)^2+x^2}\right) - \frac{y}{2}\ln\left(\frac{y^2+(L-x)^2}{x^2+y^2}\right) \\
&\quad \left.+\frac{L-x}{2}\ln\left(\frac{(L-x)^2+(L-y)^2}{(L-x)^2+y^2}\right) + \frac{x}{2}\ln\left(\frac{x^2+(L-y)^2}{x^2+y^2}\right)\right] \\
&= nkl_x\, f_L(x,y) \qquad \text{(C.5)}
\end{aligned}$$

where $f_L(x,y)$ is a function (see Fig. C.2) that depends on the parameter L, and that can be approximated by a linear function near the center of the box $(L/2, L/2)$ (the larger is the distance from the edges of the box the more the approximation is good). So linearizing $f_L(x,y)$, we have

$$\theta_{tot}(\mathbf{r}) \approx nkl_x(\pi x - \pi y) \qquad \text{(C.6)}$$

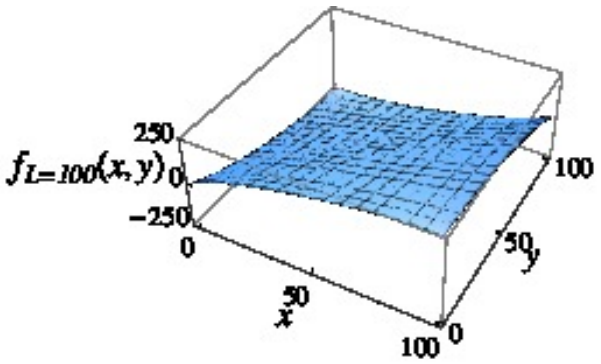

Figure C.2: three-dimensional plot of the function $f_L(x, y)$ with $L = 100$.

Appendix D

Energy of a dipolar lattice

We consider a two-dimensional system made by a collection of unitary dipoles aligned ferroelectrically in y-direction. If we assume a logarithmic interaction between each couple of TCs, the dipolar potential is given by eq. (B.9), where $\mathbf{a}$ and $\mathbf{b}$ are equal to $\hat{e}_y$. With these assumptions $\mathbf{a}\cdot\mathbf{r}$ is the projection of $\mathbf{r}$ in the direction $\hat{e}_y$, namely the y-component of $\mathbf{r}$. The same occurs for $\mathbf{b}\cdot\mathbf{r}$, while $\mathbf{a}\cdot\mathbf{b}=1$. So the interaction energy between one dipole at the origin and one dipole at $\mathbf{r}$, is given by

$$E_f(\mathbf{r}) = \frac{1}{r^2} - 2\frac{y^2}{r^4}. \tag{D.1}$$

To calculate the total energy per dipole of an infinite continuous ferroelectric system we must integrate $E_f(\mathbf{r})$ all over the two-dimensional space. This integral gives zero, since the contribution from the dipole at (x,y) and the dipole at (y,x) cancel with each other. This result arises from the fact that the total field due to the collection of dipoles, can be separated into two contributions: one from the dipoles inside a large circle and the other from the dipoles outside. While the contribution from inside the circle cancels, the contribution from outside is different from zero and can be calculated by using the classical theory of dielectrics, obtaining the result of eq. (6.13).

The correct numerical value of the total interaction energy can be obtained directly by using the screened interaction (7.1). In this case the attractive potential is proportional to $V_{att}(r) = -K_0(r/\lambda)$, and to obtain the dipolar interaction V_{dip}, we must use eq. (B.8). So we have to calculate $\frac{\partial V_{att}}{\partial r}$ and $\frac{\partial^2 V_{att}}{\partial r^2}$. From the recorsive identities for the Bessel functions

$$\frac{d}{dx}K_\nu(x) = \begin{cases} \frac{\nu}{x}K_\nu(x) - K_{\nu+1}(x), \\ -\frac{\nu}{x}K_\nu(x) - K_{\nu-1}(x), \end{cases} \tag{D.2}$$

we have

$$\begin{aligned} &\frac{d}{dr}K_0\left(\frac{r}{\lambda}\right) = -\frac{1}{\lambda}K_1\left(\frac{r}{\lambda}\right); \\ &\frac{d^2}{dr^2}K_0(\frac{r}{\lambda}) = -\frac{1}{\lambda}\frac{d}{dr}K_1\left(\frac{r}{\lambda}\right) = \frac{1}{\lambda^2}\left[\frac{\lambda}{r}K_1\left(\frac{r}{\lambda}\right) + K_0\left(\frac{r}{\lambda}\right)\right]. \end{aligned} \tag{D.3}$$

So

$$\begin{aligned} V_{dip}(\mathbf{r}) &= \frac{dV_{att}}{dr}\frac{\mathbf{a}\cdot\mathbf{b}}{r} + \frac{(\mathbf{a}\cdot\mathbf{r})(\mathbf{b}\cdot\mathbf{r})}{r^2}\left(\frac{d^2V_{att}}{dr^2} - \frac{dV_{att}}{dr}\frac{1}{r}\right) \\ &= \frac{\mathbf{a}\cdot\mathbf{b}}{r}\frac{1}{\lambda}K_1\left(\frac{r}{\lambda}\right) - \frac{(\mathbf{a}\cdot\mathbf{r})(\mathbf{b}\cdot\mathbf{r})}{r^2}\left[\frac{1}{\lambda r}K_1\left(\frac{r}{\lambda}\right) + \frac{1}{\lambda^2}K_0\left(\frac{r}{\lambda}\right) + \frac{1}{\lambda r}K_1\left(\frac{r}{\lambda}\right)\right] = \\ &= \frac{1}{\lambda}\left[\frac{\mathbf{a}\cdot\mathbf{b}}{r} - 2\frac{(\mathbf{a}\cdot\mathbf{r})(\mathbf{b}\cdot\mathbf{r})}{r^3}\right]K_1\left(\frac{r}{\lambda}\right) - \frac{1}{\lambda^2}\frac{(\mathbf{a}\cdot\mathbf{r})(\mathbf{b}\cdot\mathbf{r})}{r^2}K_0\left(\frac{r}{\lambda}\right). \end{aligned} \tag{D.4}$$

This potential between two TDs implies that a dipole at the origin and a dipole at $\mathbf{r} = (x, y)$, which are both oriented along the y-direction, interact according to

$$E_f(\mathbf{r}) = \frac{1}{\lambda r}\left[1 - 2\frac{y^2}{r^2}\right]K_1\left(\frac{r}{\lambda}\right) - \frac{y^2}{\lambda^2 r^2}K_0\left(\frac{r}{\lambda}\right). \tag{D.5}$$

The integration of $E_f(\mathbf{r})$ all over the 2D space provides the correct value of the total energy of an infinite continuous ferroelectric system:

$$\begin{aligned} &\frac{1}{2}\int d^2r\, E_{dip}^{ferr}(\mathbf{r}) = \\ &= \frac{1}{2}\int_0^{2\pi} d\phi \int_0^{\infty} rdr \left\{\frac{1}{\lambda r}K_1\left(\frac{r}{\lambda}\right) - \frac{y^2}{r^2}\left[\frac{2}{\lambda r}K_1\left(\frac{r}{\lambda}\right) + \frac{1}{\lambda^2}K_0\left(\frac{r}{\lambda}\right)\right]\right\} = \\ &= \frac{1}{2}\int_0^{\infty} rdr \left\{\frac{2\pi}{\lambda r}K_1\left(\frac{r}{\lambda}\right) - \left[\frac{2}{\lambda r}K_1\left(\frac{r}{\lambda}\right) + \frac{1}{\lambda^2}K_0\left(\frac{r}{\lambda}\right)\right]\int_0^{2\pi} d\phi\, \frac{r^2\sin^2\phi}{r^2}\right\} = \\ &= \frac{1}{2}\int_0^{\infty} rdr \left\{\frac{2\pi}{\lambda r}K_1\left(\frac{r}{\lambda}\right) - \pi\left[\frac{2}{\lambda r}K_1\left(\frac{r}{\lambda}\right) + \frac{1}{\lambda^2}K_0\left(\frac{r}{\lambda}\right)\right]\right\} = \\ &= -\frac{\pi}{2}\int_0^{\infty}\frac{rdr}{\lambda^2}K_0\left(\frac{r}{\lambda}\right) = -\frac{\pi}{2}\int_0^{\infty} dx\, x\, K_0(x) = -\frac{\pi}{2}, \end{aligned} \tag{D.6}$$

where the factor 1/2 avoids double counting.

Since our model is defined on a lattice, now we consider TCs in a discrete system, trying to find numerically the correct value of the energy of a square dipolar lattice. We consider configurations in which a site of the lattice can be occupied by a single charge (positive or negative) and not by a point-like dipole. The potential between two charges is given by $k_i k_j K_0\left(\frac{r}{\lambda}\right)$, where $k_{ij} = \pm 1$. We use a lattice constant $a = 1$, in such a way that a dipole is made by two opposite charges located on two lattice sites, which are nearest neighbors in y-direction. We call l, the spacing between two neighboring dipoles in x-direction. To keep constant the density of dipoles per unit area, the distance between two neighbour dipoles in y-direction must be l too[1]. So, if N is the number of dipoles along the horizontal side of the lattice, also along the vertical side the dipoles are N. So the total dipoles in the 2D-box are N^2 and the total charges are $2N^2$. Finally the length of each side of the box is $L = N \cdot l$. In Fig. D.1 we show a snapshot of the lattice with ferroelectric (FE) and columnar antiferroelectric (AFE) structure.

[1]Actually l is the distance between two charges of the same sign, but the spacing between the "tail" of a dipole and the "head" of the nearest-neighbour in y-direction is $l - 1$.

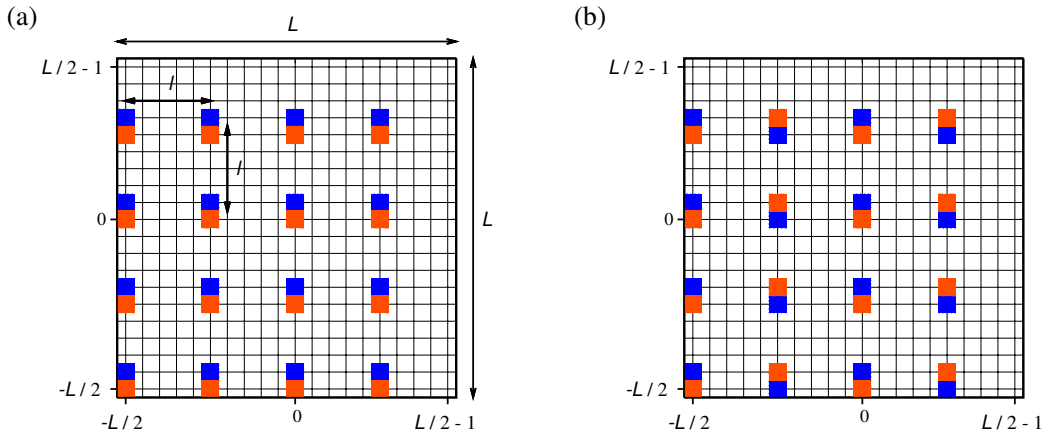

Figure D.1: (a) Ferroelectric and (b) columnar antiferroelectric configuration. Each crossing represents a lattice site. We draw each charge as a square on its own site (positive charge as a red square, negative charge as a blue square). In these snapshots we have taken $N = 4$, $l = 5$, so that $L = 20$.

The energy results obtained integrating the expression (D.4), imply a continuum distribution of dipoles. For a discrete system, this means that each site of the lattice is occupied by a dipole. So, in the calculation of eq. (D.6), we have implicitly considered $l = 1$, and all the lengths have been measured in units of l. As it can be easily shown, the energy per dipole obtained numerically with $l > 1$, must be multiplied by l^2 in order to compare it to the analytical result (D.6).

So to obtain the total energy per dipole e^{tot} of the configurations in Fig. D.1, we must sum all the interactions of the positive charge in the site $(0, 0)$ and the negative charge in $(0, 1)$ with any other charge i located in $(x[i], y[i])$. Finally we have to multiply by a factor $1/2$ (as well as by l^2) to avoid double counting. We have

$$e^{tot} = \frac{l^2}{2} \sum_{i=1}^{2N^2} \left[K_0 \left(\frac{\sqrt{(x[i])^2 + (y[i])^2}}{\lambda} \right) - K_0 \left(\frac{\sqrt{(x[i])^2 + (y[i]-1)^2}}{\lambda} \right) \right]. \qquad \text{(D.7)}$$

Since the interaction between two dipoles in eq. (B.8) has been obtained neglecting the self-energy of each dipole, we have not to consider the interaction between the two nearest neighboring charges in the sites $(0, 0)$ and $(0, 1)$. This means that we have to exclude from the sum the term i for which $x[i] = 0$, and $y[i] = 1$.

The approximation in eq. (B.2) allowed us to treat each dipole as a point-like particle located in a single site of the lattice. So the larger is the spacing l between dipoles, the more the dipole approximation becomes accurate. In Fig.D.2 we report the dependence of the total energy per dipole on the number N of dipoles along one side of the box, and on the spacing l, for both the FE and the AFE structures. From the panel (a), we can observe that increasing N, the total energy per dipole tends to the expected value for the

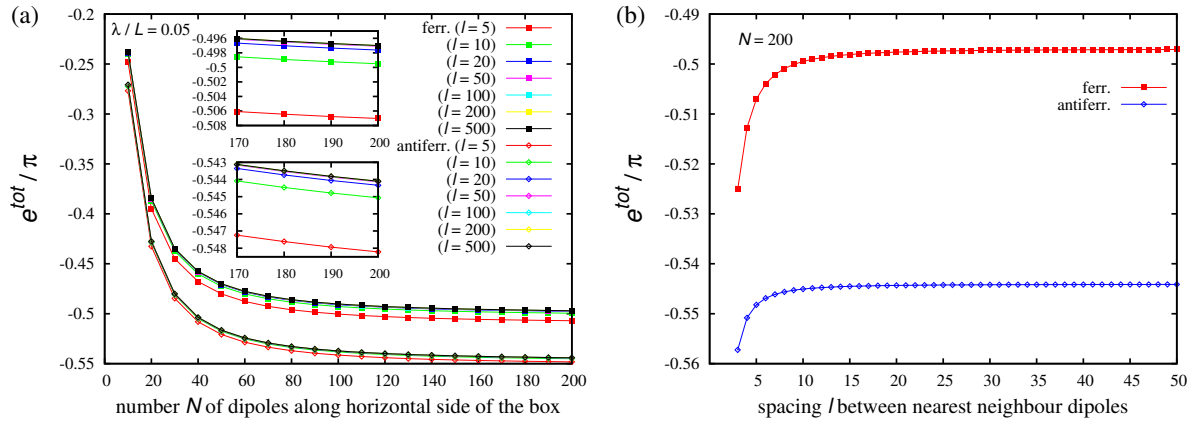

Figure D.2: (a) Dependence of the total energy per dipole on the number N of dipoles along one side of the lattice, for several values of l. Both the FE and the AFE configurations are taken into account. The insets show a zoom on region of large N for the two configurations. (b) Dependence of the energy on the spacing l for $N = 200$. The result have been obtained with $\lambda/L = 0.05$.

FE configuration. However we observe that the AFE configuration is more stable since it has a lower energy. Furthermore we see that the expected energy values of the two configurations are reached from below, for increasing values of l: we can state that the dipole approximation holds for $l \gtrsim 10$, as shown in Fig. D.2(b) where e^{tot} is plotted as a function of l, keeping N fixed.

In Fig. D.3 we show the trend of the energy as the screening length λ increases, keeping N and l fixed. They are chosen in the range of values for which the energy has saturated to its expected value (see Fig. D.2). We observe that increasing λ/L, the energy of the

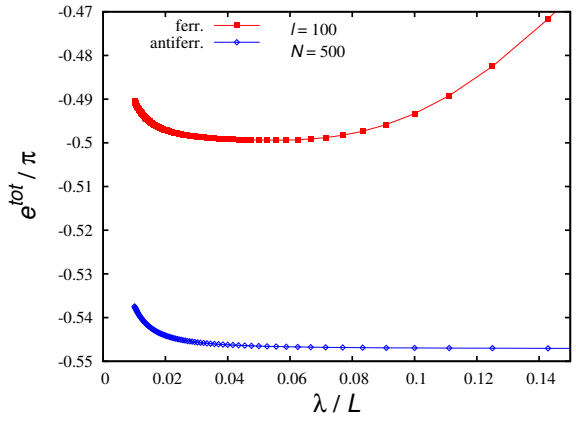

Figure D.3: Dependence of the total energy per dipole on λ/L (keeping L fixed), for both the FE and the AFE configurations. This result have been obtained using $N = 500$ and $l = 100$, so that $L = 50000$.

FE configuration, tends to saturate to the correct value $-\pi/2$, but increasing further λ/L

the total energy increases up to zero, since for $\lambda \gg r$, K_0 assumes a logarithmic behavior. This does not occur for the AFE configuration. We have tested that these plots do not depend on the values of l and N, provided that they are not too small.

These arguments show how the parameter λ, which physically represents the typical length of the magnetic correlation, actually acts as a convergence parameter for our model. The plot in Fig. D.3 suggests that we must choose the value of λ as the 5% of the entire length of the lattice. However, if we assume periodic boundary conditions, we have to consider a finite number of replica of the lattice, namely N_R for each side. In this way the total size of our box, is given by the length L of the main lattice multiplied by the total number of the replica, which is $2N_R + 1$. So we obtain $\lambda = 0.05 \times (2N_R + 1)L$. In the MC simulations of chapter 8 we use $L = 100$ and $N_R = 10$, so that $\lambda = 105$. We have checked that changing the screening length λ of the long-range interaction between TCs, the results of the chapter 8 remain substantially the same as long as λ remains larger than the typical distance between the segments.

Now we consider the configurations shown in Fig. D.4, which represent a nearly triangular Wigner crystal: the dipoles in one row tend to face gaps in the neighbouring rows. Using (D.7), we calculate the energy per dipole of such configurations. For $N = 500$,

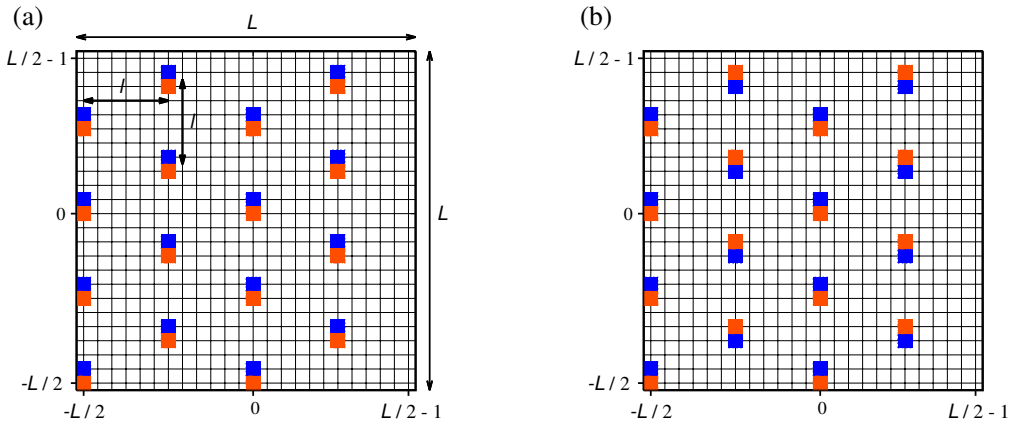

Figure D.4: (a) Ferroelectric and (b) columnar antiferroelectric configuration for a nearly triangular Wigner crystal. Each crossing represents a lattice site. Each positive (negative) charge is represented by a red (blue) square. In these snapshots we have taken $N = 4$, $l = 6$, so that $L = 24$.

$l = 100$ and $\lambda/L = 0.05$, we obtain for the triangular FE configuration $e^{tot}_{FE}/\pi = -0.549$, while for the triangular AFE configuration, $e^{tot}_{AFE}/\pi = -0.502$. Thus if the dipoles are forced to arrange within a nearly triangular disposition (for example by the effect of the Coulomb repulsion between the positive charged holes which actually constitute the TCs), they gain energy by aligning ferroelectrically.

Appendix E

Correlation functions and structure factors

In this section we define the charge and spin correlation functions and the structure factors for a lattice model. The charge correlation function is defined by

$$C_c(\mathbf{R}) = \frac{1}{N_h}\sum_{\mathbf{r}_i}[n(\mathbf{r}_i) - n_h][n(\mathbf{r}_i + \mathbf{R}) - n_h], \tag{E.1}$$

where $n(\mathbf{r}_i)$ is the occupation number of the site at $\mathbf{r}_i$, and $n_h = N_h/L^2$ is the charge concentration. The Fourier transform of eq. (E.1) represents the charge structure factor

$$\mathcal{S}_c(\mathbf{q}) = \frac{1}{L^2}\sum_{\mathbf{R}} C_c(\mathbf{R})\exp(i\mathbf{q}\cdot\mathbf{R}). \tag{E.2}$$

If we check the sum rules, we have

$$\begin{aligned}
\sum_{\mathbf{q}}\mathcal{S}_c(\mathbf{q}) &= \sum_{\mathbf{q}}\frac{1}{L^2}\sum_{\mathbf{R}} C_c(\mathbf{R})\exp(i\mathbf{q}\cdot\mathbf{R}) \\
&= \sum_{\mathbf{q}}\frac{1}{L^2}\sum_{\mathbf{R}}\frac{1}{N_h}\sum_{\mathbf{r}_i}[n(\mathbf{r}_i) - n_h][n(\mathbf{r}_i + \mathbf{R}) - n_h]\exp(i\mathbf{q}\cdot\mathbf{R}) \\
&= \frac{1}{N_h}\sum_{\mathbf{R}}\sum_{\mathbf{r}_i}[n(\mathbf{r}_i) - n_h][n(\mathbf{r}_i + \mathbf{R}) - n_h]\left(\frac{1}{L^2}\sum_{\mathbf{q}}\exp(i\mathbf{q}\cdot\mathbf{R})\right) \\
&= \frac{1}{N_h}\sum_{\mathbf{R}}\sum_{\mathbf{r}_i}[n(\mathbf{r}_i) - n_h][n(\mathbf{r}_i + \mathbf{R}) - n_h]\delta_{\mathbf{R},0} \\
&= \frac{1}{N_h}\sum_{\mathbf{r}_i}[n(\mathbf{r}_i) - n_h]^2 = \frac{1}{N_h}\left[N_h(1-n_h)^2 + (L^2 - N_h)n_h^2\right] \\
&= \frac{1}{N_h}\left[N_h(1-n_h)^2 + L^2(1-n_h)n_h^2\right] \\
&= (1-n_h)^2 + (1-n_h)n_h = (1-n_h).
\end{aligned} \tag{E.3}$$

where we have used the fact that $n(\mathbf{r}_i)$ is unitary in correspondence of the N_h occupied sites and vanishes in correspondence of the remaining $(L^2 - N_h)$ sites. Starting from the first equation of (8.4) we obtain

$$\frac{1}{L^2}|K_c(\mathbf{q})|^2 = \frac{1}{L^2}\frac{1}{N_h}\sum_{\mathbf{r}_i,\mathbf{r}'_i} n(\mathbf{r}_i)n(\mathbf{r}'_i)\exp[i\mathbf{q}\cdot(\mathbf{r}_i - \mathbf{r}'_i)].$$

Since each lattice point $\mathbf{r}'_i$ can be written as $\mathbf{r}_i \pm \mathbf{R}$ for a given site $\mathbf{r}_i$, the previous expression reads

$$\begin{aligned}
&\frac{1}{L^2}|K_c(\mathbf{q})|^2 = \frac{1}{L^2}\frac{1}{N_h}\sum_{\mathbf{r}_i,\mathbf{R}} n(\mathbf{r}_i)n(\mathbf{r}_i - \mathbf{R})\exp[i\mathbf{q}\cdot\mathbf{R}] \\
= &\frac{1}{L^2}\frac{1}{N_h}\sum_{\mathbf{r}_i,\mathbf{R}} \left\{[n(\mathbf{r}_i) - n_h]\,[n(\mathbf{r}_i - \mathbf{R}) - n_h] + n_h\,[n(\mathbf{r}_i) + n(\mathbf{r}_i - \mathbf{R})] - n_h^2\right\}\exp[i\mathbf{q}\cdot\mathbf{R}] \\
= &\frac{1}{L^2}\sum_{\mathbf{R}} C_c(-\mathbf{R})\exp[i\mathbf{q}\cdot\mathbf{R}] + \frac{1}{L^2}\sum_{\mathbf{R}}\frac{1}{N_h}(2n_hN_h - n_h^2L^2)\exp[i\mathbf{q}\cdot\mathbf{R}] \\
= &\frac{1}{L^2}\sum_{\mathbf{R}} C_c(-\mathbf{R})\exp[i\mathbf{q}\cdot\mathbf{R}] + n_h\frac{1}{L^2}\sum_{\mathbf{R}}\exp[i\mathbf{q}\cdot\mathbf{R}] \\
= &\mathcal{S}_c(\mathbf{q}) + n_h\delta_{\mathbf{q},0},
\end{aligned} \tag{E.4}$$

where $C_c(\mathbf{R}) = C_c(-\mathbf{R})$ because of the inversion symmetry in the real space. From eq. (E.4) we have

$$\mathcal{S}_c(\mathbf{q}) = \frac{1}{L^2}|K_c(\mathbf{q})|^2 - n_h\delta_{\mathbf{q},0}. \tag{E.5}$$

Since $n_h = |K_c(0)|^2/L^2$, $\mathcal{S}_c(\mathbf{q})$ can be written as

$$\mathcal{S}_c(\mathbf{q}) = (1 - \delta_{\mathbf{q},0})\frac{|K_c(\mathbf{q})|^2}{L^2}. \tag{E.6}$$

Now we repeat the previous analysis For the spin degrees of freedom. The spin correlation function is defined by

$$C_s(\mathbf{R}) = \frac{1}{L^2}\sum_{\mathbf{r}_i}\mathbf{S}(\mathbf{r}_i)\cdot\mathbf{S}(\mathbf{r}_i + \mathbf{R}), \tag{E.7}$$

with the spin structure factor

$$\mathcal{S}_s(\mathbf{q}) = \frac{1}{L^2}\sum_{\mathbf{R}} C_s(\mathbf{R})\exp(i\mathbf{q}\cdot\mathbf{R}). \tag{E.8}$$

If we check the sum rules, we have

$$\begin{aligned}
\sum_{\mathbf{q}} \mathcal{S}_s(\mathbf{q}) &= \sum_{\mathbf{q}} \frac{1}{L^2} \sum_{\mathbf{R}} C_s(\mathbf{R}) \exp(i\mathbf{q}\cdot\mathbf{R}) = \\
&= \sum_{\mathbf{q}} \frac{1}{L^2} \sum_{\mathbf{R}} \frac{1}{L^2} \sum_{\mathbf{r}_i} \mathbf{S}(\mathbf{r}_i)\cdot\mathbf{S}(\mathbf{r}_i+\mathbf{R}) \exp(i\mathbf{q}\cdot\mathbf{R}) = \\
&= \frac{1}{L^2} \sum_{\mathbf{R}} \sum_{\mathbf{r}_i} \mathbf{S}(\mathbf{r}_i)\cdot\mathbf{S}(\mathbf{r}_i+\mathbf{R}) \left(\frac{1}{L^2} \sum_{\mathbf{q}} \exp(i\mathbf{q}\cdot\mathbf{R}) \right) \\
&= \frac{1}{L^2} \sum_{\mathbf{R}} \sum_{\mathbf{r}_i} \mathbf{S}(\mathbf{r}_i)\cdot\mathbf{S}(\mathbf{r}_i+\mathbf{R}) \delta_{\mathbf{R},0} = \\
&= \frac{1}{L^2} \sum_{\mathbf{r}_i} [\mathbf{S}(\mathbf{r}_i)]^2 = \frac{L^2 - N_h}{L^2} = 1 - n_h, \qquad \text{(E.9)}
\end{aligned}$$

since one can find a spin in each site of the lattice except the sites occupied by a hole. Starting from the second equation of (8.4) we obtain

$$\frac{1}{L^2} |\mathbf{K}_s(\mathbf{q})|^2 = \frac{1}{L^2} \frac{1}{L^2} \sum_{\mathbf{r}_i, \mathbf{r}_i'} \mathbf{S}(\mathbf{r}_i)\cdot\mathbf{S}(\mathbf{r}_i') \exp[i\mathbf{q}\cdot(\mathbf{r}_i - \mathbf{r}_i')].$$

With the same considerations as for the charge case we have

$$\begin{aligned}
&\frac{1}{L^2} |\mathbf{K}_s(\mathbf{q})|^2 = \frac{1}{L^2} \frac{1}{L^2} \sum_{\mathbf{r}_i, \mathbf{R}} \mathbf{S}(\mathbf{r}_i)\cdot\mathbf{S}(\mathbf{r}_i - \mathbf{R}) \exp[i\mathbf{q}\cdot\mathbf{R}] = \\
= \; &\frac{1}{L^2} \sum_{\mathbf{R}} C_s(-\mathbf{R}) \exp[i\mathbf{q}\cdot\mathbf{R}] = \mathcal{S}_s(\mathbf{q}). \qquad \text{(E.10)}
\end{aligned}$$

Finally we can write

$$\mathcal{S}_s(\mathbf{q}) = \frac{1}{L^2} |\mathbf{K}_s(\mathbf{q})|^2 \qquad \text{(E.11)}$$